Behaviour of Masonry Arches Under Foundation Movement

Ahmed Mohamed Naggasa

B.Eng (Hons), M.Sc.

****

This thesis is submitted in fulfilment of the requirements for the

degree of Doctor of Philosophy

School of Science, Engineering and Environment

The University of Salford

2023

Abstract

A significant number of UK bridges are masonry arches, with over 60% being more than a century old and bearing loads beyond their initial design intent. This poses a challenge for long-term assessment. Current assessment tools range from simplistic to complex finite element analysis models. However, only advanced models capture the brittle nature of masonry and the structural behaviour of multi-ring arches. Despite extensive research on masonry arches, further knowledge concerning the effects of foundation movements are required. This study focuses on the masonry arch subject to foundation settlement, sliding, and rotational movements.

State-of-the-art finite element analysis of masonry arches involves 3D micro-modelling, utilising the unique material properties of masonry. The bond strength between mortar and brick is crucial since it governs failure modes. This research used a detailed micro-modelling approach, using the extended finite element method in ABAQUS, simulating masonry cracking failures and capturing the non-linear three-dimensional behaviour.

Validation of the numerical models was achieved by comparing output to physical tests conducted at The University of Salford. Experimental studies on mortar, bricks, and masonry triplets provided both material properties and further understanding. A distinctive feature was the modelling of full-thickness mortar, using a cohesive segment approach, enabling damage simulation in the mortar without pre-set crack locations.

For multi-ring masonry arches with full-thickness mortar joints, cohesive interactions captured non-linear failures. ABAQUS's normal mesh density proved optimal in load-displacement representation. Sensitivity analyses were conducted on various factors like non-linear interface values, Young's modulus of elasticity, and mortar plasticity criteria.

Results revealed accurate predictions of masonry arch failure mechanisms. The validated models were subjected to foundation settlement, sliding, and rotation tests, revealing changes in structural behaviour due to foundation movement. Sliding and rotational movements notably reduced peak load capacity and stiffness due to the widening of existing cracks. Although settlement movements had minimal impact on peak load capacity, they did reduce stiffness. Combined movements indicated a pattern in abutment reactions, with the most substantial effect observed when sliding was double the settlement.

Declaration

I, Ahmed Mohamed Naggasa, declare that this thesis is my work. I have ensured that any portion or specific phrasing from another work or publication, if exceeding twenty consecutive words, has been cited where used and thoroughly detailed in the references section of this thesis.

Signed …… Dated …….

Acknowledgement

This PhD journey would not have been possible without God's help, and I am deeply grateful for the strength and patience provided, enabling me to pursue my PhD dreams. My heartfelt appreciation also goes to my parents, whose support was indispensable. I cherish and am proud to be their son. They have always been my cheerleaders, encouraging me through both good and bad times.

I extend my profound love and gratitude to my wife and son for their unwavering support during these challenging times.

I could not have completed my research without the guidance of my supervisor, Mr. Jonathan Haynes, who deserves my deepest thanks for his patience, ongoing assistance, and support throughout this lengthy process. His determination and calm attitude greatly facilitated my understanding of the subject.

Contents

List of Figures

List of Tables

Notation

C	Cohesion
C_c	Coefficient of curvature
C_u	Coefficient of uniformity
D_{10}	Effective size
Dr	Density index
e_{max}	Max void ratio
e_{min}	Min void ratio
G_S	Specific gravity
γ_d	Dry unit weight
$\gamma_{d(max)}$	Max dry unit weight
$\gamma_{d(\min)}$	Min dry unit weight
ϕ	Angle of internal friction
FEM	Finite Element Method
DEM	Discrete Element Method
XFEM	Extended finite element method
MEXE	Military Engineering Experimental Establishment
LVDT	Linear Variable Differential Transformer
UDEC	Universal Distinct Element Code
G_m	Represents mortar's shear modulus (MPa)
G_u	Unit shear modulus (MPa)

h_m	Mortar thickness (mm)
E_m	Mortar's joint elastic modulus (N/mm^2)
E_u	Brick elastic modulus (N/mm^2)
K_{nn}	Represents masonry joint stiffness for normal direction (N/mm^3)
K_{ss}	Masonry joint stiffness in shear direction 1 (N/mm^3)
K_{tt}	Masonry joint stiffness in shear direction 2 (N/mm^3)
ϕ_{cv}	Friction angle at constant volume.
ϕ	Peak friction angle.
ψ	Dilatancy angle.
x_{pl}	Plastic shear displacement.
τ_o	Initial shear strength (cohesion).
$\sigma_{cut\text{-}off}$	Cut-off limit of the tensile stress.
E_{pl}	Tensile plastic strain.
U1	X displacement direction (mm)
U2	Y displacement direction (mm)
U3	Z displacement direction (mm)
G_I	Mode I fracture energy in the normal direction (Tension) (N/mm)
G_{II}	Mode I and mode II fracture energies in the first and second shear directions (N/mm)

Chapter One

1 Introduction

1.1 Background

Masonry arches are among the oldest structures in the world (Ryall et al., 2000), used extensively by the Romans and even earlier civilizations over two thousand years ago (Catbas et al., 2013). During the industrial revolution, masonry arches were widely used in the construction of medieval cathedrals and bridges for railways and roads (Seward, 2014). Even though they are ancient, masonry arch bridges are still admired for their beauty and structural efficiency. They are favoured because they can create large open spaces without needing materials that are very strong in tension. However, until very recently, these arches were built using a process of trial and error, as they were difficult to understand fully (Ponnuswamy, 2008). Detailed studies of how these structures perform only began in the 17th century (Naggasa et al., 2018).

The masonry arch bridge is a crucial part of UK highway and railway infrastructure. It is in secondary, minor roads and railway systems where these types of bridges are prevalent. The County of Cumbria had many masonry arch bridges that collapsed because of flooding, such as Workington's Northside Bridge (Figure 1-1), which collapsed in 2009. As a result of the collapsed bridge, the town was left split in two, which was a significant inconvenience to the town's residents, resulting in them having to drive almost 18 miles to get to the other side of town. Furthermore, a temporary road bridge was built to reconnect the town at the cost of £4.6m (BBC News, 2016b).

Figure 1-1: Workington's Northside Bridge (BBC News, 2016b).

A masonry arch bridge known as Pooley Bridge was built in Cumbria in 1764, and the bridge collapsed because of abutment movement in 2016 (Figure 1-2). Cumbria County Council replaced it with a temporary bridge at the cost of £300,000. Also, the British government decided to give the town residents an aid package of £40m (BBC News, 2016c).

Figure 1-2: Pooley Bridge collapse (BBC News, 2016c).

Figure 1-3 depicts the single span Elland Bridge located in Calderdale, West Yorkshire which collapsed as a result of settlement and sliding of the left - hand abutment caused by the flooding. The bridge cost the government £5m to rebuild, and a further £500,000 was paid to create a temporary footbridge to help the residents cross the river.

Figure 1-3: Elland Bridge collapsed (BBC News, 2016a).

There is a significant body of research on masonry arch bridges with rigid abutments. However, there is relatively little research on arch bridges subject to foundation movement. The majority of this research is concerned with multi-ring, single span arches subject to uni-directional abutment movement. Further research is required to establish masonry arch bridge structural behaviour subject to foundation movement. It is believed climate change will exacerbate the problem.

The strength of a masonry arch comes from its shape. Essentially, these structures operate under the force of gravity, depending primarily on their compressive strength, while tensile strength does not need to be (Heyman, 1969).

Their behaviour at failure is one such area of study (Salter, 2013). These structures can fail for several reasons for example their collapse can result from excessive compressive stresses and movements around the foundation (Blockley, 2012).

Arch structures can also fail because of bond failure from a pre-existing crack through localised tension forces (Frangopol & Tsompanakis, 2014). In this area of research, it is also essential to

understand their behaviour when foundation movements occur. This thesis outlines a study to examine these structures' behaviour when there are foundation movements.

So, it is evident masonry arch bridges are a necessary part of our everyday lives. Previous research about this area has provided vital knowledge on how bridges behave and interact with their surroundings. Galassi et al. (2021), Coccia et al. (2015) and Zampieri et al. (2019) have shown that there is a need for further research on masonry arch behaviour, especially on abutment rotation, sliding and settlement.

Regular inspections and maintenance should be conducted to ensure the stability and safety of a masonry arch bridge under foundation movement, and any signs of distress should be addressed promptly.

1.2 Problem statement

Masonry arch bridges perform structurally through the transfer of non-uniform axial compression. Masonry arch abutment reactions consist of vertical and horizontal forces. Structural stability relies on the foundation's ability to resist these forces without significant sliding or sinking. If foundation movements are excessive the resulting forces may cause failure. These movements are the main causes of the failure of the structure (Yang, 1991). It should be noted that arches may be deemed to fail serviceability criteria long before collapse occurs. However, arches can withstand considerable movement before actually collapsing (Ochsendorf, 2006).

Several factors can cause foundation movements. Extreme events like earthquakes, flooding, and other disasters can generate sufficient foundation movement to cause structural damage (Asteris & Plevris, 2015). Most failures in the UK are a result of long-term foundation movements in compressible soils. Also, it is important to pay attention to other factors such as the material strength and age of the structure (Harding et al., 1993). Empirical analysis does not give all the physics of masonry bridges, whereas semi-empirical analysis gives some insight of the physical behaviour, which helps to understand the structure’s behaviour in relation to the horizontal and vertical forces generated. There are some computer applications or programs such as ABAQUS and UDEC that can aid in such an investigation. Empirical studies have been attempted before, but the area remains substantially unexplored because of the complexities inherent in such an investigation.

Therefore, it is essential to re-examine tests to check the kind of foundation movements that can occur and the resulting behaviour of the masonry arch structure (Ochsendorf, 2006). It is essential to categorise the foundation movements so that the behaviour of the structure can be analysed together with the corresponding foundation movement (Aita et al., 2015). There are serious repercussions if this topic of movement in masonry arch bridges is not adequately examined. Loss of life, disruption to transport, and infrastructure damage are some of the consequences of the failure of masonry arch structures. Costly emergency remediation works are the most likely outcome once this failure occurs (Melbourne et al., 2006).

1.3 Aim

The aim of this thesis is to investigate the structural behaviour of masonry arches under foundation movements.

1.4 Objectives

This aim will be achieved by pursuing the following objectives:

1. Review existing literature on masonry arch bridge analysis and material mechanical behaviour to understand historical and current developments. This will include numerical modelling strategies which may be conducted for masonry structures.
2. Conduct physical tests to establish masonry properties and behaviour.
3. Create and validate a 3D numerical model replicating masonry triplet tests to accurately represent the shear failure of masonry.
4. Using established modelling techniques, design and calibrate a 3D finite element (FEM) model for masonry arch structures, focusing on masonry hinge failure. Validate this model against full-scale masonry arch tests, considering load capacity and crack patterns.
5. Conduct a parametric study on the validated FEM model of an arch with rigid abutments to discern the impact of input data parameters on the arch's behaviour.
6. Employ the validated model to examine masonry arch behaviour under various foundation movements, including settlement, sliding, and rotational movements, with a consistent load on the arch barrel.

1.5 Outline research methodology

In order to achieve the thesis aims and objectives, the following research outlines are pursued:

- Objective 1 will be achieved by an up-to-date review of the published literature on masonry arch bridges, including the structural behaviour response, assessment investigation methods for masonry arches, material mechanical properties, and failure types. Furthermore, this will review the results of experimental tests on masonry arch bridges. This includes a review of published literature on numerical modelling strategies, with techniques to evaluate the reliability of each method. This aids selection of the software, modelling approach and implementation of non-linear behaviour to capture the appropriate structural response in terms of cracking.
- Objective 2 will be achieved by undertaking a series of experimental tests on masonry couplets and triplets, mortar cubes, and mortar cylinders. The result of these tests will be used to inform the material properties for use in the numerical analyses.
- Objective 3 will be achieved by creating numerical prism models informed by the literature review, incorporating the material properties from the experimental tests. Furthermore, the significant purpose of this objective is to select reliable and appropriate computational modelling to ensure that all types of failure, such as tension and shear, are implemented correctly in any numerical model for this study. The prism models will be validated against experimental results identified in objective 2 and data taken from the literature. This will also include a parametric study of material properties to examine how they affect the structural behaviour of both the triplet and arch.
- Objective 4 will be achieved by creating a numerical masonry multi-ring arch model using the techniques and properties developed under objective 3, or from the literature review. The arch numerical model will be validated against an experimental masonry arch test identified in the literature review. This masonry arch test was carried out at the University of Salford for the 'Sustainable Bridges - Assessment for Future Traffic Demands and Longer Lives' research project. Chapter 4 will present the numerical model which will include all the masonry failure mechanisms identified in the masonry prism models. This will include a mesh sensitivity study.
- Objective 5 will be achieved by conducting a parametric study using the validated numerical model of the masonry multi-ring arch on rigid abutments. The parametric

study was used to establish the validity of several material and modelling parameters; these were fracture energy, tensile strength, Young's modulus of Elasticity and the constitutive law used to model the full-thickness mortar and the interaction between the elements.

- Objective 6 will be achieved using the validated numerical model of a full-scale masonry multi-ring arch to investigate abutment movement, including settlement, sliding and rotational movements of one abutment by applying various displacement values at the right arch abutment under displacement control. Some combinations of movement, e.g. proportions of vertical and horizontal movement, are also investigated. The purpose of this objective is to describe the arch's behaviour under foundation movement by increasing the displacement in each direction until the arch becomes unstable. In addition, this assists the understanding of the behaviour of the masonry arch subject to foundation movement.

1.6 Scope and limitations of the research

The primary purpose of this thesis was to investigate multi-ring masonry arch structural performance under static load conditions and under one abutment movement in various directions. The load was applied on the arch ring up to failure using numerical models validated using experimental arch test data. Furthermore, it includes masonry prisms tested experimentally and modelled numerically to investigate the mortar joint failure and ring separation under pre-compression loads. The masonry prisms' mechanical characteristics are initially described by experimental tests using a standard mortar mix, as this mix has been used commonly to construct experimental multi-ring masonry arches. Also, the actual report of the masonry arch experimental tests material properties contained only the compressive strength of individual materials. Due to this, additional material parameters were selected from previous research to create a detailed non-linear model (Table 5-4, Table 5-5 and Table 5-6). The numerical model of the arch was the same width as the physical experiment test. However, no perpend joints were included across the arch width in the numerical model to reduce computational effort because the masonry arch bridge is a plane strain problem.

This study does not cover masonry arch structural performance investigations under cyclic or dynamic load conditions. Like the physical experiments, the numerical models use displacement control to apply loading. Furthermore, the large-scale masonry arch numerical

models did not include the backfill and spandrel walls which form part of real masonry arch bridges.

The validation section for the large-scale multi-ring masonry arch was based on the published results of the experimental test, which are three load-deflection graphs and the collapse state crack pattern.

The numerical models were subject to differential foundation movement in three directions; vertical settlement, horizontal sliding and rotation. The arch ring physical tests which the numerical model was validated against did not include foundation movements of any kind, and there is no published information of equivalent multi-ring experimental tests of this kind including foundation movements.

The extended finite element method (XFEM) was utilised to simulate the crack pattern at failure and propagate cracks in the mortar joints. This method closely replicates actual conditions and does not require a predefined crack location.

1.7 Organization of the thesis

Chapter 1 provides the aims, objectives and the statement of the research with a short introduction to masonry arch bridges.

Chapter 2 presents a review of masonry arch bridges, including the history, construction of the masonry arch bridge and standard experimental tests to obtain such material properties. In addition, it provides previous research on this topic, including full and small-scale experimental tests and theoretical research. Furthermore, it presents the mechanical behaviour and factors influencing masonry arch response. Following that, previous experimental and theoretical for masonry arches subjected to foundation movements are presented and critically discussed.

Chapter 3 includes a detailed description computational modelling of masonry structure. This chapter aims to critically review and compare the analysis methods, techniques, approaches and strategies of the selected reliable method to model and investigate 3D masonry arches' non-linear structural behaviour. The selected software and the tools to model the masonry arch have been reviewed.

Chapter 4 includes the experimental work undertaken to establish masonry triplets and investigate the brick and mortar mechanical properties through shear, compressive and tensile tests later used in the numerical models. The preparations and the procedures for each material test are presented. Also included are the numerical models of the masonry triplets created using ABAQUS software using cohesive interaction at the brick-mortar interface and the extended finite element method (XFEM) to represent cracks in the mortar. Furthermore, a parametric study covering material properties was conducted in this chapter.

Chapter 5 includes a detailed description of the Arch G experimental test previously undertaken at the University of Salford; and the numerical model subsequently created of Arch G and validated against the experimental test. There is a parametric study on the non-linear interface properties of the numerical model presented later in this chapter.

Chapter 6 presents an investigation of masonry arches subjected to four different foundation movements - horizontal, vertical, rotational, and rotational inverse. It also presents a study of combinations of movement at the right-hand support of different displacement values. Finally, it presents a comparison between the behaviour of a fixed support masonry arch and the masonry arch subject to foundation movement.

Chapter 7 includes the research conclusion, the main outcomes, and further work recommendations.

Chapter Two

2 Literature Review on Masonry Arch Bridges Experimental & Numerical Research

2.1 Background

Masonry arch bridges are some of the oldest types of bridges built by humans. They first appeared around 5000 years ago in the Middle East, Mesopotamia, and China (Chatterjee, 1985; Page, 1993). About 4,900 years ago, the Chinese started using stacked horizontal stones in their construction, but this method was inefficient for longer spans (Apreutesei & Oliveira, 2005). The elliptical brick arch was the first arch made of wedge-shaped stones or voussoir arch. It was constructed in Egypt and featured in the tomb of Amenophis I around 1800 BC (Smith, 1965).

In the past, the most effective use of masonry arch bridges was in the Roman era, as early as 109BC. Also, the Romans in that period used different materials and structural forms that helped to solve the problem of bridging a gap. The use of arches is a highly suitable solution to this problem. Many of these bridges are still in service in Spain; the Alcántara Bridge is shown in Figure 2-1. The Alcántara Bridge is a roadway across the Tagus River, 47 m above the river, 7.8 m wide, and the bridge's centre span is 28.8 m. The usable length of the continuous arch structure is 150 m.

Figure 2-1: Alcántara Bridge (De Matías et al., 2013).

In the UK, about 40,000 masonry arch bridges are still in operation. Approximately 60% of these bridges are over a century old, built between the 17th and 19th centuries (Melbourne, Wang, & Tomor, 2007). This demonstrates the long-lasting and reliable nature of masonry as

a construction material. Most of these masonry arch bridges are controlled by authorities overseeing navigable waterways, highways, and railways (Melbourne et al., 2006).

Approximately 10,000 masonry arch bridges are part of Italy's railway network infrastructure. Most of its masonry arch bridges date back to the late 1800s, with the most common bridge span being between 2 m and 5 m which accounts for almost 20% of the railway network. Other masonry arch bridges include spans of 5 m to 10 m and over 10 m. These are relatively few and account for 11.5% and 8.5% of the railway network (De Santis & de Felice, 2014). During a similar period, masonry arch bridges and viaducts built in Spain exceeded 3,000, accounting for almost 45% of Spain's road and railway infrastructure (Martín-Caro Álamo, 2013).

Although the majority of masonry arch bridges are in operation (Melbourne, Wang, & Tomor, 2007), it is evident that over time these bridges have deteriorated, and their life expectancy has undoubtedly changed (Brencich & Morbiducci, 2007; De Santis & de Felice, 2014; Oliveira et al., 2010). Originally, masonry arch bridge design was based upon limited experimental principles, where factors such as foundation settlement, increased loadings and environmental changes (earthquakes, fluctuations in temperatures and flooding) had not been previously considered. These have had a detrimental impact on the primary construction material, masonry (Olofsson et al., 2005).

British masonry arch bridge design underwent major developments in the 18th century. These included stiffening and relieving arches – these additional approaches subsequently became common usage (Colla et al., 2002; Melbourne et al., 2006). A rationalised set of section profiles were utilised in arch barrels from around 1850 to 1900, meaning that the use of semi-elliptic and parabolic arches were rare (De Felice et al., 2016).

2.2 Masonry arch bridge

Masonry arch bridges may be categorised in different ways but most commonly by arch barrel shape, construction material, whether single or multiple spans, whether skew or square, and by type of vehicle traffic.

1) Structure shape type - the most common shapes of masonry arch bridges are segmental, elliptical, semi-circular, three-centred drop, and gothic (Jagadeesh & Jayaram, 2004).

However, according to Page (1993) and Bennett (1999), the Roman arch types were virtually always semi-circular, according to Melbourne et al. (2006), the semi-circular arch concept was the perfect Roman arch concept that did not distinguish between aesthetic quality and structural performance. Furthermore, during the primary arch bridge building era, most arch shapes were either three or semi-elliptical, circle segments, five or seven centred circular (this shape resembles an ellipse). Semi-ellipses and parabolic arches are rarely used in construction due to the difficulty of setting out.

2) Structure material type – brick and stone units are the primary materials used in masonry arch construction. The bricks and stone are separated using beds and vertical (perpend) mortar joints. Recent arch bridges use various construction patterns and materials, such as brick and concrete.

   Most arch bridges were built using stone until the 18th century, when the industrial revolution began. Random rubble was often used as fill within the whole bridge, such as above the arch, spandrel wall or foundations, which consisted of irregular and uncut stone (Melbourne et al., 2006).

   The mortar volume depends on the masonry structure type; the mortar volume per unit arch volume varies considerably. In contrast, in the case of ancient arches, the mortar volume started from zero per cent; in the case of bridges of random rubble, mortar volume increased to over 20 per cent. Traditionally, lime mortars, which are plastic and tolerant of minor movements, were utilised. The mortar type, properties and percentage significantly impacts the performance and behaviour of the structural elements of masonry arch bridges, especially the arch barrel.

   Stone is one of the oldest building materials, and it is quarried from natural rock. The critical physical properties of construction stone are high shear and compression strengths. In the UK, the sedimentary rocks such as sandstone and limestone are the most commonly used stone types. Due to transport cost, it was common to use the locally occurring rock in construction.

   Clay bricks are produced by firing natural clay at high temperatures. Arches are generally constructed using high strength brickwork, often Class A or B bricks of compressive strength exceeding 50 N/mm^2.

2.2.1 *Masonry arch bridge - structural elements*

The masonry arch bridge is composed of distinctly different structural elements, each of which has a specific purpose and interacts with the other structural elements. The primary purpose of the bridge is to transfer the applied load through the arch to the foundations (abutment). The fill material placed over the arch is often considered to be non-structural, which creates a horizontal surface (Blockley, 2010).

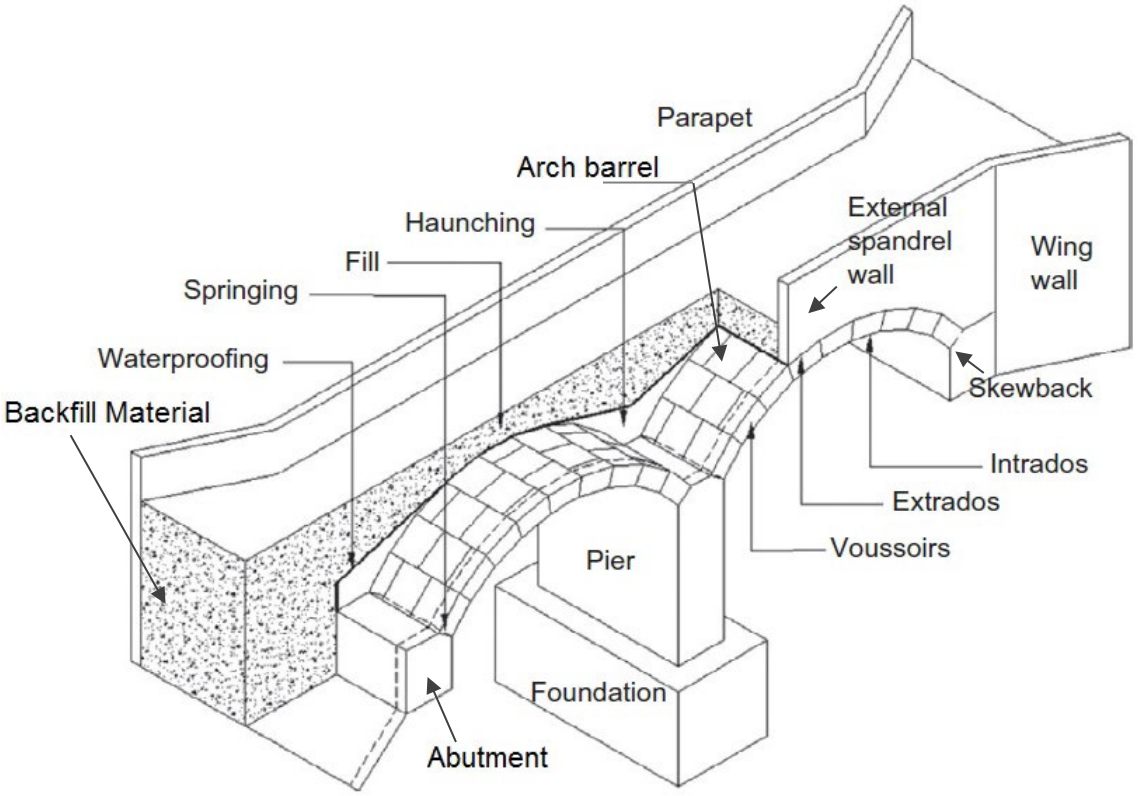

Figure 2-2: Elements of a masonry arch bridge (UIC Code 778-3R, 1994).

The typical masonry arch bridge elements as depicted in Figure 2-2 are:

1) Arch barrel: the barrel is the primary load transfer element; it transfers the load to the bridge's abutment. The arch barrel could be designed as a single layer or several layers of voussoirs. The arch barrel mechanism work in such a way that vertical forces applied to the extrados are transferred through the units as compression forces, and therefore, reactions at the abutment will have both vertical and horizontal components, ensuring the arch is always in compression.

According to Melbourne et al. (2006), critical characteristics of the arch barrel are its thickness, number of rings and the connection type between the rings. The multi-ring masonry arch is connected using uninterrupted radial mortar joints or crossed by headers, as shown in Figure 2-4. This significantly increases the connection shear strength between the arch rings. Stone arches are typically built of one ring which could be in regular-depth large blocks form. Also, the thickness of the blocks could be the arch barrel thickness. Alternatively, the stone arch can be built of various irregular blocks. As a result, the arch extrados may not follow the intrados shape.

Square bridges have no skew angle, therefore have bedding planes parallel to the abutments. Nevertheless, bridges with large skew angle introduce considerable constructional difficulties. Figure 2-3 displays three construction methods of 45-degree skewed intrados segmental arches.

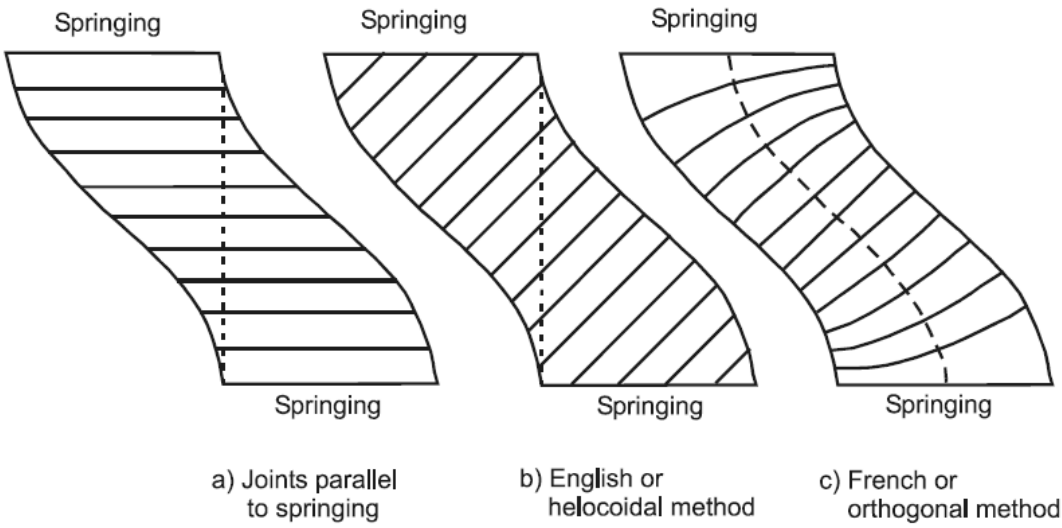

Figure 2-3: Skew bridge construction patterns (Melbourne & Hodgson, 1995)

2) Arch spandrel walls: the spandrel wall is constructed on the edges of the arch barrel and retains the backfill between road level and the barrel (Fanning et al., 2001; Heyman, 1982). The backfill occupies the spandrel wall space, retained transversely by the spandrel walls on the arch's edges. Also, the backfill material varies greatly, which is utilised to fill space between the spandrel walls. The material choice is determined by local availability (Melbourne et al., 2006).

The spandrel walls have a principal responsibility to serve as retaining walls for the backfill material and provide safety for the users by confining errant vehicles. In numerous cases, there is a difference in thickness between the spandrel walls and the parapets, the spandrel walls can increase towards their base which increases the bridge's stability. Occasionally, on plan, spandrel walls can also be arched which will also improve earth retaining capacity.

In a few cases, the original parapets for masonry bridges have been reinforced or replaced with different types of parapets. The original parapets may need more capacity to satisfy modern vehicle containment requirements.

In some cases, of large span bridges, intermediate spandrel walls may be included across the width of the barrel to increases its stiffness against sway. Furthermore, these arrangements could be used to make the masonry arch bridge structures stiffer and lighter. Another alternative is open spandrels which are used in large-span bridges, where the transition between the central arch and the bridge's surface is achieved using a series of pillars and small longitudinal arches (Melbourne et al., 2006).

3) Intrados and extrados: these are the arch barrel's lower and upper surfaces, respectively.

4) Abutment (foundation) and pier: these two have the same purpose of resisting the arch reactions and transferring them to the ground. They have different locations; the pier is constructed in the middle of the bridge with more than one span, and the abutment is placed at the end of the bridge (Heyman, 1982, 1996). Masonry arch bridge foundations are frequently composed of relatively shallow spread foundations. Timber piles were often utilised as a construction platform when solid ground was deep below the surface. However, timber piles have a substantial disadvantage; this type of foundation may have rotted over the years, resulting in movements in abutments and piers and loss of support (Melbourne et al., 2006).

5) Skewback: these are the arch barrel reaction points, where the angled thrust line is dispersed into the abutment. However, one possible failure mode is the bridge's arch sliding at the skewback, so sliding is dependent on the skewback angle. Skewback sliding can be avoided if reinforcement is added, where it acts as a shear key (Melbourne et al., 2006).

6) Backfill material: this material is used to spread the load to the arch barrel. Also, it helps to distribute the applied loads on the bridge (Callaway et al., 2012). (Fairfield & Ponniah, 1994; Royles & Hendry, 1991), suggest that the backfill also functions to provide passive resistance to lateral movement. Historically, backfill was often the material excavated to construct the arch foundations. However, its strength could be improved by compaction. According to Melbourne and Hodgson (1995) in most masonry arch bridges, the backfill material usually reaches a significant strength and maybe some degree of cementation due to loading compaction after a considerable service life.

   Puddled or tar clay waterproofing layers were occasionally used between the bridge extrados and the backfill material, enhancing the masonry's durability by preventing water from percolating through the masonry, stopping damage to the mortar joints and washing away the backfill fine particles.

2.2.2 *Behaviour of the arch barrel*

The arch barrel is the principal structural load transfer element. According to (Melbourne & Gilbert, 1995), the masonry arch barrel can be constructed in various typical bond styles, as displayed in Figure 2-4. Brickwork arch barrels are often constructed using multi-rings, and they are connected using a mortar joint or using interconnecting headers. The multi-ring arches are considered to be complex features. Figure 2-4 illustrates the common bond styles of the arch barrel, where the stretcher bond style in Figure 2-4 (c) is most commonly used as it permits the barrel to be built ring by ring, connected only by a mortar joint between separate rings, where the failure mechanism will affect each ring separately.

The primary failure mode in stretcher bond multi-rings is ring separation. However, this failure type can be prevented using header bricks in the bond which increases the shear strength of the inter-ring connection. It has to be clear that arch barrels could be built using several materials such as stone and concrete.

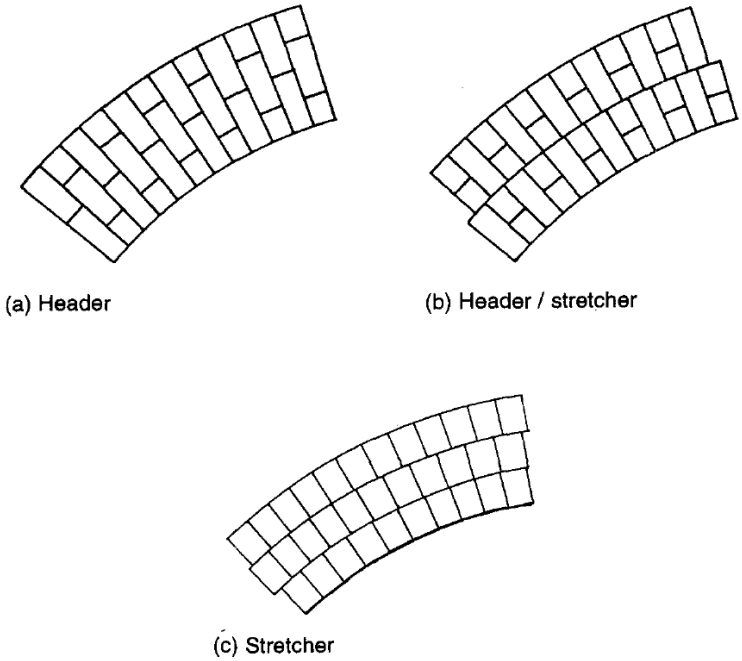

Figure 2-4: Styles of typical bonding (Melbourne & Gilbert, 1995).

In 1675, Robert Hooke was a prominent polymath who considered masonry arch bridge behaviour by publishing a book on helioscopes which contained a series of anagrams, one of which was deciphered after his death (Block et al., 2006): (translated from Latin to English) '*as hangs the flexible line, so but inverted will stand the rigid arch'*, as shown in Figure 2-5 (Heyman, 1998).

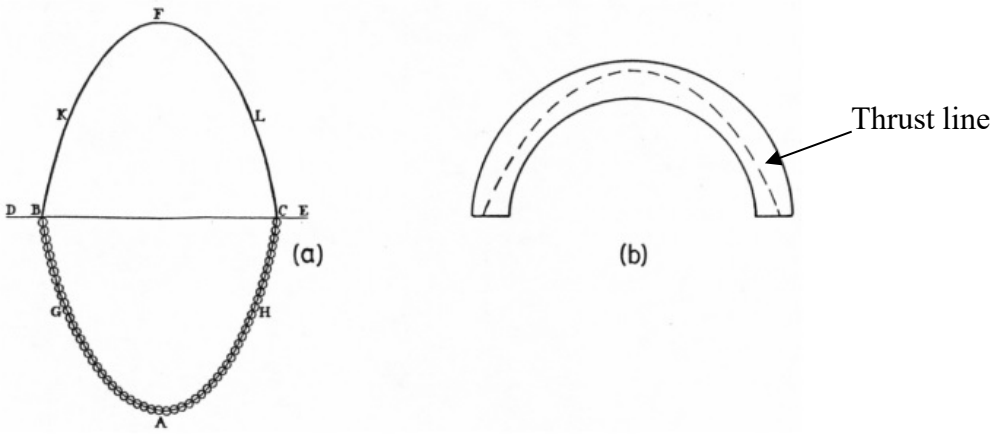

Figure 2-5: (a) Inverted cable or chain and (b) arch voussoirs on imaginary thrust line (Huerta Fernández, 2006).

Robert Hooke characterised the shape which the chain forms in tension as a catenary, as shown in Figure 2-5 (Block et al., 2006). As a result of this relationship, the shape formed when a chain hangs under its self-weight if inverted shows the compressive force path for an arched

structure under self-weight, as shown in Figure 2-5 (a). The masonry arch shape can be adequate, and the arch can stand effectively if the line fits into the inverted arch, where the line is known as the thrust line. The arch geometry provides a resistance mechanism and transfers the loads through the arch, which means that the capacity depends upon the entire arch span (Melbourne & Gilbert, 1995). The arch is also built in such a way that the applied load on the arch is transferred through the fill to the barrel and, after that, into the arch abutments, which produces vertical and horizontal forces on the arch abutment.

Since the eighteenth century, several experimental studies have used different scale models with different materials. For instance, Gautier used voussoirs of wood in 1714, Danyzy used plaster voussoirs in 1732, Robinson used chalk voussoirs in 1822; Pippard, Chitty and Tranter used steel voussoirs in 1936, and Ashby and Pippard used concrete voussoirs in 1939 (Frézier, 1738; Hodgson, 1996; Hubert, 1714; Pippard & Ashby, 1939; Pippard et al., 1936).

In 1714, Gautier used wooden voussoirs to measure the abutment thrust magnitude using several half-arch models. During this trial, he superimposed voussoirs at the half arch springing to ensure they were in equilibrium. The blocks of the arch were positioned very carefully in order, and these blocks were removed until arch failure happened. At the same time, the weight of the block was restricted to obtain the abutment thrust magnitude.

In 1737, Frézier discovered an approach to obtain the value of the thrust in a masonry abutment, which required the masonry pier dimensions. Moreover, in the discussion of the experiment, Frézier involved Couplet's reports on mechanism formation, as illustrated in Figure 2-6 and Couplet's reports were based on tests that were completed by Danyzy in 1732, where plaster voussoirs formed the arches.

The initial study to create the arch failure is shown in Figure 2-6. To create the line of thrust otherwise known as the 'hanging chain', a point load is first established on the arch. As this point load increases, the thrust line moves, where the line touches the extrados, and intrados the of the arch tensile failure points (or cracks) are identified, thus, creating the failure mechanism. This four hinge mechanism can be applied to more complex structures.

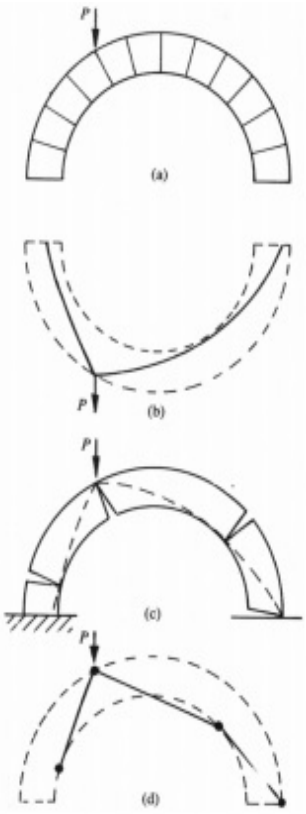

Figure 2-6: First trials of masonry arch collapse process explanation (Huerta Fernández, 2006) .

La Hire and Couplet produced masonry arch theories which led to the concept of the line of thrust and the collapse mechanism being derived (Hodgson, 1996).

Numerous rules discovered in the nineteenth century are still used in masonry arch analysis today. The middle third rule by Navier (1826), for homogeneous material applies to the masonry arch.

According to Tsutsui et al. (2010) the rule states that tension can be averted in an elastic section if the thrust line remains in the middle third of the section. Navier's formula for the thrust at the crown was used by Rankine to maintain equilibrium. Also, a horizontal pressure system was necessitated. Therefore, the function of the geometry of the arch, being horizontal at the crown and perpendicular to the abutment face at the support as shown in Figure 2-7. Rankine declared that '*The stability of an arch is secure if a linear arch (line of thrust) balanced under the forces which act on a real arch can be drawn within the middle third of the arch ring*'.

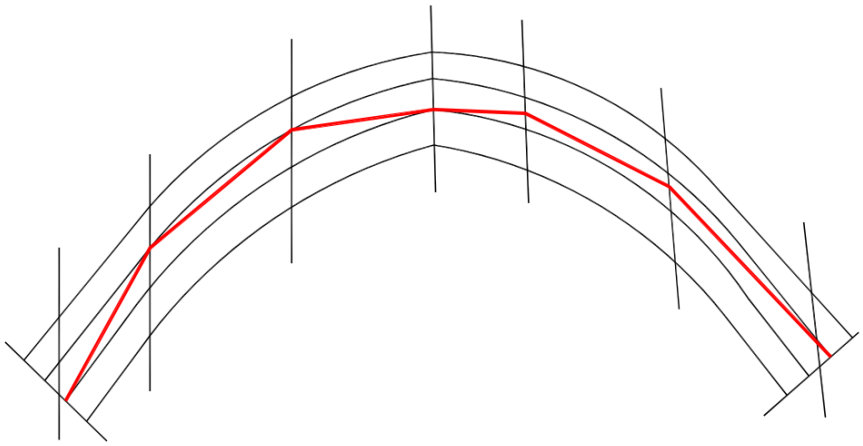

Figure 2-7: Thrust line (Heyman, 1982).

In 1846, Barlow conducted an experiment as shown in Figure 2-8, where the joints between voussoirs were provided using small wooden blocks, representing a line of thrust (Corradi & Filemio, 2004). The results obtained from Barlow's experiment showed that there are many available thrust line positions, which will exist between a maxima and minima thrust line (Ochsendorf et al., 2004). Conversely, no stable masonry arch can be connected to a single thrust line.

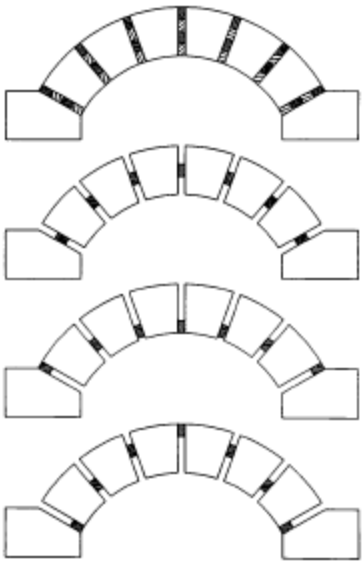

Figure 2-8: Barlow's experimental arch (Hodgson, 1996).

Barlow clarified the significance of the thrust line in masonry arches. He created an experiment which used six voussoirs of an arch barrel, where four timber blocks separated each voussoir as in Figure 2-9. As a result of this experiment Barlow concluded that the arch can stand with

joint blocks removed if the blocks of timber associated with the line of thrust remained in position.

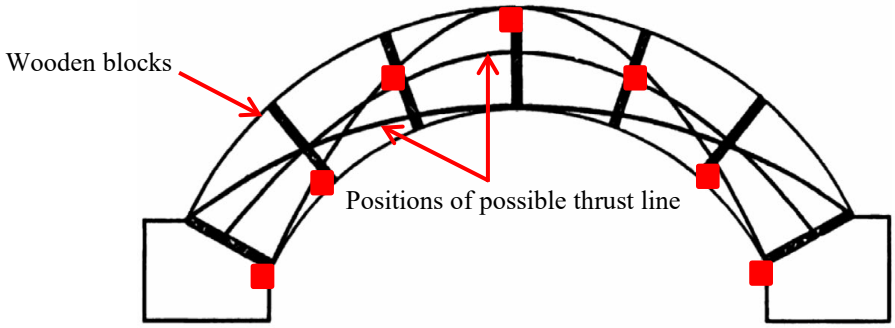

Figure 2-9: Barlow's experimental arch line thrust range (Sarhosis, De Santis, et al., 2016).

The importance of the thrust line is to determine the location of elastic failure in the arch. In addition, the thrust line may take many forms depending on the load distribution and the arch shape. Referring to Figure 2-10, it is clear that the line of thrust has limitations – there are maximum and minimum lines which can fit within the arch boundaries. If the thrust line reaches the intrados or extrados of the arch barrel, it means a plastic hinge has formed (a crack which passes through the entire depth of the arch barrel), although in masonry these are referred to as 'brittle hinges' (Taylor & Mallinder, 1993).

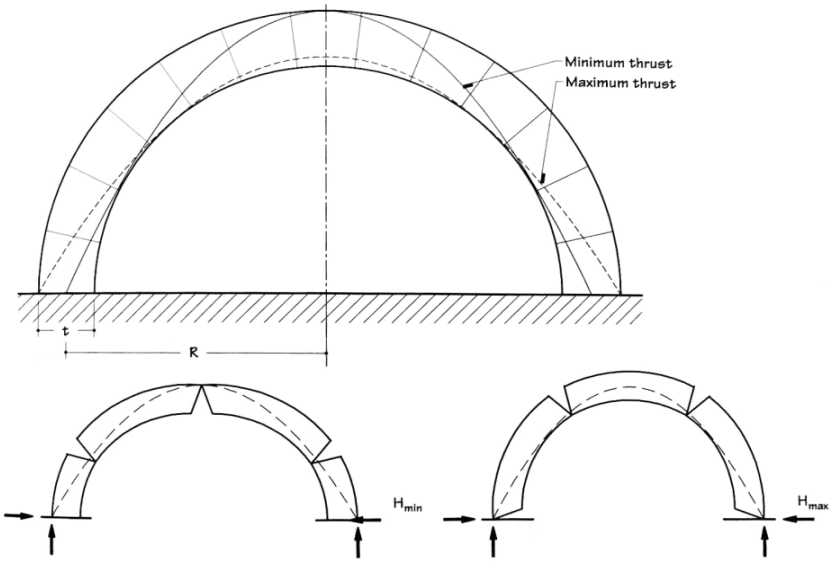

Figure 2-10: Maximum and minimum thrust lines (Nobile & Bartolomeo, 2014).

The minimal thrust line represents the minimum amount of force, which a voussoir pushes against the adjacent element. The maxima thrust line represents the maximum amount of force, which a voussoir can push against the adjacent element. This is often limited by the crushing strength of the material, or a global instability (Block et al., 2006).

The plastic hinges and the rotations create the arch deformities as the collapse mechanism advances by plastic hinge generation. Also, (Page, 1995) when the load exceeds the plastic hinges rotation resistance, the mechanism hinges will be formed.

Robert Hooke defined an elastic material by the equation $F = Kx$, where F is the applied force, K is the elastic material stiffness and x is the change in length. Castigliano used this to develop his principle of minimum stain energy, which the Austrian Society of Engineers and Architects proved can be applied to masonry arches in 1890. To use Hooke's law in terms of stress and strain, stress is the pressure imposed on a particular zone inside a material as a result of the outwardly imposed strain i.e. deformation. Within the elastic range, stress is proportionate to strain. Robert Hooke also wrote, '*None but the catenaria is the figure of a true and legitimate arch*', while Heyman adopted this formula to describe three forces imposed on a weightless string. The funicular polygon inverted defines the thrust line as displayed in Figure 2-11 (Heyman, 1982).

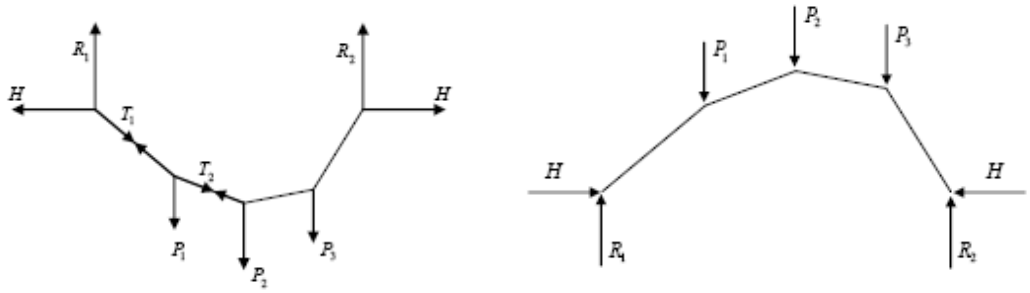

Figure 2-11: The thrust line and inverted funicular polygon (Heyman, 1982).

Pippard conducted tests using different arch voussoirs such as concrete and steel materials in the 1930's, and published a text (Pippard, 1947). In these experiments, all models were voussoir arches, and both supports were pinned. Hodgson (1996) reported good correlation between Pippard's experimental results and predictions using Castigliano's theory of strain energy. Weights were then suspended from the arch to imitate the backfill dead load (Sarhosis, De Santis, et al., 2016). When lime mortar was used between the concrete voussoirs to form a masonry arch bridge, tensile cracking coincided with the thrust line been outside the middle third.

From Pippard's experiments in 1948 much valuable information was gathered (Sarhosis, De Santis, et al., 2016):

- The voussoir arch failed when a four-hinge mechanism formed, which is the common behaviour of an elastic rib.

- More importantly even after the first crack appeared in the arch, the structure seemed to have substantial reserve of strength before collapsing.

- If slip occurred between the arch voussoirs, it happened in conjunction with crushing and spalling of the mortar.

- It was demonstrated that tensile cracking was only observed when the thrust line was outside the middle third of the section. This was the basis for Pippard's creation of the middle half rule for his elastic analysis method.

For analysis purposes arches may be conceptualised as containing three, two or no hinges. Masonry is able to withstand very little tensile stress before cracking occurs (Curtin et al., 2008), so every mortar joint is a potential crack location and Pippard observed that mechanism failures always included hinges at rigid abutments and used this to simplify his arch analysis model to include two hinges at the abutments. The vertical load acting on arch bridges, produces a lateral thrust (compression) in the arch. These forces then travel along the arch curve to the abutments, where the abutment generates opposing reaction forces, as shown in Figure 2-12.

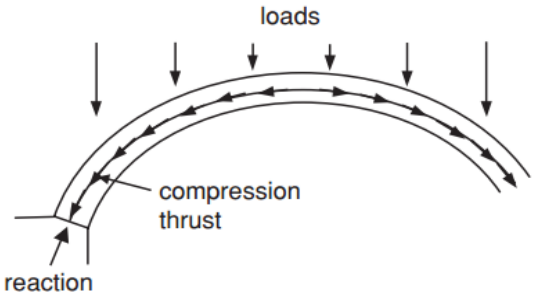

Figure 2-12: Direction of forces in a masonry arch (Curtin et al., 2008).

If the resultant force on each voussoir is plotted at each voussoir's centroid, this is equivalent to the thrust line. If this visual representation stays within the middle third, then no tension exists in the barrel. Tension can be generated by live load applied at the road surface. If the thrust line reaches the extrados or intrados of the arch, then a full tension crack exists in the barrel. This is analogous to a plastic (or brittle) hinge (Heyman, 1982). If the thrust line touches

the extrados and intrados at enough points, then a mechanism is formed, and the arch is unstable (Heyman, 1982) as shown in Figure 2-13.

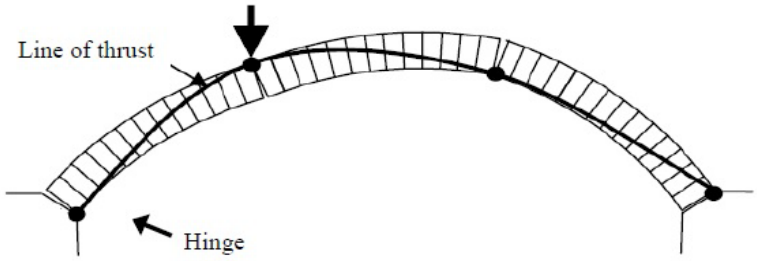

Figure 2-13: Masonry arch thrust line (Tao, 2013).

The arch backfill material assists in augmenting the compressive force in the barrel. This permits superimposed deck loads to be resisted without tension developing at the faces of the barrel (Callaway et al., 2012).

A slender strut is a structural element which is subject to compression and fails by buckling, rather than yielding. A strut which is curved in one plane is an arch. A vault is formed by extruding an arch in the plane perpendicular to its curve (Haynes, 2020). The fundamental structural form of a masonry arch therefore, is a vault. Since masonry has excellent material properties for the resistance to axial compression, it is an appropriate material for use in vault construction.

The orientation of a masonry arch means that its self-weight will generate axial compression in the arch so long as the supports are sufficiently rigid in the translational directions. Since the distribution of self-weight (backfill) is not uniform, the longitudinal distribution of axial compression will be non-uniform. Any applied non-uniform live loads will also produce a non-uniform distribution of bending moment along the masonry arch. Since masonry arches are often used as bridges, the live loads move along the bridge deck, which produces a changing deflected arch shape. To simplify the assessment process, live loads are onerǫusly considered to be located at quarter and mid-span, which produces side sway and symmetrical sway deflected shapes, respectively.

It is common to assess masonry arches by evaluating direct stress (axial and bending stress) in the cross-section, due to self-weight and live loads, using basic stress theory. This permits the displaced neutral axis to be located. This can then be used for the thrust line location which is the centroid of the compression force in the arch barrel. If this is plotted along the arch, this

becomes a useful visual tool since tension crack development is theoretically indicated to have started once the thrust line reaches the boundary of the middle third of the arch depth. If live loads are increased sufficiently, the tension crack will open further, and the line of thrust will move outside the middle third. When the line of thrust reaches the outer surface of the arch, a tension crack is considered to have developed across the full depth of the arch, this is often referred to as a (brittle) hinge. In reality, the arch can only remain standing if a compression zone still exists at the crack location, however small. The arch will become structurally unstable when sufficient hinges have formed to permit collapse to occur. If the compression zone has shrunk to an extent that the compressive stress reaches the compression resistance of the masonry, crushing failure can occur.

Pippard justifies the middle third rule for elastic thrust lines and demonstrates that ultimate capacity is independent of the first crack load. The middle third rule is as shown in Figure 2-14.

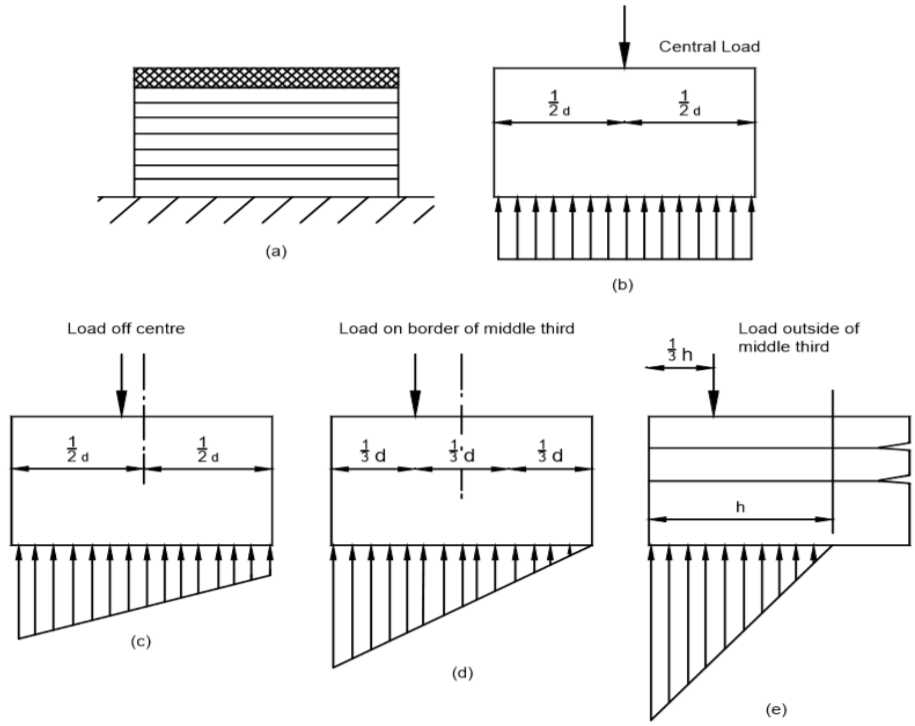

Figure 2-14: Middle third rule stress distributions (Heyman, 1982)

2.2.3 *Soil structure interaction*

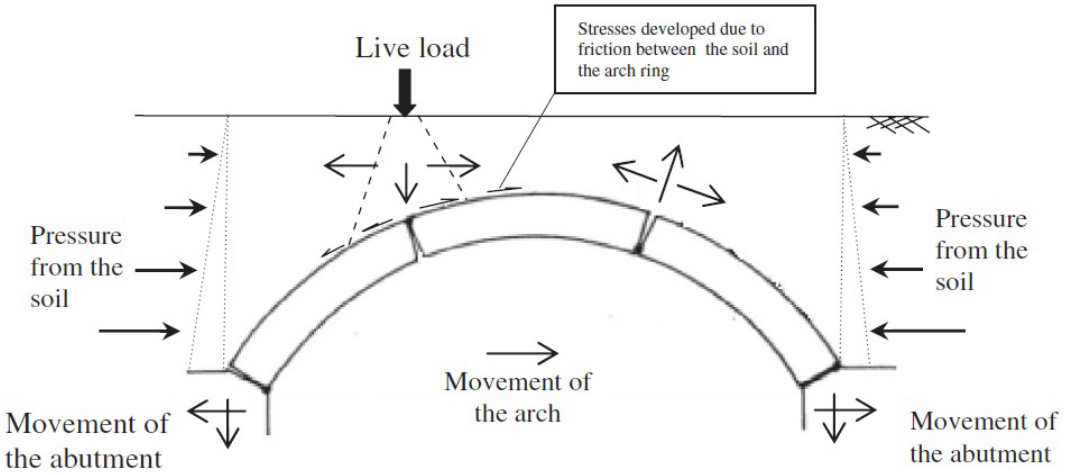

Figure 2-15: Soil arch interaction (Sarhosis, De Santis, et al., 2016).

The masonry arch bridge includes more than just an arch barrel and abutments; it also comprises backfill material and spandrel walls on the edge of the arch barrel. The backfill has various functions in the masonry arch bridge as shown in Figure 2-15, for instance, it is used to level the road surface, and it has a significant purpose in arch performance, such as (Gilbert et al., 2013);

- Live loads generate arch barrel movements which may be into, or away from the backfill. Most common is side-sway generated by non-concentric loading, which is partly resisted by the self-weight of the backfill.
- Live load applied at the top of the backfill surface is dispersed through the backfill material to the arch barrel and reduces the effect of bending stress in the arch barrel.
- The backfill dead load and barrel self-weight pre-compresses the barrel providing resistance to the tension developing effects of live loads.

It is imperative that the soil material properties are derived correctly to ensure they are a realistic representation of the backfill material; for an accurate representation this would require some sort of elasto-plastic stress-strain relationship. The backfill material is an integral part of the masonry arch bridge as it allows loads acting upon the structure to dissipate, while at the same time providing transverse resistance. Therefore, providing an accurate behaviour illustration of the backfill interaction is imperative, the elasto-plastic method allows this to a certain point, as it is limited to backfill-arch interaction (Zhang, 2015).

Backfill is considered to have a major impact on masonry arch bridge durability. It dissipates live loadings, and reduces the impact on the arch barrel in that it resists pressures in the passive region thus reducing the sway in the arch (Callaway et al., 2012). These impacts were not known until the last century when the transport industry highlighted fatigue problems in masonry arch bridges, thus resulting in soil structure interaction being a focal point in recent research.

Pressures in the passive and active regions are only activated once loading is applied at the bridge surface. The passive motion results from the arch moving into the soil, while the active motion results from the arch moving away of the backfill. The vertical pressure has been described as straightforward to calculate, as little strain is required to activate it, whereas to quantify the pressure in the passive region is much harder (Callaway et al., 2012). Full passive pressures are often not activated, as soil strains are not large enough. To overcome this, earth pressure theories have been used to quantify the passive pressure.

Smith et al. (2004) concluded from full-scale experimental results, that the masonry arch load-carrying capacity with backfill is ten times stronger than it is without backfill as shown in Figure 2-16.

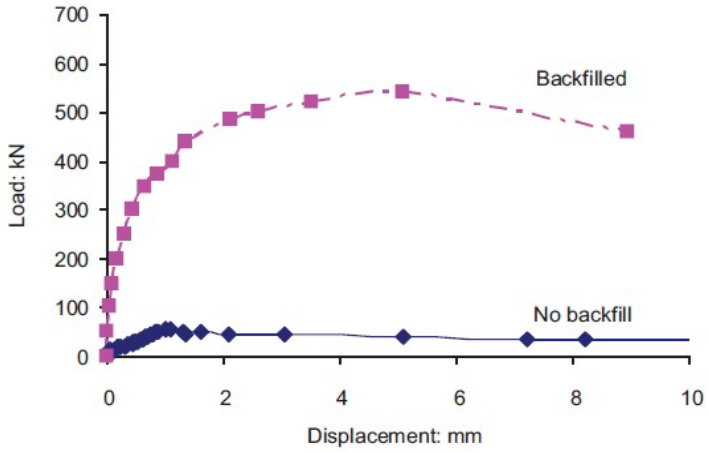

Figure 2-16: Soil backfill influence (Callaway et al., 2012).

Several factors may affect the load-carrying capacity, such as; active pressure, distribution of live load and pressures of passive restraint (without backfill and with backfill). These are recognised in model experiments carried out by Gilbert et al. (2012) to research the load capacity effect of an arch. The active pressures were used to represent the distribution of live load from the load plate through dry sand and onto the arch barrel.

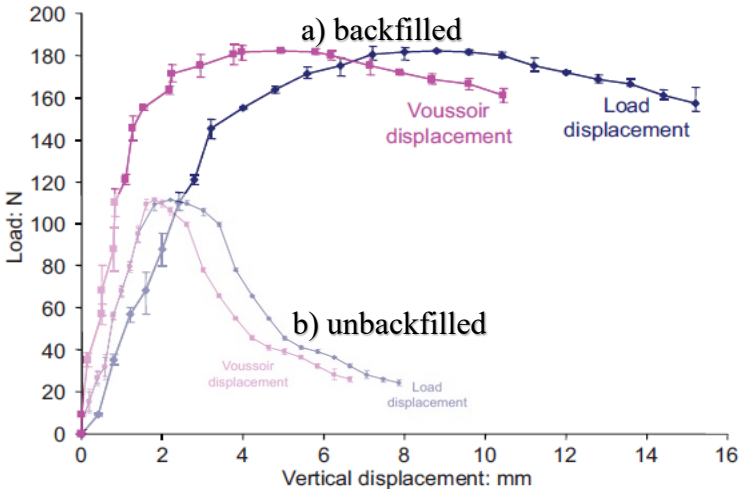

Figure 2-17: Load capacity against displacement results for a) backfilled and b) unbackfilled arches (Callaway et al., 2012).

From the experimental results displayed in Figure 2-17 the backfilled model bridge load capacity was 182 N and without backfill, the load capacity was 110 N. The masonry arch bridge with backfill was 40% stronger than without backfill. Also, it can be seen that the masonry arch bridge with backfill sustains the same displacement as the unbackfilled bridge but is significantly stronger and exhibits significantly more ductility (sustained peak load with ongoing displacement). To conclude, the backfill has a major effect on the load a masonry arch can sustain.

2.2.4 *Modes of failure*

The potential failure mechanisms of masonry arch bridges can be seen in real and model scale experimental tests (Hughes & Blackler, 1997; Melbourne, Wang, & Tomor, 2007; Page, 1993). There are potentially six modes of failure (as depicted in Figure 2-18):

a) Hinge mechanism
b) Shear sliding
c) Ring separation
d) Abutment movement
e) Masonry crushing
f) Arch buckling (snap-through).

There may also be more complex combinations of these six failure modes.

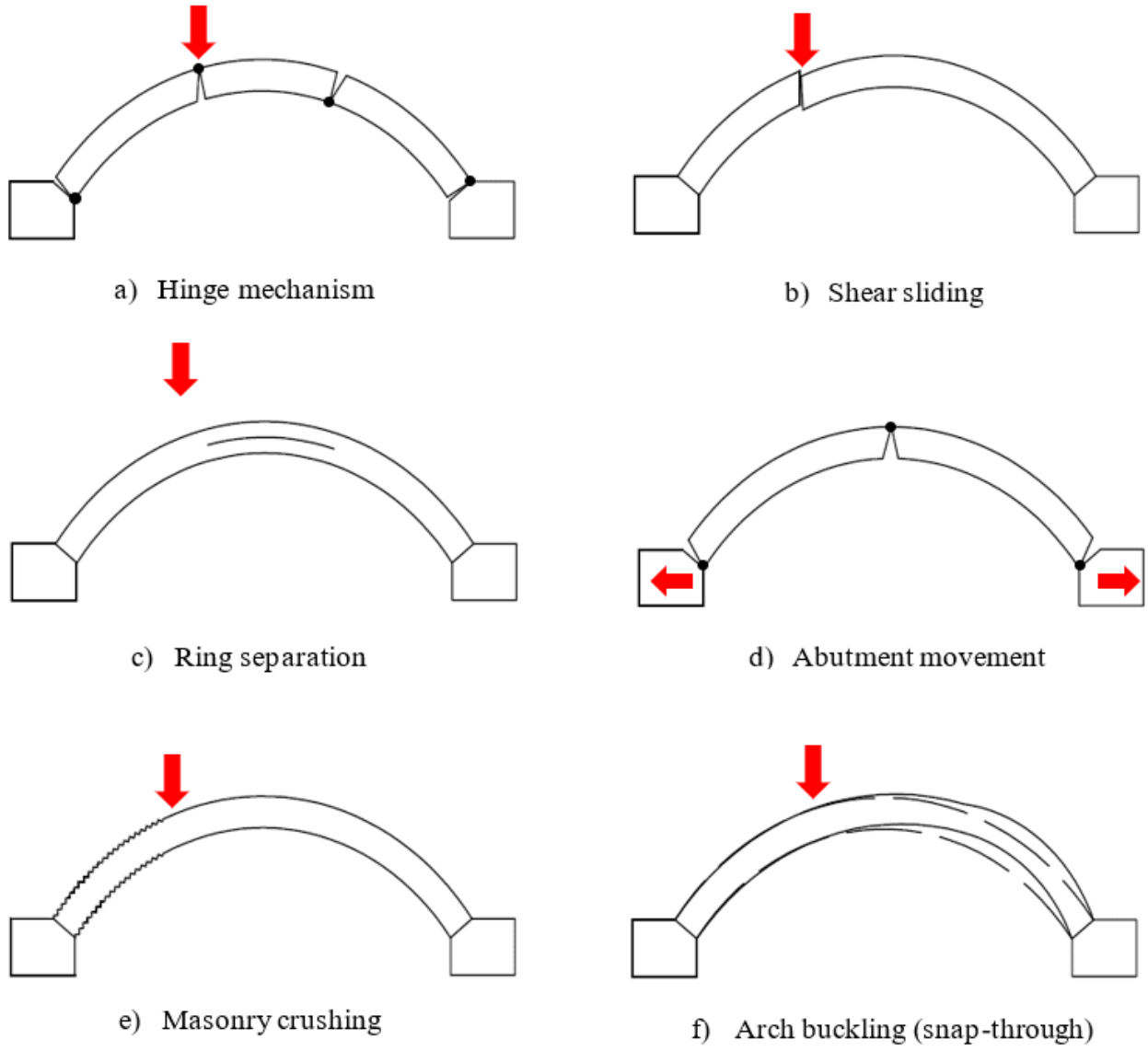

Figure 2-18: Six potential failure modes of a masonry arch (Adapted from Melbourne, Wang, Tomor, et al., 2007).

Hinge formation is the most common mode (Gilbert, 1993). The classical ultimate collapse mechanism involves four radial fracture lines in the masonry arch. This failure type leads to the collapse of the masonry arch bridge as shown in Figure 2-18 (a). In multi-ring arch barrels, a diffused hinge is often formed in a localised area, whereas in single ring brick arches a large hinge is formed in the mortar bed joint.

Concentrated loading on a masonry arch can lead to the shear sliding failure mode. This occurs when a radial crack is established in the arch ring due to intense local loading, as shown in Figure 2-18 (b).

The ring separation failure mode is often a direct result of multi-ring arches built using stretcher bond (Hodgson, 1996; Melbourne et al., 1995). This only connects the arch rings by mortar joint, which have weak surfaces and thus, the arch rings eventually separate due to longitudinal shear, as shown in Figure 2-18 (c).

Differential settlement in the foundations may contribute to the masonry arch developing hinges. Although a single span fixed base arch generally requires four hinges to transform into a collapse mechanism (Gilbert, 1993), when settlement is involved it is possible to form a collapse mechanism with only three radial hinges, as shown in Figure 2-18 (d).

Once the internal stresses in the arch surpass the masonry compressive strength, it may collapse due to compression failure of the material (e.g. crushing). Many FEA modellers use elements developed for concrete analysis in their investigations of masonry structures. This is because they share similar material behaviours, though of starkly different strengths. The ability to assess compressive strength as well as shear and tension strength is therefore important in any masonry analysis. Analysis models which attribute different strength properties to mortar and bricks will be superior in identifying the location of crushing failure. The highest compression forces are likely to exist close to abutments, in arches which carry large volumes of backfill. This is shown in Figure 2-18 (e).

Additionally, when radial hinges form in the arch ring, a zone of high compression stress must also exist. As the hinge grows, the compression zone reduces in depth and therefore the compression stress increases, until material fails by crushing. This is because this kind of failure is highly brittle which can instigate global failure of the arch.

As depicted in Figure 2-18 (f), Gilbert (1993) states that snap-through can occur in multi-span arches where inner spans are restrained from moving. When large rotations occur under the load, instability causes a local failure, prior to the formation of the final collapse mechanism. Shallow arches can also fail because of snap-through type buckling. These are forms of a general sway failure mode which involves lateral displacement of the arch barrel.

Loo and Young (1991) researched the cracking and crushing behaviour. Based on their stress and strain characteristics, the research treated brick and mortar as a single material. They based their approach on an assumption about the average properties of masonry, which was derived from experimental findings by Ali (1987). The criteria developed by Chen and Saleeb (1982)

was to assume the masonry was perfectly elastic and brittle until reaching a failure criteria. It was developed for a tensile fracture in plain concrete, as the masonry had isotropic behaviour before cracking. The same approach was used by Ali and Page (1998) which predicted crushing and cracking patterns.

2.3 Masonry arch bridge - experimental research

To understand the behaviour of the masonry arch bridge up to the collapse phase, numerous researchers have undertaken experimental laboratory tests on model-scale and full-scale masonry arch bridges. The experimental studies allowed an insight into key areas such as the masonry arch collapse modes, understanding the most onerous loading conditions, establishing key structural components (abutment, arch barrel and backfill material) and how they interact. As such the full-scale and model-scale experimental studies are discussed.

In 1953, (Davey, 1953) discovered that bridge abutment movement is a very significant variable, after analysing the results of experiments on 22 bridges (Gibbons & Fanning, 2016; Sarhosis, De Santis, et al., 2016). As a moving load approaches the abutment the arch will be subject to increased soil pressure in the active zone and the crown will lift. When the moving load is on the span the crown will descend and soil pressure in the passive zone will be generated in the backfill.

The study by Gibbons and Fanning (2016) explicitly examines the movement and progressive cracking in masonry arch bridges. It investigates the impact of various loading conditions and structural weaknesses on these bridges' movement and eventual cracking. The research utilizes advanced finite element models to simulate the movement patterns and the resulting stress distribution and cracking in different bridge components. This method comprehensively explains how movement affects masonry arch bridge structural integrity and longevity. A significant finding of the study is that substantial damage can occur at serviceability load limits, but there is still a considerable reserve capacity before failure. Considering that masonry arch bridges frequently exhibit damage signs when subjected to operational loads and are rarely loaded to their maximum capacity, the study concludes that the assessment of these bridges should concentrate on the loads they encounter during regular service and the complexities of their three-dimensional response.

The computer models that predict bridge movement may not encompass all possible real-world scenarios. Such oversimplification could lead to less accurate predictions regarding bridge dynamics. Furthermore, it is challenging to ascertain the applicability of these findings to all types of masonry bridges, given the diversity in their designs, materials, and environmental settings. This represents a considerable limitation. Additionally, the accuracy of the study's results is heavily reliant on the quality of data used in these models. Inaccurate or biased data could result in misleading or incomplete representations of bridge behaviour under various conditions. In this study, the models of masonry arch bridges treated the units and mortar as a singular continuous material. Consequently, the stiffness and strength values assigned were lower than those of the masonry itself, which could affect the models' fidelity.

Pippard produced the method of rigid block collapse analysis and adopted the middle half rule to limit the elastic thrust line position, which was later incorporated into the Military Engineering Experimental Establishment (MEXE) method (Pippard, 1948; Sarhosis, De Santis, et al., 2016). Wang and Melbourne (2010) produced research at the University of Salford, and this study improved the knowledge of relationship between ring and span. Furthermore, limitations on various bridge types and modifications were noted. This study concluded that the axial strain energy influences are included to evaluate the load-bearing capacity of small-span masonry arch bridges. Furthermore, in cases of larger spans, the work confirmed that the compressive stress limit at the bridge's crown might be surpassed under the dead load alone.

In examining the stability of masonry arches, Heyman (1982) stated that even minimal abutment movements significantly impact their equilibrium. Pippard's research observed that a slight spread in arch abutments typically leads to the development of hinges at the supports. However, Pippard did not consider the potential emergence of a third hinge, which would alter the arch into a statically determinate three-pin structure. The analysis was focused on a simplified two-pin arch model, replacing the actual arch ring with a theoretical two-pinned rib along the arch's central axis for analytical purposes. This simplification was crucial for deriving practical structural metrics. Although Pippard's assumptions are not always explicitly stated (Wang & Melbourne, 2010), his work predominantly aimed to find an elastic solution to the architectural challenges of arch structures. Notably, omitting abutment movement in the analysis could preclude modelling snap-through behaviour in a geometrically linear context, thus potentially overlooking critical aspects of arch dynamics.

In the context of Pippard's method for analysing arch structures, several critical critiques emerge for a comprehensive understanding. Firstly, simplifying the arch to a two-pinned structure might not accurately reflect the more complex behaviour of real arches, particularly those that develop a third or more hinges, potentially leading to a misunderstanding of movement and stress distribution. Secondly, the lack of explicit assumptions in Pippard's methodology could pose challenges in replicating or expanding upon his analysis, as clarity and detail in assumptions are vital for the validity of structural analyses. Thirdly, while Pippard's emphasis on an elastic solution is insightful, it may not cover all aspects of arch behaviour, especially under non-elastic or extreme loading conditions, thereby limiting the applicability of his results. Finally, using a hypothetical rib for analysis, aligned with the arch's centre line, may not fully capture the behaviour of actual voussoir arches, which often have more intricate geometries and load distributions. These critiques highlight the need for more comprehensive and nuanced approaches in structural analysis.

Research experiments implemented on arch bridges were executed by The Transport and Road Research Laboratory, which is now known as The Transport Research Laboratory. Furthermore, Hendry tested two full-scale bridges at the University of Edinburgh. According to (Hendry & Royles, 1985; Hendry et al., 1986; Royles & Hendry, 1991), the bridges were specifically the Bargower and Bridgemill bridges. Also, the experiments were with different spans: 1 m, 2.08 m and 2.48 m and these had different span-to-rise ratios between 2 and 6.4. A small-scale model was constructed, with the main aim of trying to investigate interaction between the arch and the backfill (Hodgson, 1996). Fill depths and soil density were two of the main criteria that were controlled during the testing. The backfill used was granular dry sand that was compacted using a vibrating steel plate. To record the soil interaction, markers were placed in the sand layers to allow observation of the soil movement during interaction (Fairfield & Ponniah, 1994). The test models highlighted that as the loading point moved across the arch, the interaction between earth pressure and load dispersion contributed to the deformation in the arch. A problem with the testing was highlighted; the test did not record the pressure changes due to not installing the necessary equipment. Thus the contributing pressure changes were purely observations from the soil displacements and could not be stated with any confidence (Gilbert et al., 2013).

An investigation of masonry arches by Yang (1991) highlighted that besides the effects of concentrated loads, movements in the supports are paramount in determining the structural

behaviour of arches. Masonry arch structures are notably rigid, leading Harvey (1986) to conclude that minor shifts in their supports can precipitate significant alterations in stress distribution across the arch. Despite its importance, experimental research on support movements in masonry arch structures is sparse, primarily due to the intricate nature of such investigations. However, this knowledge gap can be bridged using the analytical approach suggested by Yang. Within this context, both Towler's Arch 2 and the Bridgemill Bridge were examined under imposed abutment movements until their respective points of failure.

Ochsendorf (2006) provides a valuable analysis of horizontal movements impacting the stability of masonry arches, particularly those of historical significance. However, the study neglects crucial factors like vertical settlements often seen in masonry arch foundations due to weight, age, flooding and unstable soil. The research also omits potential sliding and rotational movements, especially in uneven terrains. While the adoption of computer programs and thrust line analysis is notable, the absence of the Finite Element Method (FEM) is a missed opportunity for deeper structural behaviour insights. The study's focus on rigid-block arches might only partially represent the diversity of masonry arch construction techniques, materials, and designs. Relying predominantly on a single case study limits capturing the broader nuances of arch structures. While Ochsendorf's work is insightful, it necessitates broader considerations and methodologies for a comprehensive understanding of masonry arch stability.

Zampeieri has performed small scale experimental tests looking at abutment movement in conjunction with numerical modelling, this is addressed in chapter 3.

The research determined that, predictably, an arch with a shorter span is inherently more rigid. This translates to reduced tolerance for support movement in short-span arches compared to their longer-span counterparts. Notably, given the same conditions, arches can accommodate more vertical support movement than horizontal. This phenomenon can be attributed to the observation that a span length alteration is less noticeable when supports shift vertically as opposed to horizontally. This trend was particularly evident in the comparative behaviour displayed by the Bridgemill Bridge during vertical and horizontal support shifts.

In conclusion, support movements significantly influence the robustness of arch bridges, with this effect being particularly pronounced in shorter-span arches. It was also discerned that by keeping other variables constant, an arch could withstand more significant vertical movement than horizontal.

Yang's (1991) study of masonry arches presents valuable insights but needs more depth concerning foundational settlement, sliding, and rotational movements. While there is a brief mention of lateral movements, the specifics of sliding, its dynamics, and associated challenges, like soil cohesion and frictional resistance, are not addressed in detail. The study also overlooks rotational movements, pivotal in understanding torsional stresses and effects of minor foundational shifts. A more thorough examination of these foundational movements in masonry arches is essential to derive effective engineering solutions.

It is now known that the backfill has a major impact on the masonry arch bridge behaviour. Finite element analysis has allowed significant progress to be made into soil and structure interaction in bridges. Small-scale models were introduced as a direct result of the high costs of implementing large-scale experimental tests (Fairfield & Ponniah, 1994).

Hendry and Royles (1991) investigated the capacity of a wing-wall masonry arch and the arch bridge spandrel effects, also studying masonry structure behaviour as one of the aims. The results of full scale and experimental models were compared, where the models were constructed as exact scale replicas of the actual masonry bridges to ensure good replication of geometric properties. The tests showed that the wing-wall and the spandrel effects depended on the span-to-rise ratios and the influence was highest for semi-circular masonry arches. Moreover, the vault strength increases significantly when a spandrel wall is present (Royles & Hendry, 1991). The effects of lateral restraint from the backfill were not considered during the experiment. The scaled maximum load and behaviour of the structure were expected to be reflected by the full-scale test, but due to the limitations in the scale factors (material property), no valid conclusion could be made from this test.

A series of experimental tests were undertaken on redundant masonry arch bridges. The tests allowed an insight into how much strength the backfill had (Page, 1993) but the tests did not accurately categorise the backfill material, essential data was neglected or missing e.g. soil cohesion, friction angle etc. and therefore further bridge tests were required.

Gilbert and Melbourne (1994) developed a straightforward and practical computational approach, the rigid block technique, to calculate the collapse load for masonry block structures. By integrating the plasticity upper-bound theory with geometrical compatibility criteria and precise linear programming methods, they could find solutions, even without detailed information on the material properties of masonry arch bridges. Experiments that followed the

redundant bridge tests included another large-scale experiment, this time in a laboratory. The test conducted at Bolton Institute by Melbourne in 1995 tried to rectify issues highlighted from previous experiments. The soil parameters were recorded and the backfill consisted of limestone, which was compacted using a vibrating plate compactor. When the maximum passive pressure occurred, the displacement in the arch was small and this result did not occur when the bridge load was at its greatest (Melbourne et al., 1995). As the arch approached the collapse state, results did not provide conclusive data from the soil pressure cells.

Further experimental tests were conducted at Cardiff University on two different arch models, one a semi-circular and the other segmental (span to rise ratio of four). The small-scale tests were a direct response to investigating passive pressure in masonry arch bridges (Burroughs et al., 2002). A roller was used on the scaled models to provide the loading, allowing the loading to imitate the loading of a HGV on a full-size bridge. Limestone backfill was used in the tests, which was also subjected to laboratory shear box tests to obtain the soil properties. A series of pressure sensors were introduced within the fill material to allow stress in the soil to be determined. The tests showed that the backfill material shifts away quickly as the arch deformation continued and the results showed pressures to drop gradually as a result.

Investigation into backfill material interaction was conducted by Gilbert et al (2007), in which clay and limestone were chosen as the two different backfill elements. As well as the chosen backfill types for the masonry arch bridge experimental tests, to anchor the backfill in place, low friction transparent tanks were installed (Gilbert, Smith, et al., 2007). Thereafter, to analyse the movement of the soil, instruments such as soil pressure cells, acoustic gauges, displacement transducers and the Particle Image Velocimetry (PIV) technique was introduced. The PIV technique allows the backfill soil movement to be recorded through photographic digital images. The two experimental test results established that the ultimate load in the arch bridge with the limestone backfill was almost double that of the clay backfill material. This is most likely because the limestone material is stiffer than clay. Although both bridges failed in the experimental tests through hinge formations, clay backfill allowed some movements at the unrestrained supportive skewbacks. This is again partly due to the fact that limestone material is much stiffer.

Callaway, Gilbert and Smith (2012), undertook 27 small-scale tests on backfilled masonry arch barrels as shown in Figure 2-19, these were physical tests, and they were compared with

software models. The aim was to get a better understanding of backfill influence on masonry arch bridge capacity. The results determined the distribution of live load and passive restraint contribution to the capacity of masonry arch bridges. LimitState: Ring 3.0 analysis software was also able to confirm this (Callaway et al., 2012).

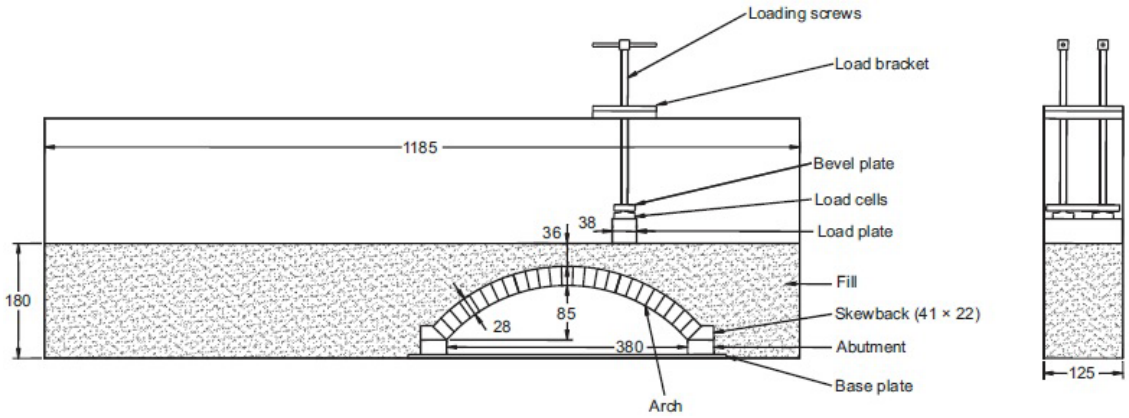

Figure 2-19: Detailed masonry arch bridge small scale (Callaway et al., 2012).

Ahmad *et al*. (2015) produced a Discrete Element Method (DEM) model, validated it against a full-scale experimental test of a back-filled masonry arch bridge, and compared the behaviour and ultimate capacity. They found that there was a significant difference between the load-displacement results of software and physical tests. The numerical tests conducted in UDEC modelled rigid elastic bodies and interfaces with no tensile capacity. These results matched the physical test results at ultimate limit state.

Augusthus-Nelson et al. (2017) undertook large-scale experimentation of soil filled masonry arch bridges subject to railway loading. Practical tests were undertaken to observe the interaction of soils with masonry arch bridges and abutments, as shown in Figure 2-20. The tests conducted produced high-quality results. High-quality software (PIV) was used to analyse the physical test results; this software determined how the soil and structure interact in a masonry arch bridge. The tests distinguished between bridge service loading and ultimate carrying capacity. The study revealed that frequently used bridges experiencing repeated loadings significantly increase load-carrying capacity. However, overall capacity may decrease due to soil compaction around the arch barrel. Even a considerably damaged masonry arch bridge can perform well under railway loads.

Figure 2-20: Masonry arch bridge full scale at University of Salford (Augusthus-Nelson et al., 2017).

Several experimental tests on multi-ring masonry segmental arches were undertaken at the University of Salford Heavy Structures Laboratory. This research aimed to investigate and focus on the masonry arch multi-ring fatigue performance under static and cyclic load and their durability limitations due to the significant increase in rail and road traffic (Melbourne, Wang, Tomor, et al., 2007). The experimental masonry arch rings were a series of arches of 3m and 5m span multi-ring arches, as shown in Figure 2-21. Two brick types were also used to construct the masonry arch rings, where high-strength brickwork was represented using class A Engineering bricks and Britley Olde English bricks used to represent the quality of older, weaker bricks. Mortar mix of 1:2:9 (cement: lime: sand) was used for masonry arch tests.

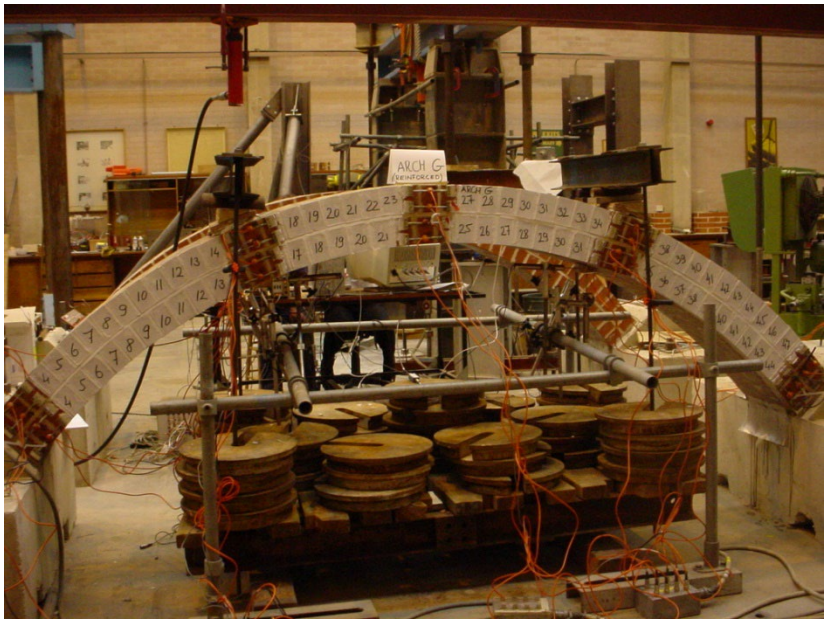

(A)

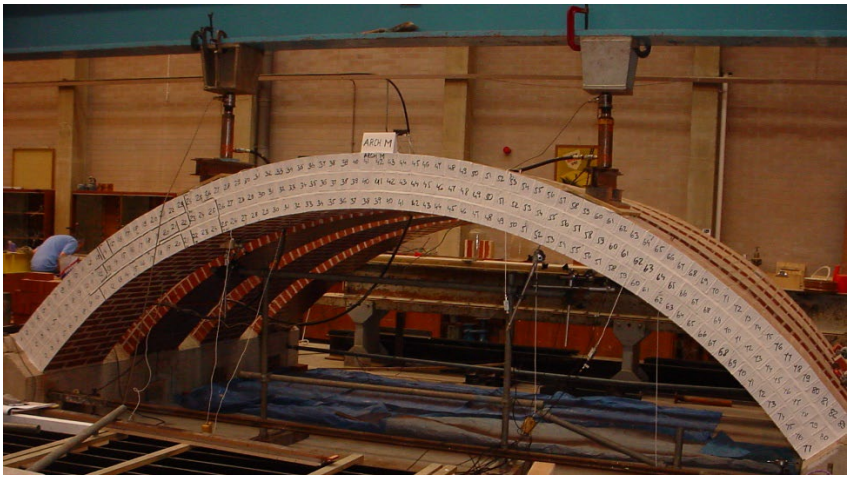

(B)

Figure 2-21: Masonry arch experimental tests; (a) 3 metre span arch & (b) 5 metre span arch (Melbourne, Wang, Tomor, et al., 2007)

The masonry arch rings under static load failed through different failure mechanisms, where two multi-ring 3m spans failed via four-hinge failure mechanism and the three-ring 5m span failed via ring separation. The load-deflection curve became non-linear after the third and fourth hinges started to occur. Also, the ring separation failure in the 5m spans masonry arch rings happened unexpectedly without any changes in the force-deflection curves for all the masonry arch rings. Melbourne and Tomor (2005) and Melbourne et al., (2007) discovered that multi-ring masonry arches built without headers (bricks that extend through the mortar joints between rings) are particularly susceptible to failure due to ring separation. This type of failure is more likely to occur under cyclical loading conditions after the arches have experienced a significant monotonic loading event.

2.4 Masonry material properties research

This section aims to represent and define the standard masonry behaviour experimental test under various types of stress. Masonry is a heterogeneous aggregation of units and mortar. The units may be stone, block or bricks, and the mortar is a mixture of cement, lime and sand. The mortar strength depends on the composite ratio of the components. Therefore, an arch's wide range of possible constituent strength and geometrical arrangements results in a uniquely variable structural strength (Angelillo et al., 2014).

Accurate modelling and comprehension of the fundamental behaviour of masonry structures requires understanding of the material of unit and mortar behaviour under different conditions.

Achieving accurate simulation results depends on the material properties of these composite materials to be implemented in the software. This point has also been brought up by Sarhosis and Sheng (2014) and Lourenço et al. (1998).

Current research and simulations of old experimental masonry structure tests depend on assumptions, as most of these tests do not provide the actual material property values. This section aims to identify and clarify the experimental tests of masonry behaviour under different stresses.

In general, masonry properties are influenced by many reasons, such as unit and joint material properties, the joint thickness and width, the unit dimensions and the construction workmanship quality. Also, there are some critical test data that are very difficult to accurately predict and are sensitive to test conditions. These data are required in any masonry arch analysis investigation to accurately predict structural performance.

Until very recently, there was no clear framework to establish the laboratory experiments that should be performed to evaluate the material properties necessary for the examination of static and fatigue behaviour in masonry arches. Liu et al. (2023), produced a study which offers a framework, as shown in Figure 2-22. The study undertook an extensive experimental tests to determine the masonry arch bridges material properties, using newly constructed specimens that mimic the materials found in actual bridges, such as solid units and weak mortar. Their research aimed to establish a systematic framework that connects experimental methods with identifiable parameters.

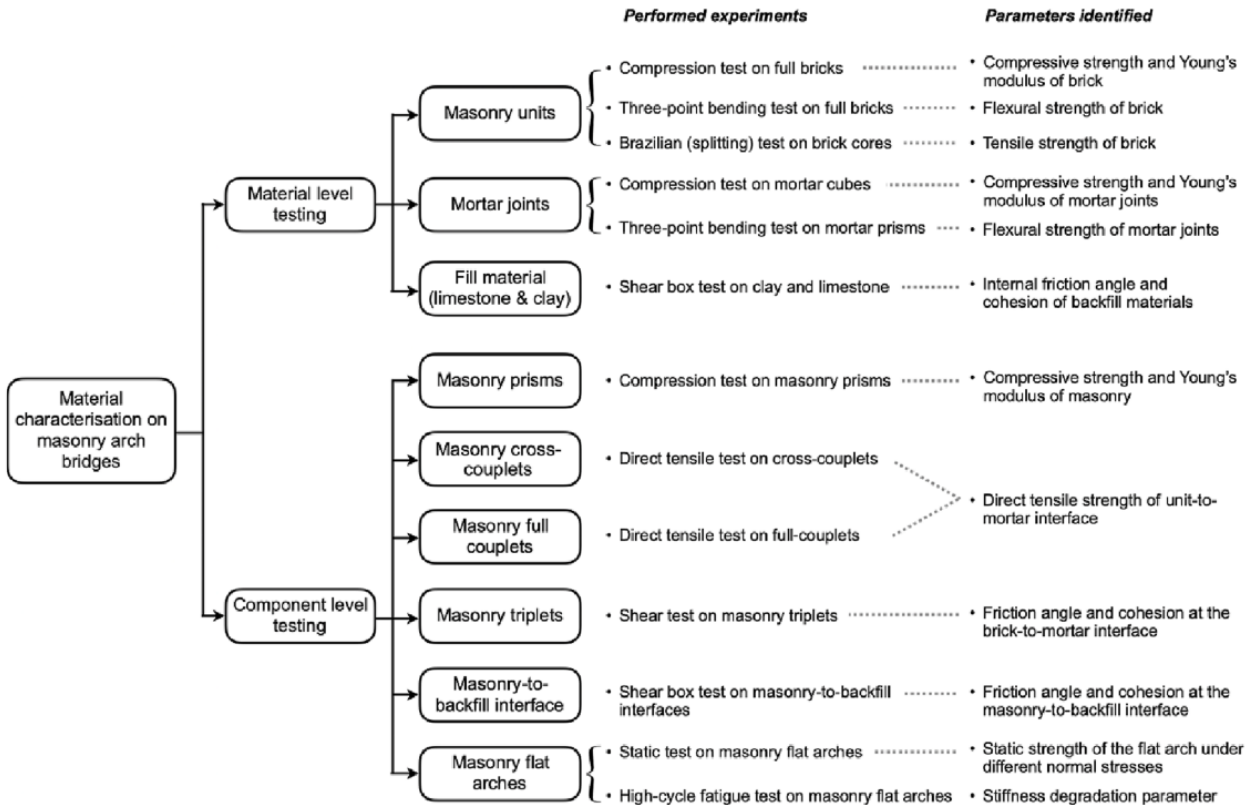

Figure 2-22: Framework for Characterising Materials: Identifying Experiments and Parameters (Liu et al., 2023).

According to Liu et al. (2023) the framework includes two levels of testing framework applicable in laboratory settings, which include testing at the material level as the first level. This level focuses on determining the characteristics of masonry arch bridge materials such as the backfill material, mortar joints, and masonry units, through component-level testing. The second level focuses on understanding the behaviour of interfaces and the cross interactions of various elements within the bridge, such as the connection between units and mortar and between the masonry and the backfill. Furthermore, this level assesses how masonry components perform under static and fatigue stress conditions.

The framework and this extensive study indicate parameters relating to laboratory experiments that can be performed to evaluate the material properties for any numerical or experimental investigations.

2.4.1 *Masonry uniaxial compressive behaviour*

Compression failure can occur through tension cracks aligned with the load axis or shear failure along other weak lines. The mortar has weaker mechanical properties and a lower Young's modulus than brick and tends to expand more under uniaxial compression. The connection between bricks and mortar, maintained by friction and cohesion, causes the mortar to be laterally restrained by the bricks. This confinement increases shear stresses at the brick-mortar interface, creating triaxial compressive stress within the mortar. Simultaneously, this confinement induces lateral tension and axial vertical compression stresses in the bricks as shown in Figure 2-23 (Sarhosis, Oliveira, et al., 2016; Singhal & Rai, 2014).

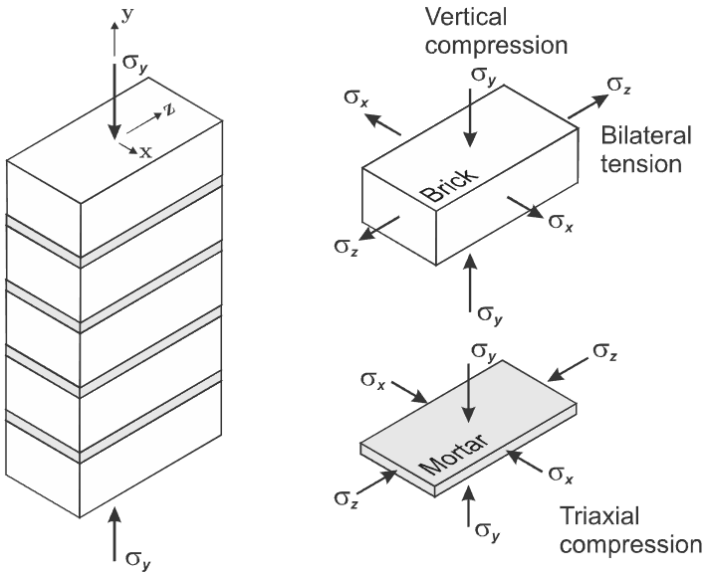

Figure 2-23: Triaxial stress state in masonry prism at the brick mortar interface (Singhal & Rai, 2014)

The compressive strength in the direction normal to the bed joints is the most critical factor in masonry material design. The standard method to determine and investigate the masonry compressive strength characteristic is 'stack bond prism' through testing under uniform compression, as shown in Figure 2-23. This test determines the Young's modulus and compressive strength of masonry parameters, which is considered under component-level testing for masonry characterisation, as shown in Figure 2-24 (a).

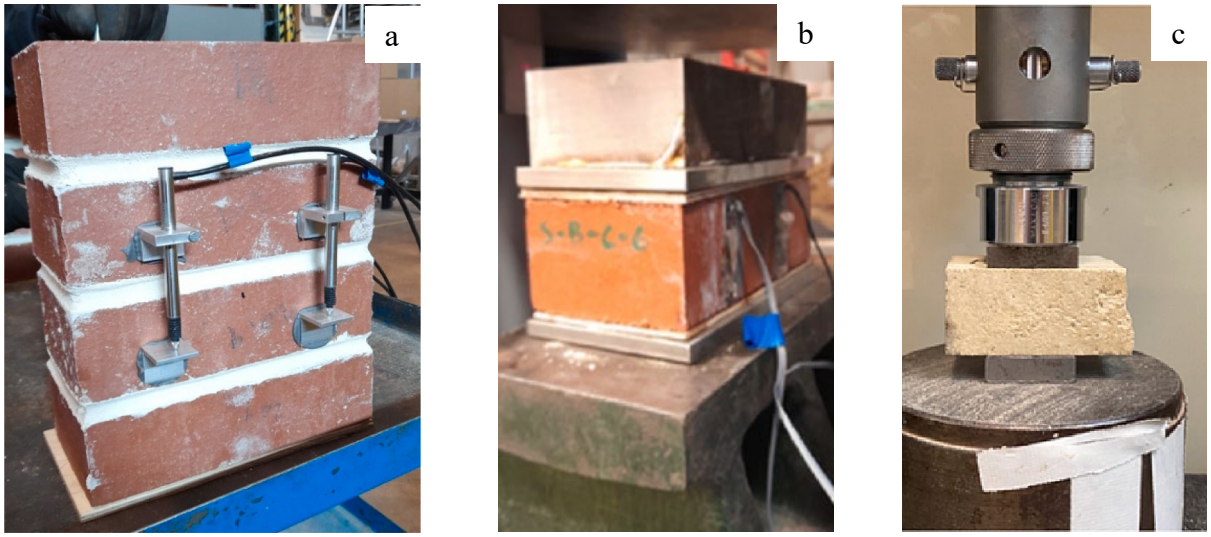

Figure 2-24: Material properties compression tests. a) masonry prism, b) full brick, c) mortar cube (Liu et al., 2023).

The direct compression test identifies and determines the masonry units and mortar compressive strength and Young's modulus by crushing mortar cubes specimens, and brick samples using the BS EN 772-1 method for brick compressive strength and BS EN 1015-11 method for the mortar compressive strength, as shown in Figure 2-24 (b) & (c) (British Standards Institute, 2011, 2019).

The failure of masonry under compressive load results from tension cracks that develop parallel to the loading axis or from shear failure along the mortar joints, which are weaker than the bricks.

Masonry arches are designed to resist compressive stress. According to Crisafulli (1997), masonry structures under compression loading exhibit an almost linear stress-strain relationship. It is known that constituent parts of masonry have a significant impact on the overall quality of masonry; and the main factor influencing masonry failure and compressive strength is the relative size of the unit and mortar elastic properties (Lourenço, 1996; Lourenço, 2002).

Significant research has been undertaken to explore the influence on the mechanical behaviour and strength of masonry under various types of loading. This research aims to understand particular needs, evaluate structural performance, and develop methods for retrofitting and rehabilitating structures (Hendry, 1998; Rots, 1997).

Some factors affecting the masonry compressive strength can be stated (Hendry, 1998; Miller et al., 1979; Sarhat & Sherwood, 2014):

- Mortar characteristics include the strength of mortar, thickness and relative deformation.
- Brick characteristics, such as unit types, arrangement of units and strength.
- Stress direction on masonry.
- Bond (interfaces) between brick and mortar.
- Workmanship.
- Compressive loading direction.
- Bonding method and patterns.

Mortar compressive strength is one of the critical factors influencing masonry behaviour up to failure. Furthermore, it affects the bond strength of the brick-mortar bond.

According to research (Sarhosis, Oliveira, et al., 2016) on previous experimental tests, several researchers have investigated these factors, and the significant factors based on their research are:

- The cement or binder type.
- The aggregate characteristics in the mortar (aggregate grain size distribution).
- The water-cement ratio.
- The units' water suction behaviour and surface texture.

2.4.2 *Masonry uniaxial tensile behaviour*

The bond between brick and mortar joint determines the masonry's resistance to tensile and shear stresses. According to (Wang, 2004), the bond between units and mortar may be one of the most challenging masonry features to understand, model and monitor. There are commonly three experimental test methods used to measure and investigate the masonry tensile strength under uniaxial tension - bond wrench, direct tensile pull test and prism beam test, as shown in Figure 2-25.

Extensive experimental research has confirmed that masonry is highly resistant to compression. However, it can withstand limited tension, particularly along the bed joints (McKenzie, 2001).

Analysing the relationship between the bond's tensile strength and the masonry brick can clarify the characteristics of tensile behaviour (Lourenço, 1996).

If the tension loading is applied across the masonry bed joint, failure occurs because of the low tensile bond between the brick and the mortar joint. According to (Lourenço, 1996), masonry tensile strength equates to the brick and mortar joint's tensile bond strength. Also, masonry has a linear stress-strain relationship under tension, leading to brittle failure once the stress reaches the maximum level (Crisafulli, 1997).

Two possible failure types can happen when the tension loading is applied parallel to the mortar joint, depending on the unit and joint strengths. These failures are: (a) a stepped crack through the bed and head joints and (b) a vertical crack through the head joints and the units, as shown in Figure 2-26.

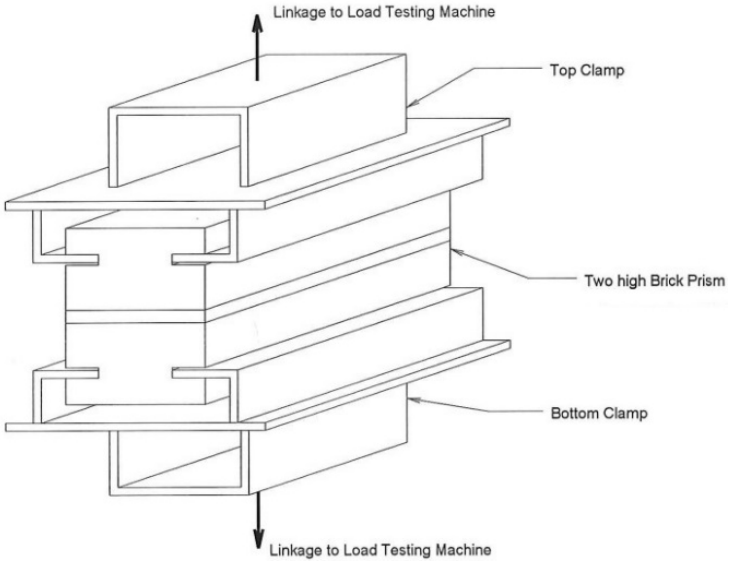

(A) Direct Tensile Test

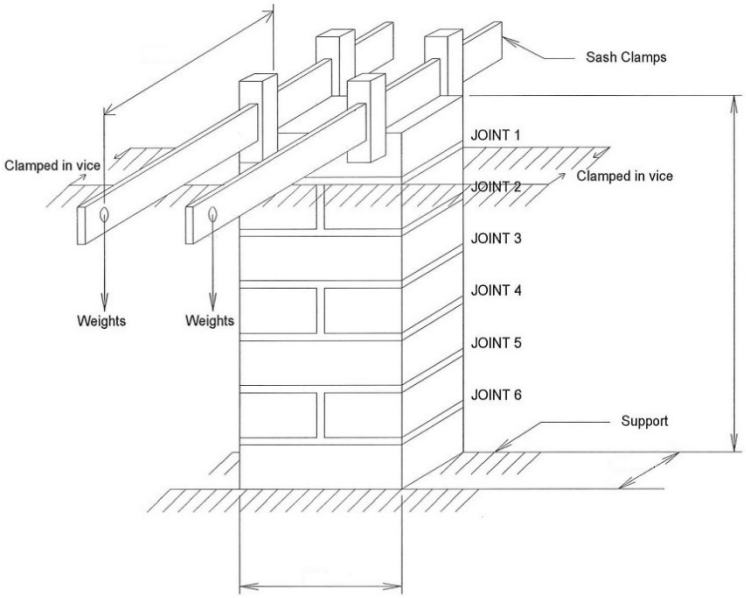

(B) Bond Wrench Test

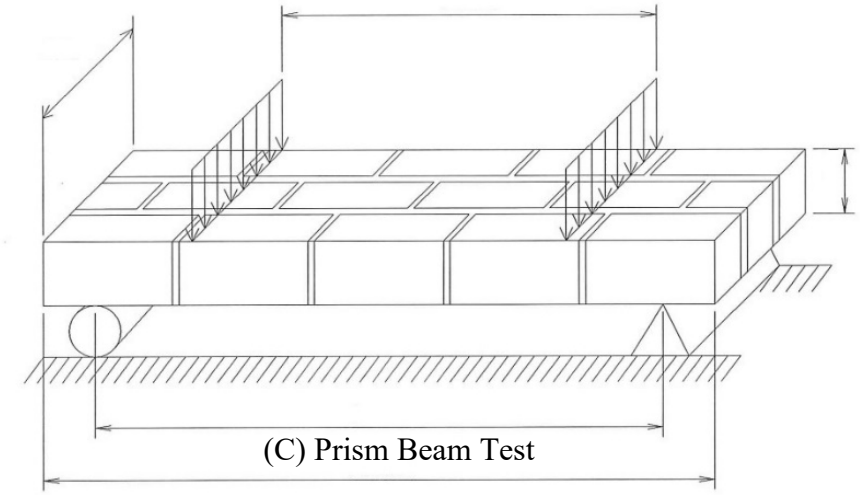

(C) Prism Beam Test

Figure 2-25: Masonry tensile test methods (Weekes, 1998).

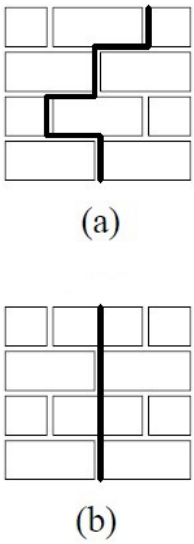

Figure 2-26: Direct tension masonry mode failures: (a) a stepped crack through the bed and head joints and (b) a vertical crack through the units and the head joints (Lourenço, 1996).

The masonry failure mechanisms are five fundamental failures shown in Figure 2-27, which Lourenço and Rots (1997) noted. They identified that the occurrence of each failure mode depends on the direction and magnitude of the normal and shear stresses on the masonry. They also noted that some are joint mechanism, some are unit mechanism, and some are a combination of these; (a) joint tension cracking, which is a tensile failure at the unit-mortar interface, and (b) joint slip, which is a shear sliding between the unit-mortar interface. Also, the failure of (a) and (b) are described as bond failure between unit-mortar interfaces.

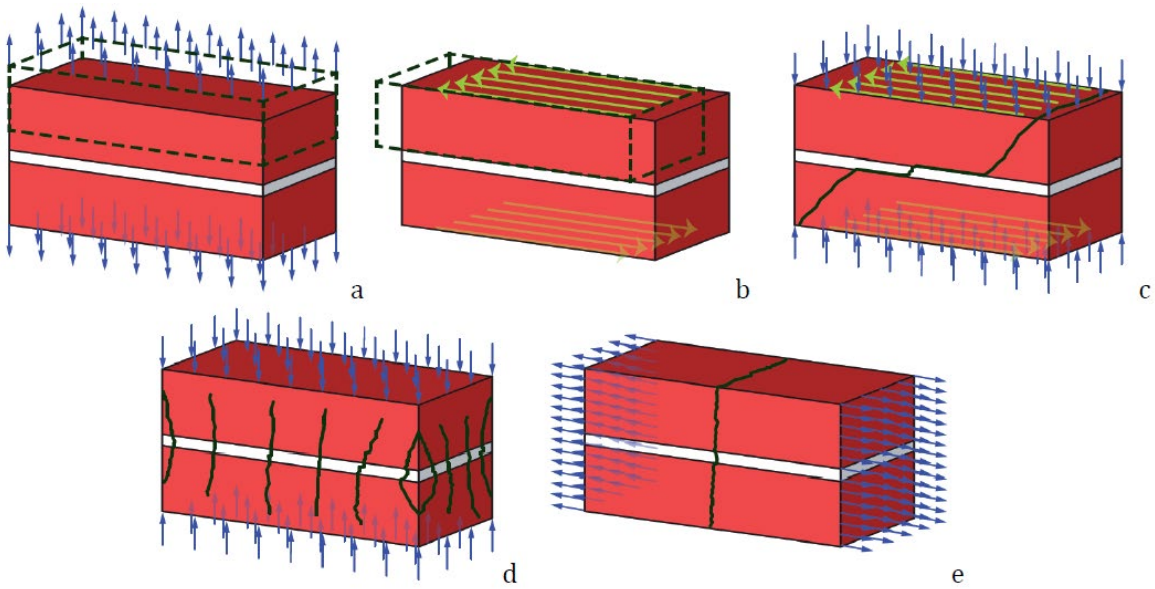

Figure 2-27: Failure mechanisms of masonry (D'Altri et al., 2018).

Extensive studies have examined the determinants affecting masonry's mechanical properties and robustness when subjected to load. These studies have aimed to elucidate masonry structures' specific attributes and behaviour patterns, evaluate their structural capacity, and formulate effective strategies for retrofitting and repair (Hendry, 1998; Rots, 1997; Sarhosis, Oliveira, et al., 2016). The most important factors that play a pivotal role in shaping the mechanical response of masonry, the most critical are the characteristics of the masonry units, the properties of the mortar joints, the nature of the bond between brick and mortar, as well as the curing processes and the quality of workmanship involved.

2.4.3 *Masonry shear behaviour*

Masonry material under shear loading presents various types of failure, such as mode II shear failure occurs when there is slip between the interface of the unit-mortar. There are three different test methods to predict and analyse masonry shear strength. The first test method was proposed by Van der Pluijm in 1999, as shown in Figure 2-28 (a). The second test method was proposed by Lourenco in 2004, as shown in Figure 2-28 (b). The first two tests are known as Couplet shear tests (Greco et al., 2020). The third shear test is the Triplet test and was adopted as a standard setup using BS EN 1052 – 3:2002. Methods of testing for masonry and mortar, as shown in Figure 2-28 (c).

The shear strength of masonry structural systems is usually limited by the masonry unit-mortar interface shear strength. Numerous investigators have used the Mohr-Coulomb equation to interpret the shear test results, as the relationship between the initial shear strength, friction coefficient and normal compressive strength is linear and can be expressed based on the criterion of Mohr-Coulomb failure using Equation 2-1:

$$\boldsymbol{\tau = c + tan\phi * \sigma} \qquad \text{Equation 2-1}$$

Where:

- τ is shear stress.
- c is cohesion.
- $tan\phi$ is the friction angle tangent at the brick - mortar interface.
- σ is normal stress.

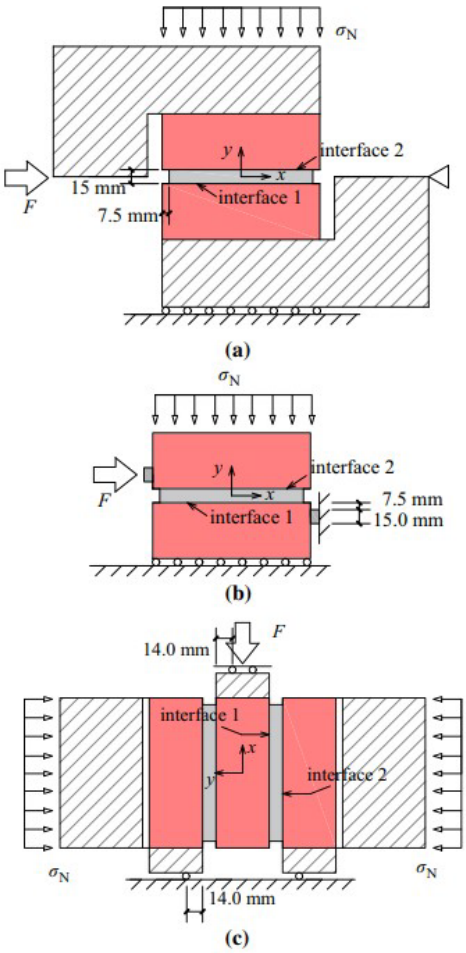

Figure 2-28: Various shear strength experimental test setups (Zhang, Richart, et al., 2018).

The masonry mode failures under various loading conditions must be understood to model the masonry properly and to be considered during modelling. According to the BS EN 1052 – 3:2002, to determine the initial shear strength value, there are four types of failure, as shown in Figure 2-29. These four failures are:

a) Failure occurs in the unit-mortar bond area, where it could be either on one side or between the two faces of units, as shown in Figure 2-29 (a).
b) A crack occurs only in the mortar joint, as shown in Figure 2-29 (b).
c) Shear failure only in the unit, as shown in Figure 2-29 (c).
d) Splitting and crushing failure occur in the two units with the mortar joint, as shown in Figure 2-29 (d).

The primary failure during the shear strength load condition is a crack into the mortar joint, and failure of the interface between the brick and mortar joint known as slip as indicated in

Figure 2-29 (a) and (b). Shear crack propagation is complicated to predict according to the following factors (Kim et al., 2014):

- Mortar joint geometry influences crack propagation.
- The complicated stress condition at the brick - mortar interfaces.
- The unit and mortar have a significant difference in tensile strength.

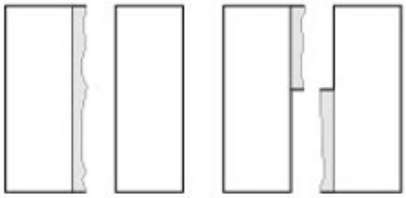

a) failure in the unit-mortar bond area either on one or divided faces

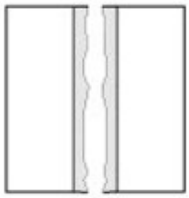

b) shear failure only in the mortar

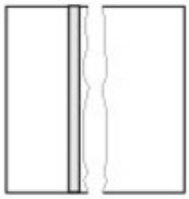

c) shear failure in the unit

d) crushing and or splitting failure in the unit

Figure 2-29: Failure types (British Standards Institute, 2002).

2.4.4 *Unit-mortar interface properties*

The unit-mortar interface, where mortar bonds to the units, are typically weaker than the other elements in masonry structures. Nonlinearity in joint response is dependent on such interfaces

and is an essential characteristic in studying the masonry behaviour. The unit-mortar interface failure displays two separate types of occurrence: mode I, which is related to tensile failure, and mode II, which relates to shear failure (Rots, 1997).

2.4.4.1 Mode I failures

Deformation-controlled experiments were conducted by van der Pluijm (1992) using small scale samples of masonry comprising units of calcium silicate and solid clay, as illustrated in Figure 2-30. The findings revealed an exponential curve for tension softening and mode I fracture energy G_{If}, ranging between 0.005 and 0.02 Nmm/mm^2, where tensile bond strengths ranged between 0.3 and 0.9 N/mm^2, depending on brick-mortar combinations. Here, the fracture energy represents the total energy used to generate a single cracking area along the mortar and the unit interface (Lourenço, 1998; Rots, 1997).

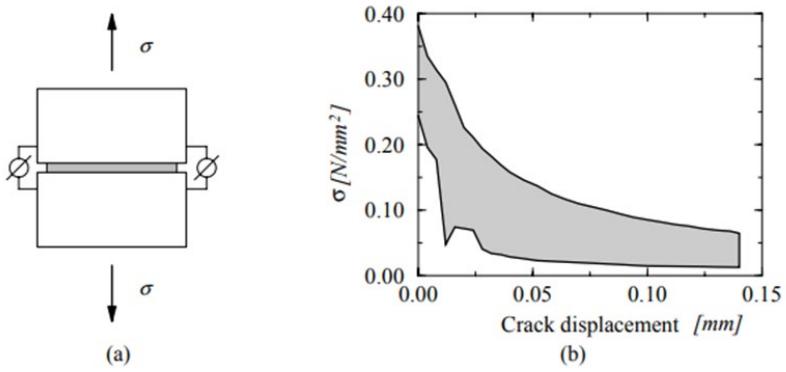

Figure 2-30: Masonry's tensile bond behaviour, Van der Pluijm (1992): (a) specimen tested; (b) Sample findings for the stress crack displacement experiment for masonry using solid clay bricks (shading shows the 3-test envelope) (Lourenço, 1998).

2.4.4.2 Mode II failures

When establishing shear responses in masonry joints through testing, it is highly beneficial if stress is applied uniformly to joints. However, this is challenging due to equilibrium constraints which cause normal stress to be applied non-uniformly within a joint. Discussion and evaluation of the various possible test arrangements and their effectiveness, can be found in Lourenço (1996) who refers to work by Atkinson et al. (1989) and van der Pluijm (1993). The most comprehensive presentation of shear behaviours in masonry is given by Van der Pluijm (1993), using calcium silicate and solid clay units. Figure 2-31 shows a testing arrangement that allows for steady normal confining pressure when shear is applied. Confining (compressive) stress was implemented at three stresses; 0.1, 0.5 and 1.0 N/mm^2. It was not possible under the testing arrangement for tensile stress to be applied, the results show that

brittleness was high even where the confining stress applied was low, and the testing arrangement was potentially unstable. Significantly, a number of samples showed diagonal unit cracks along with mortar-unit interface shearing under higher levels of confining stress.

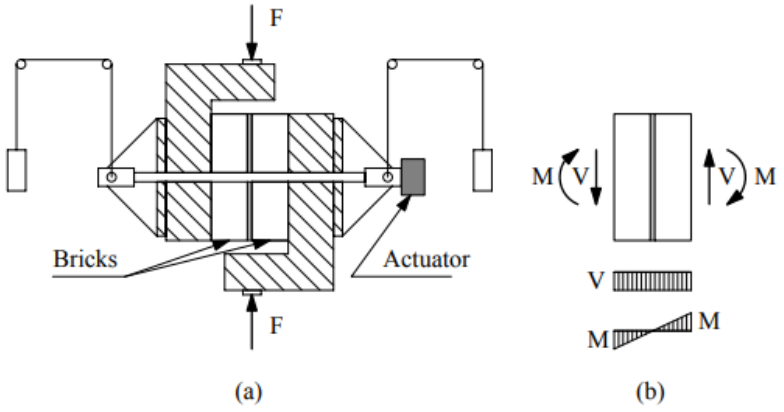

Figure 2-31: Testing arrangement for shear bond behaviours, Van der Pluijm (1993); (a) sample fully prepared for test; (b) application of force to sample in the test (Lourenço, 1998).

The findings from experiments show exponential softening of the shear diagram and residual levels of dry friction, as shown in Figure 2-32 (a). $G_{II\,f}$, as second mode fracture energy, is identified for residual dry friction shear and the area shown through the stress-displacement diagram. This ranges between 0.05 and 0.25 Nmm/mm^2 where starting values for cohesion range between 0.1 and 1.8 N/mm^2. Fracture energy is dependent on confining stress levels, as shown in Figure 2-32 (b).

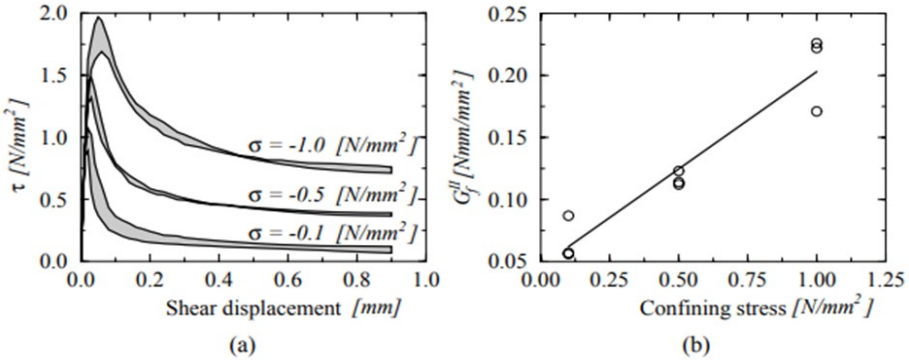

Figure 2-32: Shear bond behaviour typically seen in solid clay unit joints, van der Pluijm (1993): (a) various normal levels of stress in a stress-displacement diagram (shading indicates the 3-test envelopes); (b) G_{IIf} mode II fracture energy as a function of normal stress (Lourenço, 1998).

It is impossible residual internal friction is found through Tan$\emptyset_r$, which is generally constant at a value of 0.75. Measurement of a single unit's uplift in comparison to another where shear is

applied is measured through ψ as the dilatancy angle, as shown in Figure 2-33 (b). Notably, dilatancy angle corresponds to confining stress levels, as shown in Figure 2-34 (a). When confining pressure is low, Tanψ average values range between 0.2 and 0.7, in line with unit surface roughness. When confining pressure is high, Tanψ falls to zero. As slip increases, Tanψ is also reduced to zero because of sheared surface smoothing, as shown in Figure 2-34 (b).to assess net bond surface for the samples: however, the assumption is made that tensile bond strength values remain the same. This type of experimental setup can be used to derive other parameters of materials, as indicated in Figure 2-33 (a). The initial angle of internal friction $\emptyset_0$, linked to the Coulomb model for friction, is calculated through tan $\emptyset_0$. It ranges between 0.7 and 1.2 in various combinations of mortar and unit. Moreover, $\emptyset_r$ is the angle of residual internal friction is found through Tan$\emptyset r$ which is generally constant at a value of 0.75. Measurement of a single unit's uplift in comparison to another where shear is applied is measured through ψ as the dilatancy angle, as shown in Figure 2-33 (b). Notably, dilatancy angle corresponds to confining stress levels, as shown in Figure 2-34 (a). When confining pressure is low, Tanψ average values range between 0.2 and 0.7, in line with the roughness of the unit surface. When confining pressure is high, Tanψ falls to zero. As slip increases, Tanψ is also reduced to zero because of sheared surface smoothing, as shown in Figure 2-34 (b).

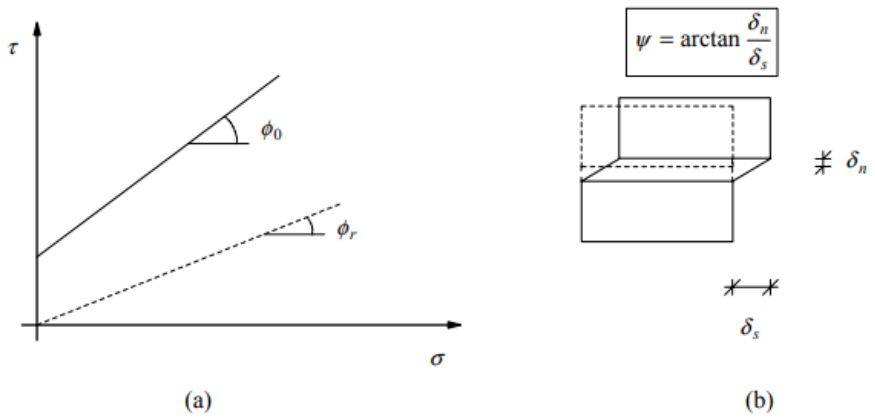

Figure 2-33: Dilatancy angles and friction defined: (a) Coulomb's friction law, including initial and residual friction angles; (b) dilatancy angle, showing rise in adjacent units when shear is applied (Lourenço, 1998).

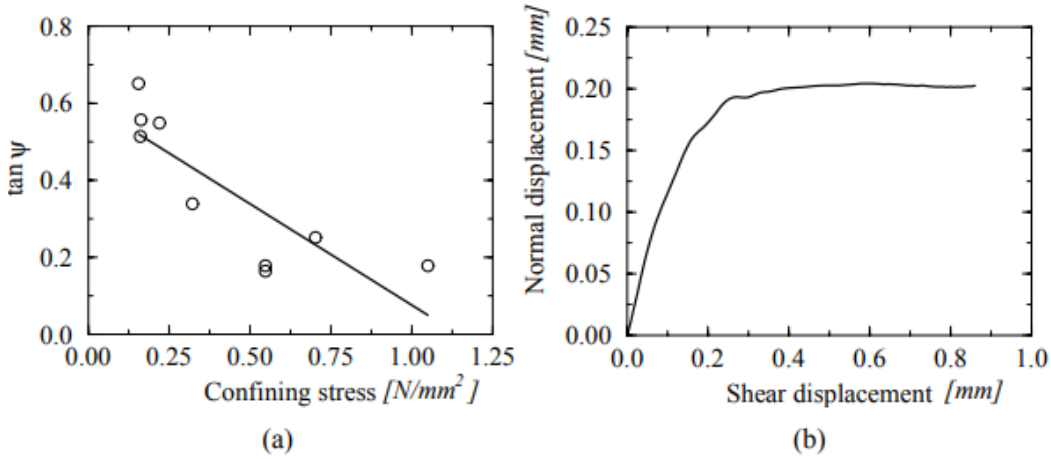

Figure 2-34: Typically observed shear bond behaviours in a solid clay unit joint, Van der Pluijm (1993): (a) dilatancy angle ψ tangent as a function of normal stress levels; and (b) relationship of normal to shear displacement under loading.

2.4.5 *Fracture Energy*

The fracture energy is a fundamental mechanical parameter to understand the nonlinear behaviour of masonry structures and to evaluate the actual behaviour of brittle materials such as masonry (Lourenço, 1996). The fracture energy is a material property and is derived using force-displacement diagrams. Also, it is defined as the area under the stress-displacement curves of shear, compression and tension diagrams. The fracture energy is recognised as shear, compression and tension fracture energies, as shown in Figure 2-35.

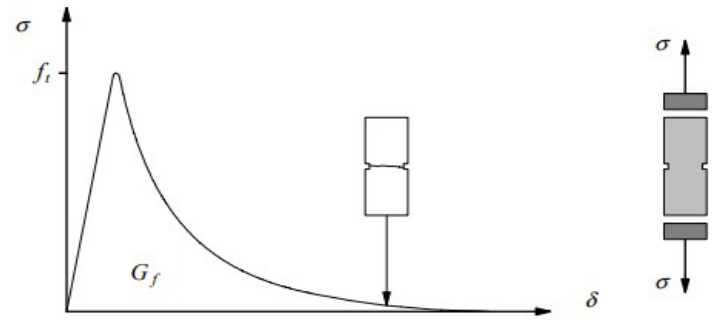

(a) Tension

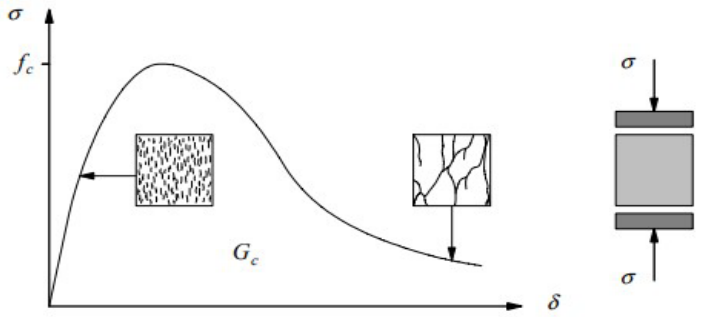

(b) Compression

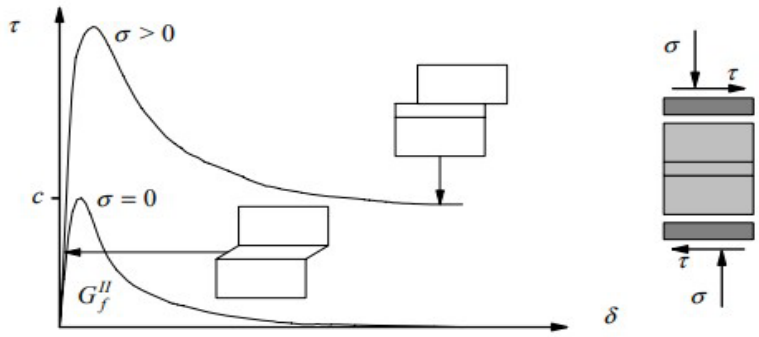

(c) Shear

Figure 2-35: The brittle material stress-displacement diagrams under tensile, compressive and shear loading (Lourenço, 1996).

According to Lourenço (1998), the tension fracture energy is a mode I failure, and the mode II failure is shear fracture energy. Also, as detailed and stated in 2.4.4, the mortar joint non-linear behaviour response and failure mechanism are controlled through the shear and tensile strengths between the interfaces of brick and mortar. According to (Rots, 1997), the shear and tension fracture energies are the energy that is required to create a crack per element. Therefore, fracture energy is a key factor in establishing nonlinear behaviour at ultimate limit state.

2.5 Summary

This chapter reviewed research on masonry arches and masonry arch bridge experimental tests, brick-mortar mechanical properties and their investigation, the types of material failure, and their influence under various loadings.

The following are a summary of the main findings:

- It is noted that as the traffic volume on masonry arches increases, assessment of serviceability is becoming increasingly vital and necessary. However, currently, there is no suitable and accurate method to assess masonry defects.
- Due to masonry being an anisotropic and heterogeneous material, masonry mechanical properties vary. The units and mortar mechanical characteristics, workmanship quality and the brick-mortar bond (interface) properties effect the masonry structural behaviour and properties under load.
- The brick-mortar bond strength (interface) is one of the most significant factors influencing the non-linear behaviour of the mortar joints under applied loading. Furthermore, it significantly influences the masonry structure's cracking and load transfer.
- There are several masonry failure mechanisms, such as material compressive failure (crushing), shear failure at the joints and units, joint tensile failure, and unit-mortar bond failure, such as joint slip cracking.
- The relative value of normal and shear stress and their directions influence the type of masonry structure failure occurrence.
- The mortar type affects the elastic modulus and the lateral masonry strain, which significantly influences the behaviour of masonry structures. Furthermore, lime mortar was historically used to build most masonry structures. As a result, the mortar's mechanical properties have a much lower value of Young's modulus than the bricks. So, the computational model in this thesis will present a full-thickness mortar element and complete mechanical properties of mortar.
- Brickwork masonry arch bridges are composed of rigid brick units and weaker mortar. The mortar and its bond to the brick units is weak in tension; thus, it tends to be the location for accumulation of deformation and local failure.

- The crack growth and propagation in a masonry arch could happen in the joint, at the unit-joint interface, or a combination. However, the crack can grow in the masonry unit depending on the brick's strength.

The next chapter will provide a literature review of masonry structure computational modelling methods. It will include a complete description of the numerical modelling approaches, techniques, and strategies. It will also review previous research on modelling masonry structures, and it will make a considered choice of the most suitable tools and techniques to model a masonry arch ring.

Chapter Three

3 Numerical Modelling of Masonry Structures

3.1 Background

This chapter investigates, reviews and explains the different strategies, techniques and approaches of numerical masonry structure computational models, for masonry arch rings and forced abutment movement. This chapter also compares modelling strategies as well as constitutive laws to establish the most influential computational approach.

Masonry arch mechanical properties, characteristics, and behaviour must be considered to choose a suitable method and software package to present a simple and accurate outcome. Due to this, the criteria to select the applicable numerical method and model to simulate masonry behaviour are:

- Must be able to describe the real masonry arch geometry. Also, the method has to be able to describe and investigate any arrangement of stress or force applied to the structure.
- Capable of recreating the observed failure mechanisms of masonry arches. Furthermore, the ability to model a full thickness mortar joint and brick-mortar interface non-linear behaviour.
- The ability to simulate and analyse the damage caused by foundation movement in the full-thickness mortar joint.
- The ability to model and simulate cracking failure in the mortar joints.
- Capable of presenting and predicting the masonry model's stress-strain and load-displacement behaviour at any part of the model.

3.2 Masonry arch bridge - numerical methods

3.2.1 *Introduction*

Several factors affect the arch capacity such as, span-to-rise ratio, mortar quality, applied loading including its position and form, backfill material, and stiffness. The range of parameters which can be studied through experimental testing is limited, hence the focus has been on the effects of certain parameters of significant interest.

Ng (1999) noted that the four-hinge mechanism is the most common failure mode for masonry arches. Despite this well-understood behaviour and over 300 years of study, research into the structural behaviour of masonry arches is still ongoing. Experimentation is a significant step toward understanding the behaviour of the masonry arch. It provides insight into the complex nature of the structural behaviour resulting from abutment movement or interaction between soil and structure, the latter of which has not yet been fully quantified through theoretical methods. It was determined that brittle hinges develop within the structure of a masonry arch bridge when the foundation rotates. This rotation allows the blocks in the arch to undergo significant rotation, leading to a plastic collapse mechanism in the structure.

The SMART assessment method (Melbourne, Wang, & Tomor, 2007) defines four possible levels of investigation. The first level of analysis involves an approximate calculation like the MEXE method. The second level involves simpler 2D modelling techniques, such as rigid block analysis and line of thrust methods. A more advanced structural analysis using 2D and 3D models, such as the mechanism analysis method, or DEM is suggested for the third level, and FEM is recommended for the fourth level. The appropriate method is to be determined based on the required accuracy of the analysis (Haynes, 2020).

The classification of investigation methods into four distinct levels in the SMART assessment method demonstrates a structured and hierarchical approach beneficial for guiding decision-making processes in engineering projects. Nevertheless, the guidelines for selecting a method based on the *required accuracy of the analysis* lack specificity. Providing detailed criteria or illustrative scenarios would significantly enhance the practical utility of these guidelines, aiding engineers in choosing the most appropriate method for their specific needs.

While the methods outlined (MEXE, thrust line analysis, rigid block methods, mechanism analysis method, DEM, FEM) are widely recognized and respected in the field of structural analysis, the description fails to adequately compare and contrast these methods in terms of their suitability for various types of structures or engineering conditions. This comparative analysis is essential for practitioners, as it would offer valuable insights into the strengths and limitations of each method, thereby facilitating more informed and effective decision-making in diverse engineering scenarios.

3.2.2 *The mechanism analysis & plastic analysis*

Pippard et al., (1936) developed the mechanism method theory based on assumptions of the masonry material alone. The assumptions Pippard made were no tensile strength in masonry, limitless compressive strength and no movement in the masonry arch joints. The method makes no consideration of the soil (backfill) material strength.

Heyman's research work concerning the masonry arch took place between 1966 and 1982. His work revived the mechanism analysis method based on four assumptions. It was assumed that sliding failure would not occur because of the block friction. Also, the masonry blocks were thought to have unlimited compressive strength. The blocks were regarded as incompressible, meaning they were believed to have an unlimited Young's modulus of elasticity. Due to the assumed properties, hinges could only form in the arch mortar joints, leading to collapse through a hinged mechanism. Moreover, the arch had no tensile strength; cracking would only occur following thrust line movement outside the middle third, resulting in collapse. Heyman (1969) developed these four assumptions to establish methods for plastic analysis. De Rubeis (1998) refined the approach by introducing a geometrical factor of safety, defined as the ratio of the actual thickness of the arch to the theoretical minimum thickness needed for stability.

The structural design of masonry arches and arch bridges has not been completely understood and continues into the twenty-first century. Also, current researchers are exploring all potential failure modes, including ring separation, and are examining the entire structure of the bridge to assess its load-bearing capacity.

Experimental field and laboratory tests have allowed some validation of research, but with the amount of work that is still required to understand the interaction in masonry arch bridges, numerical models are needed. Small and large-scale models created in various software

packages have allowed further understanding of the collapse state. Various researchers who have obtained data and validated it against previous experimental tests, have deployed Rigid Block Analysis, Discontinuity Layout Optimisation (DLO) and Finite Element Analysis.

Mechanism analysis limitations may oversimplify complex soil-structure interactions that are critical in foundation movement scenarios, and often assume rigid-body mechanics, which might not capture the intricate responses of masonry and soil under varying conditions.

The plastic method was first developed for steel structures and is based on plastic theory. In this method, the arch bridge fails when a collapsed mechanism forms in the arch. Also, it is based on the upper bound approach because it is a kinematic method. There are external and internal constraints on the structure which are governed by mechanism rules. Masonry arch bridges collapse when four hinges alternately close and open (or form at the intrados and extrados). The locations of the hinges are unknown, but commonly the hinges form at the quarter spans of the arch and close to the arch abutments, as dictated by the line of thrust location. Several experiments confirm these hypotheses (Hughes, 1995).

LimitState: Ring 3.0 is a computer programme for rigid block analysis and may be used to identify the critical failure load, the associated mechanism and the distribution of the internal forces, thus allowing for the assessment of safety and reliability regarding arch bridges. The software can account for several factors, such as multiple spans, masonry unit weight and compressive strength, the backfill friction angle, the fill cohesion material, and possible passive pressure effect, load dispersion angle, masonry damage, and mortar loss (LimitState, 2019).

Bögöly (2012) reports that the bond between blocks in masonry can be considered using friction coefficients. They also found that the span-to-rise ratio of masonry arch bridges significantly affects the emergent failure mechanism. In cases involving low rise arches (span/rise $\geq$ 4.0), the mechanism of a three-hinge failure often occurs, typically involving sliding. In contrast, arches with a higher rise usually exhibit a four-hinge failure mechanism.

The Rigid Block Analysis, method was developed by Livesley, which is a mathematical approach to find the critical collapse mechanism (Livesley, 1978). Gilbert enhanced this, with the extension of soil backfill and soil pressures, developing the RING software (LimitState, 2019). Constant unit weights and geometrical properties were used. The active pressure was ignored as it was assumed too small to make a difference to the results. Passive pressure was

required and to calculate this, RING software uses Rankine pressure distribution as the default method. As certain factors and parameters were simplified or neglected, the results gained were within 10% of the experimental results. However, as the numerical models neglected wall friction and assumed it to be smooth, the experimental load capacities were higher than the results from numerical models. Therefore, it was concluded that to achieve similar results to the experimental results, arch interaction and soil roughness could be implemented, thus creating a better soil structure interaction model.

The Discontinuity Layout Optimisation tool enabled soil modelling to be discretised into nodes and therefore this method builds upon the Rigid Block Analysis method. The upgraded follow-on tool enables direct modelling of the backfill and masonry by treating the parameters in the displacement as stress fields. For tests conducted by Callaway, Gilbert and Smith (2012) on small-scale models, soil and interface properties were required. The soil strength factor used assumed loose-medium soil, thus a mobilisation factor of 0.33 was used where large strains were predicted. This model did not assume the interface as smooth, thus a roughness factor of 0.5 times that of the adjoining soil mass was applied. Other assumptions for the interface elements for this small-scale model were that sliding would not occur in the arch elements and the voussoirs would be incompressible. The tests concluded the backfill interaction with the arch was very sensitive to the load carrying capacity; using a higher roughness factor would also bring the results closer to the experimental data. The results also concluded that where the soil strength was low, implementing the mobilisation factor instead of the peak soil strength would have been better suited.

It is rarely necessary to calculate deformations in a masonry structure. The deformations result, almost without exception, from external forces, such as the settlement of foundations or the expansion of abutments (Aita et al., 2015). Notably, these deformations, including cracking, are mainly independent of the elastic properties of the masonry material. Therefore, an analysis based on elasticity does not provide any meaningful insights into masonry structure deformation. Furthermore, the internal force distribution and magnitudes are determined through the movements imposed by the environment, which are often unknown.

Heyman recognizes deformations in masonry structures due to external forces, such as foundation settlement. However, it is not clear whether this pertains to uniform or more complex differential settlement. The importance of rotational movements stemming from

factors like differential settlement is not explored sufficiently, even though they significantly influence structural deformations. While Heyman critiques traditional elastic analyses, advanced methods like the Finite Element Method (FEM) were still in their infancy and so were not discussed. Utilising FEM offers a deeper understanding of masonry movements, potentially filling existing knowledge gaps. In summary, while Aita et al. (2015) highlight challenges in analysing masonry deformations, there is a need for a more detailed exploration of foundational movements and the benefits of advanced analytical methods like FEM.

Mechanism and plastic analysis methods in masonry arch bridge assessment have inherent limitations in capturing the complexities of soil-structure and brick-mortar interactions. Mechanism analysis, with its rigid-body mechanic's assumption, may inadequately represent the nuanced behaviour of masonry and soil, leading to an oversimplified understanding of foundation movement. Plastic analysis, although different in approach, might also fall short in addressing soil behaviour's heterogeneous and non-linear nature. While insightful, both methods require a more nuanced and integrative strategy, potentially including advanced geotechnical modelling, to assess the stability and integrity of masonry arch bridges accurately.

3.2.3 *The discrete element method (DEM)*

The discrete element method is a particle-based approach, and it is an efficient and accurate method due to the compatibility equations, linear behaviour response and constitutive relations consideration. Furthermore, this method can model structure elements using blocks and joints because some material behaviours cannot be simulated using continuous approaches. Cundall and Strack (1979) first developed this method for analysing rock mechanics problems. This method's strategies are established on explicit integration schemes and the contact penalty approach using elastic or rigid blocks.

The discrete element method (DEM) is effective for studying rigid body motions involving deformable interfaces under shock, as it allows for the arrangement between blocks to be characterised. However, accurately capturing the strain and stress fields within the structure using this method can be challenging.

The main principle is a chain of classical mechanisms determining the dynamics between grains through repulsion laws. This method's mechanism divides the structure into several elements, in contact with each other using interaction properties. According to Sarhosis (2011),

this method accurately simulates the fracture pattern and crack width estimation. Also, DEM is used to simulate behaviour and discontinuity failure, such as a unit-mortar interface.

DEM has been deployed in two computer software packages: UDEC and 3DEC, where UDEC can handle consistent meshes and large displacements. However, UDEC is a two-dimensional numerical software. UDEC interface allows blocks to be connected by creating points of contact which are situated around the perimeter of the blocks. In most instances, these are at the corners of each block. Spring connections are at each point which can transfer shear force or normal force onto the adjoining block. This is shown in Figure 3-1.

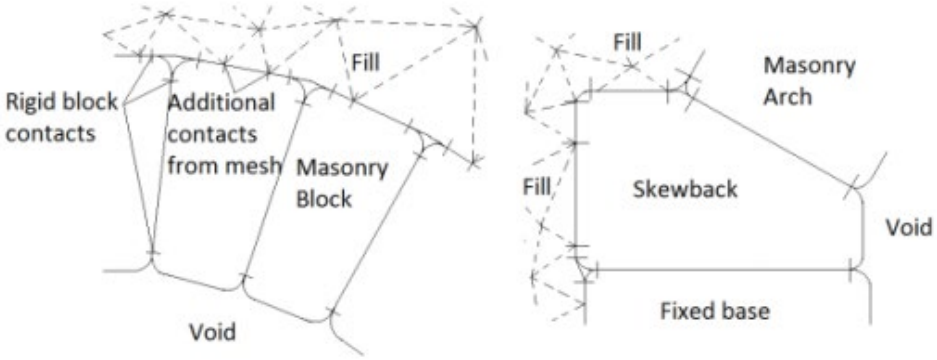

Figure 3-1: Contact creation in the UDEC model (Ahmad et al., 2015).

In terms of modelling full-scale masonry arch structures, this method has used elastic and rigid blocks in previous numerical research (Forgács et al., 2017; Foti et al., 2018). It is also used to simulate the mortar joint and the brick-mortar interface discontinuities.

According to Thavalingam et al. (2001), the masonry arch bridges may be conceptualised as a stacked blocks. In every scenario, there is sufficient contact between all the blocks, and an equation of motion is applied to describe their interactions.

According to Mohebkhah et al. (2008), a gradual resolution process is used where the position of the blocks is recalculated at each time step. This process also involves identifying new gaps between the blocks and tracking the formation of new contacts.

Barattucci et al. (2020) evaluated masonry triplet shear strength when subject to monotonic and cyclic loadings. Furthermore, the experimental results were validated against DEM models using UDEC 2D. Figure 3-2 illustrates the development of the DEM approach to model the joint mortar layers as an assemblage of voronoi-shaped particles. This type of shape is used to

obtain the crack initiation and propagation in brick, mortar and brick-mortar interfaces. There was a satisfactory agreement between the numerical and experimental outcomes based on the load-displacement results and failure modes. As a result, the reported DEM approach has a significant possibility for modelling masonry structure discontinuous and highly non-linear behaviour.

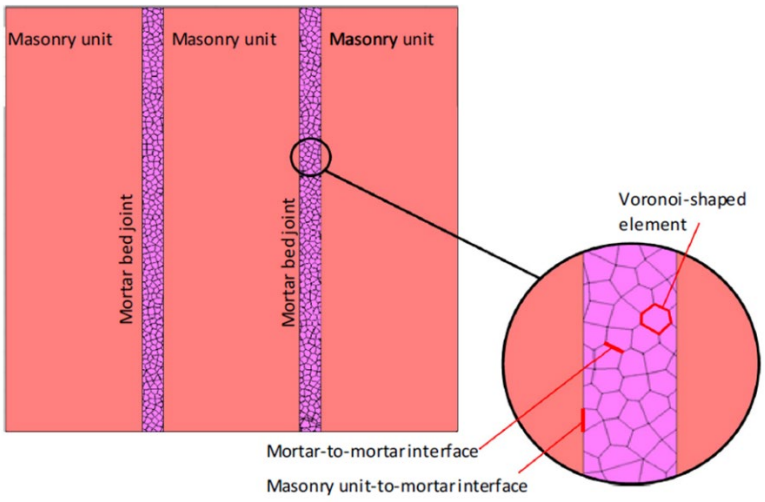

Figure 3-2: Masonry triplets are represented using voronoi elements (Barattucci et al., 2020).

Sarhosis et al. (2019a) used the discrete element method to simulate the backfill material in masonry arch bridges by modelling and simulating the actual experimental masonry arch bridge using UDEC software. The numerical models were created as a 2D model, and all of the model's discrete components were modelled using linear elastic behaviour. In addition, the mortar joints of the arch barrel were modelled as zero-thickness interfaces to restrict shear stress along the mortar joints. The experimental and numerical results were in good agreement, and the novel modelling approach indicated enormous potential. In addition, the presented approach had one significant advantage: the capability of simulating the crack initiation and propagation in the masonry arch ring and the backfill.

Forgács et al. (2021) investigated the railway masonry arch bridges' dynamic and shakedown behaviour under various traffic load conditions. Static and dynamic loading analyses were undertaken to analyse the influences of transient traffic loads on masonry arch bridges. In addition, a nonlinear and mixed discrete-finite element was developed to evaluate the Prestwood masonry arch bridges' static and dynamic behaviour. This study's numerical model was created using UDEC software. The arch voussoirs were defined using a distinct block. Also, joint was modelled as a zero-thickness interface to open and close depended upon the

direction and stress amount level. The results revealed that plastic deformations and residual stresses occur in the arch barrel as the external load crosses the bridge. Furthermore, the size of the external load influences the dynamic amplification, which varies along the arch barrel. As a result, continuous plastic deformation was observed in subsequent dynamic load cycles, if the external load exceeded half of the ultimate load.

Giordano et al. (2002) used two approaches to model historic masonry structures. The finite element method within ABAQUS software was taken forward, where smeared cracking constitutive law and homogenised material approach were used. The discontinuous element method is the second approach where CASTEM and UDEC software packages were used. It was noted that additional research into developing a masonry-orientated constitutive model was required due to the ABAQUS model being unable to predict cyclic behaviour (Giordano et al., 2002).

Asteris et al. (2015, in Table 3) lists the limitation of the discrete element method and suggests poor performance in stress accuracy, which would be problematic in terms of brittle hinge location and computational demand (Asteris et al., 2015). Bui et al. (2017, in Table 5) suggests that the discrete element method cannot capture the structural behaviour of highly heterogenous interface elements.

According to Giamundo et al. (2014) DEM can model masonry arch voussoirs as separate elements, which can rotate and move relative to each other, completely detach and identify re-contact. However, the main disadvantage is computationally intensive, even when compared to FEM. Therefore, such requirements may not be feasible or practical for all research scenarios.

While innovative, the Discrete Element Method (DEM) encounters significant challenges when applied to masonry arch bridges. These bridges often present complex geometries, irregular masonry units, and varied material properties, which DEM struggles to represent accurately due to its particle-based nature. This leads to a necessary simplification in modelling, potentially resulting in the loss of critical structural details.

A further limitation arises from the interaction laws central to DEM, typically calibrated for small-scale experiments. When applied to the scale of natural masonry arch bridges, these laws may not adequately reflect real-world behaviours, possibly resulting in inaccurate predictions or assessments of structural integrity.

A critical aspect of masonry structures is the initiation and propagation of cracks, which is crucial to understanding failure mechanisms. However, DEM may not effectively model these complex fracture processes, often oversimplifying them, which undermines its utility in accurately predicting structural failures in masonry arch bridges.

3.2.4 *The finite element method (FEM)*

FEM is a numerical modelling technique that treats a structure as a continuum, divided into small discrete elements to analyse and understand structural behaviour. This method connects elements at points called nodes, with the number of nodes varying based on the type of mesh element used. The mesh consists of a network of cells and points designed to enhance the understanding of stress distribution within each element. Consequently, FEM can offer a detailed and accurate description of the way masonry structures respond under various conditions.

In general,the Finite Element Method (FEM) simplifies a problem that has an infinite number of degrees of freedom by breaking it down into a finite number of elements, each with specific material properties. FEM program modelling is an approximate explanation that imitates the actual structure so that structural engineers can design based on forces and deflections (Pelà et al., 2010).

The finite element method is particularly effective in describing the masonry structure materials representation and response behaviour. Masonry is considered a homogeneous anisotropic or isotropic material of units, mortar and interface depicted as an analogous continuum material (Silva et al., 2022).

The masonry constitutive models are accurate in modelling masonry arches with damage of varying localisation and dimensions and providing insight into global structural behaviour. However, large scale models of masonry structures are less effective at modelling localised behaviour such as cracking, which requires the use of fine mesh or contact elements (Silva et al., 2022).

FEA is a means of analysing and understanding the local behaviour of structures. If combined with masonry nonlinear material descriptions, it enables an accurate portrayal and

understanding of the bridge's complex geometry, boundary conditions and material features (Silva et al., 2022; Yazdani & Habibi, 2021).

According to Franck et al. (2020), the following are the significant characteristics of the proposed analysis for masonry arch bridges using nonlinear finite element simulations:

- The ability to simulate dynamic load effects. This includes assessing the stress-strain conditions and displacements at various loading increments.
- The ability to demonstrate various cracking (longitudinal), ring separation and pre-existing damage.
- Complex bridge 3D models can be created and investigated. Such geometry includes spandrel walls, backfill and skewed multi-span bridges.
- Material failure criteria application corresponds to characteristic failure modes of masonry arch bridges.

Many FEM programs are available, such as ABAQUS, ANSYS, PLAXIS, etc. ABAQUS is a finite element program designed to model the behaviour of structures under any loading. The following features are included (ABAQUS, 2019):

- Competence in both dynamic and static queries.
- The capability to model large shape variations in solids with different element types, in both 2D and 3D.
- An aptitude to model contact between solids.
- The ability to model different types of loading, including vibrations, acoustics, buckling and deformation of the settlement of structures.
- The ability to provide various options for damage simulation, such as cracking.

Finite Element Analysis (FEA) packages are widely available and many have been used to model small and large-scale masonry arch bridges. Some researchers have modelled existing bridges and others have modelled laboratory experiment bridges.

Past structural modelling of the soil and the arch initially used one-dimensional elements, reaction of the active and passive fill depended on an elasto-plastic relationship (Cavicchi & Gambarotta, 2005). Two models were produced using the FEA method. These numerical

models used the kinematic approach to model the soil-arch interaction. To allow the displacement discontinuities, interface elements were applied at the extrados locations. To model the soil element correctly, Mohr-Coulomb theory was used. This part was modelled as cohesive frictional material and this method assumed the soil element as isotropic linear elastic–perfectly plastic material. The numerical model created of the Prestwood Bridge did match the experimental test data, both developed four hinges. However, this was the only similarity, the simplified model had many assumptions and the soil interaction was limited. The interface elements did provide a problem, in that the triangular form manages to fix the direction interface elements used to allow discontinuities and therefore assuming perfect plasticity is a problem.

The numerical modelling presented by Cavicchi and Gambarotta produced results in some way that did correspond to the experimental results. However, modelling the elements in two dimensions affected the results; a better representation incorporates three-dimensional masonry elements. The upper and lower bound limit approaches of estimating the load capacity were too far apart and as a result, the numerical data could not be directly compared with the experimental data (Gilbert et al., 2013). The lower and upper bound approach required further research and Gilbert et al, (2007) addressed the issues highlighted from the Cavacchi numerical model tests. Both the upper and lower boundary models shown in Figure 3-3 and Figure 3-4 manually refined the mesh to replicate the soil backfill. The initial upper bound model had some issues such as, unanticipated soil stresses found at the left abutment as a result of excessive soil dilation. The interface between the arch and backfill, and soil friction parameters were reduced allowing the issue to be rectified.

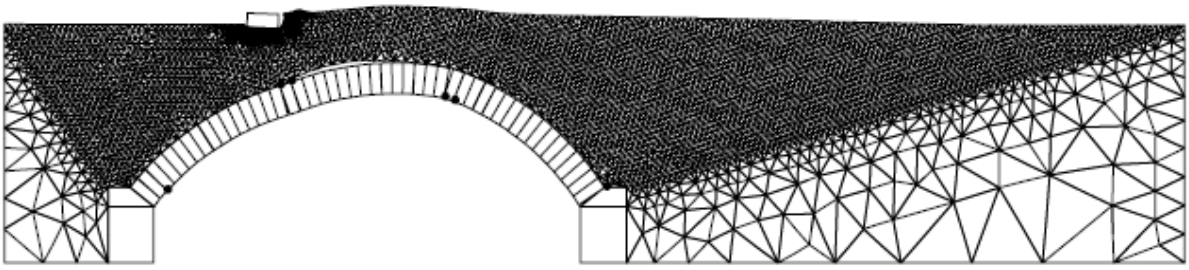

Figure 3-3: Upper bound deformed shape model (Gilbert, Nguyen, et al., 2007).

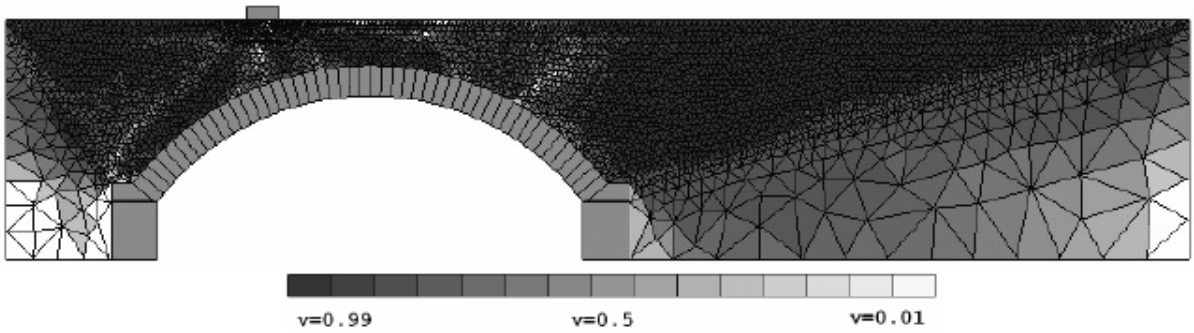

Figure 3-4: Maximum shear stress variations (Gilbert, Nguyen, et al., 2007).

The results from these tests show that load carrying capacity is directly affected by the soil structure interaction, and the loading beam, which was assumed to have a smooth surface and had very little impact upon the results. However, this could not be the case for the backfill and arch interface as the roughness of the element has a major effect on the load carrying capacity. The results from the numerical testing in the FEA package showed that the gap between the upper and lower bound was significantly reduced, thus showing an improvement on testing conducted by Cavicchi (Gilbert, Nguyen, et al., 2007). Historically, numerical models have used the peak soil strength in the analysis and found this to be an issue. Therefore, Gilbert et al (2007) found that it is necessary to use the mobilised soil strength to obtain data that is similar to the experimental tests.

Silva et al. (2022) simulated the post-crack condition in a masonry arch bridge under static and dynamic operational loading. Two non-linear modelling methods that used FEM continuous homogeneous models using ANSYS software. The masonry arch bridge was a single arch stone railway bridge, and the first model was created utilising an interchangeable continuous homogeneous Drucker-Prager failure criteria model for the entire bridge model. In contrast, the second model was created using a combination of discrete crack modelling and FEM's ability to simulate opening of a longitudinal crack in the arch barrel. This study established that the finite element method demonstrated computational efficiency in non-linear analysis, and that good cracking representation is achieved when the finite element method combines with contact elements.

Giamundo et al. (2014) assessed suitability of the DEM and FEM approaches in the analysis of two low strength masonry structures of different types, by comparing experimental data and numerical results. The numerical modelling used DIANA software for the FEM application with continuous elements, and UDEC software was used for the discrete element method. The

two low-strength masonry structures were wall panels with a 2.025m span opening; one built using low bond strength brickwork and the second used low strength *tuff* masonry. In conclusion, both DEM and FEM techniques were effective in modelling the behaviour at the large scale, up to first crack. However, to predict the behaviour of masonry until failure, the DEM was the more reliable in analysing low bond strength masonry. The FEM method was more dependable regarding brickwork with low unit strength. FEM was used to approximate the experimental behaviour. Validation looked at the failure crack pattern and location of initial cracks.

Zhang et al. (2016) investigated masonry arch bridge collapse using a mesoscale technique to produce 3D masonry arch bridge models implemented using a nonlinear finite element program called ADAPTIC. The units (bricks) were modelled as 3D elastic solid elements, and the mortar element was modelled as 2D interface nonlinear zero thickness elements instead of using full-thickness mortar, as shown in Figure 3-5. The study simulated different span-rise ratios, loading locations, and bridge types (Zhang et al., 2016). However, the shortcomings of this study are rooted in the use of zero thickness mortar which reduces the accuracy of complex behaviour prediction and does not represent mortar as a brittle material. Also, the mesoscale strategy combined with the partition approach to simulate the models in parallel computations increased the computational cost.

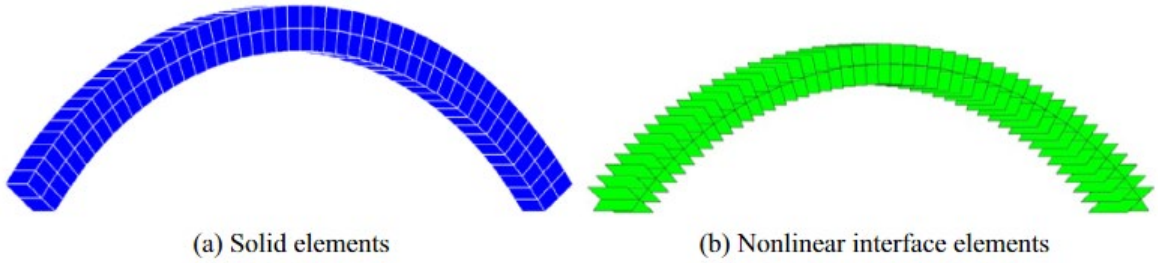

Figure 3-5: Masonry arch mesoscale modelling technique (Zhang et al., 2016).

Yazdani and Habibi (2021) simulated two existing masonry arch bridges using FEM and XFEM to predict masonry arch bridge residual capacity using ABAQUS software. However, in this study, all the structural bridge parts were mass concrete constructions. The concrete damaged plasticity criteria (CDP) was used in the FEA model to represent the nonlinearity of the material behaviour. The numerical model results were validated against experimental tests, and the results indicated that this method has a very high level of agreement.

3.3 Numerical research on masonry arch bridges subject to foundation movement

This section is on past numerical research on the movement of masonry arch bridges and arch rings under various displacement directions and values.

Ye et al. (2018) proposed a new assessment method that used point cloud data to monitor the geometry of masonry arch bridges. This technique involves capturing the bridge's geometry in a point cloud format, subsequently analysed by segmenting it into distinct 2D and 3D structural elements such as piers and barrels. The process includes fitting primitive shapes to these components and examining the discrepancies between the shapes and the point clouds, which reveal characteristic distortion signatures indicative of various structural issues. Specifically, in their application to two UK masonry rail viaducts, Ye et al. demonstrated the method's efficacy in deducing past support movements that resulted in observable damage. This was achieved by comparing the distortions against theoretical distortion traces derived from kinematic analyses. However, the method's utility might be limited due to its heavy reliance on detailed geometrical scans of distorted arch barrel shapes and the potential challenges in generalizing the findings across different types of bridges. Furthermore, the dependence on accurate point cloud data and theoretical models could be a point of contention, as these may not fully encapsulate the complexities inherent in real-world bridge behaviours, thereby limiting the broader applicability of this assessment method.

Many researches including Zampieri et al. (2017) and Coccia et al. (2015) investigated masonry arches on settling abutments. Dalgic et al. (2018), Galassi et al. (2013), tackled this problem by processing the masonry as a continuum. Researchers, such as Iannuzzo et al. (2018a) and Iannuzzo et al. (2018b) improved their models in a series of publications using approximate numerical techniques. In contrast, Tralli et al. (2020) provide a detailed summary of the literature relating to masonry arch bridge analysis composed by a finite number of rigid blocks in order to analyse for settlements.

Tralli et al. (2020) delve into modelling masonry structures affected by foundation settlements, presenting a novel perspective by examining the resulting crack patterns and mechanisms. Their approach employs variational formulations, primarily focusing on structures that can be modelled as assemblies of multiple no-tension rigid bodies. This method is particularly

insightful for understanding masonry structure behaviour and load-bearing capacity under foundation settlement conditions. The study also addresses the limitations of Heyman's hypotheses in the limited analysis of masonry structures, underscoring the need for more comprehensive approaches. Furthermore, the paper discusses the deformation of masonry arch rings and bridges due to foundation movements, emphasizing that these structures must adapt to such settlements. This adaptation is characterized by the formation of crack patterns, leading to the displacement of masonry as rigid bodies. This phenomenon is described in 2D (as lines) and 3D (along surfaces) contexts, requiring the analysis model to be partitioned into separate blocks, as illustrated in Figure 3-6. However, the paper's reliance on specific theoretical models and assumptions about material properties may restrict its applicability across various real-world scenarios, suggesting a need for further research and validation in diverse structural contexts.

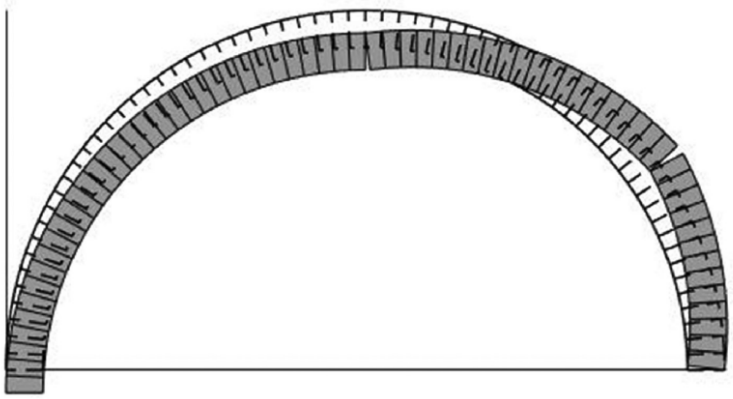

Figure 3-6: Pier vertical settlement analysis model (Tralli et al., 2020).

The numerical analysis heavily relies on variational formulations and treats masonry as a collection of rigid, no-tension bodies. This assumption of rigidity may not fully capture the actual behaviour of masonry, particularly under various loading conditions and material ageing processes. The method simplifies masonry structures into discrete elements while addressing unilateral contact problems, which aids computational analysis. However, this simplification could overlook the continuous nature and material heterogeneity of real masonry structures, potentially impacting the accuracy of stress distribution and crack propagation predictions. Developed for specific cases and conditions, the methodology may not directly apply to all masonry structures, notably those with distinctive architectural features or those constructed from modern materials that do not adhere to the no-tension assumption. Furthermore, masonry structures exhibit nonlinear behaviours under diverse loads, which the proposed linear

programming approach might not completely capture. Consequently, the model's capacity to accurately predict failure mechanisms under complex loading conditions, including dynamic loads, remains uncertain.

Drosopoulos et al. (2008) investigate the ultimate failure load of stone arch bridges using finite element models. It focuses on how the geometry of stone arches and the movement of abutments impact mechanical behaviour and collapse mechanisms. Drosopoulos et al. (2008) used a non-linear finite element model that includes contact interfaces to simulate potential cracks. This model used a non-associated flow rule in transition and shear failure regions and an associated flow rule in the cap region. A parametric study was used to investigate the influence of span to rise ratio on an arch of span 9.425 m, and subject to horizontal or vertical movement of one support in conjunction with load at the quarter span, as shown Figure 3-7. They conclude that ultimate load capacity is unaffected by support movement, though this was not entirely replicated when load was placed at midspan. When addressing the behaviour of the arch approaching the collapse load, they conclude that the fourth hinge to develop does not appear immediately, and the location of the last hinge to form depends upon the direction of movement of the abutment and position of the applied live load. The irregularity and temporary degradation of stiffness shown in the load displacement graphs is attributed to this variable behaviour of arch hinge formation close to collapse. The study's parametric investigation, focusing on the impact of span-to-rise ratio, does not encompass all critical factors influencing arch bridge behaviour. Real-world conditions like material degradation, weathering, and long-term load effects are not explicitly considered. Neither does it study the influence of the nonlinear material properties or interaction properties on the masonry arch under foundation movements. The study compares its results with Heyman's classical method based on simplified assumptions.

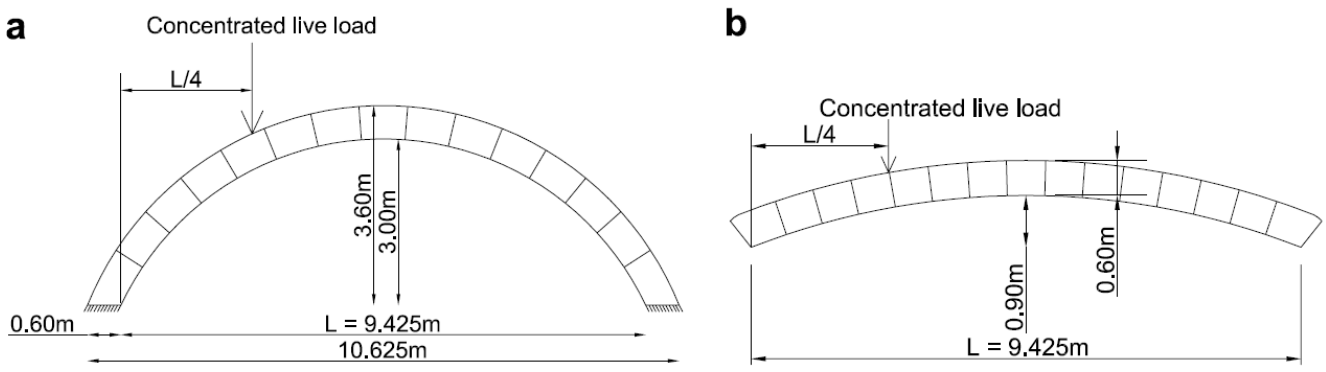

Figure 3-7: (a) Initial arch geometry with abutments horizontally fixed; (b) a shallow arch without abutments fixed (Drosopoulos et al., 2008).

Zhang et al. (2017) investigated the effects of numerous parameters using the mesoscale modelling strategy in an extensive numerical study on the masonry arch. The abutment stiffness and the abutment movements were included in this study as one of the various parameters to investigate, because they are commonly overlooked during experimental assessments of masonry arch rings and bridges (Zhang et al., 2017). This study included three movement directions: settlement, sliding outwards, and sliding inwards. However, the maximum displacement value of each movement was 6mm, which is a minimal abutment movement value. Also, the study did not involve combination or rotational movements at the abutments.

The numerical model's geometry was different from the experimental geometry, where the brick layout of the experimental test was 47 bricks for the first ring and 49 bricks for the second ring. However, the numerical brickwork layout for the two rings was created of 48 bricks. The abutment movement numerical investigation response was computed under force control, whereas the experimental tests for this multi-ring masonry arch were under displacement control. Furthermore, the validated numerical model for this study was under displacement control, which will cause unclear results of the movement abutment.

Figure 3-8 shows the outcomes of varying levels of movement at the support of the masonry arch in three distinct directions, where the line load at the quarter span is plotted against the quarter span arch vertical displacement. However, the numerical results are presented only up to the ultimate load point. This is because the numerical models were analysed under force control, explaining why the results do not represent the post-peak behaviour.

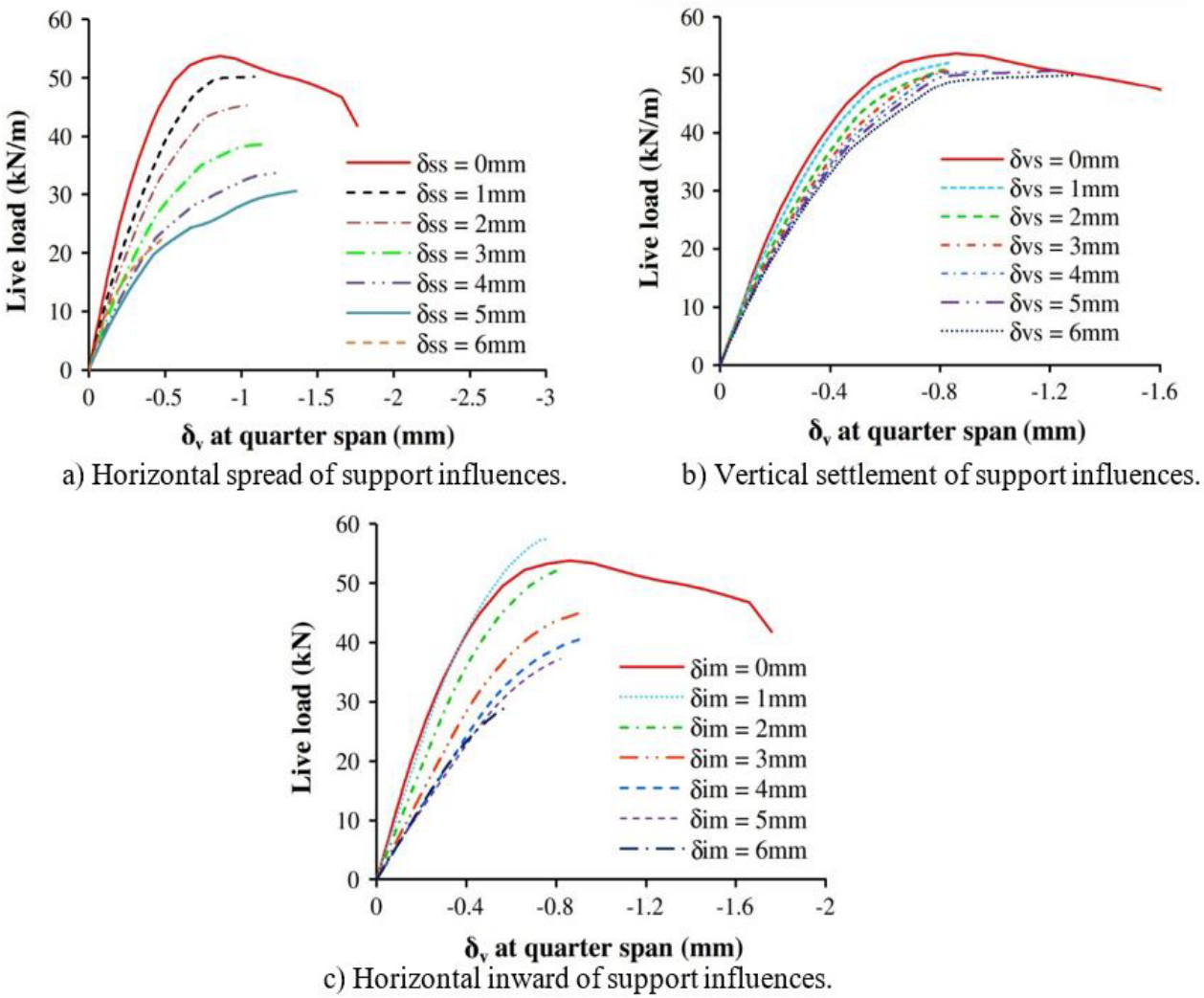

Figure 3-8: Influence of three different movements at the abutment results (Zhang et al., 2017).

Zhang et al. (2017) present results for the same arch with similar support movement directions but using different values of movement. The applied displacements at the masonry arch abutment are plotted against the reaction forces, as shown in Figure 3-9. The numerical model simulations in this analysis were conducted under displacement control to investigate the reaction force of the masonry arch weight, without applying any additional load following the movement of the arch.

The results from the support's horizontal spreading and inward movement indicate that the ultimate load point was around 2mm, exhibiting no ductile behaviour and had steeper post-peak softening behaviour. In contrast, the support's vertical settlement movement demonstrates more ductile behaviour compared to the other two movements. The results of these numerical

models are based on the weight of the masonry arch alone, without any additional load applied after the support movements.

It is evident that following the post-peak softening behaviour, the post-failure behaviour of the three numerical results began at approximately 10 mm and continued smoothly up to 40 mm, as illustrated in Figure 3-9. In addition, the results did not provide which direction of the reaction force had been plotted against the foundation movement, as the results display three different foundation movement directions.

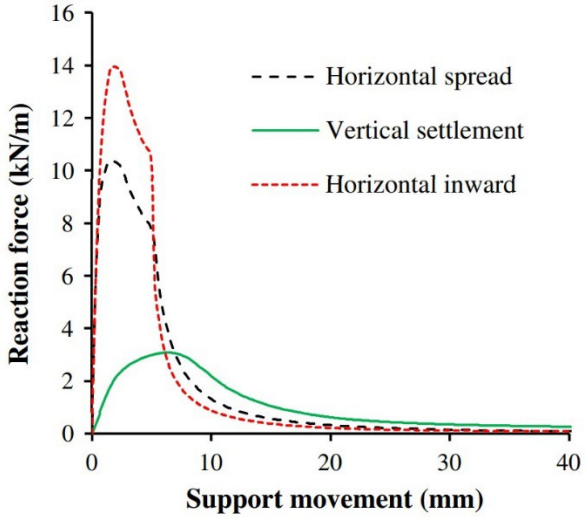

Figure 3-9: Reaction force-abutment displacement results for different support movements for the masonry arch self-weight only (Zhang et al., 2017).

Zampieri et al. (2018) presented two experimental tests of an arch subject to settlement in two directions and rotation, validated by limit finite element modelling of single-ring masonry arch tests made of 37 voussoirs, to identify hinge locations. The joints were modelled as one-dimensional point contact elements in the numerical model, whereas the bricks were modelled as linear elastic elements. They show that as displacement increases and the arch shape changes, there is a significant change in the reaction values, which peak and quickly drop to a minima. It was noticed that the experimental arch test (shown in Figure 3-10) focused on identifying hinge locations instead of concentrating on the effect of movement on the arch barrel. This is because the joint was specifically made with no-tensile strength between masonry units. This was resolved by inserting a plexiglass plate in the middle of each mortar joint, hence resulting in the arch barrel settling more without any resistance. The assumptions made during the

analysis might oversimplify the real-world behaviour of the arches, leading to conclusions that might not be universally applicable.

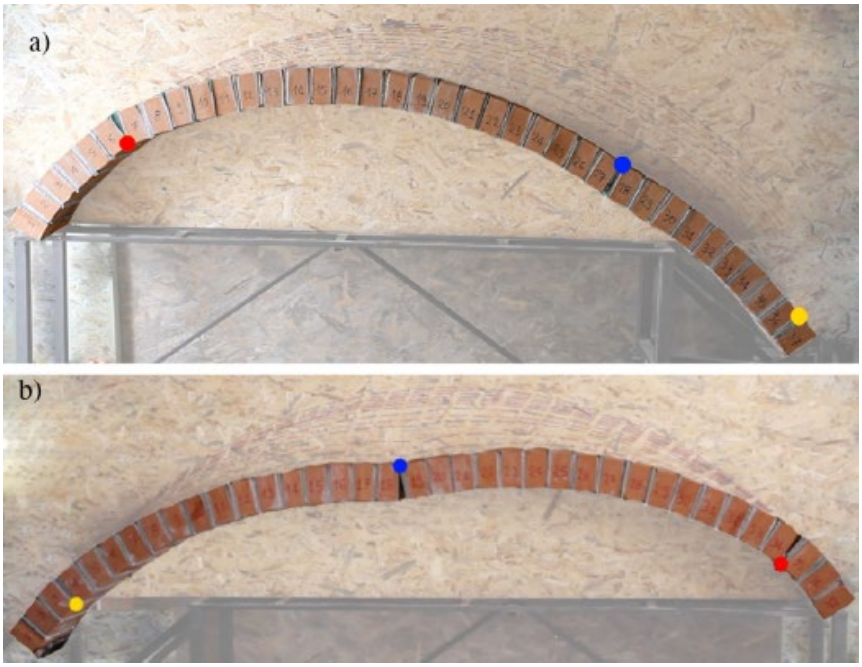

Figure 3-10: Experimental failure arrangement: (a) α=90°; (b) α=45° (Zampieri et al., 2018).

Tubaldi et al. (2018) investigated a two-span segmental masonry arch viaduct in which the central pier was supported on Winkler soil springs, in order to simulate loss of support due to scour, as shown in Figure 3-11. A succession of models with horizontal and vertical springs removed, or with reduced stiffness on one side were used to determine the behaviour of a viaduct subject to progressive scour of the foundation.

The results of this study were utilised to determine the degrees of scour responsible for surpassing various threshold states pertinent to the performance of masonry arch bridges. The employed model facilitates the cracking prediction in the arch model and between the spandrel walls and the arch. A parametric analysis involving progressive increments in scour depths up to structural collapse revealed that scour significantly reduces stiffness. However, the vertical load-bearing capacity remains largely unaffected until scour depths reach considerably elevated levels. This phenomenon can be attributed to the intrinsic redundancy inherent in the arch design and the ductility of the backfill material.

The study offers an in-depth, mesoscale approach to comprehensively understanding masonry arch bridge behaviour under scour conditions. It introduces advanced modelling techniques,

enhancing understanding of structural behaviours in complex scenarios. However, the model was not modelled using detailed micro modelling to investigate the behaviour of the whole masonry arch bridge as mortar is the weakest material type in these bridges.

This study applied a specific type of movement to their model to simulate the influences of scour on the masonry arch bridge structure. This movement was a roto-translational movement of the pier base imposed on the model. This type of movement involves rotational and translational components, simulating the complex motion that a bridge pier might undergo due to scour effects. The settlements, mimicking this roto-translational movement, were incrementally increased, with the maximum settlement reaching 2.5 mm at the upstream side of the pier base. This approach allowed the researchers to examine the effects of such movements on bridge structural integrity, mainly focusing on the resulting crack patterns and overall stability under simulated scour conditions.

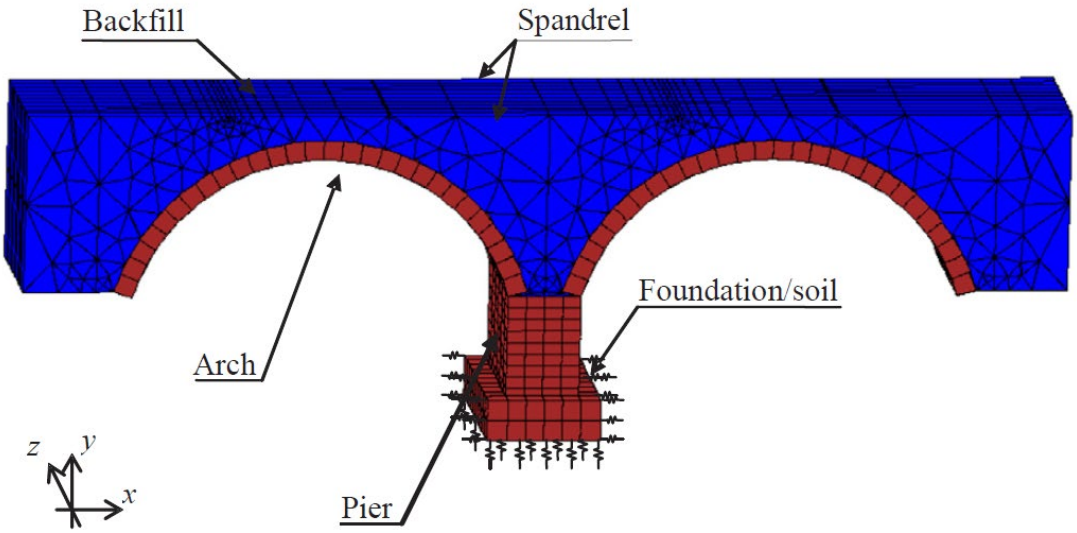

Figure 3-11: 3D masonry arch bridge model (Tubaldi et al., 2018).

Zampieri et al. (2019) investigated semi-circular masonry arches supported by slender rectangular abutments, focusing on scenarios involving imposed settlements. Their approach was grounded in using the principle of virtual work, combined with thrust line analysis, to thoroughly analyse the ultimate states of these structures. This analysis was especially relevant in situations where one support was subjected to imposed settlement, in addition to the self-weight of the structure. The study found that buttressed masonry arches are more susceptible

to horizontal sliding when the buttressed height-to-arch span ratio is high, and conversely, more prone to vertical settlement when this ratio is low.

While the study relies on well-established principles such as virtual work and thrust line analysis, it could face criticism for not incorporating a more comprehensive array of analytical methodologies or modern computational techniques, such as the Finite Element Method (FEM) or Discrete Element Method (DEM). These advanced methods might offer a more holistic understanding of the masonry structural behaviour of buttressed arches.

Furthermore, the specificity of the study's context may limit the generalizability of its findings to other types of masonry structures or modern architectural designs. The research methodology, with assumptions such as the exclusive possibility of radial ruptures, potentially oversimplifies complex real-world interactions, thus casting doubts on the validity and broader applicability of the conclusions drawn.

Additionally, the theoretical and analytical nature of the study opens it up to critique regarding empirical validation. A significant limitation is the absence of experimental verification or real-world case studies to substantiate the analytical findings. Integrating empirical data would strengthen the study's conclusions and provide practical insights into the behaviour of these structures under real-life conditions, thereby enhancing the study's relevance and practical applicability in engineering scenarios.

Ferrero et al. (2021) examined a single-ring dry-joint masonry arch structural response subjected to large foundation displacements. Utilising both finite element and rigid block models, grounded in a micro-modelling strategy, the authors sought to accurately replicate the behaviour of masonry arches under stress. Notably, these models were rigorously validated against physical tests sourced from existing literature, enhancing the credibility of their findings. The study notably achieved a commendable correlation between the ultimate displacement and hinge configuration at the point of collapse with the results of these physical tests, indicating robustness in their modelling approach.

However, the researchers identified a critical factor in the micro-modelling process: the stiffness of the interface elements requires careful evaluation. This insight is pivotal as it underscores the intricate balance needed in modelling to simulate real-world conditions accurately. Furthermore, the study revealed that the discretization of the arch elements

significantly impacts the hinge location. This detail might be overlooked if the actual bricks of an arch are being modelled. This finding is particularly insightful, highlighting how modelling choices can influence the interpretation of structural behaviour.

Nevertheless, the study's reliance on certain simplified assumptions, such as infinite compressive strength, absence of tensile strength, and a lack of consideration for sliding, could pose limitations. While these assumptions simplify the modelling process, they may not entirely encapsulate masonry arches' nuanced and often unpredictable behaviour, especially under varying environmental conditions and material heterogeneity. This gap indicates a potential area for further research and refinement of modelling approaches.

Moreover, the study aims to understand the impact of displacement direction on the response of masonry arches, which is a significant contribution, particularly in preserving cultural heritage structures. This aspect of the study adds to the existing body of knowledge and presents a practical avenue for applying this understanding to the conservation and maintenance of historic buildings. However, the extent to which this research propels the field forward, offering new, actionable insights, remains an area for further exploration and discussion within the academic community.

In summary, the study by Ferrero et al. represents a significant step in understanding the structural behaviour of masonry arches under stress, combining detailed modelling with practical application. While the findings bring valuable insights, especially regarding hinge dynamics and model accuracy, they also highlight the ongoing need for model refinement and consideration of real-world complexities in structural engineering research.

Galassi, S., & Zampieri, P. (2023) developed a new procedure for analysing masonry arches subjected to horizontal and vertical support movements, considering both right and left supports. Integrating an incremental approach and Somigliana's distortions method, this method evaluates internal forces and addresses material and geometric nonlinearity without updating the stiffness matrix. Its effectiveness is confirmed through case studies aligning with existing research. However, the approach's reliance on certain assumptions might limit its applicability in varied conditions, and it may oversimplify complex structural behaviours, necessitating cautious interpretation and further comparative analysis with contemporary methods.

3.4 Modelling techniques and approaches

This section reviews the different material modelling types, techniques and strategies as there are several for capturing the nonlinear masonry behaviour available to model masonry arches. Furthermore, it will consider the previous research numerical analysis using these strategies and techniques. Figure 3-12 is derived from Asteris et al. (2015) and indicates the various strategies of numerical approaches to characterise masonry structures' mechanical behaviour, which will be explored in the following section.

The finite element method (FEM) is an excellent tool for modelling continuous structures such as masonry bridges with a virtually infinite quantity of elements. The finite element method may be subdivided into two different approaches. These approaches are homogenous and heterogeneous; where the heterogeneous approach considers units and mortar joints separately, making a more representative model. In the homogeneous approach, a morphed composite material is used to model all of the masonry elements.

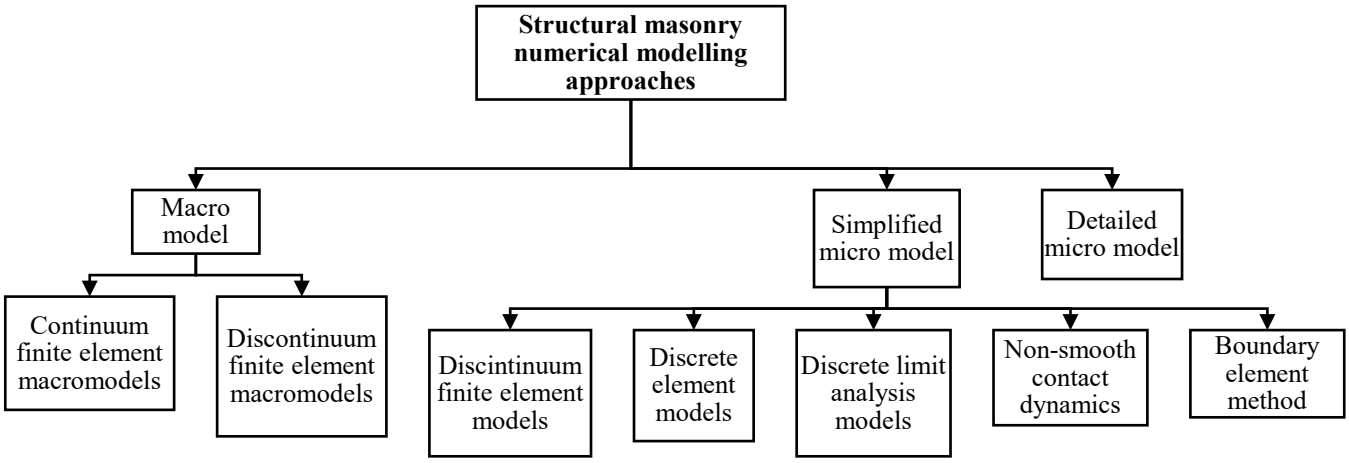

Figure 3-12: Different numerical modelling strategies for masonry structure analysis (adopted from (Asteris et al., 2015)).

Figure 3-12 presents various numerical modelling approaches for structural masonry analysis. It classifies these approaches into three broad categories: macro-modelling, simplified micro-modelling, and detailed micro-modelling. Each of these categories is further divided into specific methods, as detailed below:

- Macro-modelling:
    1. Continuum finite element macro models: These models treat the masonry as a continuous medium, simplifying the geometry and the mechanical properties across the masonry.
    2. Discontinuum finite element macro models: These models represent the masonry with discrete elements, allowing for the structure's simulation of cracks and joints.

- Simplified Micro-modelling:

    1. Discontinuum Finite Element models: A more detailed approach than macro models, focusing on the individual elements of the masonry and their interactions.
    2. Discrete Element models: These models consider the individual bricks as separate entities that interact with each other.
    3. Discrete Limit Analysis Models: Utilizing the principles of limit analysis, these models evaluate the ultimate load capacity without detailed modelling of the structure's response.
    4. Non-smooth contact dynamics: A method that deals with dynamic problems involving collisions and friction between discrete bodies.
    5. Boundary Element Method: A method for solving boundary-value problems of the potential theory and elasticity. It is often used for problems with complicated geometries.

The selection of a particular method depends on the level of detail required, the specific characteristics of the masonry structure, and the type of analysis (e.g., static or dynamic) needed. Each method has advantages and limitations, and the choice will be dictated by the balance between computational efficiency and the accuracy required.

3.4.1 *Modelling material behaviour types*

There are two types of masonry structure material behaviour: linear and non-linear. Non-linear material behaviour analysis is considered an appropriate method to simulate masonry arch behaviour. According to (Zucchini & Lourenço, 2004), due to low tensile strength, cracking is responsible for most non-linear masonry behaviour. As a result, the stiffness will be reduced

in mortar joint cracked areas. Since masonry arches and bridges were built using a brittle material, they generally show a complex response under traffic and extreme loading.

Numerous computational studies have been conducted to investigate the behaviour of masonry arches and bridges using material nonlinearity using various plastic models. The purpose of modelling and analysing masonry structures using non-linear material is to reach a better understanding and realistic prediction of their behaviour.

Masonry non-linearity depends on brick and mortar joint properties and brick-mortar bond interaction. According to (Plumbridge et al., 2003), there are three types of non-linearity:

- Geometric: (large strain and large deformations).
- Material non-linear behaviour: (plasticity).
- Boundary contact: interaction between the elements and the support.

3.4.1.1 Homogeneous models

This approach type is very suitable for large-scale structures. In this model, the masonry units and mortar joints are characterised as an isotropic material (same section properties in all directions), and the properties are smeared. The investigation of any structure must represent the original conditions in order to achieve a representative result and the correct behaviour. However, this approach assumes the model as composites. Bolhassani (2015) used the homogeneous approach to model masonry walls, although the masonry was not a homogeneous material. Due to the responsive homogeneous models, the experimental and numerical results did not match. As mentioned in Chapter 2, masonry is a heterogeneous material. Figure 3-13 describes the homogeneous approach process.

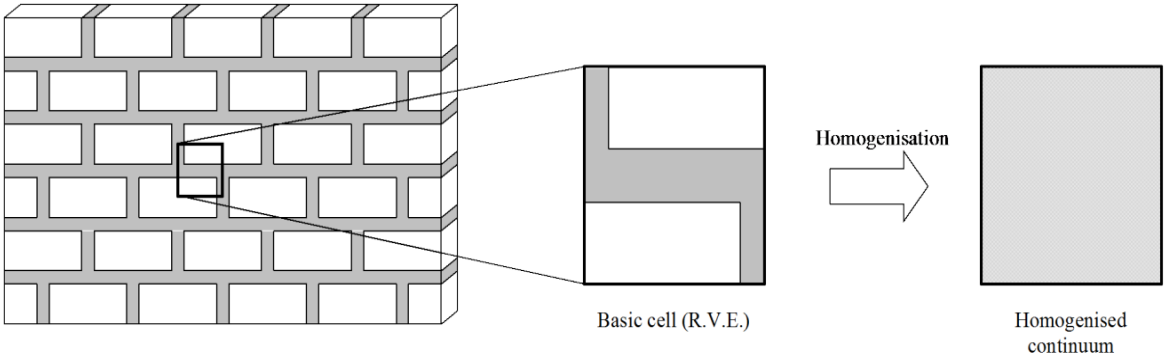

Figure 3-13: Masonry basic cell of homogenisation (Zucchini & Lourenço, 2002).

The advantage of assuming homogeneous material behaviour is that computational effort is low. However, this approach is insufficient for detailed modelling of masonry structures and capturing failure mechanisms (Lourenço, 1996).

3.4.1.2 Heterogeneous models

Masonry is a heterogeneous material made of bricks and mortars with various directional properties. Also, the mortar joint is the weakest component in this type of structure (Lourenço, 1996). This technique can be used to construct masonry structure models with different essential material properties. The heterogeneous approach is more complicated than the homogeneous approach. Therefore, there are complicated and straightforward ways of modelling the material, to achieve varying levels of accuracy.

3.4.2 *Modelling approaches*

According to (Lourenço, 1996), there are three strategies: macro-model, simplified micro-model and detailed micro-model. These strategies have various descriptions and masonry representations of the material and the interaction between each element. Each of these strategies has a different computational cost for running the numerical models. Furthermore, the detailed micro-model strategy is the most detailed and accurate by separately representing the masonry unit (bricks) continuum as non-linear and the mortar joints continuum as non-linear. The unit-mortar non-linear interface (bond) is represented separately, as shown in Figure 3-14 (b).

The simplified micro-model strategy uses a non-linear interface to define the mortar joint (zero thickness) and the unit-mortar interface, where the unit element is a continuum element, as shown in Figure 3-14 (c). The macro-modelling strategy assumes masonry elements to be homogeneous using isotropic material behaviour. Also, the model describes only one continuum element, as shown in Figure 3-14 (d).

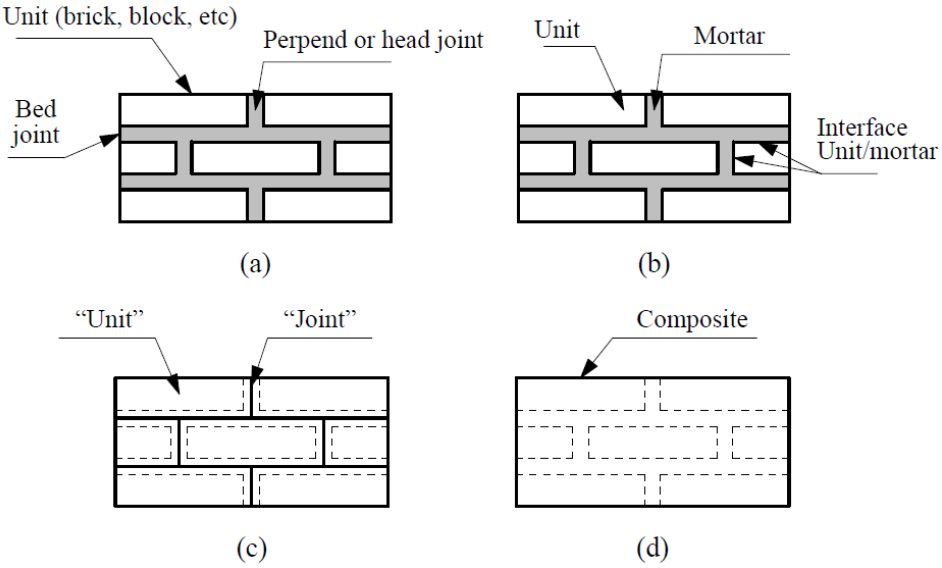

Figure 3-14: Masonry modelling strategies : (a) masonry sample; (b) detailed micro-modelling; (c) simplified micro-modelling; (d) macro-modelling (Lourenço, 1996).

The numerical literature review indicates that macro-modelling and micro-modelling are currently the most commonly studied approaches in developing masonry structure computational representation. Furthermore, modelling developed in this thesis will consider modelling separate unit and mortar joint elements, which could be modelled using detailed micro-modelling. It is appropriate to investigate, review and describe all the common modelling methods.

3.4.2.1 Macro-modelling

This method considers composite materials for masonry (Rots, 1991). A macro method is one of the homogenous techniques and can be used to model complete structures. However, these methods have advantages and disadvantages; macro modelling does not provide sufficient local influence for detailed numerical analysis. Units, joints, and interfaces are all represented using one homogeneous element in the macro-modelling method. As a result, the macro-modelling

approach does not distinguish all the masonry structure components, such as units or mortar joints (Lourenço, 1996; Zucchini & Lourenço, 2004).

Milani and Lourenco (2012) investigated the masonry arch bridge behaviour using 2D and 3D models. The masonry bridge models were created using a macro modelling homogenous approach with nonlinear interface *parallelepiped* rigid elements, as shown in Figure 3-15. The backfill material was modelled using isotropic Mohr-Coulomb as elastic-plastic solid elements with tension cut-off. The numerical results were obtained using 2D and 3D description and these were compared with experimental results to investigate the 2D limitations and to have better insight for the 3D actual capabilities, where it was established that 3D models provide a better understanding of the masonry arch bridge response (Milani & Lourenço, 2012).

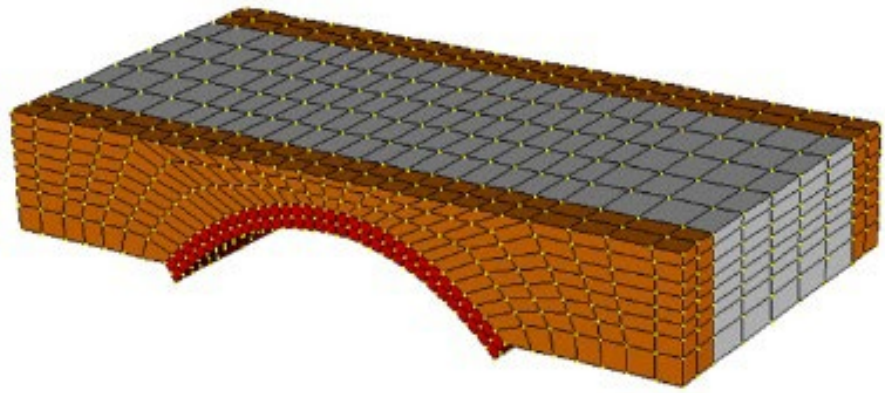

Figure 3-15: 3D macro model of masonry arch bridge (Milani & Lourenço, 2012).

Wang (2004) investigated the behaviour of two types of masonry arch bridges, being square and skew arches. Experimental and numerical results were compared using 3D models with two types of finite element software (ANSYS and ABAQUS) as shown in Figure 3-16. Complex masonry arch behaviour was simplified by using a homogenous strategy and the two arch models were analysed using solid elements. The comparison showed correct prediction in terms of failure mechanism. However, the load-displacement relationship displayed differences between the experimental and numerical curves, where the numerical results showed a stiffer response than the experimental results, and the ultimate load capacity was higher than experimental (Wang, 2004).

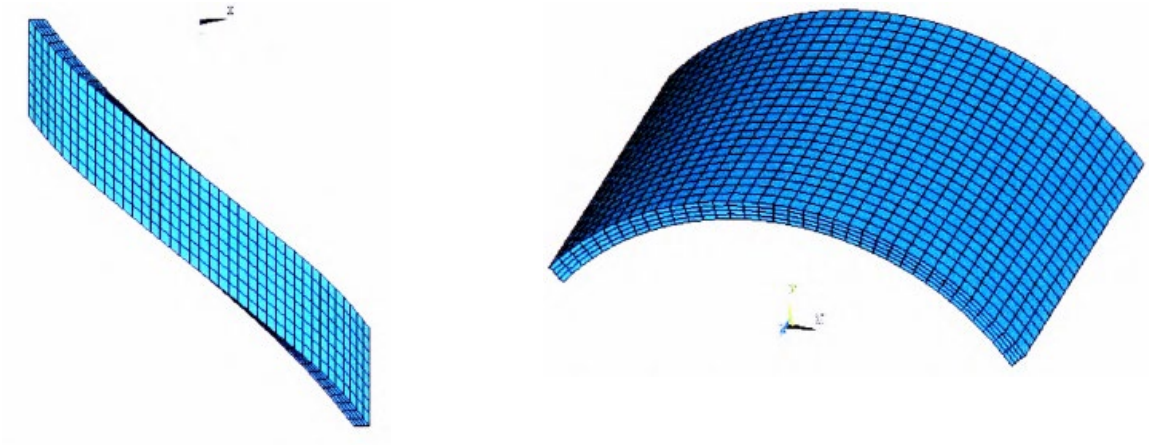

(A) Skew arch (B) Square arch

Figure 3-16: Masonry arch bridge 3D models (Wang, 2004).

Macro-modelling is the least computationally demanding approach available for masonry arches numerical analysis due to there being fewer input data requirements. Nevertheless, this approach cannot present the complex material behaviour of the masonry and critical failure modes such as ring separation, bond failure, and cracking in the mortar elements.

3.4.2.2 Micro-modelling

This approach is divided into simplified micro-modelling and detailed micro-modelling (Lourenço, 1996). The micro-modelling approach is mainly used to analyse small masonry structures. Furthermore, the masonry structure components and the surface interactions are the main interest to model using this approach.

The structural behaviour accuracy in micro-modelling is significant and the nonlinear behaviour cracks are of great importance. However, it has posed problems, in that high performance computers are required to solve fairly large structures.

Micro-modelling is used to model heterogenous masonry structures, which need a better understanding of behaviour and failure modes. Also, this approach has the ability to model all mechanism failures.

A. Simplified micro-modelling

The simplified micro-modelling method can be used to investigate the behaviour and response of masonry structures such as arches, bridges and walls. The mortar joints and the unit mortar

interface are both merged as discontinuous elements. However, the dimensions of mortar joints are extended up to a partial thickness in all directions as shown in Figure 3-17.

The simplified micro-modelling method is executed using expanded units defined by continuous elements with the mortar joint and an interface to connect the expanded unit elements. This means the mortar joint is ignored and defined using fracture interaction by the two interfaces of the expanded units' two elements.

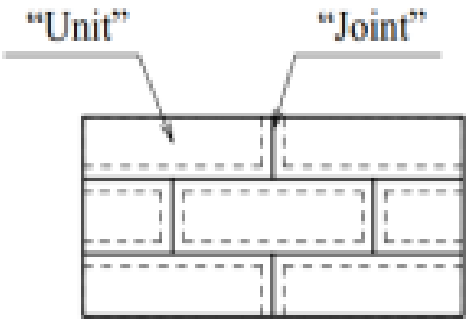

Figure 3-17: Simplified micro-modelling approach (Lourenço et al., 1998).

Lotfi and Shing (1994) and Rots (1991); (1997) modelled early masonry structural behaviour simulations until the masonry model collapsed, using a non-linear interface. Previous studies on the finite element method, such as Berto et al. (2004); Lourenço and Rots (1997); Shing et al. (1992); Lotfi and Shing (1994) used interface micro models.

Lourenço and Rots (1997) have significantly improved the simplified micro-modelling approach by developing the interface model to include all types of non-linearities; compressive crushing, shear sliding, and tensile cracking to be executed in the interfaces between the continuum unit elements. Furthermore, the models created using this approach are computationally intensive, so Sutcliffe et al. (2001) recognised an improved simplified micro model, which obtains a rigorous lower bond value of collapse loads in unreinforced masonry shear walls.

Another improvement for the interface approach that has been used for real applications reported by Macorini and Izzuddin (2011) which is a strategy of interface elements that accurately describes a mesoscale method for material and geometric non-linear analysis of

masonry structures. Unlike previous interface strategies the unit-mortar interface and mortar are modelled using 2D non-linear interface elements. The units are modelled using 3D continuum solid elements, as shown in Figure 3-18. Carol et al. (2001) suggest using non-linear interface elements to model the slip planes or prospective cracks, which permits the numerical result accuracy to be improved through mesh refinement.

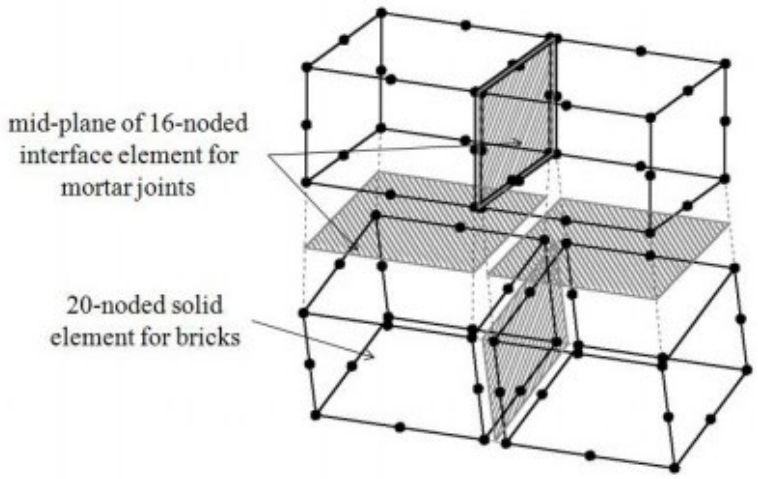

Figure 3-18: 3D bricks and 2D non-linear interface elements (Macorini & Izzuddin, 2011).

This technique allows the representation of 3D arrangements of masonry by accounting for the through-thickness geometry and the in-plane stacking. It also permits the in and out-of-plane investigation of the behaviour of masonry structures (Macorini & Izzuddin, 2011).

Mesoscale models for masonry structures are developed to model the in-plane mortar and bricks (Macorini & Izzuddin, 2011). Furthermore, some models cannot adequately assess the performance of structures under extreme loading conditions, e.g. masonry panel behaviour cannot be investigated in both in-plane and out-of-plane loading.

The mesoscale method provides strain results and deformation analysis of both linear and nonlinear structures. In addition, it gives an accurate outcome for material and geometric nonlinear models with various loadings (Macorini & Izzuddin, 2011). The ability to produce results that are reliable is another advantage, especially when involving deformations and strain.

As shown in Figure 3-19, the interface elements have zero thickness, are organised in vertical mid-plane blocks, and run along a shorter horizontal direction. Thus, shear and tension failure of the unit can be considered, while Lourenço and Rots (1997) utilised the 2D planar elements

of linear bricks with 1D interface nonlinear elements used together (Macorini & Izzuddin, 2011).

A non-linear interface element is an influential tool; it produces an interaction between two different solid elements. Furthermore, it helps to capture failure mechanisms in large structure systems. In the past, interface elements were used to simulate discontinuities in mechanics of jointed rock, to simulate brittle material cracking in materials such as concrete, and it has been recently used to create a particle fracture in composite multi-layers (Goodman et al., 1968; Mang et al., 2003; Segurado & Llorca, 2004). This strategy offers simplicity and accuracy to model a complex masonry structure and understand the non-linear behaviour.

Also, it must be noted that increasing the structure size by expanding unit elements will bring problems to the numerical simulation analysis. As a result, this affects the masonry unit stiffness and reduces the masonry model accuracy outcome (Sarhosis, 2011; Schlegel & Rautenstrauch, 2004).

There is little difference when using the micro and meso-scale modelling technique. Deformed shape results of 2D and 3D shapes obtained by Kamiński (2008) suggests this, even though both methods allow 3D modelling and the results show good correlation. The simplified approach obtains results in one direction (2D), thus allowing quick and accurate deformation results.

As mentioned earlier, simplified micro-modelling can be adjusted by applying the non-linear properties and behaviour for the expanded units and the interfaces. However, for masonry arches, this will affect the whole geometry of the arch. According to (Greco et al., 2020), it is impossible to capture the complex interaction at unit-mortar interfaces using this approach due to neglected mortar joint Poisson effects in both elastic and plastic regimes.

The discrete technique (Brocks et al., 2003) was used to model the brick-mortar interface, bricks, and mortar behaviours through non-linear materials. This was established from fracture mechanics non-linear principles, in which the mortar joints are decreased to interface elements with zero thickness and display the mortar non-linear behaviour.

B. Detailed micro-modelling

In detailed micro-modelling, bricks and mortar joint are represented by continuous elements and are modelled separately, whereas discontinuous elements show the interface behaviour between bricks and mortar joint. To this end, Figure 3-19 shows continuous elements of separated units, mortar joints and unit-mortar non-linear interfaces.

In this modelling strategy, all component characteristics can be considered, thus more fully reflecting actual component behaviour and units and mortar mechanical material properties such as; density, Young's modulus and Poisson's ratio will be required (Lourenço, 2002).

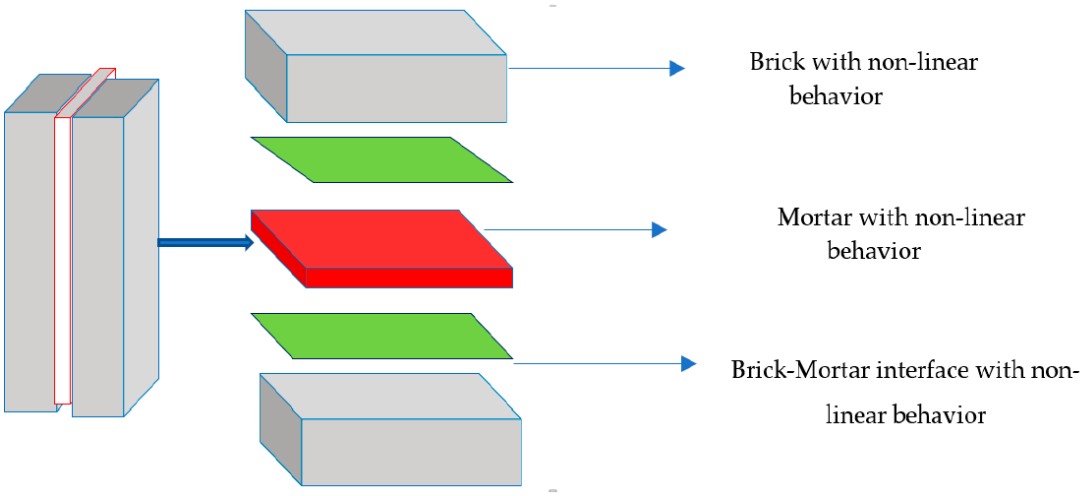

Figure 3-19: Detailed micro-modelling approach (Hernoune et al., 2020).

Detailed micro-modelling represents mortar units and interface units through discontinuous and continuous elements. As a result, the combination of these joints and units can provide an accurate result and behaviour of masonry arch bridges (Lourenço et al., 1998). Due to the mortar joint being modelled separately, the plastic material behaviour parameters are required. According to Sarhosis (2011), this approach introduces an appropriate constitutive law, enabling it to depict the realistic behaviour of the units, mortar and the unit-mortar interface.

The detailed micro-modelling advantages compared to the simplified micro-modelling are due to the continuous and discontinuous detailed element. It can capture the interaction between unit-mortar interaction and the damage failure in the mortar joint by incorporating failure inside the joint (Greco et al., 2020). As a result, the model will predict accurate crack patterns in the mortar joint.

According to Sarhosis and Lemos (2018), this approach's critical advantage is implementing cracking in the mortar joint as discontinuity among particles and not just modifying the material properties. Furthermore, reliable masonry strength prediction can decrease the requirement for experimental cost and time which also helps to avoid dependence on traditional empirical formulae.

Hernoune et al. (2020) present a reinforced masonry wall behaviour study, under compression-shear loads, and compared the experimental result with a finite element model. The wall was modelled using the detailed micro-modelling approach using ABAQUS software, as shown in Figure 3-20. Concrete damaged plasticity (constitutive laws) simulated the non-linear behaviour of units and mortar elements. As a result, the detailed micro-model provided an excellent prediction of the interface post-peak behaviour and the masonry wall failure mode, compared with the experimental result.

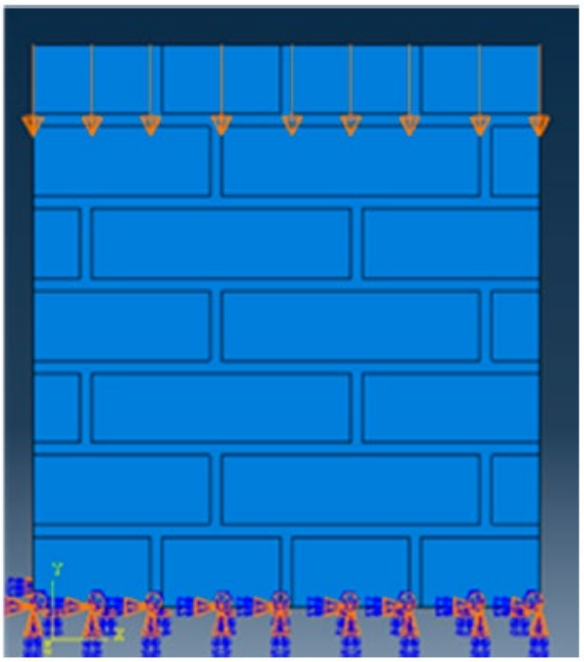

Figure 3-20: Detailed micro-modelling numerical model of the masonry wall (Hernoune et al., 2020).

The detailed micro-model approach keeps the cracking phenomena realistic within the mortar joint. This approach will capture the different failure mechanisms within the mortar joint and

at the unit-mortar interfaces, such as tension cracking into the mortar thickness and shear sliding across the mortar interface.

According to Sutcliffe et al. (2001), using a detailed micro-modelling approach for masonry structure models leads to more accurate results compared to other approaches. However, it requires intensive computational effort. Furthermore, using the detailed micro-modelling will identify all the failure modes of masonry structures.

3.5 Numerical modelling method & software

There are two principal numerical methods to model masonry arch bridges using the detailed micro-modelling approach: Finite Element Method (FEM) and Discrete Element Method (DEM). Each method has various software packages to model and represent masonry structures. These two methods have different abilities to simulate and analyse realistic masonry arch bridges and their natural behaviour.

Masonry arch bridges are described as heterogeneous brittle materials, so the software must be able to simulate these properties.

The software must offer the facility to model complex geometry and simulate non-linear behaviour in both material and geometry. To understand and evaluate the masonry arch bridges behaviour, it has to be able to model interaction properties, a range of loading types and boundary conditions.

ABAQUS software can solve non-linear behaviour structure problems including offering the extended finite element method (XFEM) to model natural crack initiation and propagation. Previous researchers used this software to produce effective simulations and report flexibility in modelling and investigating masonry structural behaviour (Abdulla et al., 2018; Abdulla et al., 2017; Bayraktar & Hökelekli, 2021; Hernoune et al., 2020; Kareem et al., 2022; Susila et al., 2016; Susila et al., 2015).

The extended finite element method (XFEM) has been used recently in a small number of numerical analyses (Abdulla et al., 2017; Susila et al., 2015), where these used ABAQUS software and XFEM to simulate masonry structures.

Abdulla et al. (2017) presented a 3D masonry wall model using a simplified micro-modelling approach and included the behaviour of surface cohesion in the masonry joint. Furthermore, XFEM simulated the crack at the mortar joints. Also, Susila et al. (2016) proposed a 3D masonry wall under monotonic and cyclic loading to investigate the dynamic behaviour and evaluate the wall performance. The numerical analysis accuracy was assessed by comparing the load-displacement behaviour and the crack patterns for the experimental and numerical results.

ABAQUS is the only finite element method software to simulate cracking using XFEM. In contrast, other software does not simulate cracks and only display damage in the model. Therefore, the FEM technique and ABAQUS software are the most suitable for modelling and simulation of masonry arches at collapse. According to D'Altri et al. (2020) although a limited number of papers have been published, analysis using XFEM offers a powerful alternative for simulating masonry structures.

3.6 Constitutive model for detailed micro-model approach

The constitutive law is a material behaviour response mathematical description, of mechanical and strength properties. This section describes the detailed micro-model constitutive models that were used to simulate masonry arches. This section describes how the failure modes were modelled.

3.6.1 *Cohesive interaction modelling*

The purpose of implementing cohesive interaction is to simulate the interaction at unit-mortar interfaces, which will help to simulate and obtain the natural behaviour of the masonry between the interface elements. The joint fracture response behaviour is captured based on the traction-separation behaviour at the unit-mortar interface. The simulated mortar failure modes are joint tensile cracking and joint shear sliding between the two surfaces.

3.6.1.1 Mortar joint interface elastic behaviour

The mortar joint interface's initial response depends on the linear traction-separation relationship before the damage occurs. Furthermore, an elastic stiffness matrix represents the general elastic behaviour. When simulating the masonry, both traction separation damage and cohesive interaction will be applied in examining systems of interface bonding. ABAQUS allows elastic properties to be defined through nominal strain and traction, and the cohesive

behaviour specification creates constraints that implement the cohesion in both normal and tangential directions.

Equation 3-1 is provided for localised component's directional responses, where the *K* is the elastic stiffness matrix, *t* is the nominal traction stress vector, and ε is the corresponding separation vector.

$$\begin{pmatrix} \boldsymbol{t_n} \\ \boldsymbol{t_s} \\ \boldsymbol{t_t} \end{pmatrix} = \begin{bmatrix} \boldsymbol{K_{nn}} & \boldsymbol{0} & \boldsymbol{0} \\ \boldsymbol{0} & \boldsymbol{K_{ss}} & \boldsymbol{0} \\ \boldsymbol{0} & \boldsymbol{0} & \boldsymbol{K_{tt}} \end{bmatrix} . \begin{pmatrix} \boldsymbol{\varepsilon_n} \\ \boldsymbol{\varepsilon_t} \\ \boldsymbol{\varepsilon_s} \end{pmatrix} \qquad \text{Equation 3-1}$$

Where, nominal traction for the normal direction is given by quantity t_n, and nominal traction in the two locally occurring shear directions is given by t_t and t_s. Meanwhile, nominal strain which corresponds to the above is given by ε_n, ε_t and ε_s respectively.

There are various procedures to calculate the stiffness of mortar joint interfaces to represent the original mortar joint interfaces. These methods depend on the modelling approach if the mortar joint is modelled separately or has been modelled within the expanded unit.

According to (Lourenço & Rots, 1997; Rots, 1997) the mortar joints could be modelled using Equation 3-2 and Equation 3-3, which are used to obtain the cohesive contact stiffness:

$$\boldsymbol{k_n} = \frac{\boldsymbol{E_{joint}}}{\boldsymbol{h_{joint}}} \qquad \text{Equation 3-2}$$

$$\boldsymbol{k_t} = \frac{\boldsymbol{G_{joint}}}{\boldsymbol{h_{joint}}} \qquad \text{Equation 3-3}$$

An alternative method can accurately measure the joint stiffness by calculating the linear slope of the stress-displacement curves derived from direct tensile and shear tests on masonry joint interfaces, where this method was used by Abdulla et al. (2017). This method will obtain the joint stiffness from the tensile and shear tests in Chapter 4.

3.6.1.2 Mortar joint interface plastic behaviour

It should be noted that damage within surface-based cohesive behaviour represents a property of the interaction between brick and mortar surfaces. This discussion relates to the properties

of cohesive behaviour for implementation using ABAQUS, considering ways of identifying properties and their place in ABAQUS interactions:

a) Surface-based cohesive behaviour allows for simplification in modelling cohesive joints using a traction-separation law.
b) When using ABAQUS/Standard solver for defining cohesive interaction, the surface to surface contact method must be used.
c) There is high similarity between laws/formulae governing surface-based cohesive interaction and constitutive behaviour of cohesive elements:
   i. Linear elastic behaviour before damage initiation,
   ii. Criteria for damage initiation,
   iii. Criteria for damage evolution.

A. Defining damage – damage initiation

The damage initiation criterion indicates the beginning of the cohesive interaction response degradation at the contact points. Furthermore, crack propagation follows the mortar joint linear response behaviour.

The process of crack propagation into the mortar joint when the damage initiation criterion is satisfied is based on the traction (contact stresses) values that have been specified, such as mortar joint tensile and shear strength. ABAQUS provides several damage initiation criteria to specify damage initiation in the mortar joints.

In this study, the maximum nominal stress criterion has been chosen to be used and specified along with the damage evolution to provide using the energy evolution type, which can be linear, exponential or tabular softening.

B. Defining damage – damage evolution

Damage evolution describes the material behaviour of the post damage initiation criterion. Also, it defines the material stiffness degradation rate once the value of damage initiation is reached, as this leads the joint to failure and strength loss. The damage evolution equation is written as:

$$\boldsymbol{\sigma = (1 - D)\,\bar{\sigma}} \qquad \text{Equation 3-4}$$

D is the damage evolution scalar value; the value ranges between 0.0 to 1.0, where 0.0 is no damage, and 1.0 is a complete failure. The damage stress calculates using *(1-D)* multiplied by

undamaged stress, where σ is the damaged response value, and $\bar{\sigma}$ is the value of undamaged response. The damaged response represents when *D=0*, and when *D=1* represents the material complete failure response.

The traction-separation softening behaviour graph can be specified based on linear exponential softening, as shown in Figure 3-21. Furthermore, the mixed-mode fracture energy behaviour is specified based on the defined contact interfaces for fracture energy values in three directions.

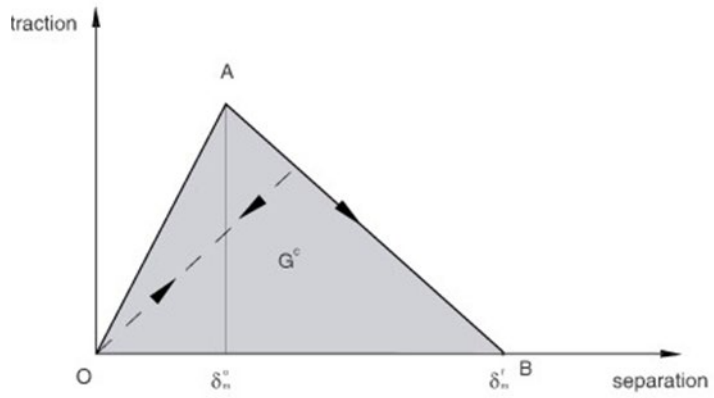

(A) Linear softening damage evolution

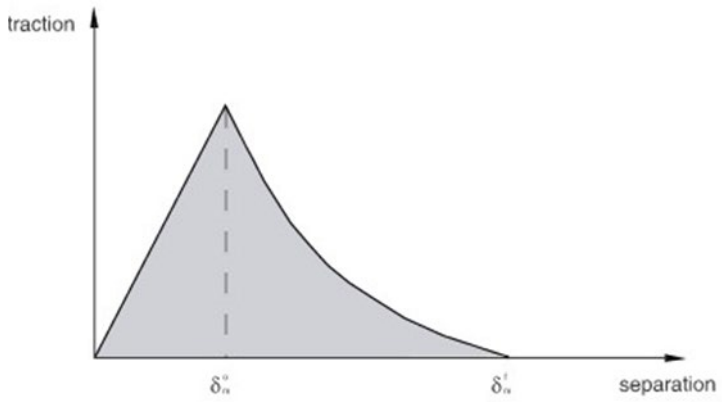

(B) Exponential softening damage evolution

Figure 3-21: Cohesive surface joint damage propagation types (ABAQUS, 2019).

C. Defining damage - damage stabilization

The masonry joints softening behaviour and joint stiffness degradation leads to numerical convergence difficulties during the simulation. Therefore, damage stabilisation is an ABAQUS function which allows a viscosity coefficient to be obtained that determines viscous

regularization to avoid these difficulties for the surface-based cohesive behaviour to simulate the masonry joints full failure.

3.6.1.3 Behaviour of Normal and Tangential Model

The contact pressure-overclosure relationship defines hard contact behaviour in normal behaviour interaction contact between the unit-mortar surfaces. The hard contact behaviour contact supposes that two surfaces come into contact and are compressed and transmit pressure. The hard contact relationship minimises the slave surface's penetration into the master surface and does not allow the tensile stress transfer between the contact surfaces. The tangential behaviour defines the unit-mortar surface friction coefficient (elastic slip), and then the mortar joint post-failure shear sliding behaviour will be simulated.

3.6.2 *Evaluating cracking through XFEM*

XFEM is used as a more appropriate approach to examining cracking. This is due to the fact that discontinuities are allowed within elements in the approach to this, which ABAQUS offers. The crack can be initiated and propagated using the extended finite element method (XFEM). Hence, based on these criteria, ABAQUS and XFEM were chosen as the best software and method to simulate the masonry structural response for this study. XFEM's approach does not demand re-meshing yet still gives a solution-reliant pathway that works effectively. The definition of an element's discontinuities is performed through enriching degrees of freedom utilising special functions for displacement. Thus, in approaching numerical solutions, this enrichment is connected to developing classical shape and displacement functions and enrichment. The XFEM method can be used for initiating and propagating cracks in simulations in order to address singularity and discontinuity occurrence (ABAQUS, 2019).

There are two distinct types of procedures for implementing cracks using XFEM in the numerical models, based on the cohesive segments approach or linear elastic fracture mechanics approach (LEFM). In the case of the LEFM approach, the virtual crack closure technique (VCCT) for crack propagation is used. This method requires the user to set and define the crack locations.

Conversely, the cohesive segment approach uses the traction-separation law, which is defined in the material definition in the module property. This study chose the cohesive segment approach to model cracks within XFEM. Using XFEM, damage evolution can be simulated in

the mortar without predefining the initial crack location. This method was chosen to accommodate the material's brittleness (mortar joint) since the location of the crack would be unpredictable in a real scenario.

Using modelling of fractures by XFEM for ABAQUS, cracking can be predicted using the process for analysing static stress. Where cracking takes place, two output variables are beneficial in identifying where cracking takes place, as follows:

1. CSDMG: this shows the damage variable for cohesive surface interaction, presenting the bond failure between the interface of unit-mortar in this study. Cracks formed at the unit-mortar interface are located through CSDMG where 0.0 a value means undamaged and 1.0 means complete opened crack (*delamination*) formed at the unit-mortar interface.

2. STATUSXFEM: this output provides the status of enriched elements. If the element is undamaged the output value is 0.0, whereas if the output value is 1.0 the element is completely damaged (where the crack cuts through the whole element, leaving no traction forces). The other possible scenario is where the output value is between 0.0 and 1.0, which shows the element is somewhat damaged (some traction forces remain).

The traction-separation law is used to define cohesive interaction to predict damage initiation and propagation. Also, the traction-separation law defines mortar's mechanical behaviour. It is used alongside XFEM (Extended Finite Element Method) to predict crack initiation and crack propagation in the mortar's thickness. Furthermore, the maximum principal stress criterion (MAXPS) has been chosen to predict the damage initiation. The damage starts to initiate when the value of maximum principal stress is exceeded.

3.6.3 ***Boundary conditions***

Boundary condition specification is needed for FEM when applying typical biaxial loads within structures. The current research sets such boundary conditions as an appropriate mechanical support in modelling the masonry arch. For this FEM, loading and support mechanism boundary conditions are linked to the relevant constraints within the modelling.

3.7 Non-linear plasticity material behaviour criteria

In ABAQUS, non-linear material behaviour may be defined using several options. Soil and masonry are often modelled with Drucker-Prager or Mohr-Coulomb criteria. The mortar joints in masonry arch rings should be modelled using non-linear elements.

3.7.1 *Mohr-Coulomb criterion*

The Mohr-Coulomb method sets out a series of equations and conditions for which an isotropic material will fail. Jeagar and Cook (1979) explained that this principle can be expressed in two different ways; (a) shear stress τ and normal stress σ on plane failure, or (b) minor σ_{III} and major σ_I principal stresses. Originally Coulomb set out a list of conditions in 1776, allowing the determination of shear and normal stresses that cause a material to fracture (Coulomb, 1776). While Coulombs criterion is based upon linear failure envelopes, Mohr in 1900 introduced a criterion based on linear and non-linear failure planes (Mohr, 1900). The later method deduced that failure is dependent on the principal stresses (minor and major) and the failure plane shape.

The retaining wall theory investigated by Coulomb proposed Equation 3-5.

$$\boldsymbol{\tau = S_0 + \sigma tan\phi} \qquad \text{Equation 3-5}$$

The equation expressed the relationship between the shear stress of the material against the normal stress applied and is classically represented by Figure 3-23. The equation requires two conditions to be constant, the inherent shear strength (S_0) and the internal friction angle (ϕ).

The failure envelope represented in Figure 3-22 was developed by using Coulombs criterion, which allows the inclined line to be constructed. These failure envelopes were created by introducing the principal stress Equation 3-6, developed by Mohr.

$$\boldsymbol{(\sigma_1 - \sigma_m) = (\sigma_1 + \sigma_{III})\, sin\phi + 2S_0 cos\phi} \qquad \text{Equation 3-6}$$

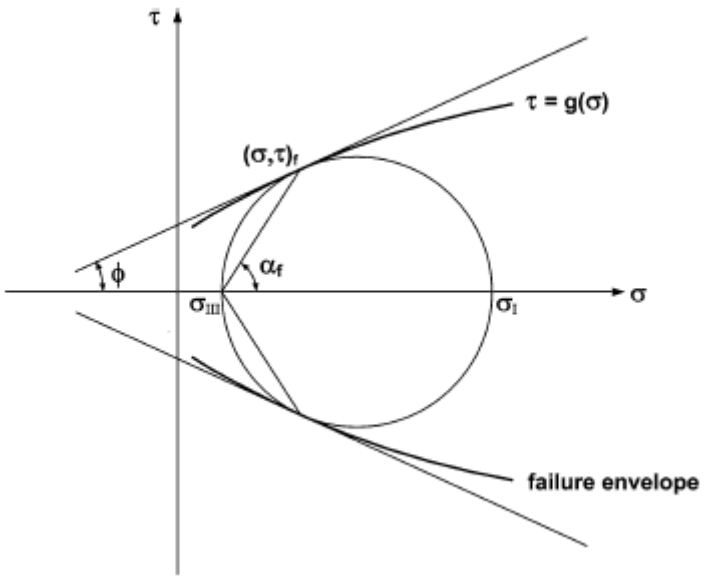

Figure 3-22: Mohr failure envelopes (Labuz & Zang, 2012).

To achieve the stress state at failure, diameter of the circle is a tangent to the failure envelope and therefore Mohr's envelope assumption is assumed to be equivalent to Coulomb's criterion. Jeagar and Cook (1979) noticed that during experiments the failure envelope on Mohr diagram representing the shear, normal stress and the angle, α_f is not always observed.

Mohr-Coulomb criteria failure was the first to consider the hydrostatic pressure effects on granular material strength. This method is still used extensively in areas of geotechnical design (Labuz & Zang, 2012).

The criterion of Mohr-Coulomb has universal recognition and thus has led to many researchers implementing this approach. This approach clearly sets various material parameters, especially for materials such as rock, mortar or concrete; and materials that fail under small strain plasticity or fail in the elastic range (Labuz & Zang, 2012).

Zampieri et al. (2017) utilised the Mohr-Coulomb criterion in multiple aspects of finite element modelling. Specifically, the Mohr-Coulomb elastic-plastic constitutive law was employed to characterise the soil elements, playing a crucial role in analysing the soil behaviour under various load conditions, especially under the influence of scour. This criterion was also pivotal in modelling the backfill material alongside a Drucker-Prager model for the masonry material.

The Mohr-Coulomb model provided a detailed understanding mechanical response of the backfill, which is essential for assessing masonry arch bridge structural integrity and response in scour conditions.

Sarhosis et al. (2019b) used the Mohr-Coulomb failure criterion to simulate the behaviour of mortar joints between bricks in masonry arch bridges. This approach represented these joints as zero-thickness interface elements within a discrete element model. The model constrained shear stresses along these joints according to the Mohr-Coulomb criterion, setting the cohesion and tension of the mortar joints to a relatively low value of approximately 7 kPa.

While effective, the Mohr-Coulomb criterion has limitations in capturing non-linear and anisotropic behaviours of materials under varying stress states. Relying solely on this criterion may not fully represent the complex mechanical behaviour of mortar joints under different loading conditions. However, using the Mohr-Coulomb failure criterion for modelling the behaviour of mortar joints is a strong point. This criterion is widely accepted for its effectiveness in representing shear stress limitations in geotechnical and structural engineering contexts.

While computationally efficient, using zero-thickness interface elements may oversimplify the complex interactions in actual mortar joints. These joints have a finite thickness and more complex material properties that might influence the overall bridge structural behaviour.

3.7.2 *Drucker-Prager criterion*

This approach models the stress at which the material reaches its ultimate capacity using a pressure-dependent three-dimensional model. The method assumes that octahedral shear stress at failure depends solely on the normal stress. This criterion is a development of Mohr-Coulomb for non-linear material behaviour and is expressed by Equation 3-7:

$$\sqrt{J_2} = \lambda I_1' + k \qquad \text{Equation 3-7}$$

The material constants within the Drucker-Prager equation are λ and k. The second invariant of the stress deviator tensor is J_2, with I_1' representing the first variant of the effective stress tensor. This original Drucker-Prager method was further modified and can be written in the form of Equation 3-8:

$$\sqrt{J_2} = b\sqrt{\frac{\alpha^2(I_1^2 - 2a_i I_1) + a_2^2}{b^2 + (1-b^2)sin^2(45^\circ - 1.5\theta)}}$$ Equation 3-8

The parameter that defines the shape is b (usually = 0.75), θ is the load angle. The other parameters such as α, a^1, $a^2$are further expanded below:

$$\alpha = \frac{2sin\phi}{\sqrt{3}(3 - sin\phi)}$$ Equation 3-9

$$a^1 = \frac{1}{2}(C_o - T_o) - \frac{C_o^2 - (\frac{T_o}{b})}{6\alpha^2(C_o + T_o)}^2$$ Equation 3-10

$$a^2 = \sqrt{[\frac{\frac{T_o}{b^2} + C_o}{3(C_o + T_o)} - \alpha^2]C_o T_o}$$ Equation 3-11

The uniaxial compression and tension are represented as C_o and T_o respectively, and the internal friction angle of the material as ϕ. Following on from these equations there are four ways the Drucker-Prager cone can approximate the Mohr-Coulomb hexagonal surface and this is represented in Figure 3-23.

The principal aim of this criterion was to defeat the problems of Mohr-Coulomb standard, such as the univocal technique does not define the plasticization function gradient on the pyramid corners. However, the Drucker-Prager model defines a failure surface that is oriented along the hydrostatic axis. The biaxial stress failure domain is shown in Figure 3-23.

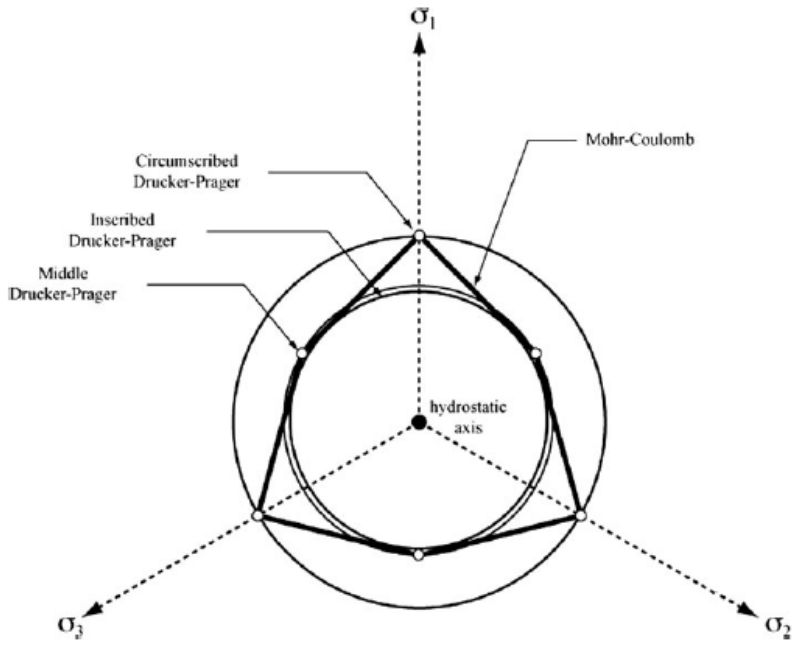

Figure 3-23: Mohr-Coulomb and Drucker-Prager failure criteria (Alejano & Bobet, 2012).

The features of the cap yield surface add to the models of Drucker-Prager, which serve two primary purposes:

- Plastic compaction is represented by providing an inelastic hardening mechanism, due to restrictions in hydrostatic compression by the yield surface.
- Assists in managing volume dilatancy during material shear yield by inducing softening relative to the inelastic volume, thereby enhancing the material's yield along the Drucker-Prager shear failure surface.

This approach is used to determine crucial points with a relatively small modelling exertion, and it is grounded in the limit analysis theorems. It is used to employ uncomplicated models of homogenous material (Lourenço, 1996).

The material properties allow the model to develop cracks and hinges. Furthermore, this approach permits the behaviour of hinges to be plastic. The arch hinges are formed when the load factor is increased, yield criteria are exceeded at specific locations, and the boundary conditions of the arch are transformed. This results in the bending moment sustained at hinges remaining stable. The process is repeated until the fourth hinge is formed (Koksal et al., 2016) and a collapse mechanism ensues.

Elasto-plastic analysis is a choice that Drucker-Prager plasticity models have used because of the smooth yield surface for a frictional material and the failure criterion (Koksal et al., 2010; Lucio & Bartolomeo, 2015). The principal Drucker-Prager criterion material parameters are; i) flow stress ratio; ii) friction angle; iii) dilation angle (Hojdys et al., 2013).

Tubaldi et al. (2018) used the Drucker-Prager and Mohr-Coulomb criteria to simulate the plastic behaviour of the backfill in their study on masonry arch bridges. The backfill domain was discretized using 15-noded elastoplastic tetrahedral elements characterized by elastoplastic material behaviour. Specific values for Poisson's ratio and Young's modulus determined these elements' isotropic elastic response. Meanwhile, their plastic behaviour was represented using a modified Drucker-Prager yield failure criterion that incorporated limits for both compression and tension.

The Drucker-Prager yield envelope is created by smoothing the Mohr-Coulomb yield envelope. The parameters of the Drucker-Prager model, specifically α and k, were function of the cohesion, c and the friction angle, ϕ associated with the Mohr-Coulomb yield surface. These parameters could be adjusted so that the Drucker-Prager yield envelope coincided with the Mohr-Coulomb yield surface's outer or inner edges. The usual recommendation was to achieve coincidence at the inner edges, for which specific formulae were used to calculate the parameters α and k.

This approach allowed for more nuanced and accurate modelling of the backfill's plastic behaviour under various stress conditions, essential for predicting the response of masonry arch bridges subject to foundation scour.

Silva et al. (2019) utilised the Drucker-Prager model in their finite element modelling to simulate the nonlinear behaviour of masonry and infill materials. This model was produced in ANSYS software, was treated as showing perfectly plastic behaviour without any representation of softening, which is a significant limitation, especially in the tension/shear aspects. The Drucker-Prager model was characterised by elastic-plastic behaviour, defined by parameters like friction angle, cohesion, and dilatancy angle.

The research centred on the Durrães railway bridge, using a nonlinear modelling strategy with FE (finite element) continuous homogeneous models. This method was employed to assess the bridge whilst in use, specifically under traffic loads. The Drucker-Prager model was utilised

for both the masonry and infill materials of the bridge, helping to analyse how the structure responds to dynamic loads, such as a train represented by moving loads passing over the bridge. However, this simulation did not consider the interaction between the train and the bridge, showing a simplified approach to dynamic analysis.

While the Drucker-Prager model is adept at simulating the elastic-plastic behaviour of masonry and infill materials, essential for assessing masonry bridge structural response, it has notable flaws. Its strength lies in enhancing the realism of finite element analysis simulations by representing the nonlinear behaviour of bridge materials under service loads. This is key for a thorough evaluation of bridge performance.

However, the model's assumption of perfectly plastic behaviour, without accounting for softening, is a significant shortcoming. Masonry materials often exhibit softening, especially under high-stress conditions, and ignoring this can lead to inaccuracies in predicting the bridge's response to extreme loads. Additionally, the model's non-null tension cut-off might need to capture the intricate interplay between tensile and shear stresses in masonry more effectively, potentially compromising the accuracy of failure mode predictions.

The Drucker-Prager yield surface is utilised as a Mohr-Coulomb yield surface smooth version, enabling the calculation of Drucker-Prager material parameters based on cohesion and the angle of internal friction, key Mohr-Coulomb parameters (Zhang, Tubaldi, et al., 2018). This approach is particularly advantageous in enhancing numerical robustness and addressing computational challenges at the yield and plastic potential surface corners in the Mohr-Coulomb model. A modified Drucker-Prager yield criterion is developed for this purpose (Zhang, Tubaldi, et al., 2018).

Furthermore, in the numerical analysis of masonry arch bridges, the Drucker-Prager yield surface fitted to the inner edges of the Mohr-Coulomb yield surface represents the backfill's plastic behaviour. This fitting provides a capacity prediction more aligned with analytical solutions than if fitted to the outer edges (Zhang, Tubaldi, et al., 2018). This comprehensive application of the Drucker-Prager and Mohr-Coulomb models underscores their significance in accurately and efficiently analysing structural behaviour in masonry bridges, particularly in soil-structure interaction and backfill material modelling.

3.8 Finite element method mesh

Although the material components are isotropic, the meshing method allows for the differing material properties along the orthotropic directions (Koksal et al., 2016).

The analysis of nonlinear masonry structures is considered isotropic; there will be an artificial weakness produced through the mesh topology in the horizontal direction. In addition, a maximum size will be determined along the masonry structure, and it will be much smaller in size, where the size of the mesh in the vertical direction is limited to the mortar thickness and the unit height (Koksal et al., 2016).

Mesh density is important in finite element analysis. High density models require longer computing time but offer higher accuracy (up to a point). Conversely, models with coarse mesh could lead to less adequate results but shorter computational time. The primary dilemma is to pick an adequate element size, which will produce adequate analysis results and minimise computational time.

Previous studies have investigated how the size of elements affects the accuracy of results in numerical analysis, yielding essential findings. According to More and Bindu (2015), Yanning Li and Tomasz Wierzbicki demonstrated the importance of mesh size when applying semi-coupled plasticity/damage theory and the Mohr-Coulomb ductile fracture model. They discovered that variations in stress and strain in certain areas caused the effects seen with different mesh sizes in finite element simulations. As a result, a model was created to handle the changes in the stress-strain relationships that occur because of varying mesh sizes (Li & Wierzbicki, 2009).

Weibing Liu, Mamtimin Geni, and Lie Yu observed that at the boundary of the curved surface, higher-order elements could model the boundary accurately, using hexahedral elements rather than tetrahedral elements. Therefore, the model analysis is significantly enhanced by increasing the quantity of nodes (Liu et al., 2011).

Padmakar Raut assessed the effectiveness of linear, quadratic, and hexahedral elements in different structural situations involving shear, torsion, and axial deformations. The results showed that the accuracy of the outcomes from using quadratic tetrahedral elements was comparable to those obtained with hexahedral elements (Raut, 2012). Similarly, Yucheng Liu's

research focused on the impact of the size of finite elements on the precision of numerical analysis results. This study incorporated guidelines for selecting optimal finite element sizes in models, and it included an examination of buckling and static analysis to understand the influence of element sizes on numerical analysis (Liu & Glass, 2013).

3.8.1 *Types of element*

A range of elements are available in the ABAQUS element library (ABAQUS, 2019) which are applicable for simulating 3D solids. The most common block components used to simulate masonry are described below:

The first element is C3D8R, which has 8 Gauss points in a reduced integration model, with 2x2x2 points of integration, forming a hexahedron for this linear brick component (ABAQUS, 2019). Without enhanced hourglass control the C3D8 shows poor performance in terms of isochoric material (constant volume) behaviours when plasticity behaviours or Poisson's ratio is high (ABAQUS, 2019). Moreover, C3D8 is unsuitable for representing thin plates/beams when considering bending, due to its excessive stiffness in this condition (Zienkiewicz et al., 2005).

The second element is C3D20R, which has 20 Gauss points, and also represents reduced integration, with 3x3x3 points of integration: this component is a quadratic brick (ABAQUS, 2019). C3D20R performs well for linear models of elasticity, with good capturing of integration point locations as well as surface concentration of stress. However, this type of element does not support using the XFEM technique to crack elements, where XFEM supports linear brick element not the quadratic geometric order (ABAQUS, 2019). In terms of modelling elasticity, this component is comparable to the previous component, while it outperforms C3D8R in terms of models of plasticity and controlling hourglass modes (modelling option), with the sensitivity of the mesh, so the size of elements are of reduced importance.

The hourglass is a phenomenon that happens when reduced integration is applied to the solution of first order bending elements. Their shape is changed to something like an hourglass, in a 3D phenomenon similar to anticlastic bending. This problem leads to a decrease in accuracy. To resolve this problem, more than one element must be used in the thickness direction at the regions that experience bending moment (ABAQUS, 2019).

Both (Logan, 2016) and (Bathe, 1996) offer detailed insight on shape functions for the different kinds of element. Initial modelling of masonry employed C3D8R for elastic elements within

the bridge, including mortar and bricks. Meanwhile, C3D8R was implemented in plastic modelling of materials in the masonry arch bridge. Specifically, it is essential to use C3D8R in modelling elastic-plastic deformation (modelling option) to simulate this appropriately.

3.9 Summary

This chapter reviewed the available modelling strategies, techniques, and approaches used to model and simulate masonry structures to investigate and understand the masonry mechanical behaviour and failure modes. Also, previous numerical studies have been used to analyse masonry structures. The principal summary points of this chapter are:

- The principal goal of using numerical simulations and masonry structures modelling using software is to integrate complex and reliable analysis, which can predict the structural behaviour at relatively little cost, though with considerable computational effort.
- A linear elastic analysis cannot anticipate the masonry arch bridge behaviour structure because there is material and geometrical nonlinearity at points in the structure at working, and ultimate stress levels. Realistically, a nonlinear finite element analysis can model the nonlinear characteristic aspects of masonry structures, including arches.
- Numerical methods can be used to obtain detailed data about the masonry structure and behaviour under loading. Analysis methods such as MEXE and RING only offer arch capacity or available load factor rather than detailed information about displacement and stress.
- The discrete element method (DEM) and finite element method (FEM) allow incremental static loading to be applied, where the masonry arch bridge materials behave nonlinearly. Other modelling approaches are used for comparative purposes and are based on the simplified rigid block analysis.
- The finite element method has been used in this area frequently, possibly due to the masonry arch bridge behaviour features, where specifically, the interest lies in the cracking at mortar joints leading to nonlinear stiffness loss. In addition, if conventional continuum elements are used, the masonry arch four hinge mechanism simulation can become very complex.
- By using computational resources based on both FEM and DEM methods, the masonry arch bridges structural behaviour simulation can be achieved. Both modelling

techniques take into consideration the materials' nonlinearity behaviour, and also suitable geometrical discretisation, thus leading to an evaluation of the masonry arch bridges load carrying capacity.

- The purpose of choosing the most appropriate constitutive law is to better predict masonry arch ring behaviour. Depending on the linearity of the numerical model components, several constitutive laws can be appropriate but Mohr-Coulomb is widely used.
- Despite significant advances in masonry structures modelling strategies, each computational solution has a specific application area and unique limitations. As a result, the best modelling strategy should be chosen based on the masonry structure's complexity and characteristics. Also, based on the natural response behaviour of the masonry structures.

- Many computational modelling strategies, techniques and approaches have been reviewed to investigate and understand realistic behaviour in masonry structures. Furthermore, choosing a suitable method depends on the research aim and objectives and also on the level of accuracy desired.
- The homogenous modelling technique considers the model to be composite, and does not need a great computational effort or a high-performance computation device. However, it does not simulate the details of complex masonry structures and cannot provide detailed behaviour of failure modes.
- Masonry is a heterogeneous material, and to create a realistic model to investigate and understand the masonry arch rings' behaviour, and identify failure modes, requires a heterogeneous modelling technique which creates the components separately. As a result, the heterogeneous modelling strategy has been chosen, though it is computationally intensive.
- Mortar exhibits brittle material behaviour, so non-linear material behaviour is adopted to model the mortar joint and the unit-mortar interfaces behaviour.
- The macro-modelling approach models a simple masonry structure as a single element, with no details modelled into the interfaces, hence, it is less accurate when simulating a complex masonry structure. Therefore, this approach is insufficient for detailed modelling of masonry structures and capturing failure mechanisms.

- The micro-modelling approach can incorporate various mode failures into the masonry arch model using the interaction between elements since bricks and mortar joints are modelled separately. Conversely, the macro-modelling approach cannot incorporate various mode failures into the masonry arch model since the mortar joints are modelled as smeared in an anisotropic homogeneous continuum element.
- Accurate numerical models depend on good quality material property input data. However, experimental data, particularly in the softening domain, are scarce.
- The micro-modelling approach (simplified and detailed micro-modelling) is sufficient for masonry arch bridges and arch rings. In addition, it can capture failure mechanism modes which macro-modelling cannot. The detailed micro-modelling approach has been chosen to create the further models in this study.
- The finite element method breaks the original geometry into small components (meshing) to better understand the stress and strain of the model and gives a good representation of the complicated masonry structures behaviour under varied conditions.
- ABAQUS is specified as the powerful and suitable FEM software to simulate and analyse masonry arches. Detailed masonry modelling is possible using the available methods in ABAQUS without any user defined subroutines (codes), due to the availability of non-linear material properties, crack initiation and propagation.
- There are certain benefits regarding using XFEM to crack the mortar joint:
  1. There is no need to identify the crack path and initial crack location.
  2. Without having to remesh the model, XFEM enables the investigation of crack growth along arbitrary, solution-dependent paths, which means the mesh is created independently of the crack.
  3. The geometry at the crack position does not need to be partitioned.
- The constitutive law selection depends on the type of failure. This will be a bond failure mode, and may be due to tensile, shear or compressive stress. The constitutive law assumed for this study can be designated as non-linear fracture mechanics using XFEM to crack the masonry arch model component and to model the non-linear interaction between the units and mortar joints. The non-linear material behaviour response may be represented by Drucker-Prager or Mohr-Coulomb criteria.

- It is noted that as the traffic volume on masonry arch bridges increases, assessment of serviceability is becoming increasingly vital and necessary. Furthermore, detailed masonry arch models are needed to understand and investigate the response behaviour.

In conclusion, to simulate a masonry arch ring satisfactorily, the following techniques will be adopted: heterogeneous material model, detailed micro-modelling and ABAQUS software using XFEM. These allow for a realistic arch geometry representation and material mechanical behaviour with all failure modes, such as ring separation, crack into the mortar joint and slip failure at the interfaces. In addition, it will permit accurate mortar joint crack pattern prediction. As a result, a realistic masonry arch ring model can be produced.

3.10 Research gaps in experimental and numerical studies

Chapters 2 and 3 investigated previous research on experimental and numerical studies. The following are the key outcomes of this research:

- The published experimental tests did not adequately address the movement of masonry arches, neither did the published numerical studies. The published experimental tests did not consider all the movement directions, and the values of the abutment movement investigated were too small to fully represent real structures. Furthermore, the unit and mortar joint material and interaction properties were all assumed for the numerical models, even though they were validated against published experimental tests.
- The existing experimental test data for masonry arches with rigid abutments is extensive. However, arch tests subject to foundation movement are much rarer. In both cases there is a considerable lack of material properties reported in the literature. Often test results are limited to a load-displacement curve and crack pattern.
- Full-scale testing of masonry arch bridges is very expensive, and the facilities required are rare. Full-scale testing of arch bridges with a movable abutment do not currently exist, therefore, it is expedient to use a numerical model validated using data from rigid abutment tests to numerically investigate the effect of foundation movement on structural behaviour.
- Existing numerical modelling generally adopts a simplified radial mortar joint geometry for multi-ring arches, does not fully model the mortar thickness, and is limited

to very small values of abutment movements. Furthermore, reported foundation movements are limited to settlement and sliding.

Chapter Four

4 Experimental and Numerical Investigations of Masonry Behaviour to Determine Material Properties for Detailed Micro-modelling.

4.1 Introduction

This chapter describes the experimental masonry triplet tests and the numerical modelling developed to simulate the materials and interactions of masonry in shear. The numerical modelling was developed using ABAQUS finite element analysis software. This chapter details experimental tests to establish the material properties and investigate and understand brick and mortar interface behaviour. This chapter will use the techniques mentioned in section 3.6 to simulate the material properties and the interface interaction between the elements to provide the most appropriate realistic behaviour of the non-linear masonry material.

The experimental triplet test proposes to investigate the behaviour of masonry arch constructed of unreinforced masonry units (bricks) in shear. In multi-ring masonry arches without headers, the longitudinal shear stress must transfer for the composite action to pass only through the mortar joint bed. This increases the probability of the delaminating rings separating occurs. Since the shear distorts the shape, the most considerable shear stresses occur with the most significant displacement in the masonry arch barrel. Therefore, as the allowable axle loads increase, the shear stresses and displacement within the arch will also increase.

4.2 Material property physical testing

This section reports a series of experimental tests on masonry couplets and triplets, mortar cubes, and mortar cylinders. The results of these tests inform the material property values used to create and validate a 3D numerical model replicating the tests. This ensures reliable and appropriate computational modelling (which can replicate tension and shear failure) is implemented correctly in numerical models of complete arches.

In all masonry prism tests, the mortar mix is 1:2:9 (cement: lime: sand), and Class A engineering bricks were utilised, which are significantly stronger than Britley Olde English

bricks. The chosen mortar mix aims to simulate the low-bond strength materials typically found in ancient masonry arch bridges.

4.2.1 *Brick compressive strength test*

Melbourne, Wang, Tomor, et al. (2007) and Elbeskeri (2011) conducted experimental tests using the BS EN 772-1 method to evaluate the compressive strength of masonry units. This testing involved subjecting the bricks to a gradual increase in compression until failure occurred. Their findings, presented in Table 4-1, revealed an average compressive strength of 154 N/mm², this value will be used in numerical modelling studies. This outcome signifies a notably high compressive strength for the bricks, especially when compared to the nominal minimum strength of 70 N/mm² typically associated with Class A brickwork, as specified by the British Standards Institute (2011).

Table 4-1: Brick compressive strength test result.

Masonry unit type	Average compressive strength (N/mm^2)
Brick	154

4.2.2 *Mortar compressive strength test*

This section presents the determination of the compressive strength of mortar using a series of experimental laboratory tests of cubes and cylinder.

The mortar compressive strength was determined from five 100mm x 100mm x 100mm mortar cubes, prepared and tested in accordance with BS EN 1015-11, as shown in Figure 4-1. All the physical tests were carried out under displacement control using a ZwickRoel universal compression test machine.

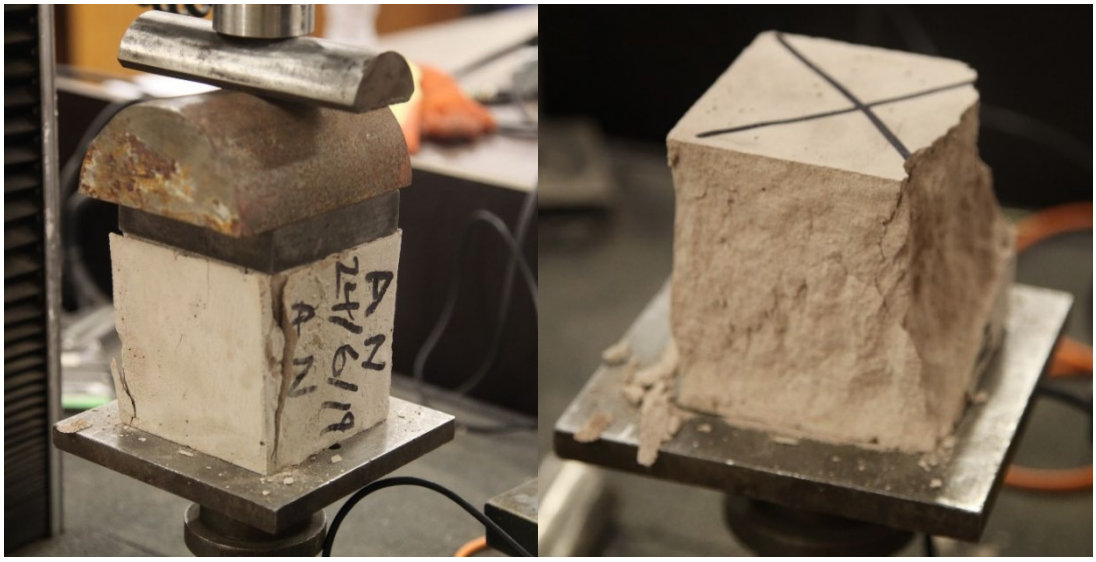

Figure 4-1: Mortar compressive strength test of the cube samples.

The mortar cube samples were demoulded after two days then tested after 28 days, cured in water. The average mortar compressive strength was 1.50 N/mm^2, as presented in Table 4-2.

Table 4-2: Mortar cube test compressive strength results.

Specimen name	Compressive stress (MPa)	Strain at peak compressive stress (mm/mm)
Sample 1	1.39	0.008
Sample 2	1.69	0.006
Sample 3	1.66	0.008
Sample 4	1.46	0.009
Sample 5	1.31	0.009
Mean (μ)	**1.50**	**0.008**
Standard deviation (σ)	0.17	0.0011
Coefficient of variation (%)	11.1	13.37

Figure 4-2, presents the stress-strain results for the five mortar cube samples. All five samples show good agreement regarding the stiffness and the peak stress under compression.

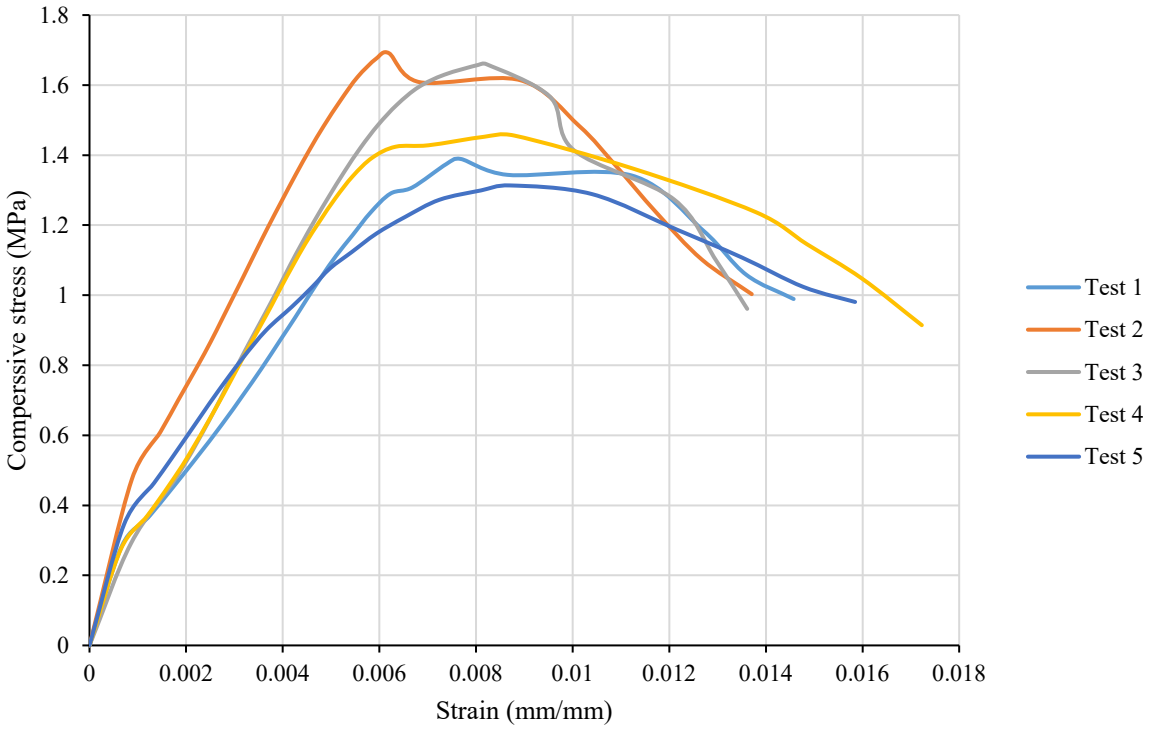

Figure 4-2: Mortar compressive stress-strain result of the cube tests.

Figure 4-3, shows the mortar cylinder sample of 150mm diameter and 300mm height. The mortar cylinder test was carried out using a ZwickRoel universal compression test machine for one sample only, where the steel frame surrounding the cylinder specimen was used to determine the strain during the compression test. The mortar cylinder specimen was tested after 28 days curing in water.

Figure 4-4, displays the result of the mortar cylinder compressive strength test, where the peak stress was 8.1 N/mm^2. This result was used to obtain Young's modulus of elasticity E_m value to be implemented in the numerical simulation for the masonry specimens. However, because only one sample was tested, the result has low reliability.

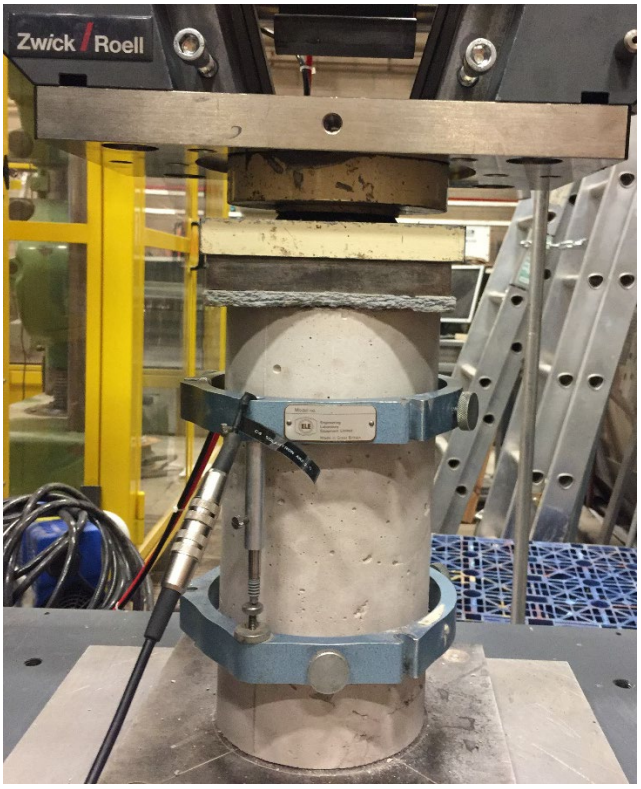

Figure 4-3: Mortar compressive strength test of the cylinder sample.

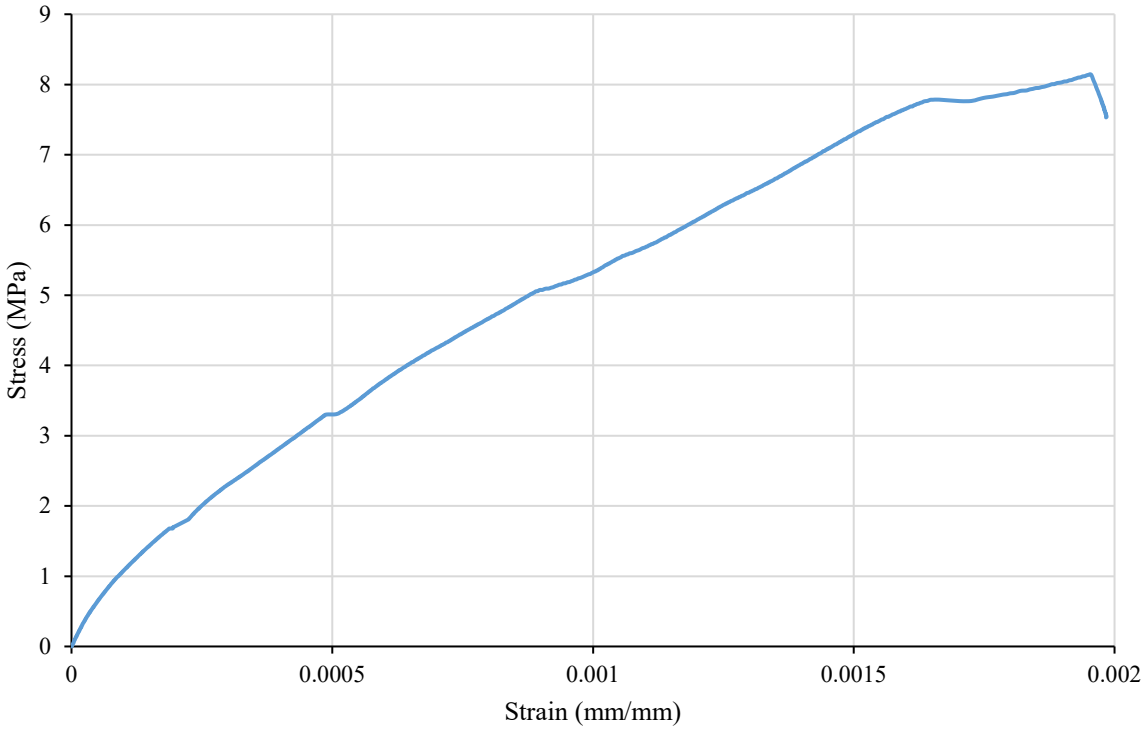

Figure 4-4: Mortar cylinder compressive stress-strain result.

4.2.3 *Couplet tensile strength test*

The primary objective of this experimental test was to estimate the corresponding tensile fracture energy and the unit-mortar interface tensile strength, which was used in the numerical modelling of masonry specimens. The stiffness of the mortar joint was also calculated and used in the numerical model to simulate the unit-mortar elastic behaviour.

The direct tension test was carried out on five samples after 28 days, where the top and bottom faces of the brick samples were glued to a steel plate using epoxy, which was clamped in the ZwickRoel test machine. Two Linear Variable Differential Transformers (LVDT) were attached to the front and back of the sample to determine the displacement during the tensile test process, as shown in Figure 4-5.

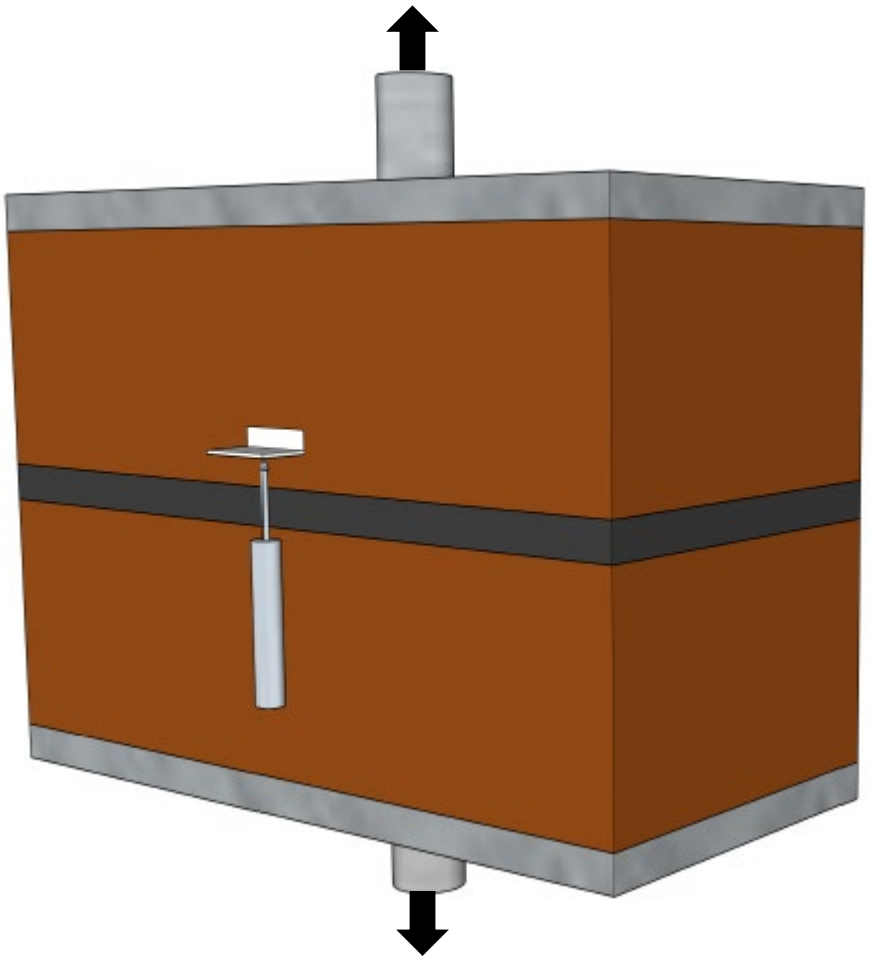

Figure 4-5: Tensile stress test sample setup.

Table 4-3 presents the results summary of the tensile test samples in terms of the tensile stress, vertical displacement at the peak tensile stress, mortar joint stiffness in tensile direction and the Mode I tensile fracture energy. In addition, the unit-mortar interface tensile strength was 0.18 N/mm^2, and the mortar joint stiffness was 303.2 N/mm^3, where the fracture energy was 0.039 N/mm and was determined using the area under the curves of tensile stress against displacement graph.

Figure 4-6, shows the three tensile stress test curves; the curves show good post-peak agreement in global behaviour. The behaviour of the samples was approximately linear up to the peak tensile stress, then exhibit strain softening before complete dislocation. However, the gradient of the initial linear loading stage is highly variable (ranging from 134-580 N/mm^3 in Table 4-3), this is believed to be due to the level of accuracy achievable using the LVDT selected for the test (the displacements measured are fractions of a micron). There was a drop in the tensile stress due to crack propagation in the mortar joint, only at the unit-mortar interface (the weakest region).

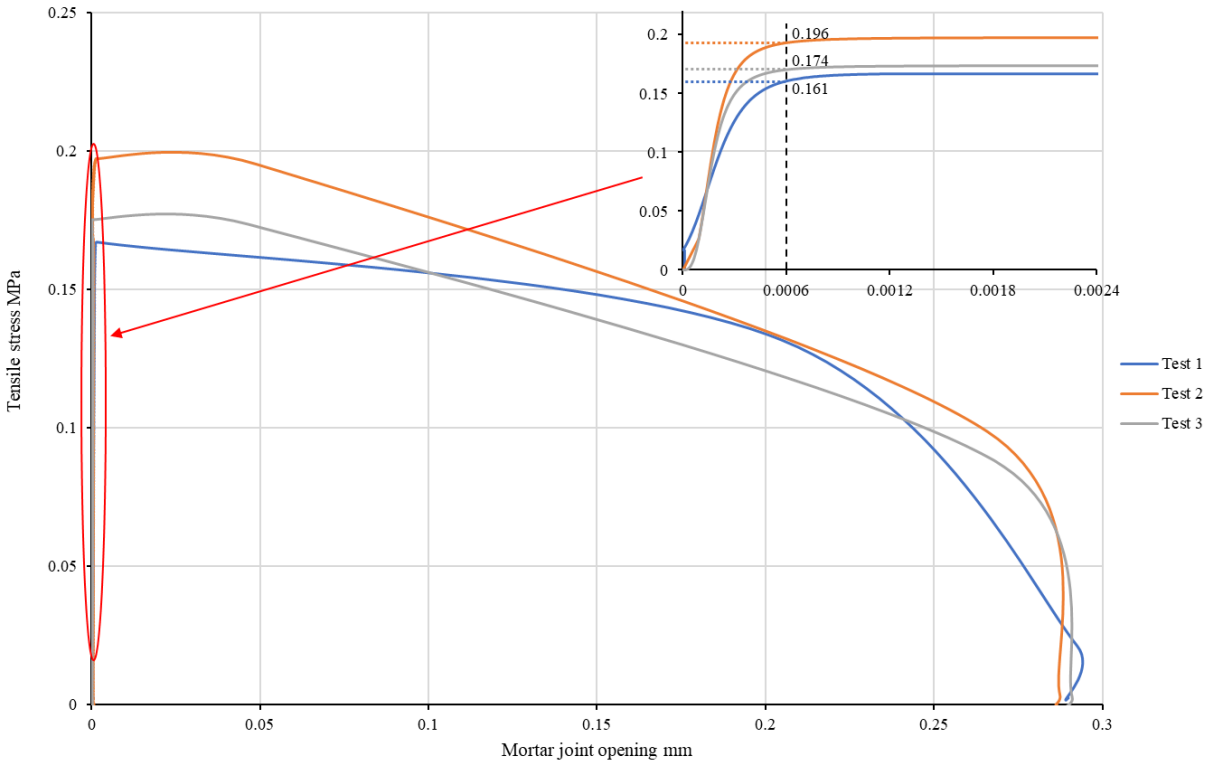

Figure 4-6: Tensile stress-mortar joint opening displacement curves.

Table 4-3: Tensile stress test results summary.

Sample name	Peak tensile stress (MPa)	Vertical displacement at Max tensile stress (mm)	Mortar joint stiffness in tensile direction, K_{nn} (N/mm^3)	Mode I Tensile Fracture energy (N/mm)
Test 1	0.161	0.0006	268	0.037
Test 2	0.196	0.0006	327	0.042
Test 3	0.174	0.0006	290	0.038
Mean (μ)	**0.18**	**0.0006**	**295**	**0.039**
Standard deviation (σ)	0.015	0.0005	241.74	0.003
Coefficient of variation (%)	8.45	57.93	79.73	7.011

4.2.4 *Masonry shear strength (Masonry triplets) test*

The experimental triplet tests required the manufacture of twenty triplet specimens, each made of three bricks (units). Batches of five specimens were tested (although EN1052-3 only requires 3 specimens) with different pre-compression loads. As the brick compressive strength was greater than 10 N/mm^2, the pre-compression loads were 0.2 N/mm^2, 0.6 N/mm^2, and 1.0 N/mm^2, where the pre-compression loads were applied by clamping the triplet specimens through a load cell, as shown in Figure 4-7.

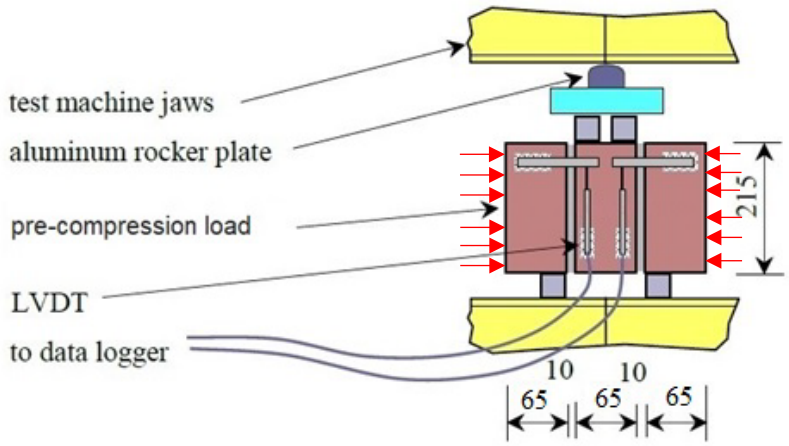

Figure 4-7: Triplet masonry experimental test setup.

The triplets were produced using standard equipment intended to minimise differences in materials and craftsmanship. Initial tests determined a mortar mix that was easy to work with and had the correct amount of water. According to Cavalheiro and Pedroso (2000), the mortar shear strength results were the same at 14 and 28 days; the experimental triplet samples for this study were air-cured for 28 days before testing.

The initial tests on bricks and mortar compressive strength are presented in Table 4-1 and Table 4-2. The mortar mix was 1:2:9 (OPC: lime: sand), with the sand being oven-dried before use. The bricks, which were Staffordshire Red Class A made by Ketley Brick Company, were previously tested by Melbourne, Wang, Tomor, et al. (2007) and Elbeskeri (2011). This mix of durable bricks and a sand-heavy (weaker) mortar was chosen to set a conservative estimate for shear strength and ensure any failure would occur in the mortar or at the joint between the mortar and the brick. The University of Salford Laboratory provided the material required to manufacture the triplet samples.

Investigating brickwork triplet behaviour was necessary to establish the input data for the finite element numerical models for this chapter and to establish the appropriate behaviour of masonry in shear. This ensures future models can adequately represent masonry arch ring separation failure. Although masonry arch bridges are generally subject to cyclic loading, the triplets were subjected to a monotonic load to failure. Shear capacity is known to be affected by lateral pre-compression (Mojsilović et al., 2010), so four pre-compression stresses were used (including a zero stress). All the testing was carried out according with the relevant British Standard (British Standards Institute, 2002)

Masonry triplet shear tests were undertaken to evaluate the Mode II shear fracture energy, friction coefficient, and shear strength at the maximum values. The bricks used in the triplet shear stress tests were of characteristic size 215mm x 102mm x 65mm, while the thickness of each mortar joints was 10mm, as shown in Figure 4-8.

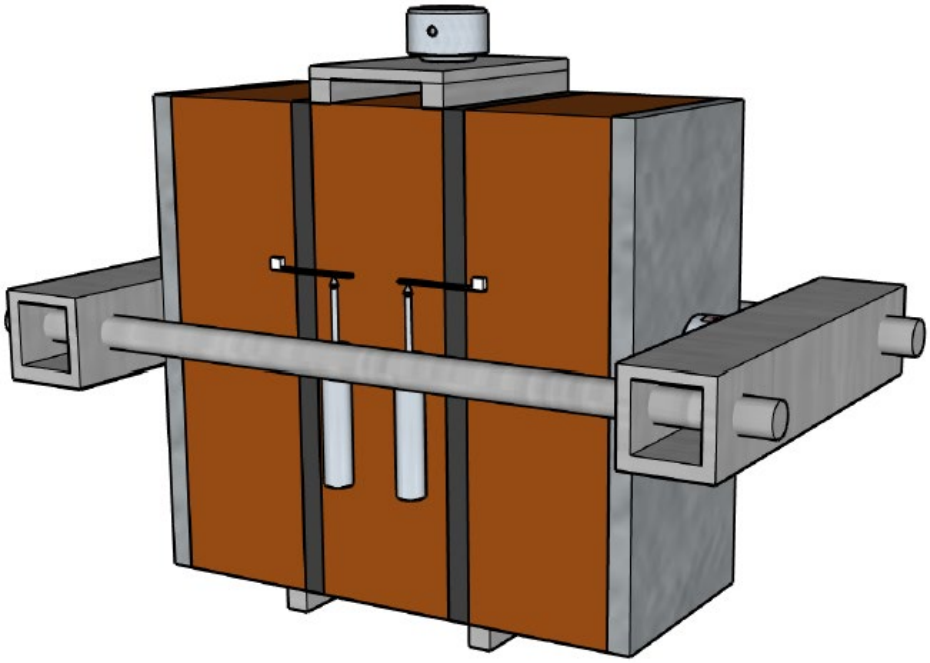

Figure 4-8: Masonry triplet shear stress test sample setup.

All triplet samples were loaded to ultimate failure using a 250kN ZwickRoel universal compression testing machine, which automatically recorded force and displacement data, as shown in Figure 4-8. The movement across each joint was tracked using linear variable differential transformers (LVDTs). Unreinforced triplets were tested in direct shear; five samples without lateral pre-compression load and fifteen samples with lateral pre-compression loads of 0.20, 0.60, and 1.00 N/mm^2. Five samples were tested to ensure that at least three consistent tests results were obtained for each pre-compression level.

Four LVDT's were used to measure the displacement in each sample. AX/S spring push LVDT's were used, as shown in Figure 4-9, as they are highly sensitive to small movements.

Figure 4-9: AX/S spring push LVDT.

Figure 4-10 displays the shear stress against shear displacement in the mortar joint for three experimental tests with zero pre-compression. It can be noted that there is a good agreement in terms of strain softening behaviour and fracture behaviour after reaching the peak shear stress value. Up to peak shear stress, the behaviour in all three tests was perfectly elastic. The displacement at the peak shear stress is very small. As a result, the test mortar is considered to be brittle.

Table 4-4 summarises the shear strength of masonry triplets, where the mean (μ) presents the average of the three triplet masonry sample results. The average of the shear stress peak was 0.25 N/mm^2, and the average shear displacement of the joint at maximum shear stress was 0.0014 mm. Also, the average Mode I shear fracture energy was 0.064 N/mm. It can be noted that the peak shear stress and the shear displacement of the three samples are very similar, as shown in Table 4-4.

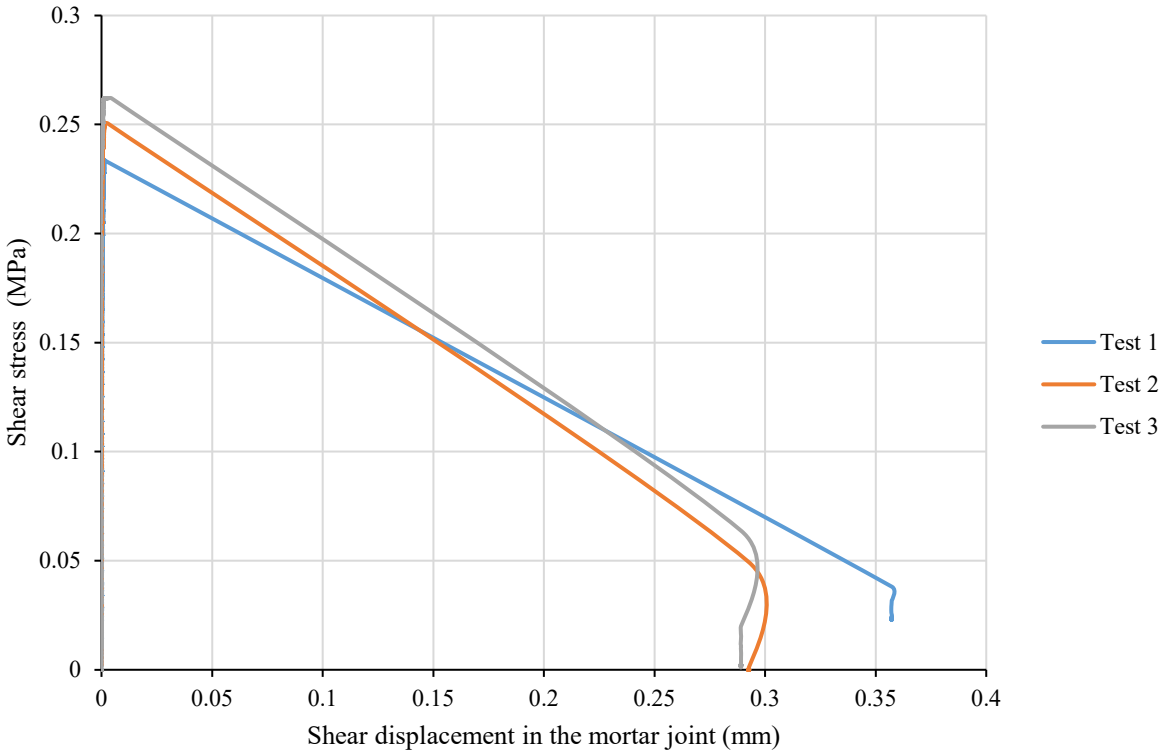

Figure 4-10: Load-displacement triplet tests result comparison, zero pre-compression.

Table 4-4: Shear stress experimental test summary zero pre-compression.

Specimen name	Peak shear stress (MPa)	Shear displacement of the joint at Max shear stress (mm)	Mortar joint stiffness in shear direction, K_{ss} (N/mm^3)	Mode II shear Fracture energy (N/mm)
Test 1	0.23	0.0014	164.3	0.083
Test 2	0.25	0.0015	166.7	0.062
Test 3	0.26	0.0014	185.7	0.047
Mean (μ)	**0.25**	**0.0014**	**172.23**	**0.064**
Standard deviation (σ)	0.015	6E-05	11.72	0.018
Coefficient of variation (%)	6.19	4.03	6.81	27.97

Figure 4-11 presents graphs of shear stress against displacement for nine triplet tests, covering three pre-compression stresses. As Figure 4-11 shows, as the pre-compression stress increases, the maximum shear strength of each test also increases. Furthermore, the greater the lateral pre-compression load, the greater the corresponding capacity and displacement at failure.

Figure 4-11 illustrates that all the samples exhibited the same sliding failure mode which occurred when the shear stress reached the maximum value.

Table 4-5 provides the data for peak shear stress and associated shear displacement for all the pre-compression shear stress samples. It can be noted that the average peak shear stress, with and without pre-compression is 0.45 N/mm^2 and 0.2 N/mm^2.

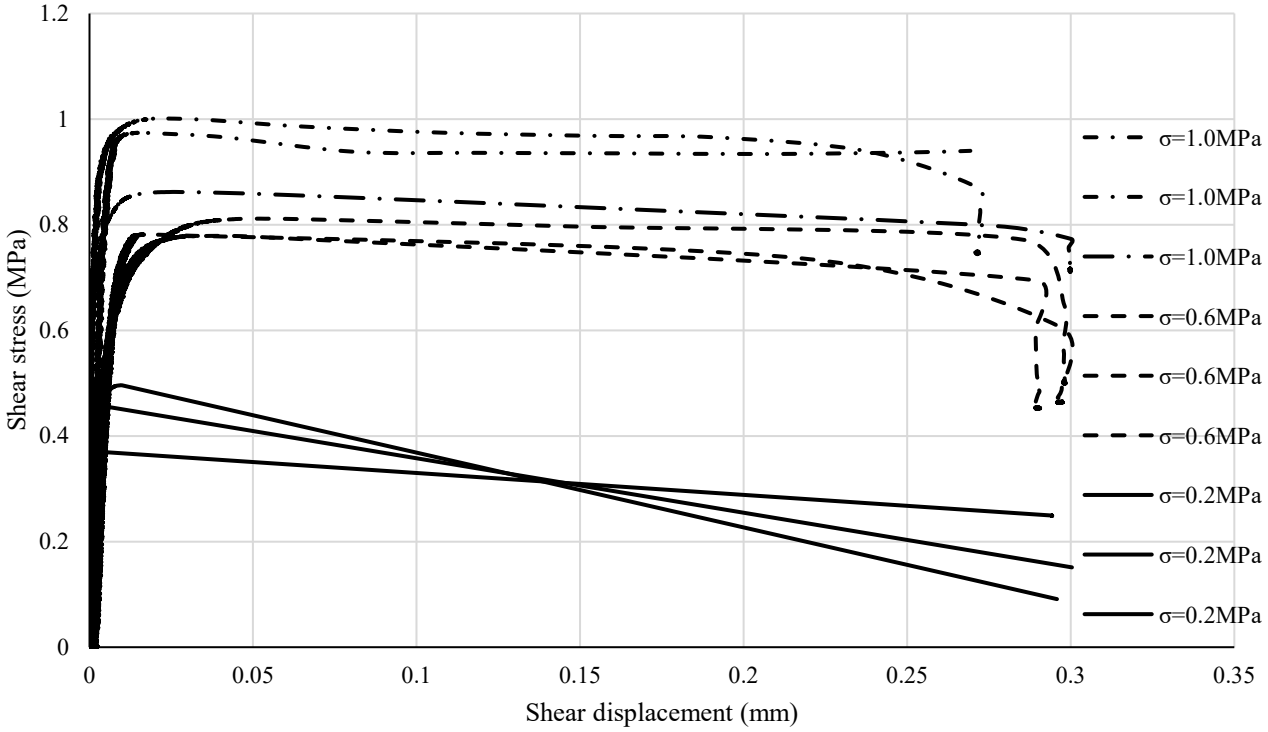

Figure 4-11: Shear stress - displacement for various pre-compression stresses.

Figure 4-12 provides the peak shear stress found from each experiment test sample against the pre-compression stress values. A linear regression line was fitted to the data to establish the initial shear stress at zero pre-compression stress, as shown in Figure 4-12. The equation determined that the initial shear stress a zero pre-compression was 0.3 and the friction coefficient was 0.63. The Mohr-Coulomb failure criterion for the residual and peak shear strength which determines a linear relationship between the normal stress σ and the shear stress τ, was as follows:

$$\tau = 0.3 + 0.63\ \sigma \qquad \text{Equation 4.1}$$

Table 4-5: Pre-compression shear stress experimental test summary.

Shear Pre-compression specimen name	Peak shear stress (MPa)	Vertical displacement at Max shear stress (mm)
0.2MPa-Test 1	0.45	0.001
0.2MPa-Test 2	0.5	0.01
0.2MPa-Test 3	0.4	0.0024
Mean (μ)	**0.45**	**0.0045**
Standard deviation (σ)	0.05	0.0048
Coefficient of variation (%)	11.11	108.42
0.6MPa-Test 1	0.78	0.019
0.6MPa-Test 2	0.78	0.033
0.6MPa-Test 3	0.8	0.053
Mean (μ)	**0.79**	**0.035**
Standard deviation (σ)	0.012	0.017
Coefficient of variation (%)	1.47	48.8
1.0MPa-Test 1	0.97	0.015
1.0MPa-Test 2	0.996	0.015
1.0MPa-Test 3	0.858	0.0156
Mean (μ)	**0.94**	**0.0152**
Standard deviation (σ)	0.073	0.0003
Coefficient of variation (%)	7.79	2.28

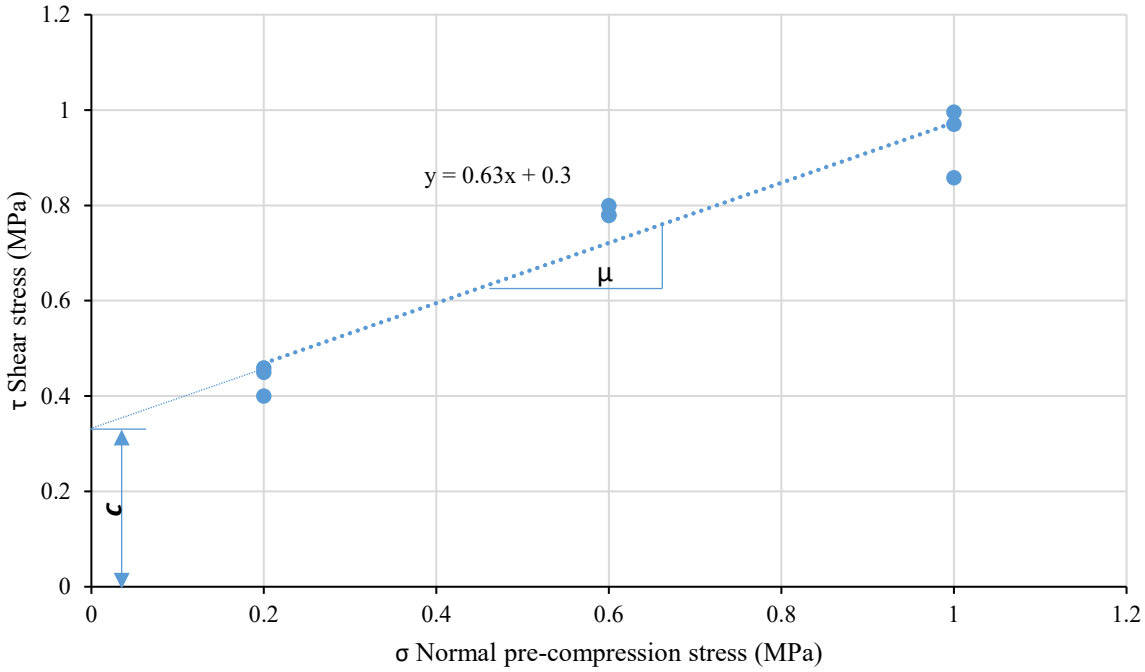

Figure 4-12: The relationship between peak shear stress versus pre-compression stress.

The results of the tensile and shear bond tests shown in Table 4-3 and Table 4-5 need to be compared with those from previous studies that used the same mortar mix ratio of 1:2:9. The tensile bond strength reported in the experimental section 4.2.3 of this study is 0.18MPa, which is similar to the values reported by Hodgson (1996) of 0.15MPa, Liu et al. (2023) of 0.21MPa and Rots (1997) of 0.26MPa. This suggests the results are within an acceptable range of values. Clearly with limited number of sample there is a degree of uncertainty in all experimentally derived parameters.

The results of the shear bond tests under three different precompression stresses—0.20, 0.60, and 1.0MPa—are presented in Table 4-5 as 0.45, 0.79, and 0.94MPa, respectively. These results are compared with those reported by Liu et al. (2023) who found shear bond values of 0.437, 0.833, and 0.936MPa for the same precompression stresses. This comparison indicates that the differences between this study's shear bond experimental test results and those of Liu et al. are negligible.

4.3 Numerical modelling of shear stress tests

This section provides an initial comparison of the numerical and experimental tests used to establish representative masonry properties. This section provides two numerical simulation models. The first model is for Van der Pluijm shear strength test as described in section 2.4.4, and the second model will be for the masonry triplet experiment test described in section 4.2.4, using the material properties obtained in section 4.2.

The purpose of numerical simulation of the Van der Pluijm shear strength test is to use and validate the detailed micro-modelling technique reviewed in section 3.6.

FEM was used to model the brick triplet shear test using ABAQUS software. The numerical and experimental results were compared using the failure shear strength against the shear displacement relationship graph.

To simulate masonry triplets with sufficient accuracy, a detailed micro-modelling approach was used. This model represented brick units and mortar bed joints as separate elements. Brick units and mortar bed joints were modelled with separate elements. However, a cohesive interface (interaction) between the two surfaces modelled the bricks-and-mortar interface. The brick units were modelled as a linear elastic material in both numerical simulation runs.

During the shear failure mode, mortar bed joint dilatancy under normal compression stress can generate a local increase in thickness under positive boundary conditions. As a result of the slip surface roughness, the brick-mortar shear strength interface at zero limiting normal stress is non-zero. Moreover, under shearing deformation, masonry joint dilatancy behaviour has been observed in most cases; the mortar volume growth is a direct product of transverse expansion. Confining boundary conditions must be established to negate the joint volume increase with an associated normal stress increase. This means a non-isochoric (volume change) plasticity, as opposed to the behaviour exhibited by plastics and metals. Therefore, even if the shearing dilatancy is restrained at large shear strains and at high-pressure levels, there will be a considerable increase in the unit-mortar shear strength interface with a normal compressive stress.

The practical consideration is that with zero precompression, the dilatancy angle reaches about 35º, whereas with a precompression of 1.5N/mm^2, the dilatancy angle is unlikely to drop below 11º (Rots, 1997). With an increase in compressive stress, the angle of dilatancy reduces. This phenomenon can be explained by the hypothesis that higher compressive stresses cause shear planes to polish against each other, leading to smoother interfaces.

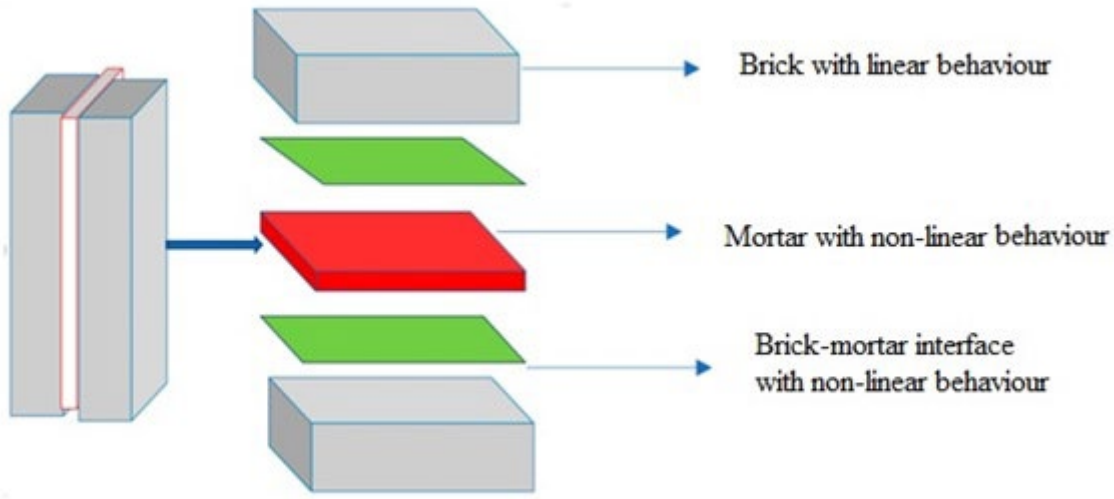

Figure 4-13: Scheme of the detailed micro-modelling approach (Hernoune et al., 2020).

The triplet numerical model was constructed in ABAQUS software version 6.19. Parameters categorised the constitutive laws for the mortar, brick and brick-mortar interfaces (interaction) described in section 3.6 and shown in Figure 4-13. The standard experimental test results

provided input values for the model, where each parameter used in the numerical tests had an obvious physical meaning.

In this model, the non-linear behaviour of masonry is restricted to the unit-mortar interfaces and the mortar bed joints because the brick units are modelled as a linear elastic material. This approach is justified as these brick units did not display any damage in the experimental tests conducted for this study. Moreover, the mortar joints mechanical properties are derived from direct shear tests.

The traction-separation law governs the unit-mortar interfaces with damage initiation and evaluation. Both elements have been modelled with cohesive interface interaction. The unit-mortar interface has two identifiable failure modes: mode I (tensile failure) and mode II (shear failure). Mode I is the normal interface separation of the mortar bed joints, whereas mode II consists of a masonry brick sliding mechanism or mortar bed joint shear failure. The masonry mechanical properties are dependent on loading direction due to the planes of weakness in the unit-mortar interface.

4.3.1 *Numerical shear stress mesh study*

This section includes the mesh sensitivity study for this chapter simulation, where Van der Pluijm couplet shear stress with 0.1 N/mm^2 pre-compression was used to validate against the experimental test results. The experimental test material properties were obtained from published tests (Rots, 1997).

Figure 4-14 displays three different mesh densities to determine the required number of elements in the numerical model to ensure that mesh size does not influence the analysis results.

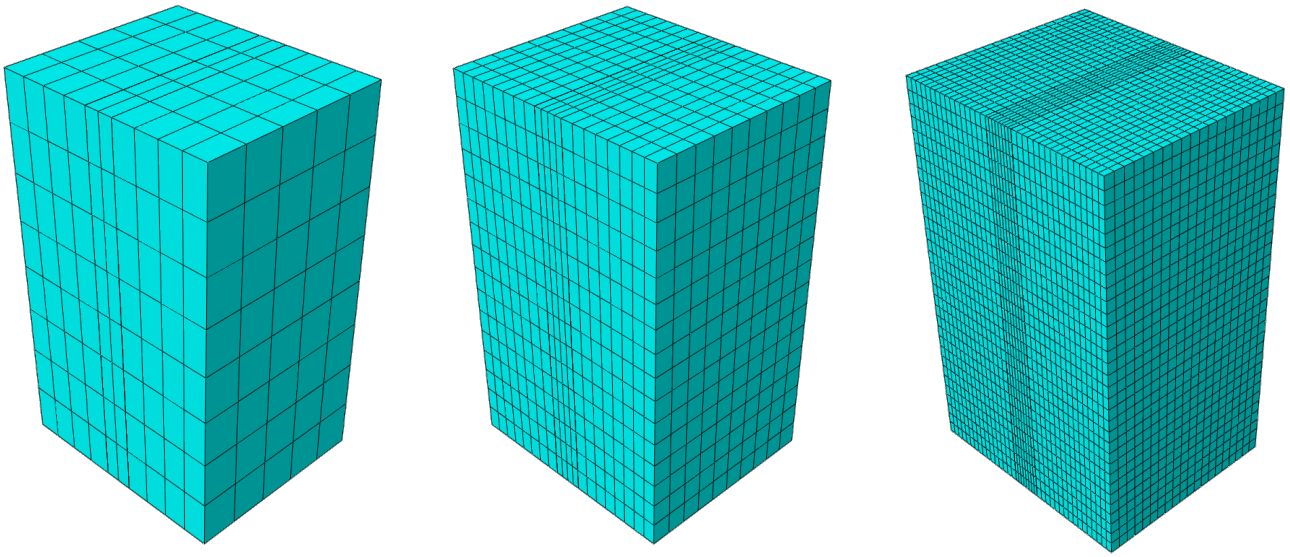

a) Normal mesh model b) Fine mesh model c) Very fine mesh model

Figure 4-14: Different mesh densities for couplet masonry shear stress models.

Table 4-6 provides the results of the three different mesh density models by the peak shear stress and the displacement at the peak shear stress. In general, there was no difference between the three models' results. Figure 4-15 provides a graph of shear stress against displacement, proving that there was no difference in behaviour regarding the elastic and plastic regions until after 0.5mm displacement, when the fine mesh model shows a small deviation when approaching failure. The fine mesh was chosen for the couplet and triplet numerical simulation.

Table 4-6: Comparison between different mesh densities.

Mesh type	Mesh elements	Peak shear stress (MPa)	Displacement at peak shear stress (mm)
Normal mesh	Brick: 4x5x8 Mortar: 2x5x8	1.00	0.05
Fine mesh	Brick: 8x10x16 Mortar: 4x10x16	1.01	0.05
Very fine mesh	Brick: 16x20x32 Mortar: 8x20x32	1.02	0.05

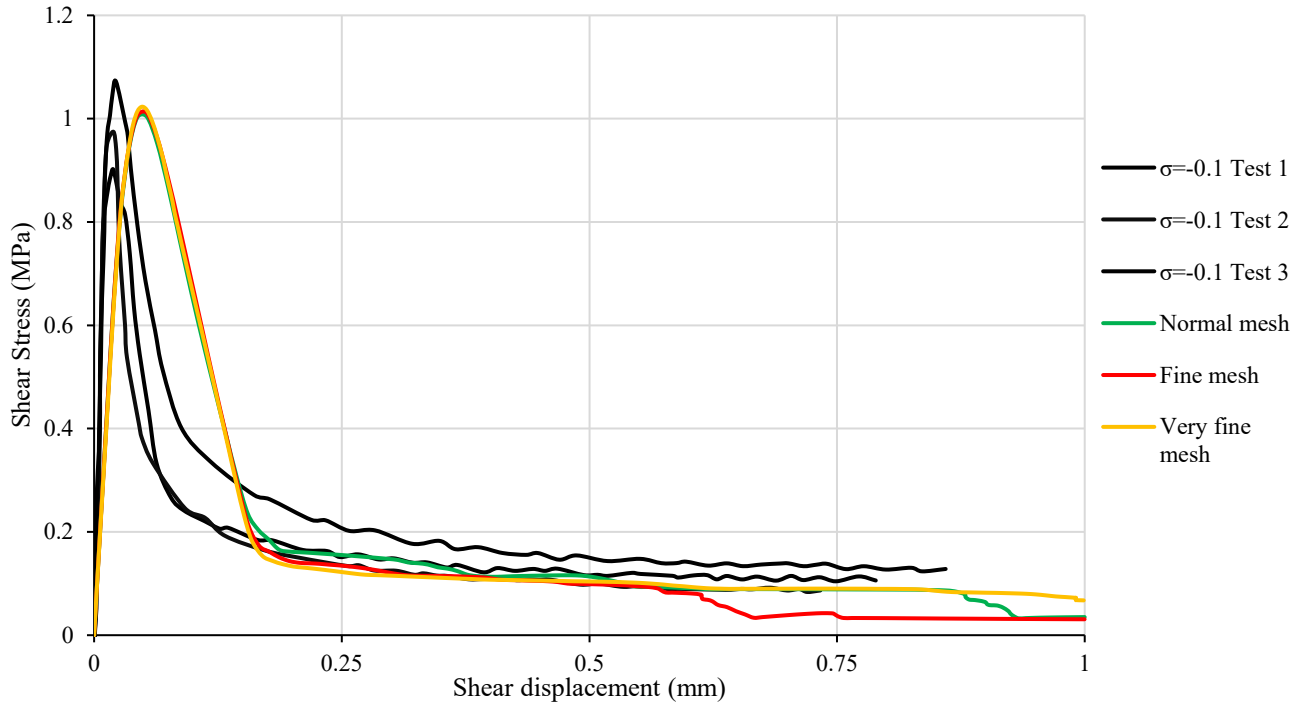

Figure 4-15: Shear stress-displacement comparison of different mesh models response.

4.3.2 *Masonry couplet shear strength test*

This section includes the experimental test and the numerical simulation details. This numerical simulation model proposes the ability of the computational detailed micro-modelling approach to be compared using previous experimental test results obtained from Rots (1997), who referenced Van der Pluijm.

Van der Pluijm undertook various tests on two brick couplets using different mortar mixes and brick types to investigate the behaviour of these tests under compression, tension, and shear stress test. The shear strength experimental test was chosen to be numerically simulated in this study (as described in section 2.4.4). In addition, previous researchers such as Sarhosis and Lemos (2018); Van Zijl (2004) validated the same shear stress test, so material properties for this test were taken from their numerical simulations, as shown in Table 4-7, Table 4-8, and Table 4-9. Also, these material properties were compared against Rots (1997). The shear test brick dimension was 204 mm x 98 mm x 50 mm, and the mortar mix was 1:2:9 (cement: lime:

sand), where the mortar thickness was 15 mm. Three different pre-compression stresses of 0.1, 0.5 and 1.0 N/ mm^2 were applied to the sides of the samples, as shown in Figure 4-16.

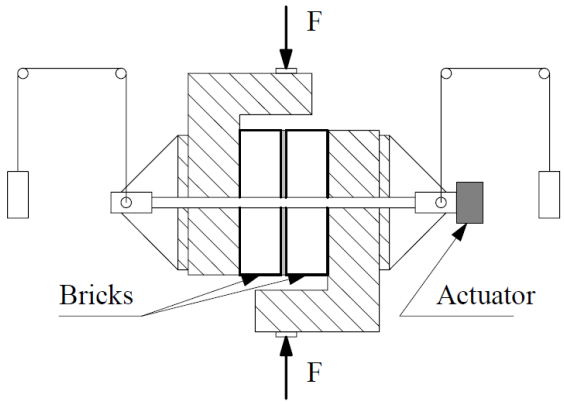

Figure 4-16: Van der Pluijm shear test setup (Lourenço, 1998).

Table 4-7: Numerical model elastic material properties.

Units (brick) *			Mortar **			Mortar interfaces **		
E_b (N/mm^2)	v	Density (kg/m^3)	E_m (N/mm^2)	v	Density (kg/m^3)	k_{nn} (N/mm^3)	k_{ss} (N/mm^3)	k_{tt} (N/mm^3)
16700	0.2	1994	2974	0.2	3250	400	200	200

* This value is derived from (Rots, 1997) and (Van Zijl, 2004).
** This value is derived from (Sarhosis and Lemos, 2018).

Table 4-8: Mortar joint and joint interface non-linear material properties.

Shear *			Tension *	
G_{II} (N/mm)	C (N/mm^2)	μ	G_I (N/mm)	f_t (N/mm^2)
0.058-0.13σ	0.88	0.75	0.012	0.3

* This value is derived from (Rots, 1997) and (Van Zijl, 2004).

Table 4-9: Mohr-Coulomb model material properties for mortar joints.

Mohr-Coulomb model	Friction angle ∅ * (degrees)	Dilation angle ψ ** (degrees)	Cohesion C ** (N/mm^2)	Tension cut off ** (N/mm^2)
	45	11	0.88	0.3

* This value is derived from (Sarhosis and Lemos, 2018).
** This value is derived from (Rots, 1997).

The numerical simulation of this shear test was performed in three static steps. In the first step, gravity was applied to the whole model to present the self-weight. In the second step, the normal pre-compression stress was applied of 0.1, 0.5 or 1.0 N/ mm^2 separately on one side, and the other side was fixed in vertical and horizontal directions. In the third step, the shear load was applied under displacement control.

The two brick elements were modelled as elastic elements of 204 mm x 98 mm x 50 mm. The mortar joint was modelled as a plastic element using Mohr-coulomb criteria to represent the plasticity and full-thickness mortar of 15mm. A detailed micro-modelling methodology was proposed to model the shear stress test model, involving plasticity based on constitutive models and the extended finite element method (XFEM). The numerical simulation using Mohr-Coulomb criteria implemented the plastic behaviour of mortar elements. The use of XFEM in modelling crack propagation in mortar joint elements was based on the cohesive interaction method, which does not require predefinition of the initial crack location. This method was chosen to accommodate material brittleness (mortar joint) since the location of the crack would be unpredictable in a real scenario.

The cohesive interaction simulates the unit-mortar interface. All this is based on the traction-separation behaviour by applying the shear and tensile linear and fracture behaviour.

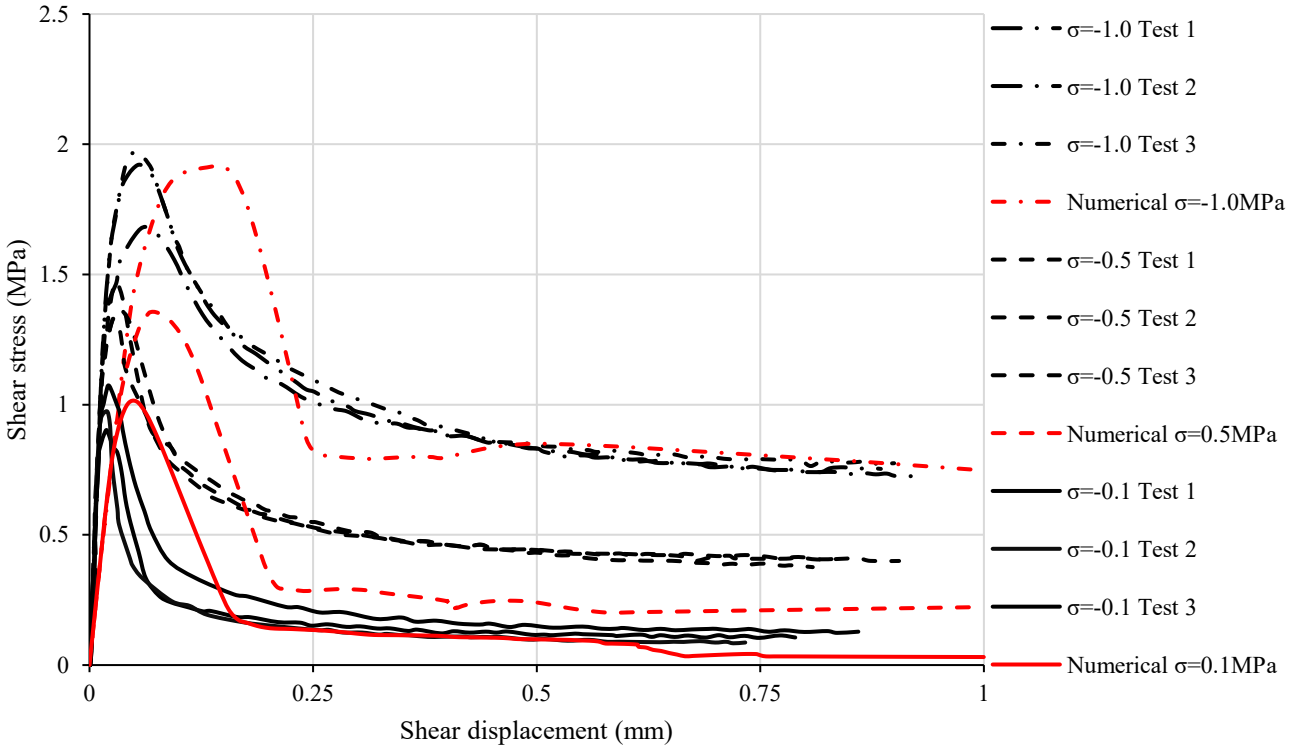

Figure 4-17: Experimental and numerical direct shear tests results comparison.

Figure 4-17 compares experimental and numerical results regarding shear stress against shear displacement and presents three precompression stress test curves of each test. The post-peak curve plastic deformation for the numerical models shows a non-smooth relationship. This is

likely to be a result of the roughness of the contact surfaces in the failure plane, and the high level of nonlinearity and discontinuity in the model at this the stage.

Sarhosis and Lemos (2018) referenced experimental findings by Abdou et al. (2006) and Beatie (2003), highlighting that the failure mechanism in brick-mortar assemblies is contingent upon the strength characteristics of the mortar and the brick-to-mortar interface. These studies elucidate that failure may occur either at the brick-to-mortar interface or through interface failure and subsequent diagonal shear cracking within the mortar. This is exactly what occurred in the couplet numerical model, as shown in Figure 4-19.

Figure 4-18 shows three stages of a simulation failure at the interface with a diagonal shear crack. Each stage has a colour-coded scale legend indicating the magnitude of a specific failure occurring at the interface between brick-and-mortar. The *CSDMG General Contact Faces* is an output value to read the failure occurring at the interfaces as mentioned in section 3.6.2.

Figure 4-18 (a) shows the interface is under low levels of stress, as indicated by the predominantly blue colour. The upper surface of the right-hand mortar joint is coloured red and indicates localised shear failure of the interface has started to occur.

Figure 4-18 (b) indicates interface is still largely intact but with increasing values of stress across most of the interface. The mechanism of failure is established at this point, as it can be noted that in the right-hand mortar joint shear failure (red) occurs at the top and stress reduces vertically down the interface; conversely, in the left-hand mortar joint shear failure (red) occurs at the bottom and stress reduces vertically up the interface.

Figure 4-18 (c) shows interface slip has occurred in the upper two thirds of the right-hand mortar joint, and the lower third of the left-hand mortar joint, as indicated by the red colouring and visible displacement of the bricks. A diagonal crack has formed part-way across the mortar joint, which is shown after complete failure in Figure 4-19 (b).

The progression from stage 1 to stage 3 shows the accumulation of shear stress leading to a critical point where the material's capacity to withstand shear is surpassed, resulting in shear failure at the interface, and eventually tension failure in the mortar joint. This failure is typically abrupt, indicating a loss of cohesion between the materials or components at the interface.

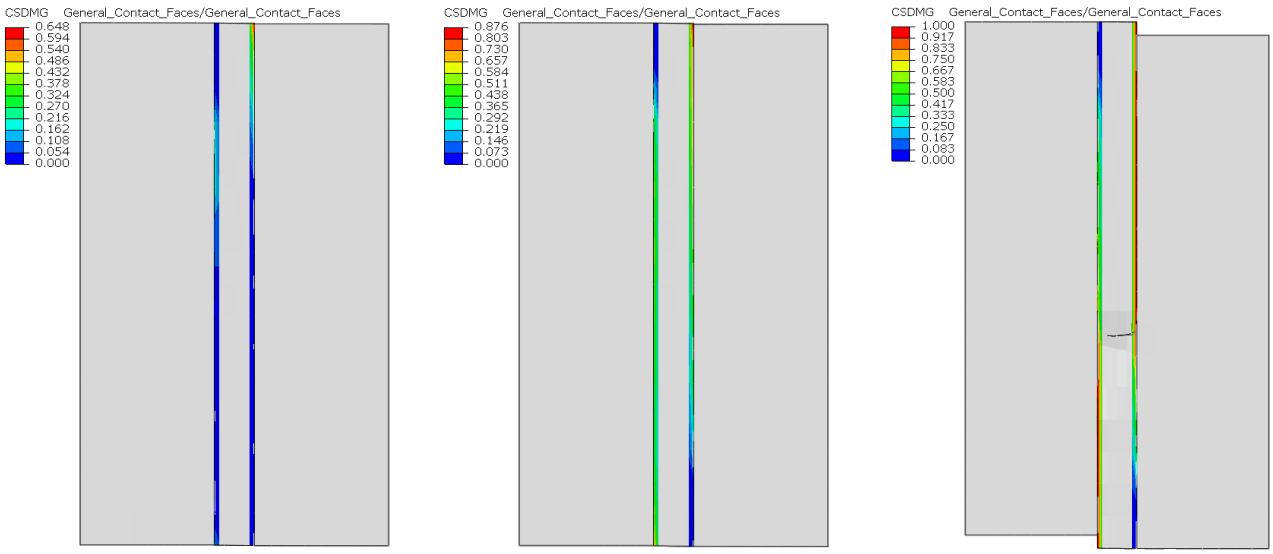

a) stage 1 b) stage 2 c) stage 3

Figure 4-18: The crack propagation and failure occurring at the brick-to-mortar interface with diagonal cracking in the couplet model.

It can be noted that the numerical model was capable of indicating the peak and fracture shear stress test results for all three pre-compression shear strength results. Furthermore, Figure 4-19 (b) presents the crack in the joint mortar element of the 0.1 N/mm^2 pre-compression numerical model. Figure 4-19 (a) evaluates the opened crack at the unit-mortar interface, and this replicates the experimental failure modes.

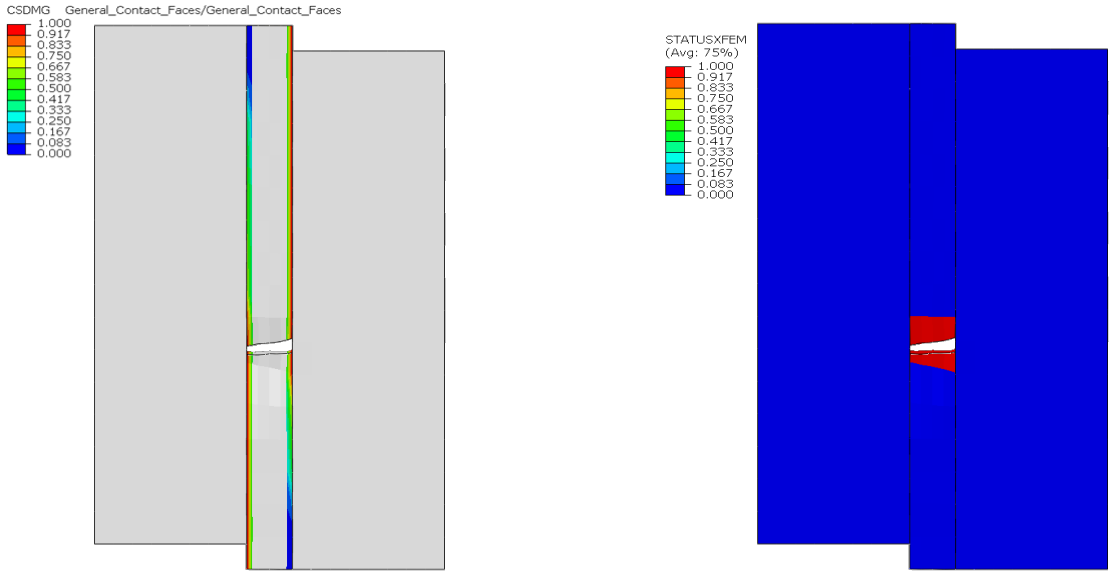

a) Opened crack at unit-mortar interface output. b) Opened crack in the mortar joint output.

Figure 4-19: Numerical model failure modes of 0.1 N/ mm^2 precompression shear test result.

4.3.3 *Masonry triplet numerical model*

This model was created using a detailed micro-modelling approach to simulate the experimental test described in 4.2.4. The numerical simulation model's geometry and the boundary conditions of the shear stress tests were created based on the experiment tests, as shown in Figure 4-20. The triplet numerical models material properties for the brick, mortar and interfaces were obtained using the experimental test results in sections 4.2.3 and 4.2.4, as described in Table 4-10,Table 4-11, and Table 4-12. Figure 4-20 shows the numerical simulation model of the masonry triplet shear test, where the brick elements were modelled as purely elastic as in the experimental test, as they were class A bricks which did not crack during the experiment tests. The mortar is modelled as a non-linear material.

Drucker-Prager and Mohr-Coulomb components with cohesion are two material model criteria that can be used to characterise the numerical model plastic behaviour, both are used in the parametric study to compare the behaviour exhibited by the two criterions. Both failure criteria should be able to replicate the elastic and plastic behaviour of the mortar joint elements, but the parametric study will provide an opportunity to determine which is most accurate.

The extended finite element method (XFEM) is implemented to capture the crack in the mortar joint elements. Cohesive interaction was implemented to simulate the interaction between the brick surface and the full-thickness mortar surfaces, where fracture response behaviour was captured based on the traction-separation behaviour at the unit-mortar interface.

The numerical model of the triplet tests was analysed using three static load steps. In the first step, gravity was applied to the model. In the second step, the transverse pre-compression pressure of 0.20, 0.60, or 1.00 N/mm^2 was applied to one external vertical brick face, whilst the opposite face was fixed against displacement. In the third step, vertical displacement was applied to the steel bars positioned on the edges of the middle brick, under displacement control. Vertical restraint was applied to the steel bars positioned under the edges of the outer two bricks.

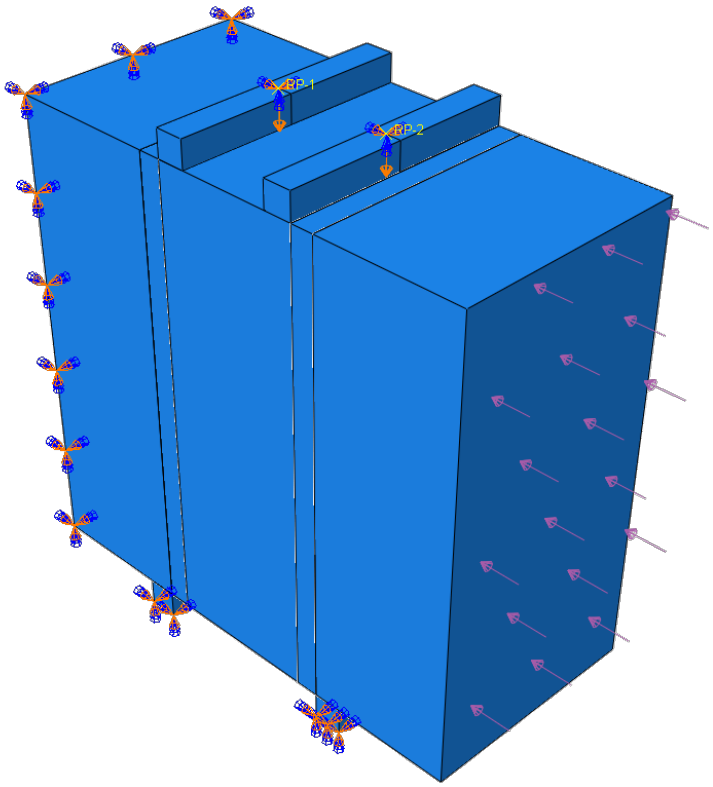

Figure 4-20: A detailed numerical micro model of the masonry triplet shear test.

Table 4-10: Triplet numerical model elastic material properties.

Units (brick)			Mortar			Mortar interfaces		
E_b (N/mm^2)	v	Density (kg/m^3)	E_m (N/mm^2)	v	Density (kg/m^3)	k_{nn} (N/mm^3)	k_{ss} (N/mm^3)	k_{tt} (N/mm^3)
16000	0.15	2200	6000	0.15	1560	295	172	172

Table 4-11: Mortar joint and joint interface non-linear material properties.

Shear					Tension	
G_{II} (N/mm)	c (N/mm^2)			μ	G_I (N/mm)	f_t (N/mm^2)
0.064	σ=0.2	σ=0.6	σ=1.0	0.63	0.039	0.18
	0.45	0.79	0.94			

Table 4-12: Mohr-Coulomb model material properties for mortar joints.

Mohr-Coulomb model	Friction angle $\emptyset$ (degrees)	Dilation angle ψ (degrees)	Cohesion C (N/mm^2)	Tension cut off (N/mm^2)
	30	20 *	0.3	0.3 **

* This value is derived from (Rots, 1997)
** This value is derived from (Weekes, 1998)

4.3.3.1 Masonry triplet numerical model validation

Figure 4-21 compares the experimental and numerical results of the masonry triplet shear tests, for all three normal pre-compression stress values, presenting the relationship between the shear stress against shear displacement.

The experimental and numerical shear stress-shear displacement curves show reasonable agreement in terms of overall behaviour – elastic response up to peak strength then strain softening until failure. The graph indicates both the experimental and numerical peak shear stress failure points are within similar range with respect to the experimental equivalents. However, slight deviations are observed for the numerical models in terms of the elastic stiffness region for 0.2 MPa and 0.6 MPa pre-compression stress curves. The 1.0 MPa pre-compression numerical model curve presents a difference in the elastic stiffness region compared to the experimental result curves.

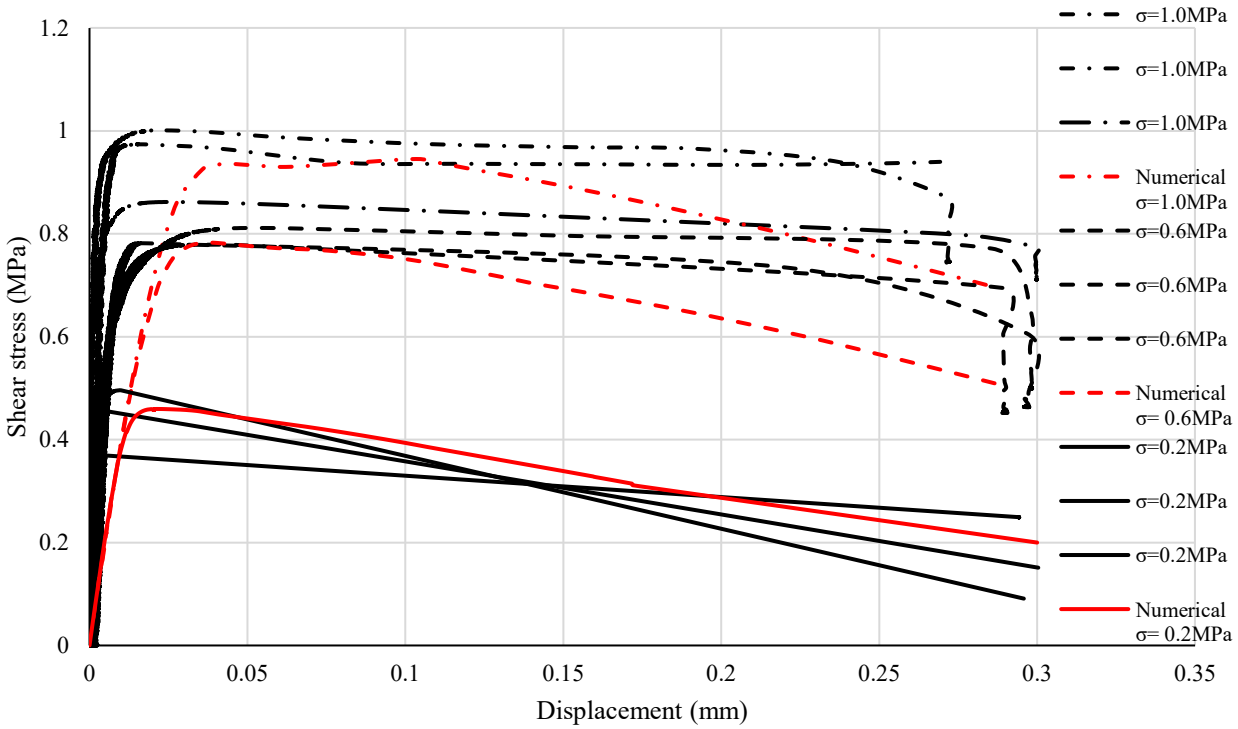

Figure 4-21: Experimental and numerical results comparison subjected to the shear strength tests.

The initial stiffness of each curve of the numerical results was shown to reasonably match the experimental curves until 0.3 MPa shear stress, where the experimental curve shows a higher stiffness. The numerical models were analysed using the general static step under displacement

control as the experimental tests were under displacement control. The XFEM method created cracks in the two mortar joint elements, as shown in Figure 4-22. Figure 4-22 (a) and (b) present the output of the opened crack in the mortar joint and opened crack at the unit-mortar interface for the 0.2 MPa normal pre-compression stress masonry triplet models, where Figure 4-22 (c) and (d) display the same output but for the 0.6 MPa normal pre-compression stress models.

Figure 4-22 shows that as models at both values of pre-compression exhibit tensile failure in the mortar joint, this suggests that the tensile strength of the mortar is less than the shear strength of the interface. So, although the failure mode would be expected to only involve shear, tensile strength of the mortar may be important. Since the mortar is only 10mm thick and all deformation must be shear displacement, the minimal vertical displacement at failure can only occur once the shear strength of the brick-mortar bond, and mortar tensile strength are exceeded.

The cohesive interaction at the unit-mortar interface, Mohr-Coulomb plasticity, and use of XFEM to crack the mortar joint have validated the experimental tests and predicted the failure at the unit-mortar interface and the crack at the mortar joint elements.

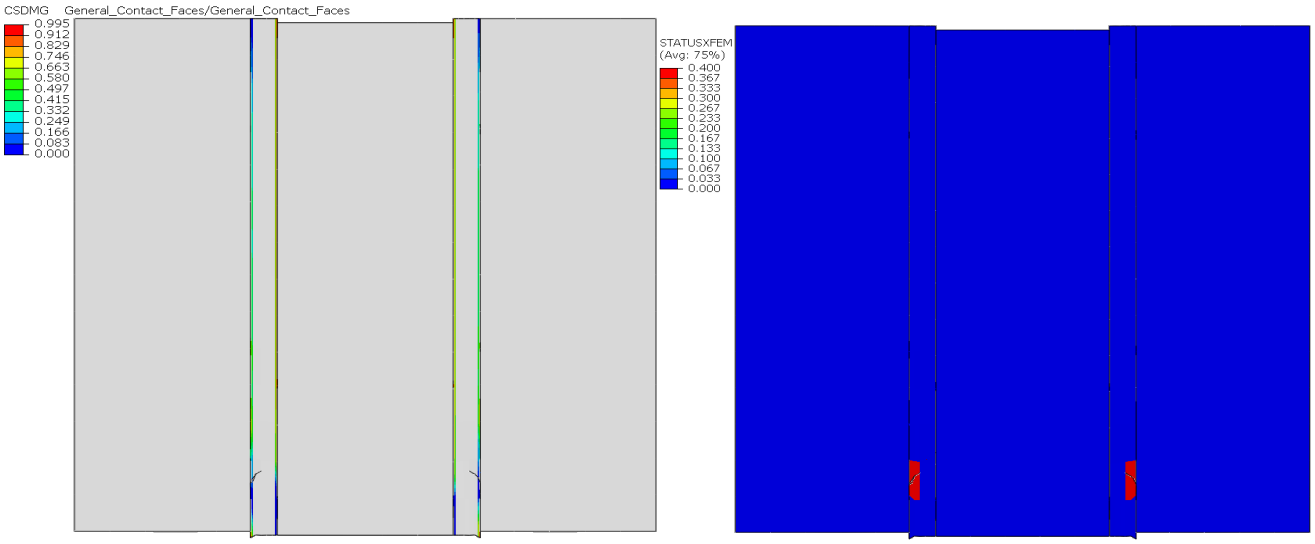

a) opened crack at the unit-mortar interfaces b) opened crack at mortar joints

σ =0.2 MPa deformed shapes

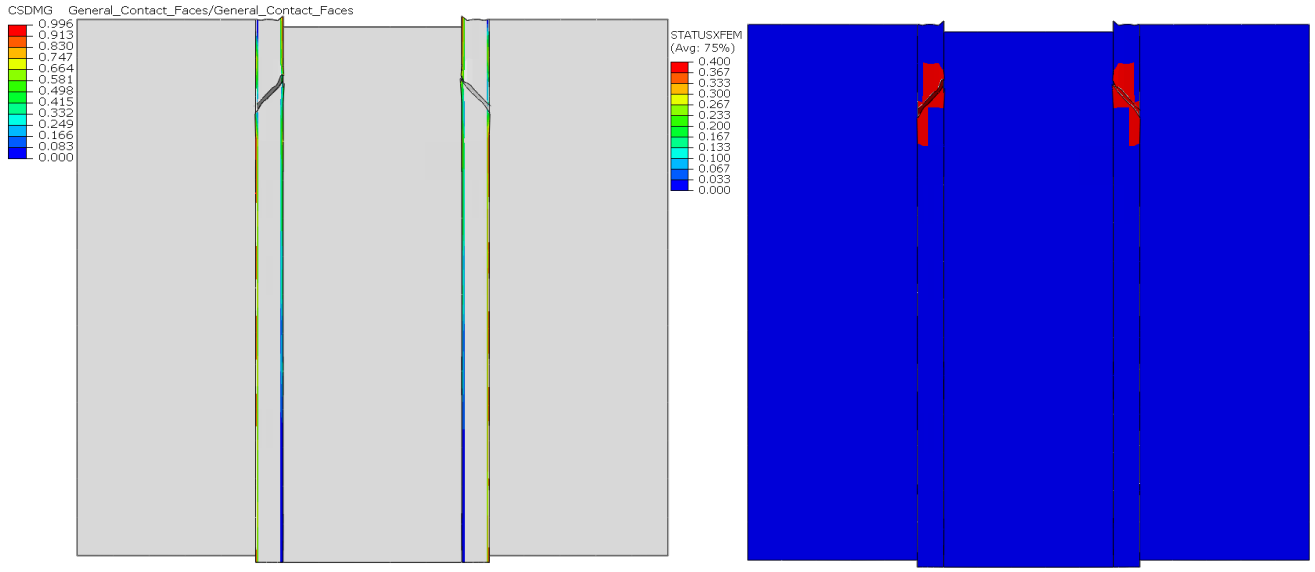

c) opened crack at the unit-mortar interfaces d) opened crack at mortar joints

σ =0.6 MPa deformed shapes

Figure 4-22: Masonry triplet numerical deformed shapes of 0.2 and 0.6 MPa pre-compression.

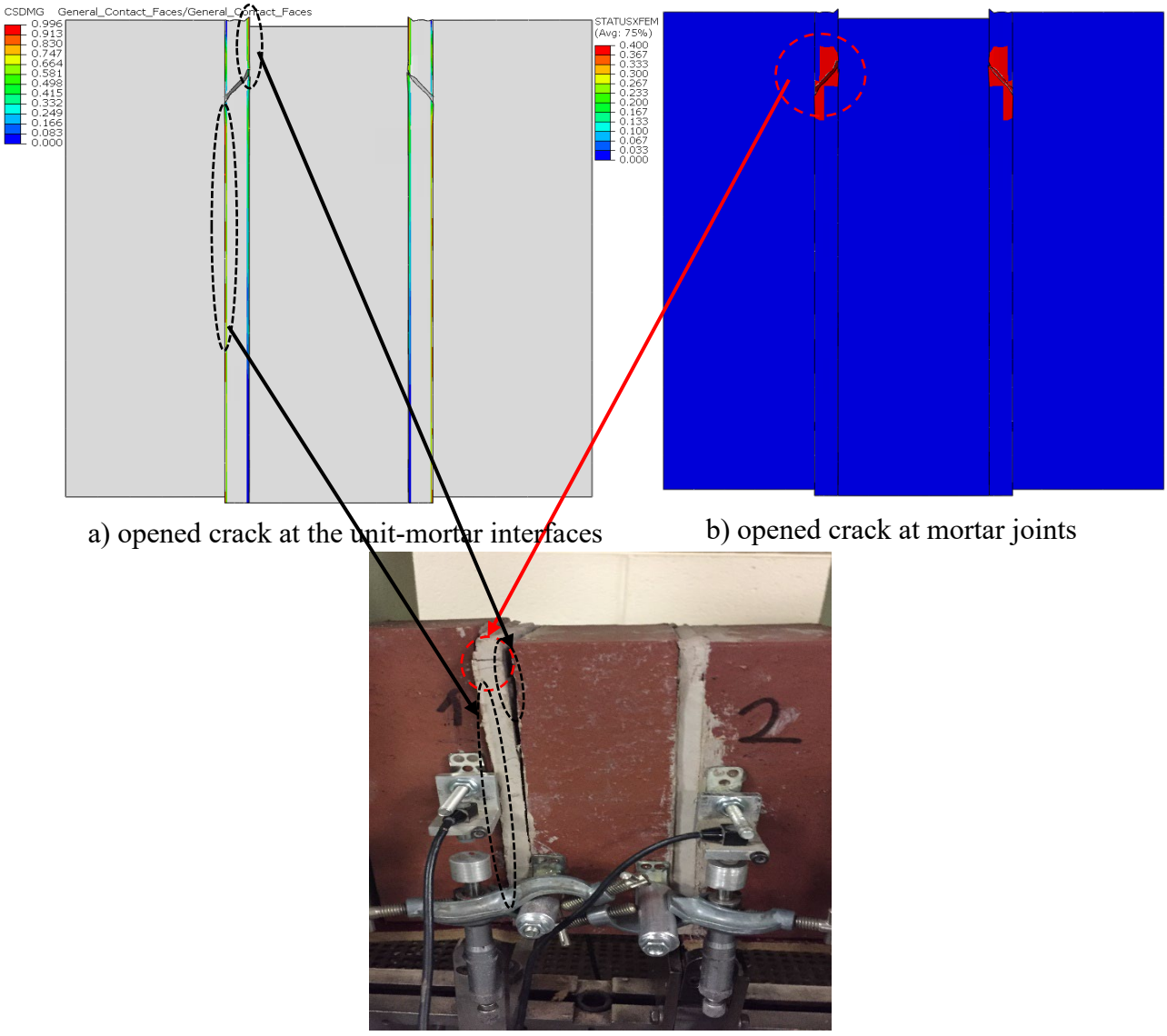

a) opened crack at the unit-mortar interfaces

b) opened crack at mortar joints

c) Failure of experimental triplet

Figure 4-23: Comparison between numerical and experimental failure for 0.6 MPa pre-compression.

Figure 4-23 shows the numerical and experimental results failure of the 0.6 MPa pre-compression. Figure 4-23 (b) shows the crack within the mortar joint compared to the experimental sample, as shown in Figure 4-23 (c). The crack is highlighted for both results at the exact location on the left-hand mortar joint side. Also, Figure 4-23 (a) shows the failure between the unit-mortar interface compared to the experimental result, as shown in Figure 4-23 (c).

4.3.4 *Material properties parametric studies on masonry triplet*

This section includes two material property parametric investigations to assess whether the validated model has an appropriate range of applications. The effect of altering material property values was evaluated by comparing the shear stress-shear displacement graph to the test data.

4.3.4.1 Mortar plasticity using Drucker-Prager criterion

In this section, the effect of using Drucker-Prager failure criteria is investigated. In section 4.3.3, Mohr-Coulomb criteria was used to validate the masonry triplet numerical models as the requirements of this criteria were available from the experimental test results. However, the Drucker-Prager criterion requirements for hardening law values were taken from experimental test results (see Figure 4-2) and are shown in Figure 4-24.

Date taken from Table 4-13 and Figure 4-24 were implemented in the Drucker-Prager model to represent the stress-strain behaviour of the mortar.

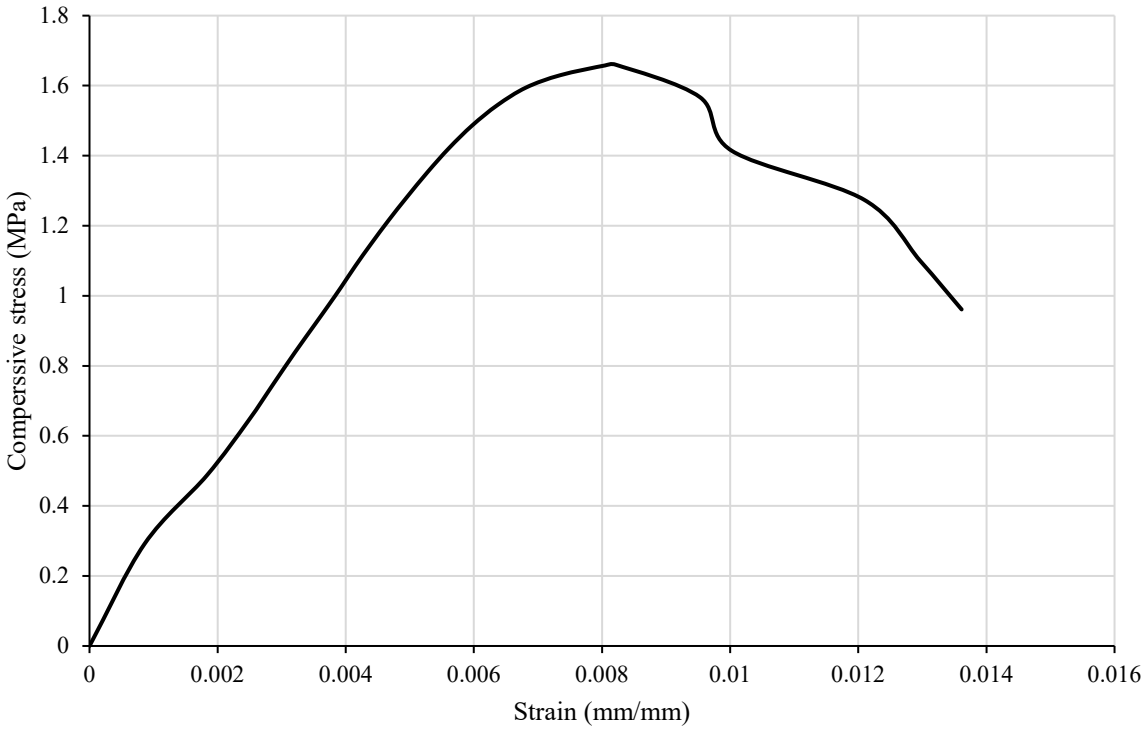

Figure 4-24: Drucker Prager compressive stress vs stain curve for mortar.

Table 4-13: Drucker-Prager model material properties for mortar joints.

Drucker-Prager model	Friction angle ∅ (degrees)	Dilation angle ψ (degrees)	flow stress ratio*
	30	20	1.0

* Input as a default of 1.0 (ABAQUS, 2019).

Figure 4-25, compares the shear stress 0.6 MPa normal pre-compression experiment results of three test curves and two numerical model results, each created using either Mohr-Coulomb or Drucker-Prager failure criteria. It can be noted that the two criterions generated very similar overall behaviour but the Drucker-Prager model exhibits a lower peak shear stress than both the Mohr-Coulomb model and the experimental test curves.

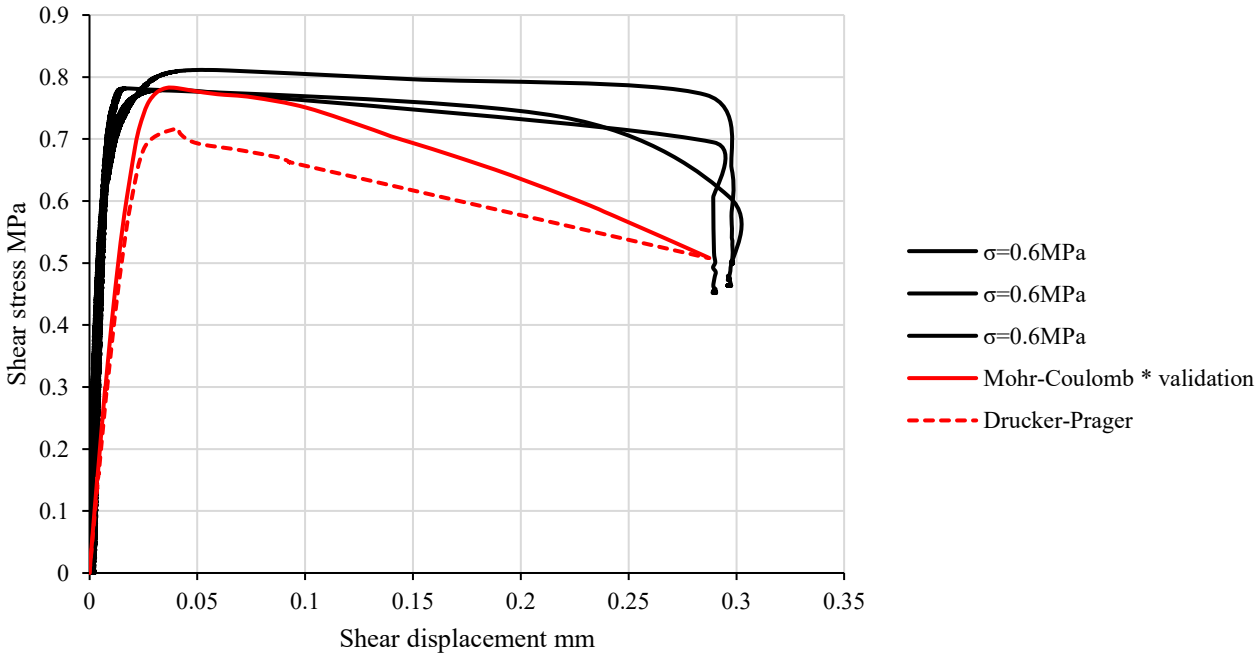

Figure 4-25: Shear stress-shear displacement comparison of the masonry triplet experimental and numerical results using various plasticity parameters.

4.3.4.2 Material properties parametric study

This section includes material parametric studies to investigate and understand the behaviour of structural masonry prisms subjected to 1.0 MPa pre-compression load using the same mortar mix material properties used in the experimental tests.

This section used the validated numerical masonry couplet (Van der Pluijm) and triplet shear stress analyses in sections 4.3.2 and 4.3.3 for these parametric studies.

A. Masonry couplet numerical model

This section provides two numerical analysis investigations by varying the value of material properties to be compared with the Van der Pluijm validated result for 1.0 MPa pre-compression load on the masonry shear couplet model, as shown in Table 4-14. In addition, this section addresses the influence of the unit-mortar interface non-linear material.

Table 4-14: Parametric analysis values of numerical models for masonry couplets on the mortar joint interfaces.

	Shear			Tension	
	G_{II} (N/mm)	c (N/mm^2)	μ	G_I (N/mm)	f_t (N/mm^2)
Masonry couplet model material properties Table 4-8	0.072	0.88	0.75	0.012	0.3
Model 1	0.0125*	0.88	0.75	0.012	0.3
Model 2	0.0125*	0.4*	0.75	0.012	0.3

* The changed value(s) in each numerical model.

Table 4-14 shows the shear fracture energy value applied to the first numerical model of this parametric study on the Van der Pluijm shear stress validated numerical model. Table 4-14 shows the second numerical model material properties, the cohesion between the unit-mortar interfaces was 0.4 N/mm^2 compared to the validated model and the first numerical model of this parametric study. The rest of the material properties remain the same, as described in section 4.3.2.

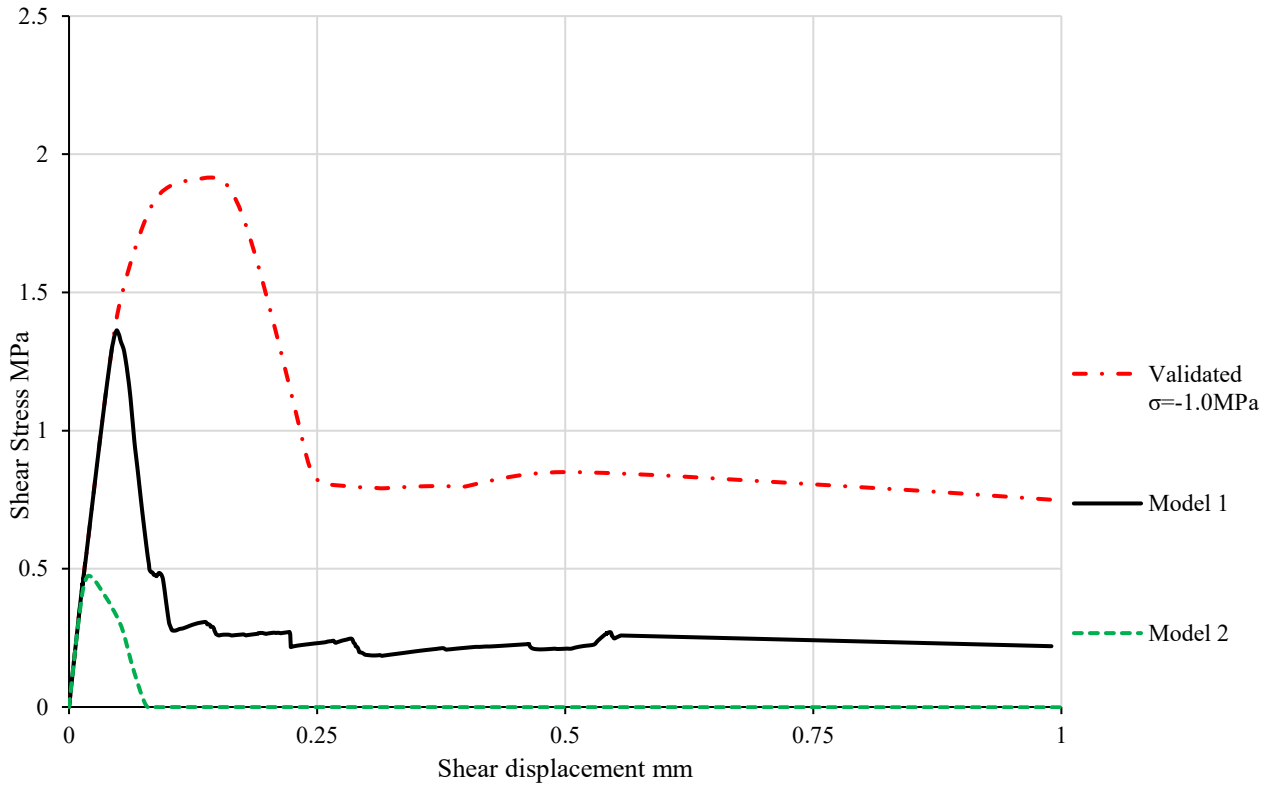

Figure 4-26: Shear strength-shear displacement comparison to establish the effect of shear fracture energy and cohesion on behaviour.

Figure 4-26 compares the two numerical models against the validated Van der Pluijm shear stress numerical model. In model 1 the value of shear fracture energy was 0.0125 N/mm, and showed the same elastic region behaviour as the validated numerical model. However, the peak shear stress was at 1.4 MPa and the behaviour of the plastic region after the peak shear stress changed to a sudden drop compared to the validated model, which was at 1.9 MPa (around 35% decrease). The shear fracture energy influenced the peak shear stress of the couplet model and the behaviour of the plastic region failure curve.

In model 2, the shear fracture energy was also 0.0125 N/mm and the value of cohesion was 0.4 N/mm^2. The peak shear stress of model 2 was at 0.46 MPa (around 280% decrease), and following a short zone of plastic behaviour the residual shear resistance was zero. The significant difference in the peak shear stress of the two numerical models were due to change of the cohesion of the unit-mortar interfaces.

B. Masonry triplet numerical model

This section provides three numerical analysis investigations of varying the value of material properties to be compared with the masonry triplet validated result of 1.0 MPa pre-compression load on the masonry shear triplet model, as shown in Table 4-15. This section focused on the influence of the unit-mortar interface and the mortar joint friction and dilation angles. The material properties of the original masonry triplet model were described in section 4.3.3.

In the previous parametric study, one value changed in each analysis. However, in this section the parametric study will address variations in several parameters, as detailed in Table 4-15. Model 3 includes reduced values of friction and dilation angles; which allows investigation of weaker mortar. Model 4 includes mortar with zero dilation angle, to investigate and understand the behaviour beyond the non-associated flow (isolate the role of dilation in mortar behaviour). Model 5 includes a reduced value of shear cohesion at the unit-mortar interfaces, this allows the effect of shear bond to be investigated. Model 6 and model 7 include reduced values for the mortar joint non-linear interface, except tension bond stress which is increased, this allows the effect of tension bond to be investigated.

Table 4-15: Parametric analysis values of numerical models for masonry triplets.

	Mortar joint properties		Mortar joint non-linear interface			
	Friction angle	Dilation angle	Shear		Tension	
	ϕ (degrees)	ψ (degrees)	G_{II} (N/mm)	c (N/mm^2)	G_I (N/mm)	f_t (N/mm^2)
Masonry triplet model material properties Table 4-11 and Table 4-12	30	20	0.064	0.94	0.039	0.18
Model 3	26*	11*	0.064	0.94	0.039	0.18
Model 4	30	0*	0.064	0.94	0.039	0.18
Model 5	30	20	0.064	0.4*	0.39	0.18
Model 6	30	20	0.0125*	0.94	0.012*	0.18
Model 7	30	20	0.0125*	0.4*	0.012*	0.3*

* The changed value(s) in each numerical model.

Figure 4-27 compares the three experiment test result curves and the validated numerical model result of masonry triplet against the five models in the parametric study.

Model 3 investigated varying friction and dilation angles and provides behaviour very similar to the validated numerical model with a minimal difference in the peak shear stress and slightly more strain softening, in a bi-linear fashion.

Model 4 investigated zero dilation angle and exhibited a drop in peak shear stress to 0.86MPa, (the validated model peak shear stress was 0.93MPa). Again, bi-linear moderately strain softening behaviour was very similar to the validated model and model 4.

Model 5 investigated decreased shear cohesion between unit-mortar interfaces and exhibited a marked reduction in peak shear stress to 0.44 MPa (less than 50% of the validated model at 0.93MPa). Perfectly linear moderate strain softening post yield behaviour was observed.

Model 6 investigated decreased shear and tensile fracture energy values, which significantly influenced the masonry triplet numerical model behaviour compared to the validated model. The peak shear stress was 0.7MPa (75% of the validated model at 0.93MPa). Also, after the peak shear stress, the behaviour was highly strain softening followed by perfectly plastic displacement until failure.

Model 7 investigated decreased shear and tensile fracture energy, and shear cohesion values and an increased tension cut-off value. Again, this significantly influenced the behaviour compared to the validated model. The peak shear stress was 0.41MPa, similar to the peak shear stress in model 5 but the post-yield behaviour was highly strain softening similar to model 6.

All five models exhibited the same initial shear stiffness of 32N/mm.

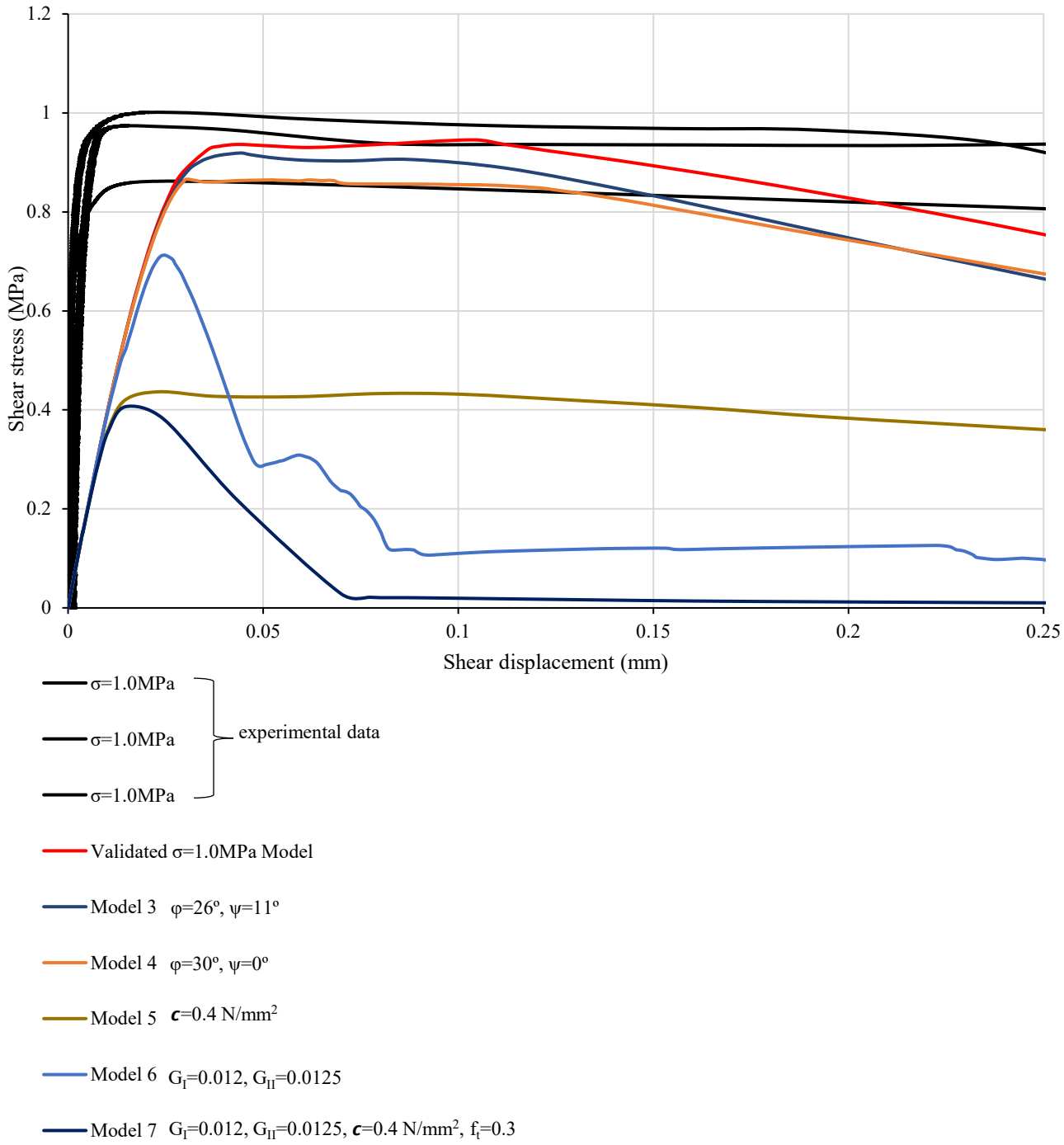

Figure 4-27: Shear strength-shear displacement comparison to establish the effect of different properties on the masonry triplet behaviour.

4.4 Summary

This chapter applied the detailed micro-modelling approach to simulate masonry couplet and triplet structural behaviour on two experimental masonry shear tests subjected to normal pre-compression loads. The modelling was successful and will be used in chapters 5 and 6.

The conclusions of this chapter are as follows:

- Referring to Figure 4-10 and Figure 4-11, it is clear that masonry subjected to 0.2MPa pre-compression or less will exhibit strain softening behaviour. For masonry subject to pre-compression of 0.6MPa and higher will exhibit elasto-plastic ductility.
- A detailed micro-modelling approach was presented to simulate the structural behaviour of brickwork couplet and triplet shear tests which implemented a combination of elastic and plastic behaviour models, and cohesive interaction with a traction separation law representing the tension and shear failure in the mortar joints and the unit-mortar interface.
- XFEM can be used to simulate cracks in the mortar without predefining the initial crack position.
- Numerical models of couplets and triplets using XFEM displayed accurate structural behaviour, failure mechanisms and peak loads. This was determined by comparing shear stress-displacement graphs and implies that validated models of masonry arches can be created.
- Finite element analysis (FEA) model validation is required to ensure the numerical model provides an acceptable representation of reality. However, many FEA parameters are uncertain; hence, differences in the real structural behaviour and the FE model results are inevitable.
- By comparing numerical models of masonry triplets which use different constitutive models, it was determined that the Mohr-Coulomb criteria provided a superior replication of experimental post-yield behaviour, peak load and ductility.
- The dilation angle has minimal influence on the masonry triplet behaviour. For variation between zero and 20 degrees the peak shear stress changes by only 5.6%. The validated model with 1.0MPa pre-compression exhibited virtually the same structural behaviour as the experimental test curve.
- The cohesion between the unit-mortar interface significantly influences the shear stress-displacement curve. The peak value of shear stress is directly proportional to the value of cohesion.
- The tensile and shear fracture energy values greatly affected the peak shear stress point and post-yield behaviour, from elasto-plastic to strain softening.

- The triplet parametric study did not produce any improvement in behaviour prediction for one pre-compression value, therefore material properties will be taken from the validated finite element model.
- Due to the small test sample size in the experimental material tests, leading to low reliability of values (mortar Young's modulus and couplet tension test), values for mortar interface stiffness have been adopted from previous successful research models.

Chapter Five

5 Masonry Arch Ring Experimental and Numerical Computational Model Validation

5.1 Introduction

As described in Chapter 4, the computational software ABAQUS and XFEM have been used in static analysis for the brickwork triplet model, where numerous numerical-experimental comparisons have been checked. Also, using cohesive interaction to represent the interface between the unit and mortar joint presented realistic structural behaviour.

This chapter uses the established detailed micro-modelling strategy to construct large-scale masonry arch numerical models. Appropriate material properties are identified, and the results are compared with the experimental masonry arch results. Furthermore, a strategy for selecting a range of analysis options was used. As a result, the most accurate analysis regime was identified and used to create realistic simulations of masonry arches.

The detailed micro-modelling approach was used to analyse masonry arches subject to static loading, and numerical results are compared to the results of the experimental arch ring in this chapter. The full-scale masonry arch tests have been considered, and the numerical models presented here realistically represent the masonry arch behaviour. These include arches that fail due to radial crack formation, leading to a hinge mechanism and those failures by ring separation (Melbourne, Wang, & Tomor, 2007).

The complex failure mechanisms of masonry arches can be represented using non-linear material descriptions that account for the existing masonry bond, as the detailed micro-modelling technique was adopted to model the bricks and mortar joints separately. Continuum elements represent the detailed micro-modelling approach for masonry units and mortar in the joints. In contrast, discontinuous elements represent the unit-mortar interface.

Lastly, it is crucial to understand the response of masonry arch bridges under operational loads, which is essential for safely evaluating these structures when they are subjected to significant cyclic loading, which was highlighted in previous studies (Melbourne & Tomor, 2004b; Wang et al., 2013). Furthermore, these cases highlighted that damage accrued over time under

operational loading might significantly reduce the ultimate capacity of the bridge (Melbourne, Wang, & Tomor, 2007).

This chapter aims to improve understanding of the physical action of a single-span masonry arch ring subject to static loading when the foundations undergo differential movements. It will not account for the effects of cyclic loading, though ring separation was observed in the FE models.

5.2 Masonry arch experimental test

This section will describe an experimental test which was part of a series of masonry multi-ring arches tested at the University of Salford for the "Sustainable Bridges - Assessment for Future Traffic Demands, and Longer Lives" research project (Melbourne, Wang, Tomor, et al., 2007). From which the response behaviour of a masonry arch tested under static loading has extracted for comparison with numerical models.

The experimental tests included masonry arches with spans of 3m and 5m, constructed in a segmental shape with a span: rise ratio of 4:1. Most arches were constructed using high-quality Class A engineering bricks. Also, some of the masonry arches were built with weaker Britley Olde English bricks to replicate the older brickwork typically found in railway network masonry arch bridges. These particular arches lacked headers to connect the two masonry arch rings (see section 2.3). The bricks used in the tests were of characteristic size 215mm x 102mm x 65mm, while the mortar joints were nominally 10mm thick (Naggasa, 2022). The mortar mix was 1:2:9 (cement: lime: sand) (Melbourne, Wang, Tomor, et al., 2007).

The arch abutments were constructed using reinforced concrete with high tensile steel ties to control spreading. These abutments were securely bolted to the laboratory's reinforced concrete floor to minimize movement. A series of experimental tests determined the properties of the bricks and mortar, such as density and compressive strength, were insufficient to completely construct numerical models of the Arch G experimental test.

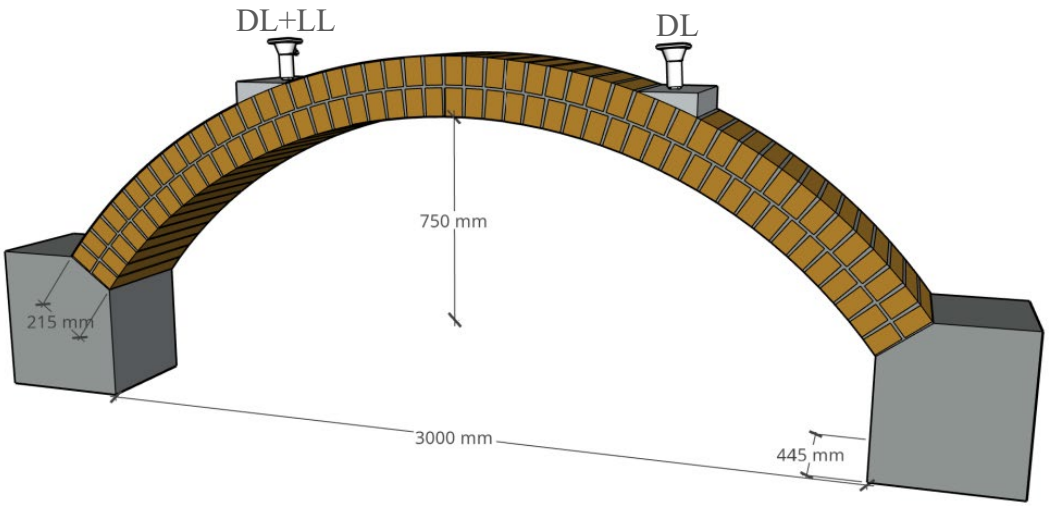

Figure 5-1: Arch G geometric and loading arrangement.

The experimental arch was subjected to pressure through hydraulic cylinders reacting against a rigid frame. According to Melbourne, Wang, Tomor, et al. (2007), a steady load of 10kN was used to mimic the dead load (DL) from backfill at the quarter-span and three-quarter-span points. To simulate live load (LL), monotonic loading was applied at the quarter span of the arch in increments of 1.0kN until the arch reached its collapse load under controlled force conditions (Melbourne, Wang, Tomor, et al., 2007). The arch displacement was measured using linear variable differential transformers (LVDTs) in vertical and horizontal directions at the quarter and three-quarter span positions. The material property test results are reported in Table 5-1.

Table 5-1: Masonry, mortar and brick material properties (Melbourne, Wang, Tomor, et al., 2007).

	Compressive stress (N/mm^2)	Density (kN/m^3)
Brick (Strong)	154	23.7
Brick (Weak)	18.9	16.2
Mortar	1.86	15.5
Masonry triplet (Strong)	18.2	21.8
Masonry triplet (Weak)	11.7	16.9
Masonry prism (Strong)	24.5	22
Masonry prism (Weak)	9.1	16

5.2.1 *Masonry arch construction and instrumentation (3m span)*

Arch G was constructed as a two-ring arch without soil backfill using strong bricks; the lower ring was made of 47 bricks, and the upper ring was made of 49 bricks. The principal arch dimensions are shown in Table 5-2; Figure 5-1 shows the loading arrangement.

Table 5-2: Masonry arch dimensions (Melbourne, Wang, Tomor, et al., 2007).

Span (mm)	Rise (mm)	Span-to-rise ratio	Thickness (mm)	Width (mm)	Dead load (kN)	Number of rings
3000	750	4:1	215	445	2 x 10	2

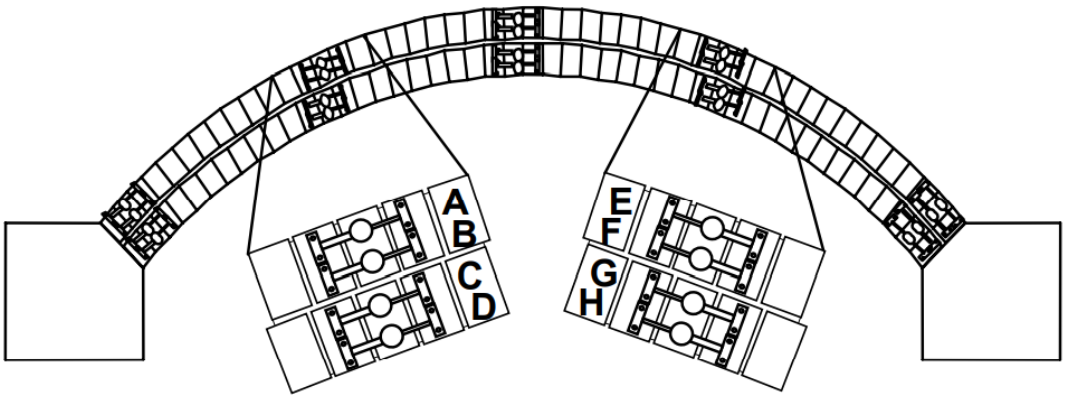

Figure 5-2: Surface strain gauges locations (Melbourne, Wang, Tomor, et al., 2007).

The surface strain of the arch barrel was monitored using vibrating wire gauges (GAUGE TYPE T/S/R, 139mm gauge length). The strain gauges can measure with a range of 0.5 - 3000 microstrain. The measurement of the surface strain was at four levels, at each of five different sections along the arch barrel, as shown in Figure 5-2. The strain gauges provided important information regarding the arch behaviour and location of the four hinges, as cracking was not visible at lower load levels.

5.2.2 *Masonry arch experimental test failure description*

According to the experimental report Melbourne, Wang, Tomor, et al. (2007), the arch barrel failed due to a four-hinge mechanism formation at the 28kN increment. Furthermore, the arch

was observed to become unstable after the fourth hinge formed near the three-quarter span of the arch. The experimental arch G test was observed until the four-hinge mechanism formed but did not collapse, as shown in Table 5-3. The arch was subsequently used in a 3,600,000 cycle fatigue test (Melbourne & Tomor, 2004a).

Table 5-3: Crack location history (Melbourne, Wang, Tomor, et al., 2007).

Hinge	Live load (kN)	Crack location- brick number		Crack type
		Intrados	Extrados	
Fist hinge	22	14/15	16/17	Radial crack
Second hinge	Not available	0/1	0/1	Radial crack
Third hinge	Not available	47	49	Radial crack
Fourth hinge	28	27/28; 29/30	28/29; 30/31	Radial crack

Vertical and horizontal displacements measured by the LVDT's at quarter and three-quarter span indicate slight and progressive change in stiffness at 15kN, as shown in Figure 5-3. At 27kN there is a notable loss of stiffness, and the load-displacement curve flattens, indicating full four hinge mechanism has formed in the arch (Melbourne, Wang, Tomor, et al., 2007).

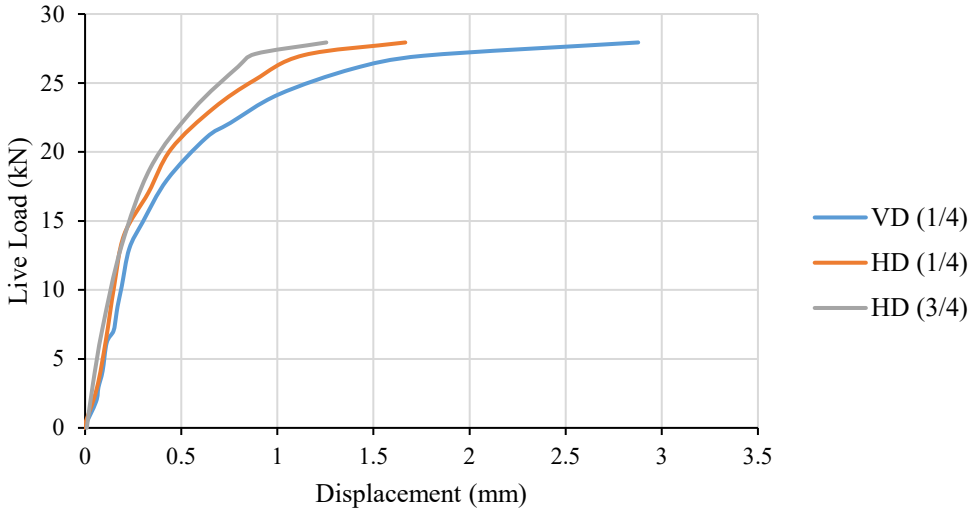

Figure 5-3: Arch G experiment test Load-displacement curves (Melbourne, Wang, Tomor, et al., 2007).

According to Melbourne, Wang, Tomor, et al. (2007), the first and second hinges most likely formed around 15kN. However, these two hinges were only apparent at higher load levels. Deflection and strain measures changed at roughly 14kN, indicating when the first hinge occurred. However, the first hinge was only visually noticeable, during the 22kN load level.

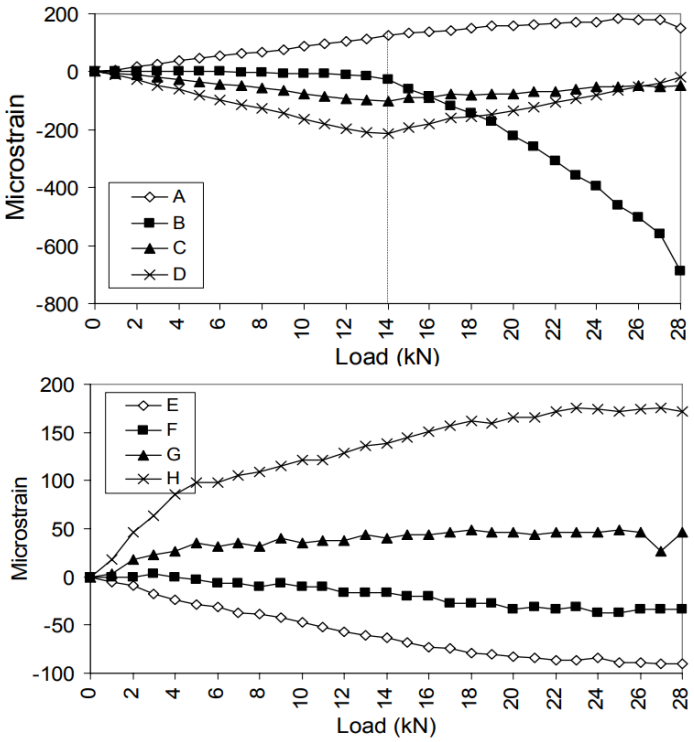

Figure 5-4: Arch G Load-Strain results (Melbourne, Wang, Tomor, et al., 2007).

Changes in the gradient of surface strain readings at gauges B, C and D prove that the first hinge started to form at the quarter span, during the 14kN load level. The gauge readings indicated a radial crack (first hinge) opening at the quarter span of the arch intrados through the arch thickness, as shown in Figure 5-4.

The first hinge occurred at the quarter span, while the second and third hinges occurred at the right and left abutments. The fourth hinge occurred at the three-quarter span.

The last change in strain is evident around 27kN, which agrees well with the deflection measurement, where these can be shown in Figure 5-3 & Figure 5-4. The fourth hinge probably occurred at 27kN, therefore, the arch became unstable at 28kN (Melbourne, Wang, Tomor, et al., 2007).

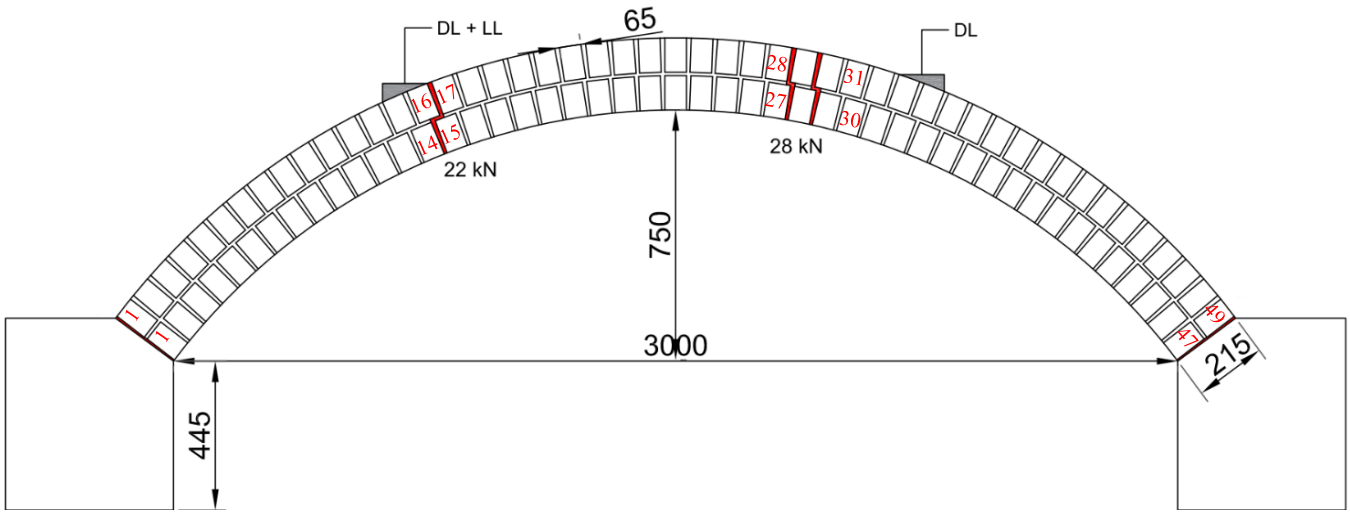

Figure 5-5: Crack patterns at the loads.

The experimental test was conducted under force control. Once a ductile response was observed all the LVDT, strain gauges and the load cells were removed after reaching the maximum load and became unstable around 28kN without investigating the peak response.

5.3 Masonry arch numerical model description

The current study uses two ABAQUS FEM analyses to simulate large-scale and small-scale deformations. In simulating solid structural forms, solid components are selected (for masonry). In considering solid structural forms, there are three relevant sources of non-linearity to be examined: nonlinear boundary conditions, nonlinear geometry, and nonlinear material. To account for the nonlinear geometry (large deformation), the analysis option Nlgeom must be set to ON. Conversely, the material behaviour must be validated by grain-parallel compression tests.

The stiffness matrix is affected by these three sources of non-linearity and is updated in each analysis increment. In general, ABAQUS iterative processes include approximated numerical values which use either modified or classical Newton-Raphson approaches, as connected with altered tangent stiffness moduli in large-scale rotational, strain-based and deformative problems (ABAQUS, 2019).

5.3.1 *Numerical model material properties*

According to Melbourne et al. (2007) experimental report, complete comprehensive material properties for the masonry arch multi-rings had yet to be provided. This report tabulated only the mortar and brick compressive strength values. The whole material properties for elastic and

non-linear materials parameters are essential to simulate a realistic masonry arch ring behaviour. Therefore, these properties, parameters, and the missing values were taken from Rots (1997), Hodgson (1996), Elbeskeri (2011) and Zhang et al. (2016) Weekes (1998). These references which include material properties, were selected because they are based on testing which utilized the same mortar mix as the Arch G experiment. Additionally, all the experimental tests conducted at the University of Salford Heavy Structures laboratory were undertaken by the same team and this implies a high level of reliability in the workmanship.

According to section 3.6, the constitutive model was described and explained for the numerical study. However, the brick elements were modelled as purely elastic as in the experimental test they were class A bricks which did not crack during the test. Brick elastic material properties are listed in Table 5-4.

As mentioned in section 3.4.1, cohesive interaction was implemented to simulate the interaction between the brick surface and the full-thickness mortar surfaces, where fracture response behaviour was captured based on the traction-separation behaviour at the unit-mortar interface, as shown in Table 5-5.

Material nonlinearity allows the modelling of plasticity by modifying linearity in the relationship between stress and strain. Two material model criteria are suitable to define the numerical model plastic behaviour, which are Drucker-Prager and Mohr-Coulomb components with cohesion. This offers typical relationships between elasticity and plasticity to develop numerically simulated materials for the full-thickness mortar joints.

The Mohr-Coulomb model material properties for mortar joint elements were taken from previous experimental research studies, which used a similar mortar mix (1:2:9) to that used to build the masonry arch G experiment. The compression mortar values are identical to the experimental mortar compression values, thus, the value of the parameter is valid. The Mohr-Coulomb model plastic material property parameters for the mortar joint are listed in Table 5-6.

Table 5-4: Numerical model elastic material properties.

Units (brick)*		Steel plate		Mortar**		Mortar interfaces***		
E_b	v	E_s	v	E_m	v	k_{nn}	k_{ss}	k_{tt}
16000 N/mm^2	0.15	21000 N/mm^2	0.2	1420 N/mm^2	0.15	90 N/mm^3	40 N/mm^3	40 N/mm^3

* This value is derived from (Melbourne, Wang, Tomor, et al., 2007).
** This value is derived from (Elbeskeri, 2011).
*** This value is derived from (Zhang et al., 2016).

Table 5-5: Brick-mortar interface non-linear material properties.

Compression*	Shear**			Tension**	
σ	G_{II}	c	μ	G_I	f_t
1.86 N/mm^2	0.0125 N/mm	0.40 N/mm^2	0.5	0.012 N/mm	0.26 N/mm^2

* This value is derived from (Melbourne, Wang, Tomor, et al., 2007).
** This value is derived from (Rots, 1997) and (Zhang et al., 2016).

Table 5-6: Mohr-Coulomb model material properties for mortar joints.

	Friction angle ∅*	Dilation angle ψ*	Cohesion C*	Tension cut off **
Mohr-Coulomb model	26.5	11	0.4 N/mm^2	0.26 N/mm^2

* This value is derived from (Rots, 1997).
** This value is derived from (Weekes, 1998).

5.3.2 *Numerical model boundary conditions*

The numerical model was created using the adopted detailed micro-modelling approach to investigate the actual behaviour of the masonry arch ring. The model analysis was carried out in three static steps using quasi-static analyses; the first step was to apply the self-weight of the arch due to the gravity force of 9.81m/s^2. According to the experimental tests, the two abutments of the arch were fixed to a strong floor in the laboratory; Figure 5-6 illustrates the fixed boundary conditions applied to the abutments for the numerical model.

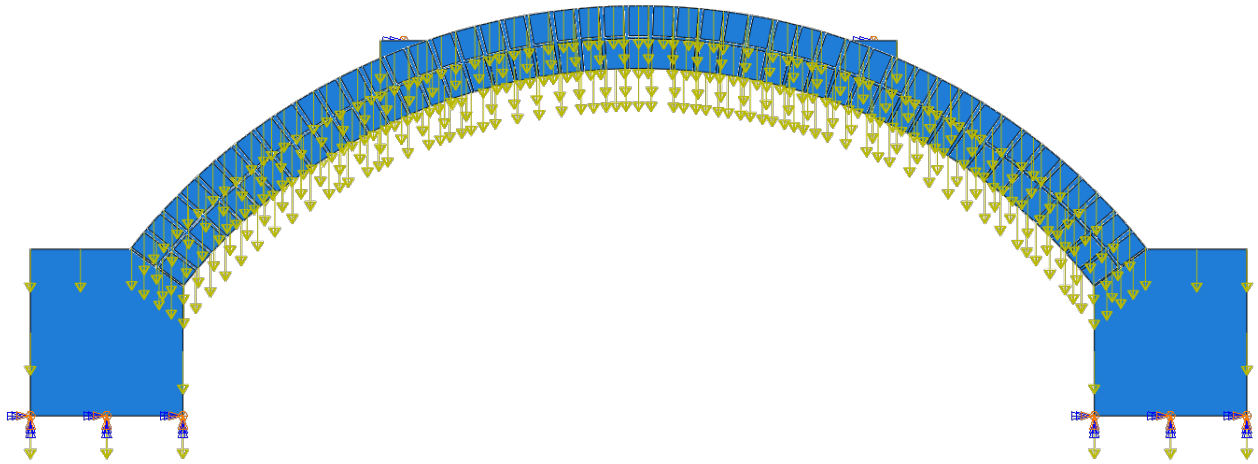

Figure 5-6: Gravity applied on the whole arch model.

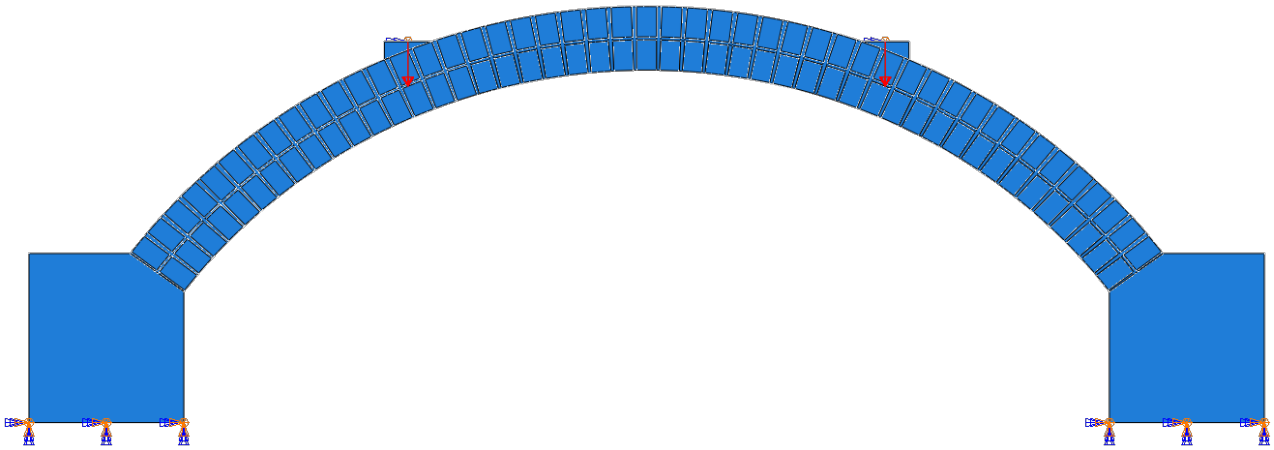

Figure 5-7: Dead Load applied at the quarter and three-quarter span of 10kN each.

The second step was to apply the dead load of 10kN, and Figure 5-7 illustrates this. It also represents the soil backfill as point loads at the quarter and three-quarter spans, in accordance with the experimental test. The third step was applying the live load at the quarter span, as shown in Figure 5-8, which was increased until the masonry arch started to become unstable, and the four-hinge mechanism formed. The live load was uniformly applied on the steel plate along the entire arch width at the quarter span (line load). The live load was applied under displacement control in accordance with the experimental test of arch G.

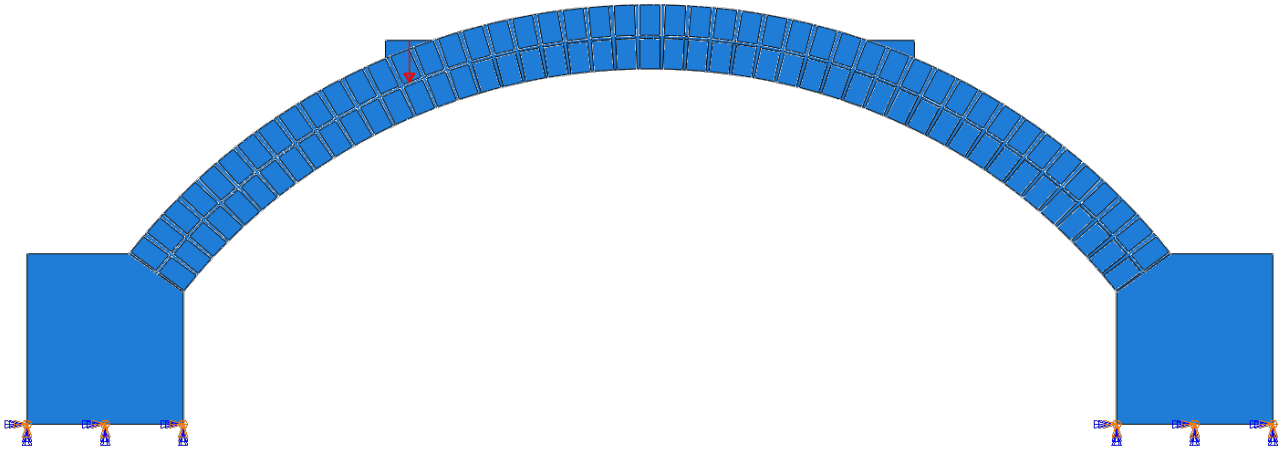

Figure 5-8: Live load applied at the quarter span.

5.3.3 *Numerical model brickwork layout*

This section describes that the arch G numerical model was created twice, each with different brickwork layouts. The purpose of the second layout was to avoid a solution problem which prevented the analysis from completing many runs.

5.3.3.1 First model brickwork layout

The experimental masonry arch test was a two-ring arch, where the top ring was built of 49 bricks and the lower ring of 47 bricks. Therefore, the numerical models were created following the actual arrangement of the experimental masonry arch along the arch length and the arch thickness. The brick-and-mortar joint width elements were modelled as an arch-width continuous element, which reduced the number of elements and nodes for the analysis to a manageable level. Furthermore, the live load was applied as a line load on the entire arch width to mimic the experimental loading arrangement. The mortar joint is shown in Figure 5-9, and the brick unit element is shown in Figure 5-10. Figure 5-11 illustrates the entire numerical model.

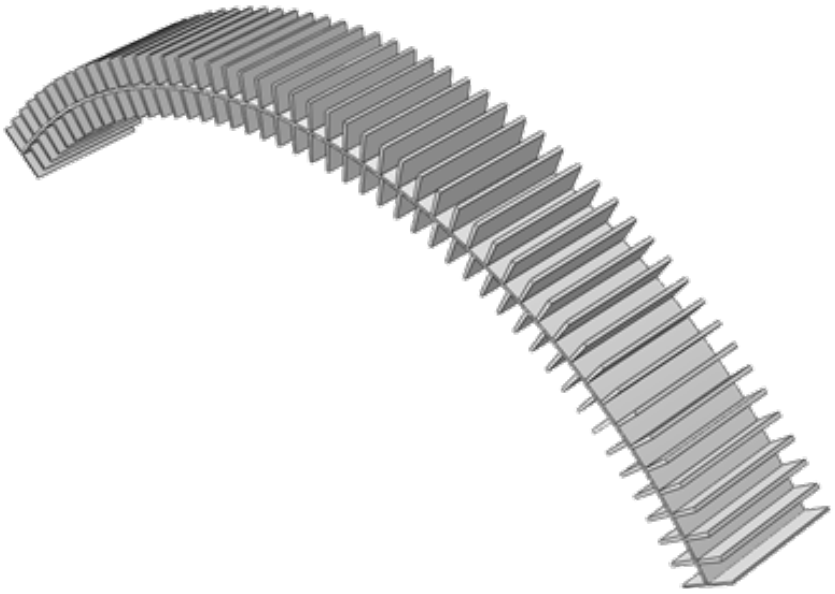

Figure 5-9: 3D mortar Joint element.

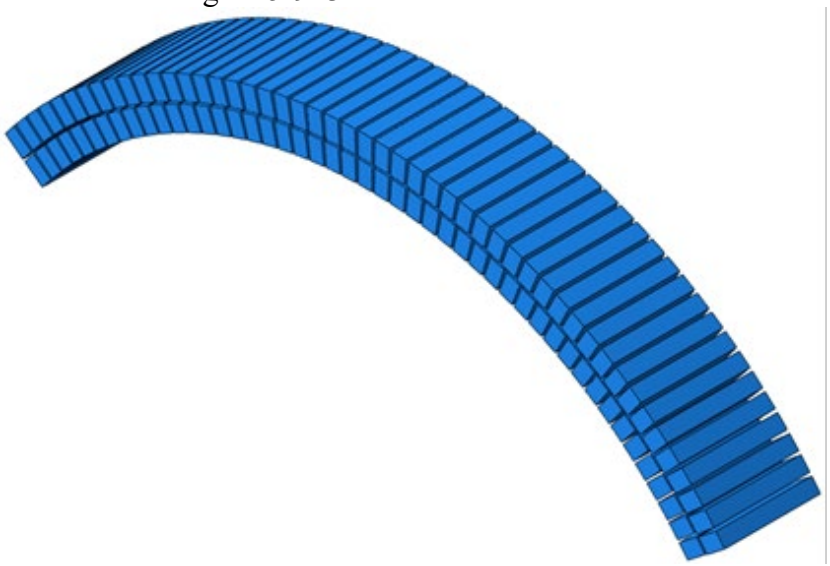

Figure 5-10: 3D brick elements.

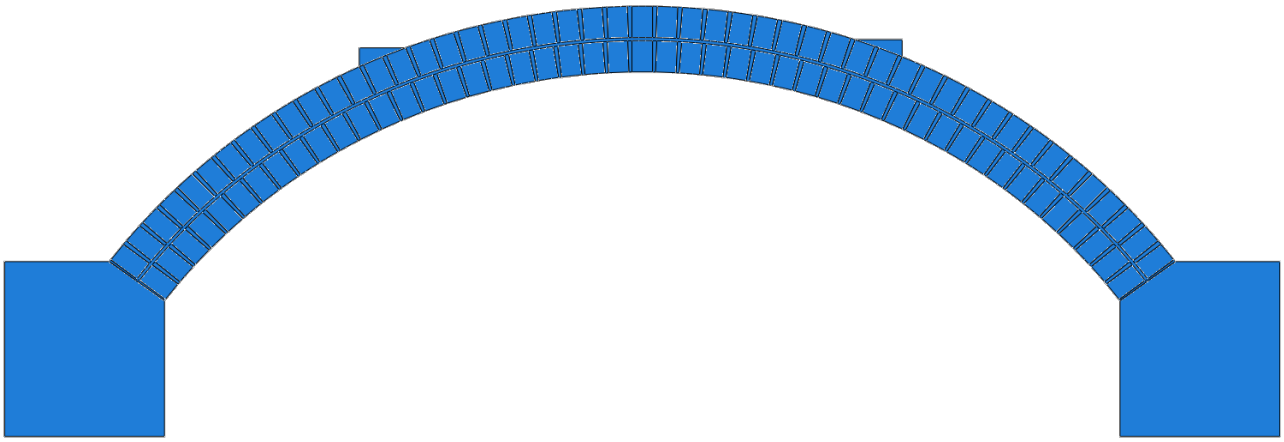

Figure 5-11: First brickwork layout for the numerical Arch G model of 47 and 49 bricks per ring.

The numerical model was analysed with the same geometry as the experimental test masonry arch geometry, boundary conditions and load arrangements, as shown in Figure 5-1. The live load was applied by imposed displacement at the quarter span.

The first crack developed at the arch barrel intrados quarter span under the live load. The crack grew towards the extrados until it reached the mortar joint between the two brick rings, as shown in Figure 5-12. However, the crack did not advance towards the extrados of the arch barrel (some depth of ring must be devoted to transferring compression); thus, the arch barrel did not entirely fail at that particular hinge. After the four-hinge mechanism failure was formed, the arch became much less stiff.

Figure 5-12 (a) shows a plot of STATUSXFEM for the first hinge formed at the quarter span. The red zones indicate complete tension fracture of the mortar. Figure 5-12 (b) indicates where the forces in the arch ring are transferred at the advanced stages of hinges formation. Where shear force exists at the hinge, it must be resisted in the compression zone.

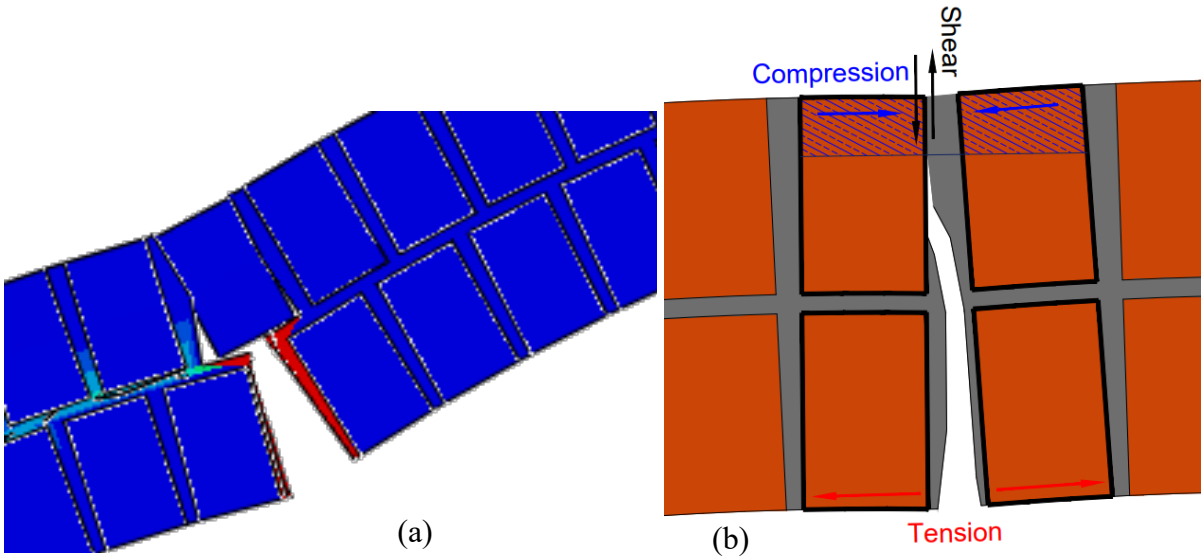

Figure 5-12: First crack formation at the quarter span.

In the experimental masonry arch multi-rings, crack growth was documented as loading progressed. Cracks were observed to grow through the intrados ring mortar joint, step sideways where bricks did not line up and continue to grow through the extrados ring mortar joint (see Figure 5-13).

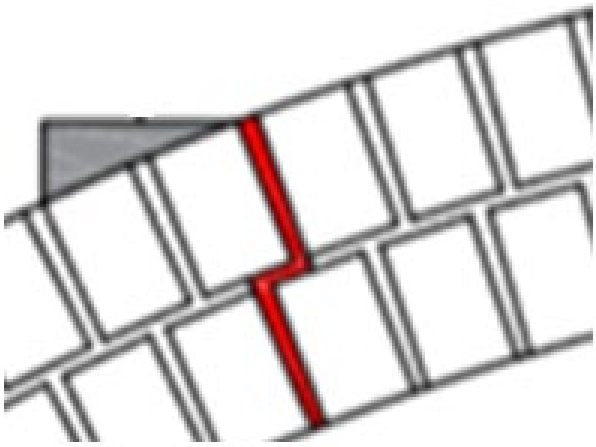

Figure 5-13: Experimental masonry arch crack growth for the first hinge at the quarter span.

The crack growth in the numerical model follows a path determined by the stress resultants. For two reasons, many analysis runs failed to complete due to the crack diverging from the mortar elements. The first reason is that the brick elements are purely elastic in the numerical analysis (as in the experimental test) and is significantly stronger than the mortar, so if the crack passes through the brick element, it will not be representative of the experimental test. The second reason is that when using XFEM to crack the mortar joint, the direction of the crack cannot be controlled or restricted to a predetermined path.

Figure 5-14 and Figure 5-15 illustrate the four-hinge mechanism failure formed. The first hinge developed at the quarter span of the arch barrel under the live load. The crack started at the arch intrados moving towards the mortar ring between the two brick rings. The second hinge occurred at the right-hand springing; there was a crack into the joint with a slip between the brick and the mortar joint. The third hinge occurred above the left-hand springing at the arch extrados. The fourth hinge formed shortly after the third hinge, where the crack started to develop at the arch extrados towards the arch intrados at the three-quarter span of the arch barrel. However, as Figure 5-14 and Figure 5-15 describe, this does not mean that complete four-hinge mechanism failure occurred as the crack in some of the hinges did not fully form. Also, this model's load-deflection results did not satisfactorily agree with the experimental curve results.

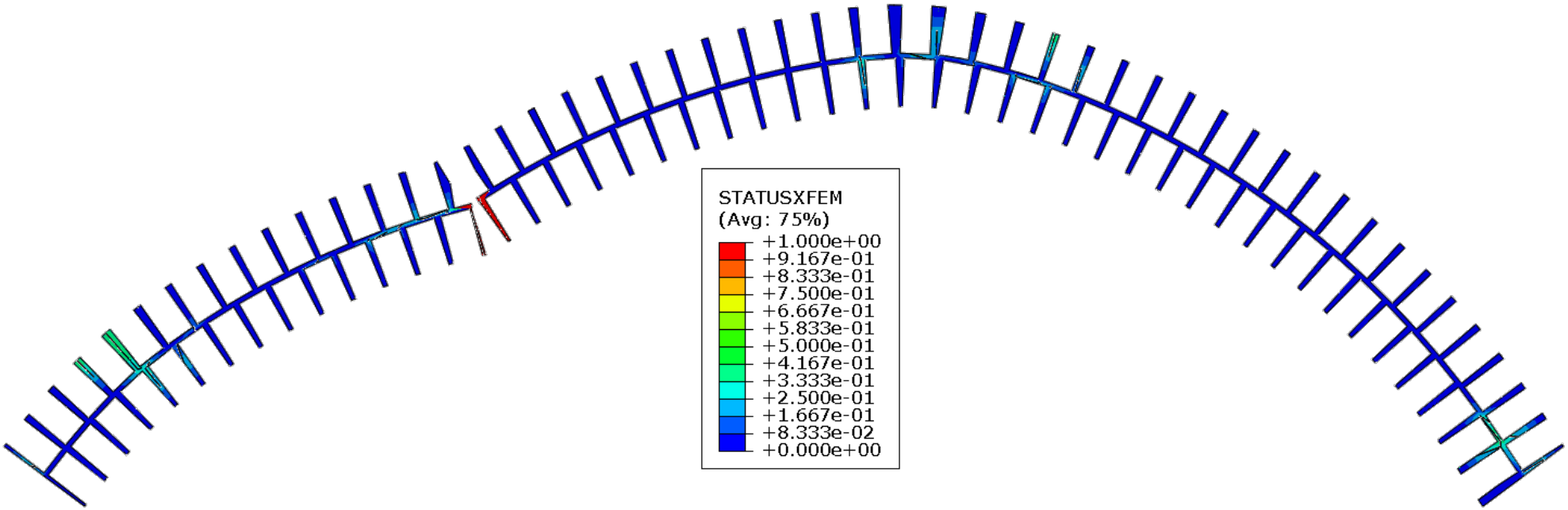

Figure 5-14: Extent of cracking in mortar joint for Arch G first layout.

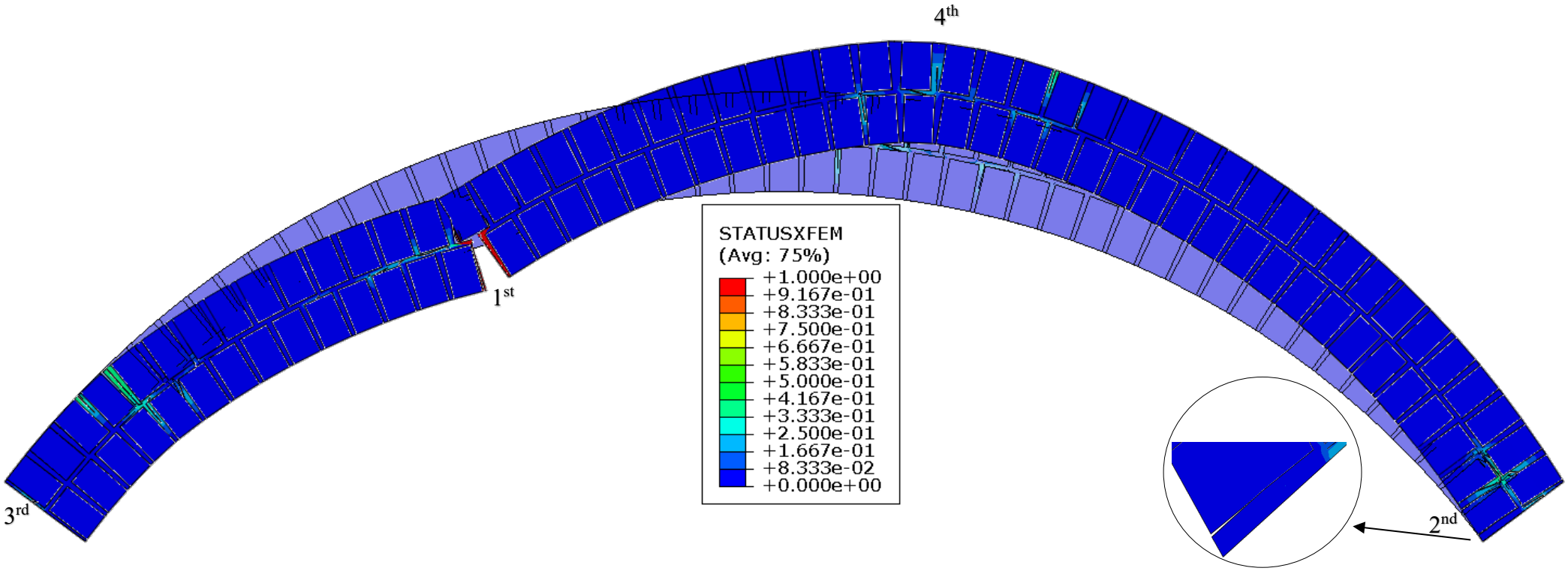

Figure 5-15: Deformed shape of arch first layout showing order of hinge formation, arch brickwork only.

5.3.3.2 Second model brickwork layout

Due to the restriction of cracking direction between the two rings, which cannot be overcome with currently available modelling techniques, another modelling approach had to be undertaken. The new approach had the same geometry (span-to-rise ratio, number of brick elements in the lower ring and the applied loading location) as shown in Figure 5-16.

Unlike the first brickwork layout model in section 5.3.3.1, the mortar elements within the new model are continuous from the lower arch ring to the upper arch ring (radial joints). The brick dimensions remained the same as the experimental masonry arch. However, the radial mortar joint thickness in the upper arch ring is thicker than the actual experimental arch test due to having 47 bricks in both the upper and lower rings.

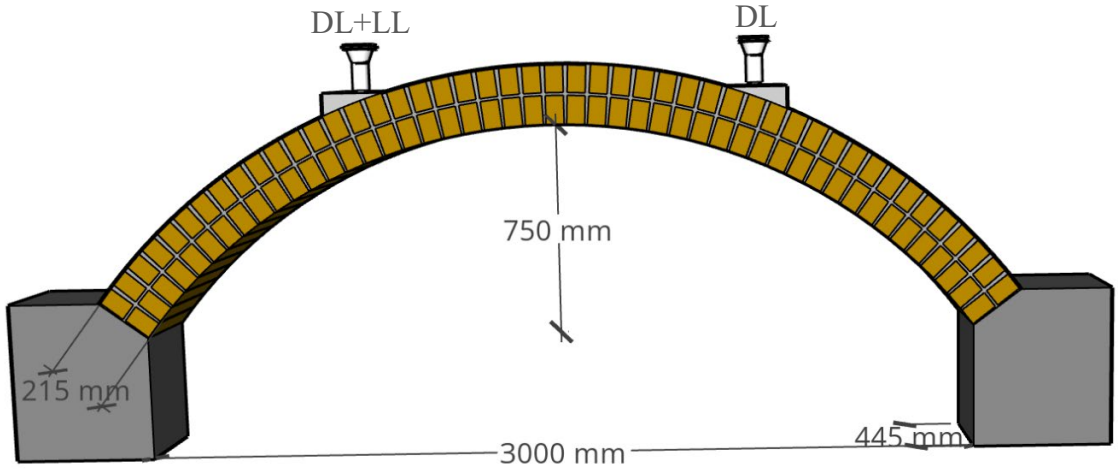

Figure 5-16: The second brickwork layout for the Arch G final numerical model.

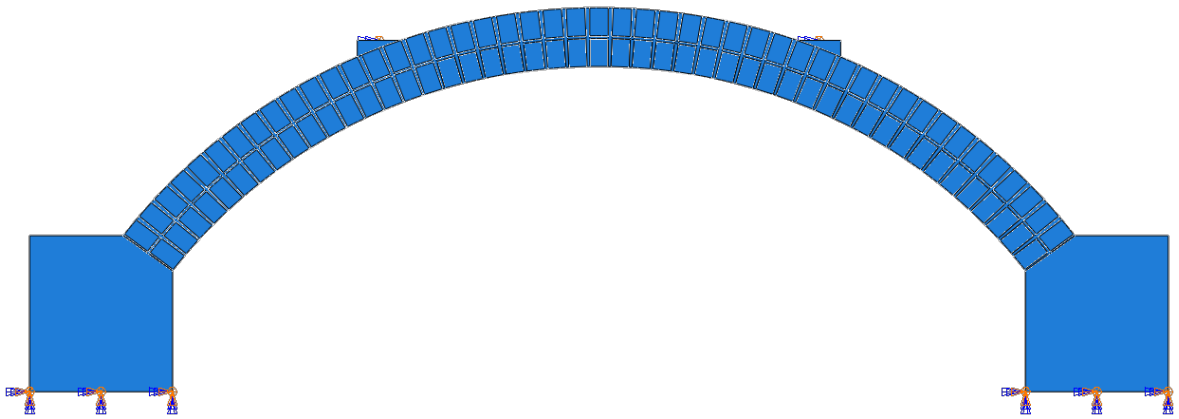

Figure 5-17: Final brickwork layout for the numerical Arch G model.

5.3.4 *Numerical model mesh sensitivity study*

This section provides a study of element mesh size density, which is one of the most critical stages during the progress of the numerical simulation. The element mesh size can influence the accuracy of the numerical model. Also, it affects the computation time required and the occurrence of convergence problems during analysis. Very fine mesh significantly increases the computational simulation time required to obtain the result and may sometimes incorrectly predict structural behaviour. Coarse mesh takes less computational time to simulate the models, but it can lead to unclear results and convergence problems.

A mesh sensitivity study was undertaken to confirm an appropriate mesh size density to simulate the masonry arch models without any convergence problems, in reasonable computational time and produce acceptable structural behaviour results. As ABAQUS has a limited ability to mesh the outer boundaries of a complex element, such as the radial and tangential mortar joints, using pre-established mesh patterns, the mortar was modelled as a single complex geometry element.

ABAQUS software limited the mesh control to one technique called the sweep technique. It was possible to gain more control over mesh density generation by using the structure mesh control technique and a partition toolset to divide the mortar complex element into more regions. This technique leads to a mesh with high-quality elements and an appropriate pattern. Also, this helped to control the mesh in every region in the mortar element to have equal mesh density.

According to ABAQUS, the number of nodes along the slave surface must be equal to, or more than the master surface nodes. The models had equal nodes along master and slave surfaces to minimise computational demand. The model complexity and stiffness matrix size increase with the number of elements and mesh density.

According to ABAQUS documentation terminology, four numerical analyses were conducted as listed in Table 5-7; coarse, normal, fine, and very fine mesh. These are depicted in Figure 5-19. Lower mesh density compared to the coarse mesh did not converge, so will not be considered further in this study.

Table 5-7: Total elements and time required for the masonry arch models.

Mesh type	Total number of elements	Mesh elements	Peak load (kN)	Arch displacement (mm)	Load at 1st hinge formation (kN)	Simulation time (hours)
Coarse mesh	4385	Brick: 1 x 3 x 5 Mortar: 1 x 3 x 5	26.6	1.2	18	6
Normal mesh	12800	Brick: 1 x 6 x 8 Mortar: 1 x 6 x 8	27.7	1.26	21.6	16
Fine mesh	26880	Brick: 2 x 6 x 8 Mortar: 2 x 6 x 8	30.9	1.2	24.2	24
Very fine mesh	45800	Brick: 4 x 6 x 10 Mortar:2x 6 x 10	30.2	1.4	20	30

Figure 5-18 illustrates the load-displacement curves produced using each of the four standard meshes as outlined in Table 5-7. Section 3.8.1 explains the choice of finite element used for this sensitivity study.

In the initial elastic region, the correlation of the very fine and fine mesh with the experiment curve is good. Furthermore, the correlation is not good in the plastic region and has an overshoot. However, finally, it converges to the experimental result asymptotically, so it is acceptable.

The coarse mesh analysis behaved well regarding the elastic and plastic response until 2mm displacement. However, in this analysis the failure mechanism of the masonry arch did not display the correct behaviour.

The normal mesh model responded correctly regarding the four hinge mechanisms and the crack patterns, which will be clarified in section 5.4. The normal mesh model result suggested that it predicted better behaviour in terms of elastic and plastic response. Also, the crack patterns of the model predicted identical results to the experimental masonry arch crack pattern. The required computational time was reasonable for complex non-linear analysis and the computational time required to simulate this model was approximately 16 hours.

Figure 5-18 shows that regardless of mesh density, the peak load occurs at the same displacement, and corresponds to the formation of the fourth hinge. Furthermore, the behaviour in the elastic region was virtually identical for all four mesh densities. However, the ultimate load values of the fine and very fine mesh models were around 16% higher than the experimental, and required significantly longer computational time.

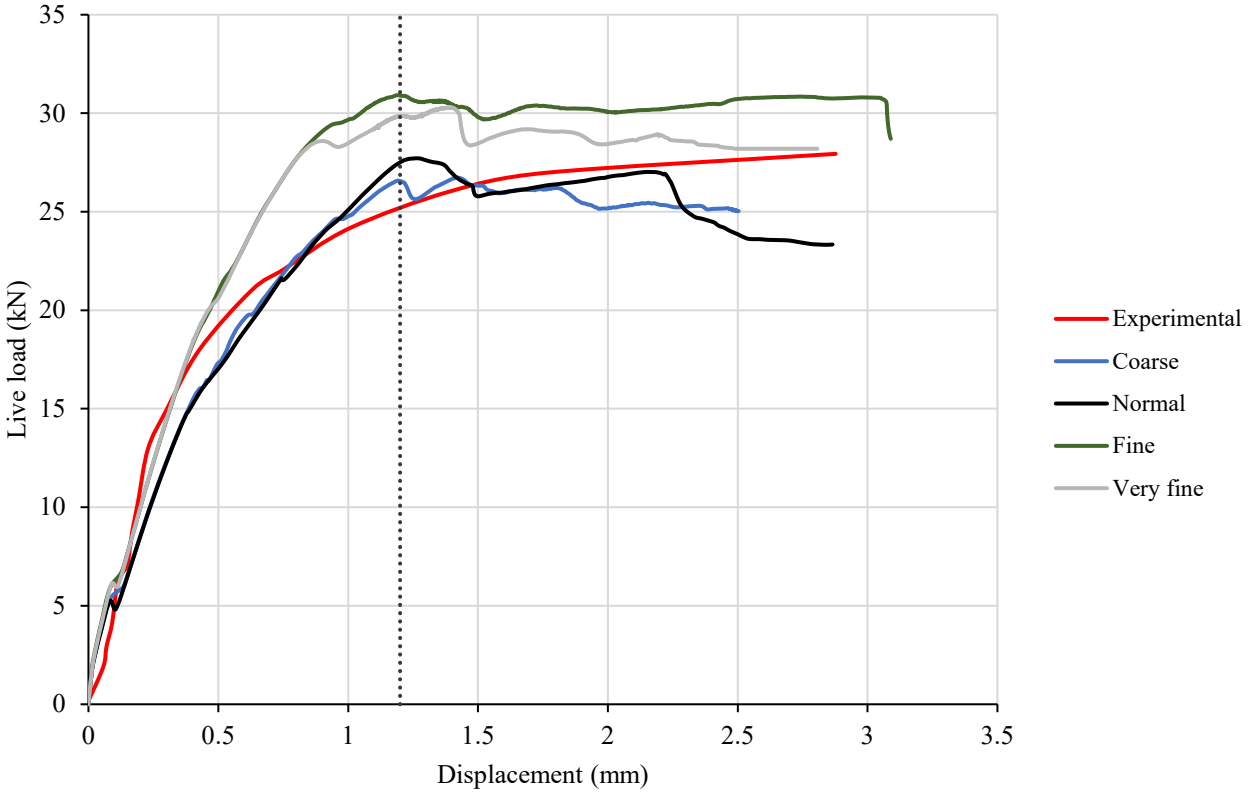

Figure 5-18: Load-displacement behaviour at the arch quarter span for models of varying mesh density.

The ABAQUS normal mesh density was therefore selected for all further numerical simulations because it offers reasonable computational effort, accurate modelling of hinge location, stiffness and peak load.

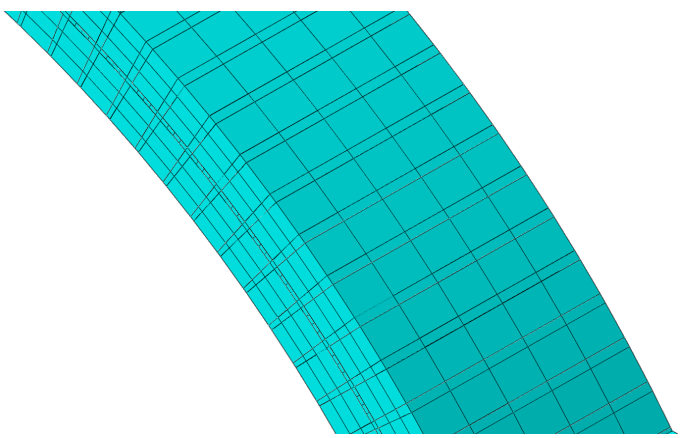

a) Coarse

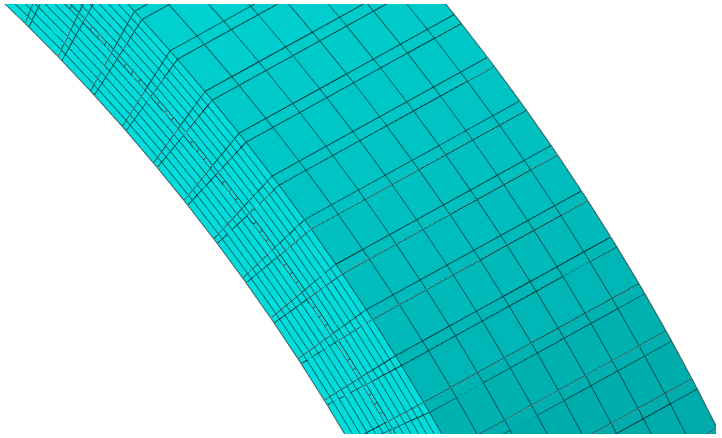

b) Normal

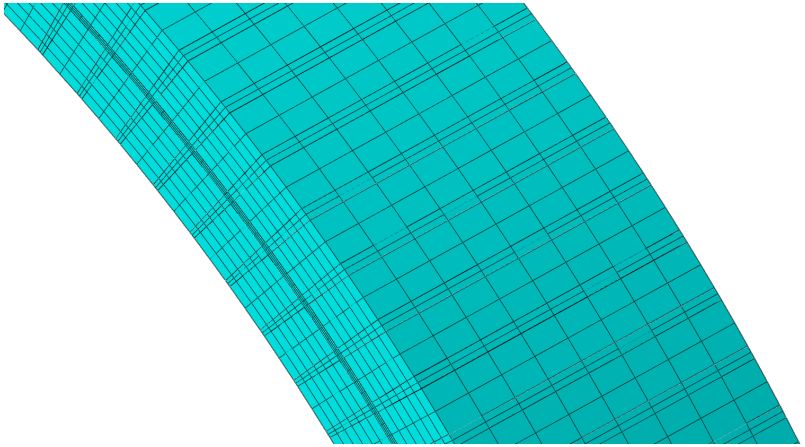

c) Fine

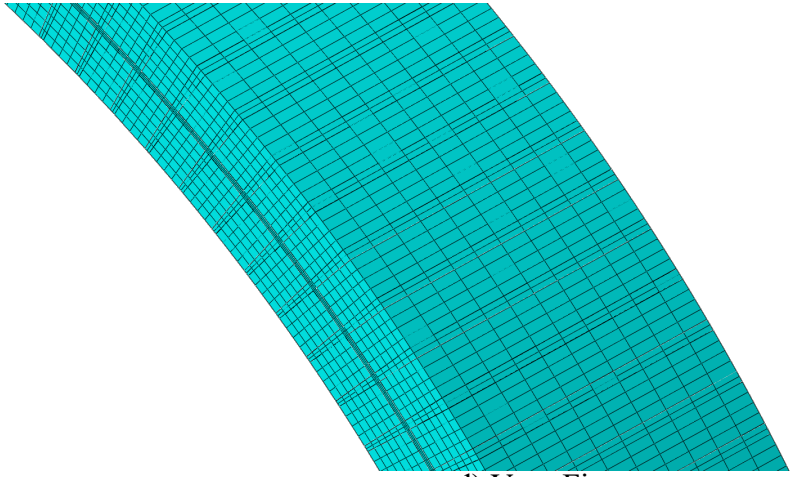

d) Very Fine

Figure 5-19: Masonry arch multi-rings models different meshes.

5.4 Numerical model validation

This section will provide a validation of the numerical model by a comparison with the Arch G results, using experimental load-deflection graphs and load-strain graphs at the quarter and three-quarter spans of the arch barrel. The load-strain graph is used to measure and describe at which load stage the hinges started to form. Also, the crack patterns of the experiment and numerical tests will be compared. One of the novelties of this study is that numerical simulation was undertaken to show the crack through the full-thickness mortar to provide the realistic behaviour of a masonry arch.

As mentioned in section 3.4.2, two ABAQUS output diagrams will be included to identify all cracking modes. Figure 5-20 diagrammatically shows a) shear slip, b) opening crack formed at the unit-mortar interface and c) opening crack formed in the mortar only. Failures a) and b) occur at the interface and can only be shown in ABAQUS output by plotting the Damage variable for cohesive surfaces in General Contact (or function CSDMG), as shown in Figure 5-22. Failure c) occurs within the mortar elements and can only be seen in ABAQUS output by plotting the status of enriched elements using STATUSXFEM, as shown in Figure 5-21. Therefore, both diagrams may be needed to show failure in some hinges.

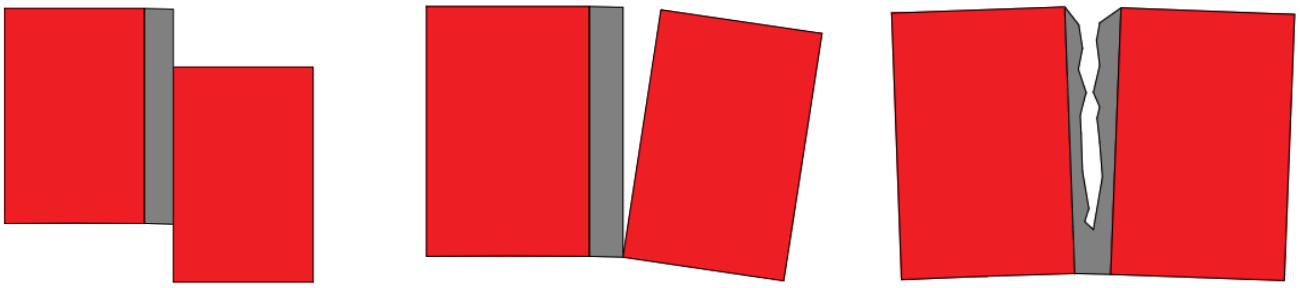

a) Shear slip.

b) Opening crack formed at unit-mortar interface.

c) Opening crack formed in the mortar only.

Figure 5-20: Mortar failure mode diagrams.

Figure 5-21 displays the undamaged STATUSXFEM output of the masonry arch model, indicating that if an element is undamaged, the output value is 0.0. Conversely, a value of 1.0 signifies that the element is completely damaged, meaning the crack cuts through the entire

element, leaving no residual traction forces. An output value between 0.0 and 1.0 indicates the element is partially damaged, signifying that some traction forces remain.

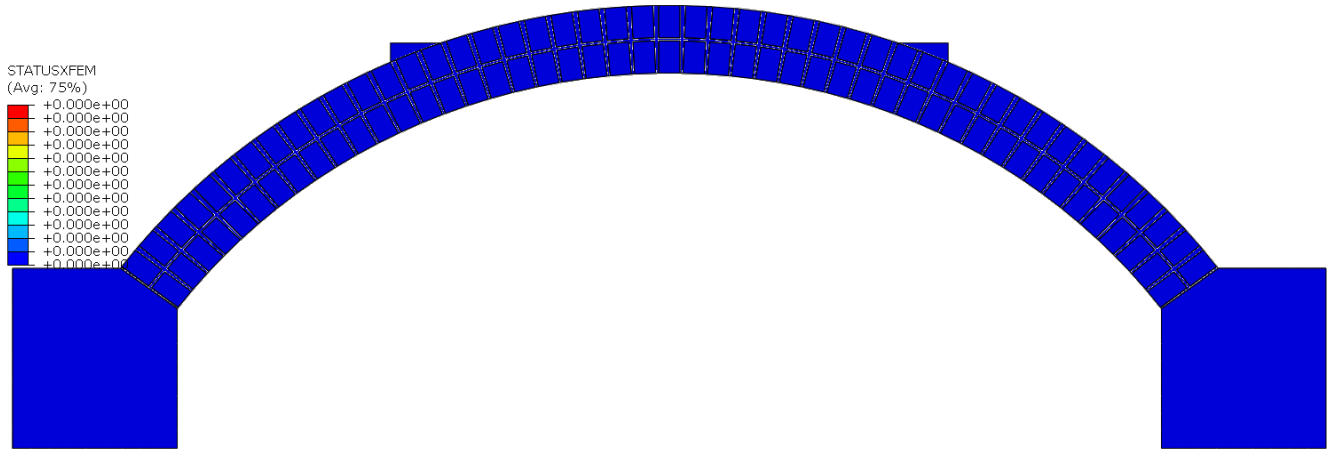

Figure 5-21: STATUSXFEM output showing crack failure in mortar joint.

Figure 5-22 presents the undamaged CSDMG output for the masonry arch model. This output represents the damage variable for cohesive surface interaction, which indicates bond failure at the unit-mortar interface in this study. Through CSDMG, a value of 0.0 signifies no damage, whilst a value of 1.0 indicates a fully developed crack or delamination at the unit-mortar interface.

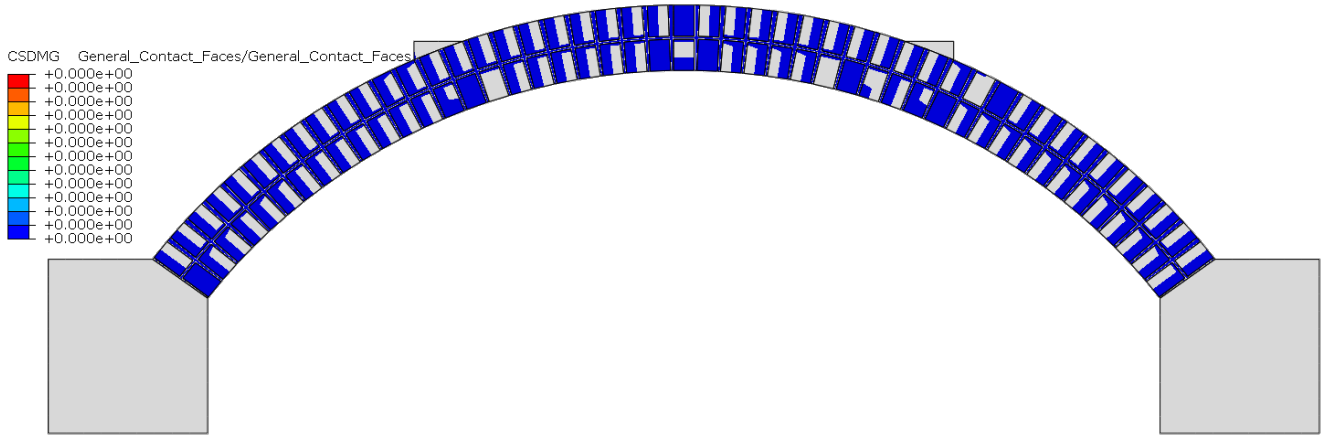

Figure 5-22: CSDMG output showing contact element failure.

5.4.1 *Result and Discussion*

Figure 5-23 illustrates a comparison of the quarter span vertical displacement of the experimental and numerical models.

Figure 5-25 provides the horizontal displacement at the quarter span of the masonry arch. Figure 5-26, illustrates the horizontal displacement of the three-quarter span. As the numerical simulation was undertaken under displacement control, these figures provide a good agreement with the experimental results at both quarter points.

The numerical result curve generally agrees well with the experimental result curve. The initial stiffness for both numerical and experimental curves correlated well until 5kN, when the intrados surface of the mortar joint reached the tensile stress limit at the quarter span, as shown in Figure 5-24. However, this initial crack could not be visually observed during the experimental test, and in the numerical model this crack still did not crack the full-thickness mortar in the Z direction. Once this initial yield point formed and passed the initial elastic region, the load-displacement curves diverged slightly in the rest of the elastic region.

The first hinge developed and reached the mortar joint between the arch's two rings around 21.6kN at the quarter span. The second hinge started developing at the same load, as an opening crack at the interface between the unit and mortar. According to the experimental test, the first hinge was visually observed around 22kN.

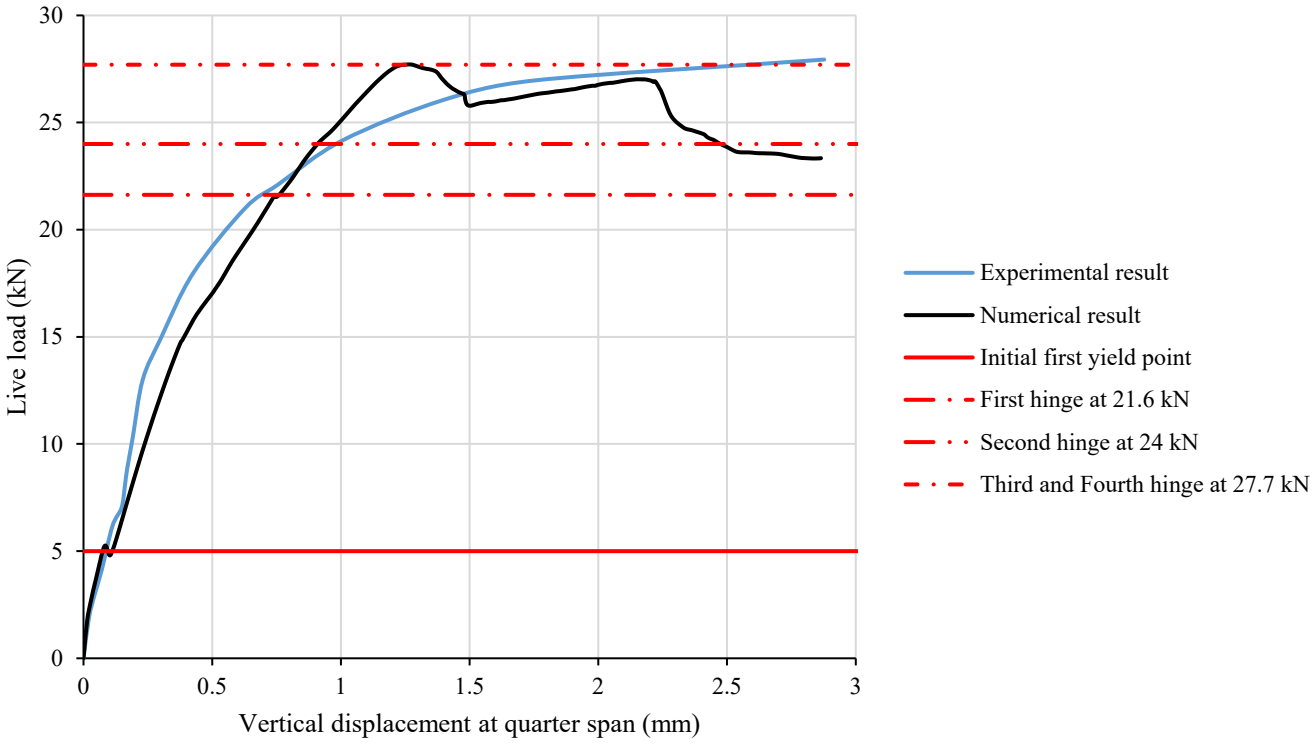

Figure 5-23: Comparison of experimental and numerical model vertical displacement results at the quarter span.

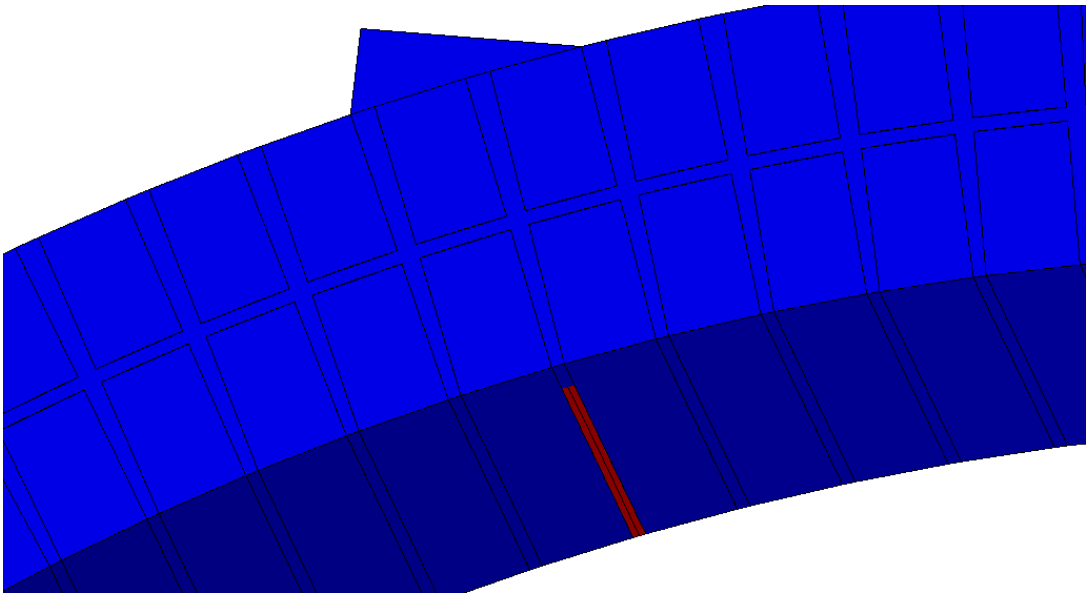

Figure 5-24: Initial first yield point around 5kN.

The first crack occurred under the live load at the quarter span and is due to the tension at the intrados reaching the tensile stress capacity of the mortar, thus the first hinge is formed at this location. Shear failure at this location does not occur because the reduced compression contact

area in the upper ring of bricks is under significant compression, which greatly enhances the shear capacity across the remaining mortar joint. Figure 5-25 and Figure 5-26 display very good agreement regarding the horizontal displacement of the arch for both arch quarters. Furthermore, it can be noticed that there is a change in elastic stiffness around 15kN in both figures, which matches well with the load-strain graph experimental result as shown in Figure 5-4.

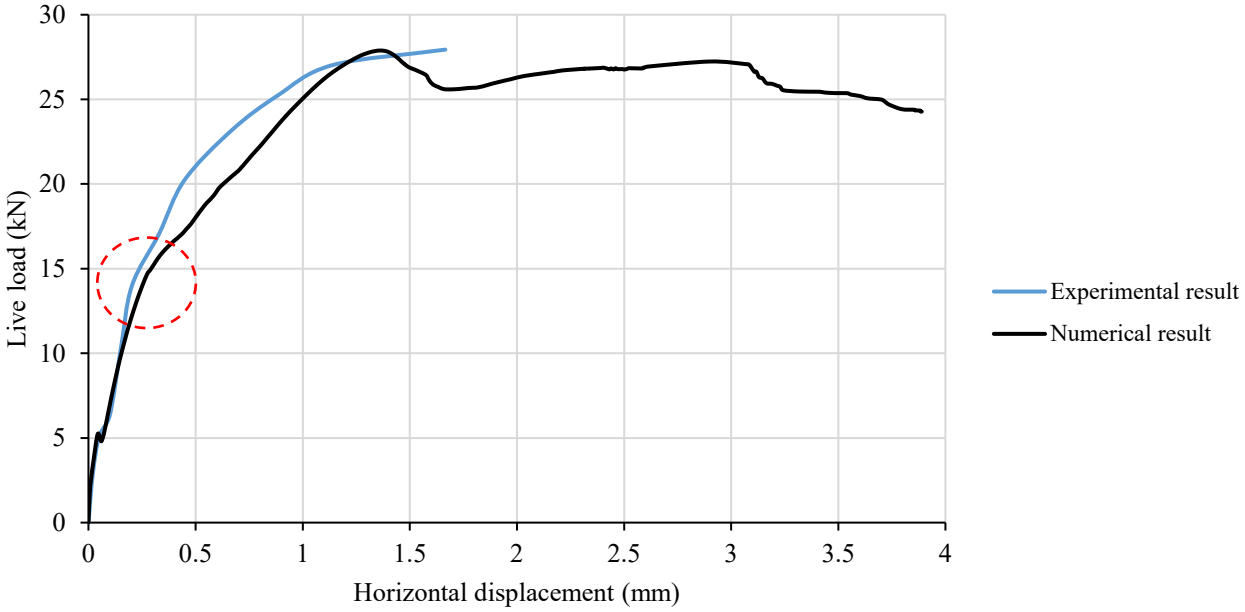

Figure 5-25: Comparison of experimental and numerical model horizontal displacement results at the quarter span.

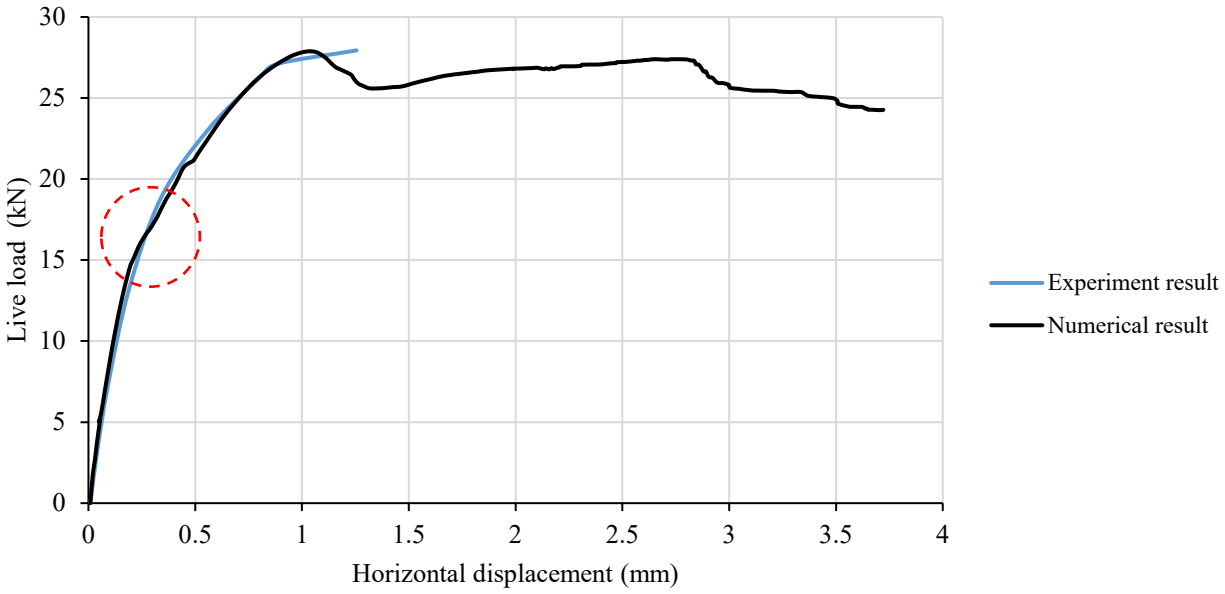

Figure 5-26: Comparison of experimental and numerical model horizontal displacement results at the three-quarter span.

The first hinge to form was at the quarter span intrados, at 21.6kN live load. The second hinge to form was at the right abutment intrados, at 24kN live load. The third hinge to form was at the left abutment extrados, at 27.7kN live load. The fourth hinge to form was at the three-quarter span extrados, at 27.7kN live load.

According to the experimental report, for Arch G the load level at which the second and third hinges formed was not recorded. However, during the test of Arch A (which is the same as Arch G in geometry and load arrangement), the third and fourth hinges formed at the same loading level at 23kN (Melbourne, Wang, Tomor, et al., 2007).

Figure 5-4 shows the results of strain measurements undertaken during the experimental masonry arch (Arch G) test. The gauges were located at the quarter span, where the maximum displacements were also located. Strain gauge A was located at the extrados, and would therefore have suffered little strain; however, strain gauges C and D were located at the intrados and would have experienced excessive strain and probable rotation, which suggest the readings beyond first hinge formation are not useful. Therefore, gauge B readings were selected for comparison with the numerical model, to complement the validation already undertaken.

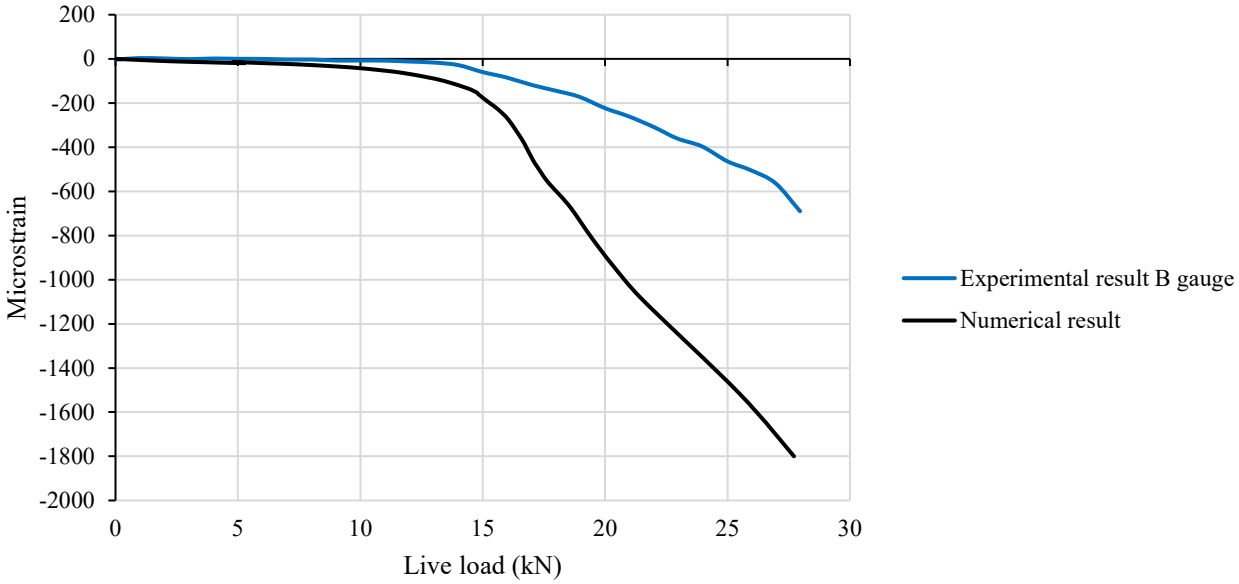

Figure 5-27: Comparison of experimental and numerical model load-strain results at the quarter span.

Figure 5-27 compares the load-strain relationship from the experimental data of gauge B with the outcomes from a numerical model at the quarter span of the arch. Primarily, the load-strain

curves from both sets of results are very similar in behaviour, i.e. an initial elastic response up to first hinge opening at a load of 14kN, with similar stiffnesses. However, after this the curves diverge in terms of stiffness but the overall behaviour remains representative.

Table 5-8 compares experimental and numerical crack history, indicating good matching in the live load values of both results. However, the experimental live load values of the second and third hinges to form were not recorded. As explained in section 5.3.3.2, the Arch G model extrados geometry has been modified to make the mortar joint radial due to XFEM not cracking the stepped joint. Due to this reason, the crack locations for the extrados are not similar to the experimental. However, the first hinge locations at the extrados for the numerical model is similar to the experimental first hinge location.

Table 5-8: Comparison of the experimental and numerical results cracks history.

	Experimental			Numerical		
Hinge	Live load (kN)	Crack location–brick number		Live load (kN)	Crack location	
		Intrados	Extrados		Intrados	Extrados
Fist hinge	22	14/15	16/17	21.6	14/15	15/16
Second hinge	Not available	0/1	0/1	24	47	47
Third hinge	Not available	47	49	27.7	1/2	1/2
Fourth hinge	28	27/28; 29/30	28/29; 30/31	27.7	27/28	27/28;28/29

Figure 5-28 indicates a comparison of the locations in the experimental and numerical tests. The first, second, and fourth hinges are formed at the same locations as the experiment masonry arch. However, the third hinge was between bricks 1 and 2 at the extrados instead of being the left abutment and brick 1. As a result, there is a good agreement in the crack pattern locations. However, the second and third hinge locations, it can be seen there is a difference in the locations. In the experimental test the second hinge formed at the left abutment and the third hinge formed at the right abutment, but in the numerical the second hinge formed at the right abutment and the third hinge formed the left abutment.

Zhang et al. (2016) report that in their numerical model the second hinge formed at the right abutment, and the third hinge formed at the left abutment. The differences between the numerical simulation in the research and the experimental test results are due to the cracks which were unable to be seen visually. Furthermore, during the masonry arch experimental test, the second and third hinges did not record the load level.

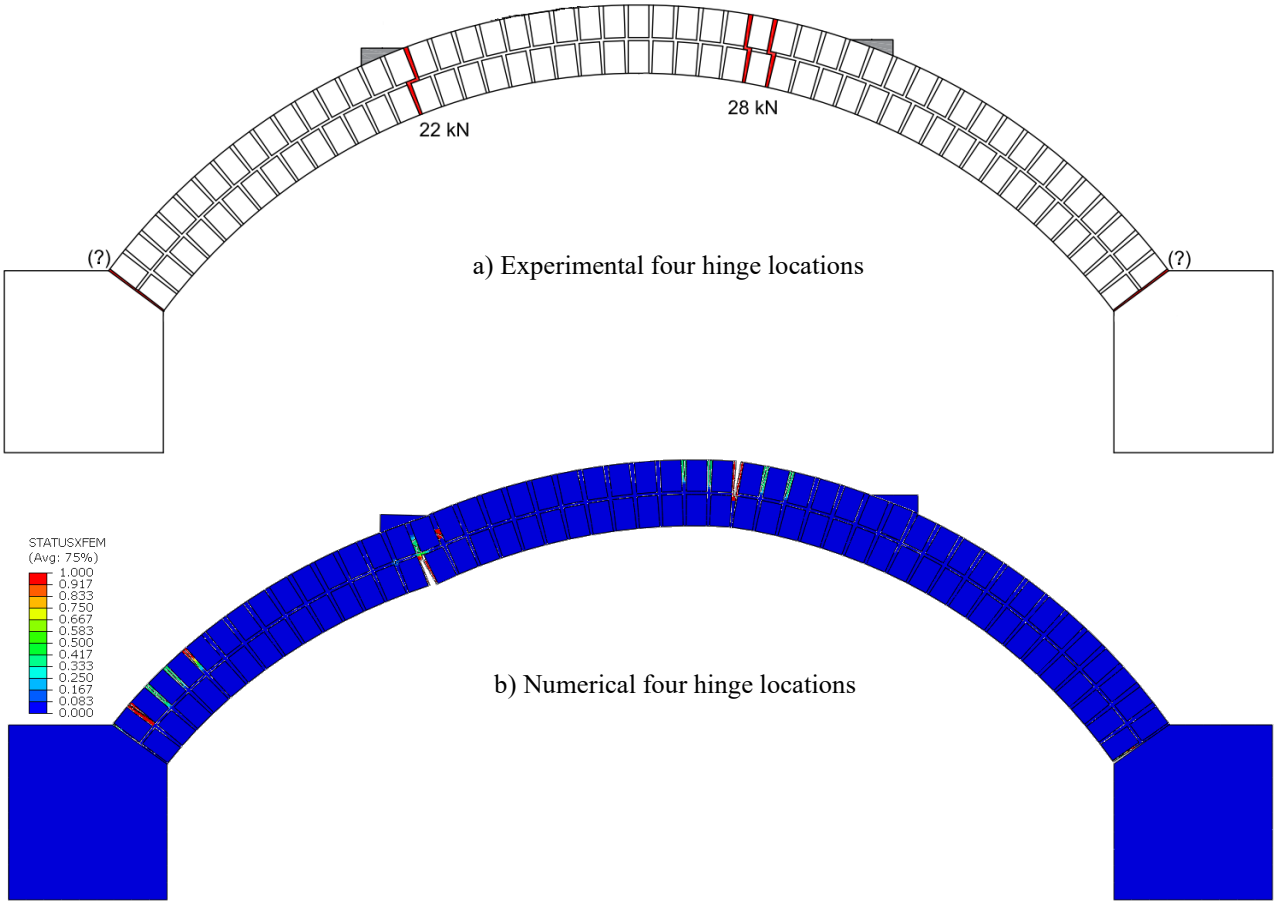

Figure 5-28: Experimental and numerical crack patterns comparison.

In comparing the two radial jointed and step jointed models, as explained in section 5.3.3.1, it is clear that there was no real difference in the crack locations and final collapsed mechanism. However, in the radial joint model, the crack developments at the four hinges are more complete. In the step jointed model, the cracking did not fully form due to crack direction limitations in ABAQUS and Figure 5-29 provides the mortar element with the entire four hinges formed, which shows a plot of STATUSXFEM for all four hinges formed. The red zones indicate complete tension fracture of the mortar.

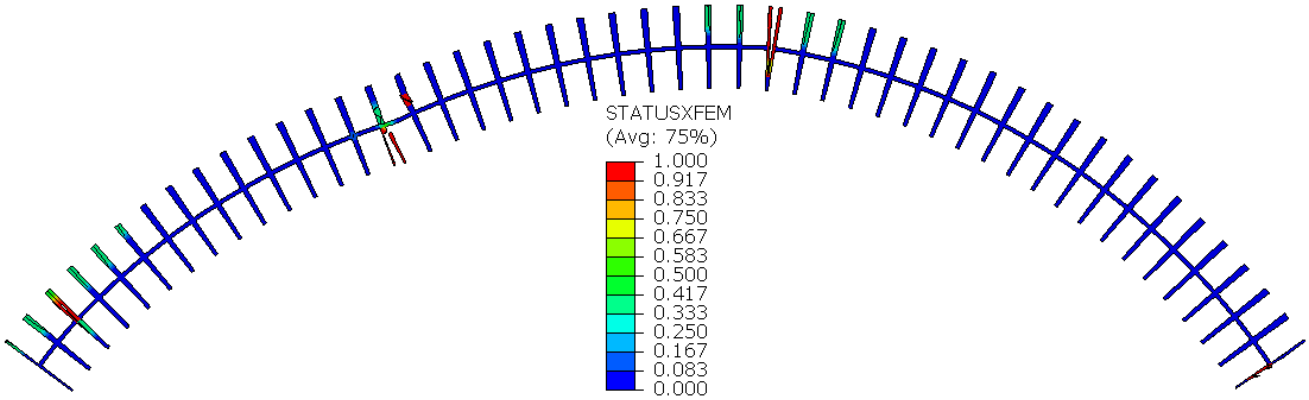

Figure 5-29: Cracked Arch G mortar ring deformed shape.

Once the four hinges of the collapse mechanism had formed, significant numbers of cracks formed around the three-quarter span hinge and left support (the green colour zones), which contributed to a significant drop in stiffness as collapse approached. Also, these cracks could not be seen visually in the numerical model as they were not substantial cracks as ABAQUS presented them in (green colour).

Throughout the numerical modelling, ring separation was observed in the circumferential mortar joint between the upper and lower arch rings, next to the first hinge, as shown in Figure 5-30. Increased longitudinal shear stresses can start to be identified after the first radial crack forms at the quarter span.

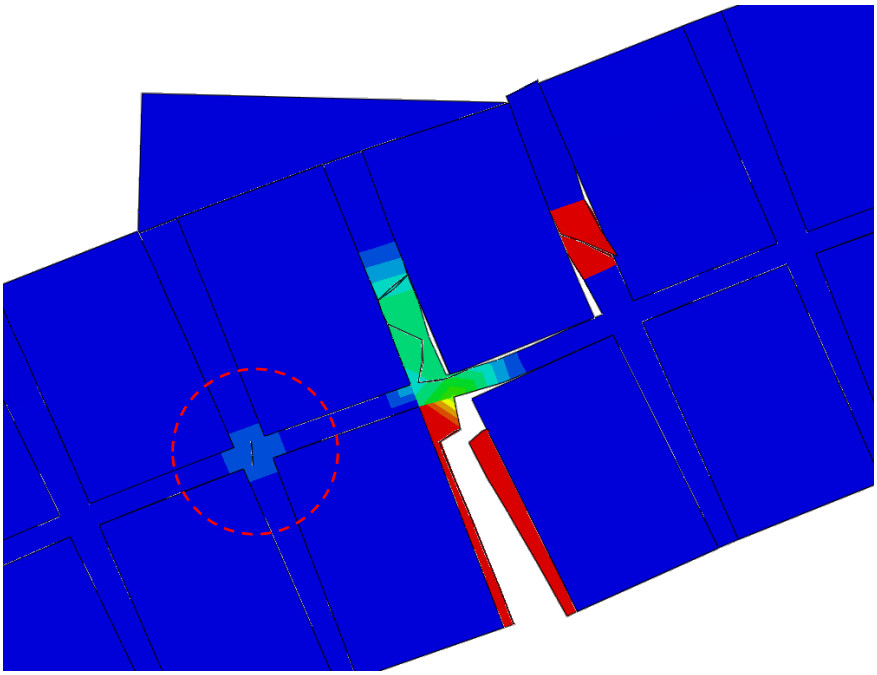

Figure 5-30: Arch G model ring separation.

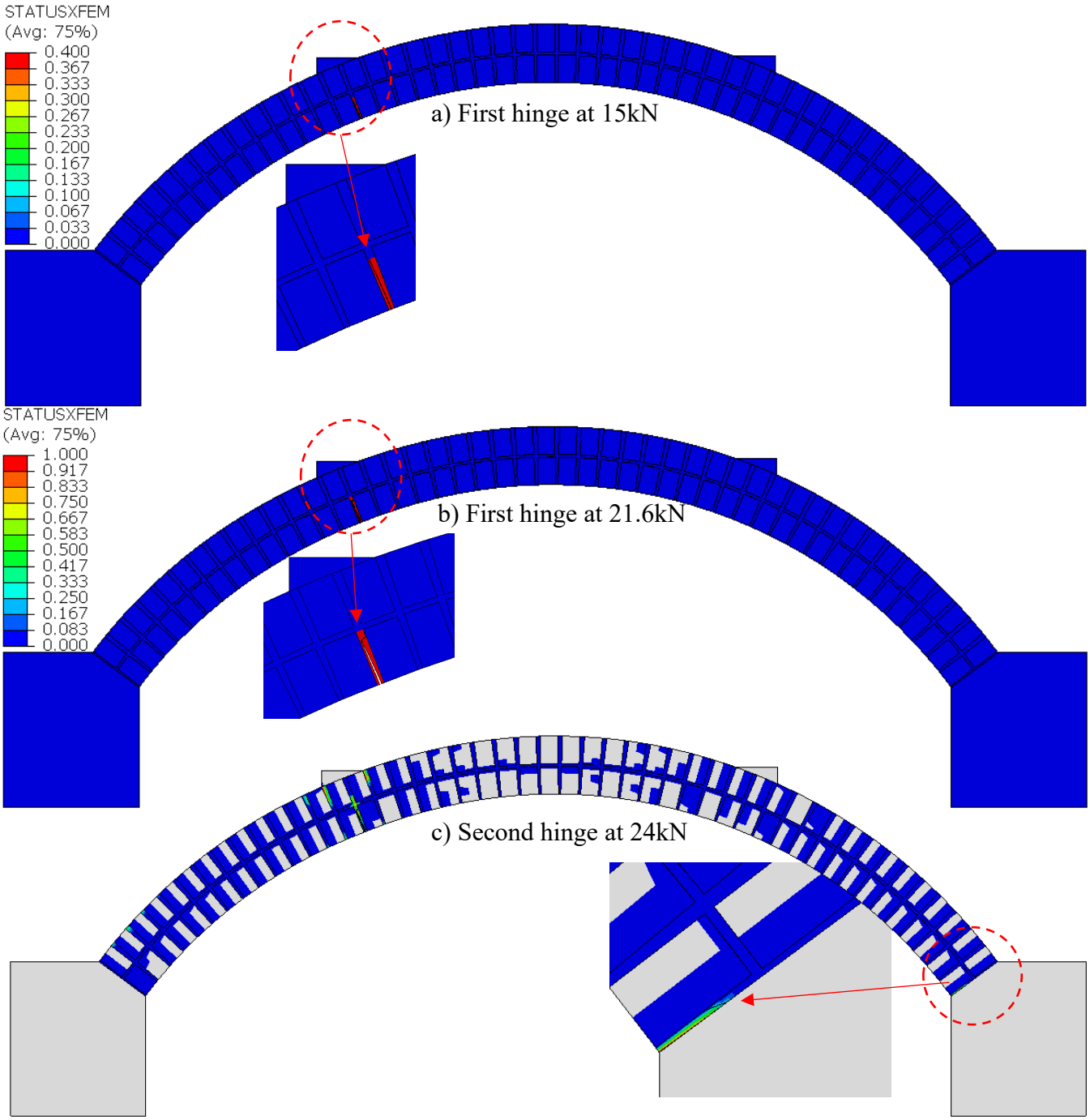

Figure 5-31: Deformed shapes of first and second cracks.

Figure 5-31 (a) displays the first hinge at 15kN, which influenced the arch's stiffness and can be noticed in the load-displacement figures at the quarter and three-quarter arch span. Figure 5-31 (b) shows the first hinge fully formed at 21.6kN (visually observed only around 22kN in the experimental test) without any other cracks in the arch barrel. However, the second hinge started as an opening crack between the unit and mortar surfaces due to cohesive interaction failure before the crack occurred in the mortar element, as shown in Figure 5-31 (c), and

occurred numerically at 24kN. The experimental test report had no record of the load level for this hinge formation.

Figure 5-33 displays the failure of the unit-mortar interface at maximum displacement, which notably includes slip failure at bricks remote from the hinge locations. Figure 5-34 displays the arch deformed shape when the four-hinge mechanism had formed at 27.7kN.

Figure 5-32 shows the deformed shape of the third and fourth cracks at the left abutment and the three-quarter span arch. Also, the cracks are coloured red and the STATUSXFEM factor reached 1.0, which means the entire width of the ring was completely cracked.

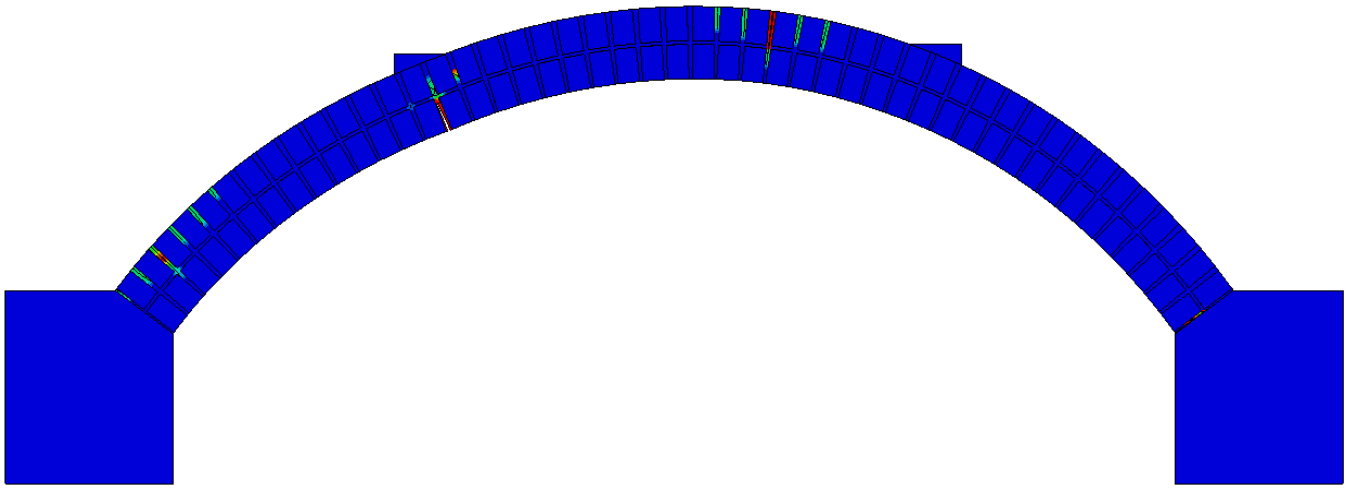

Figure 5-32: Deformed shape of third and fourth hinges.

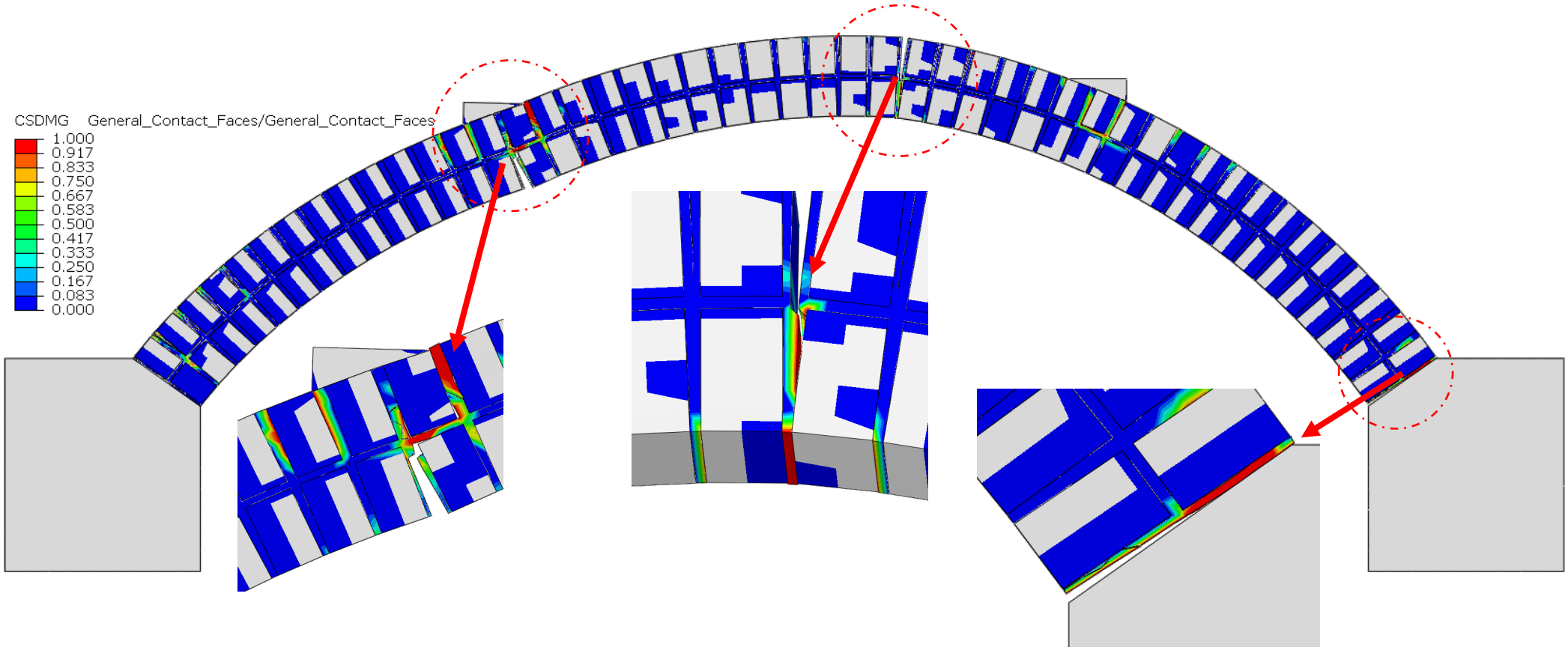

Figure 5-33: Unit-mortar interfaces failure at maximum displacement.

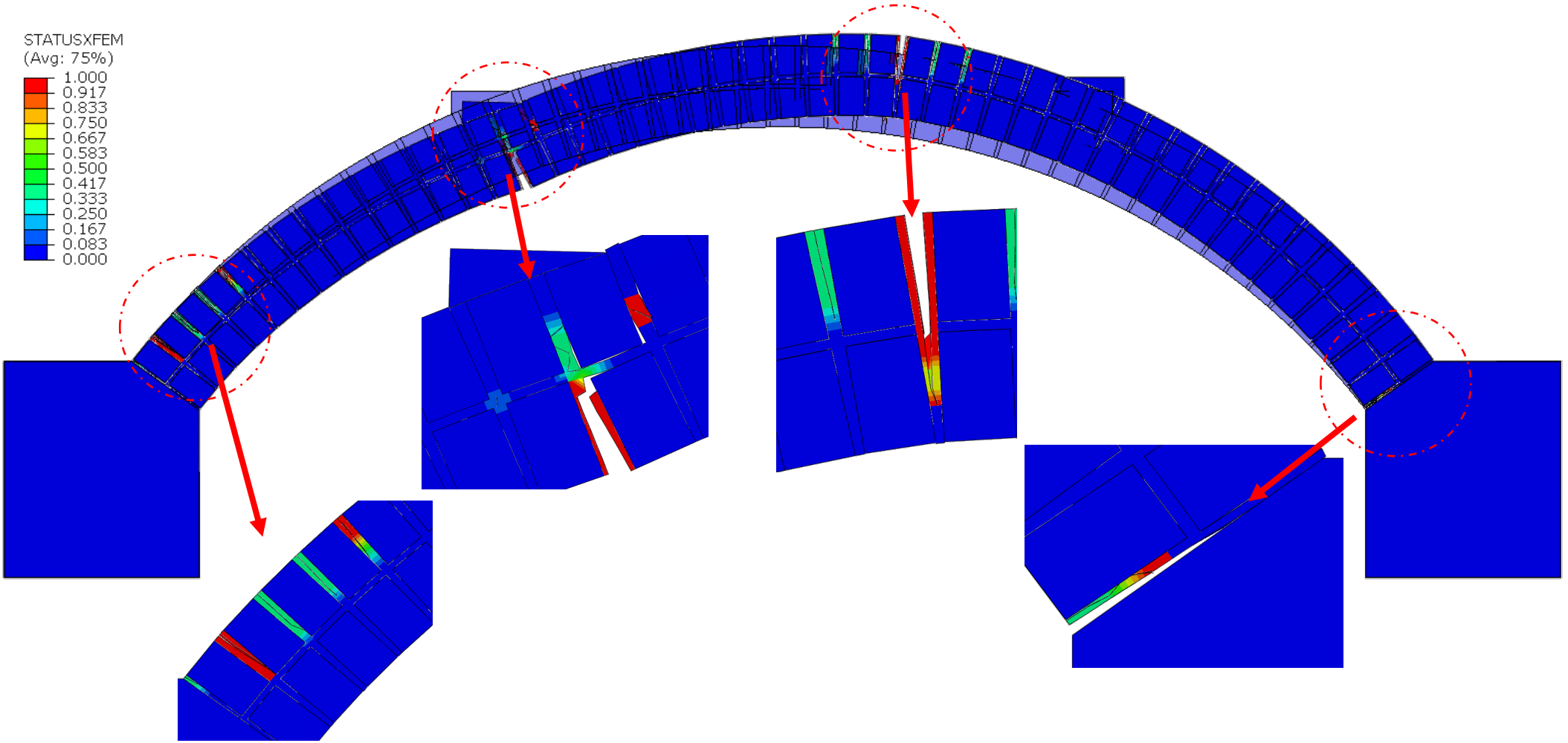

Figure 5-34: Arch G numerical model deformed shape for at maximum displacement.

5.5 Material properties parametric studies

The validated Arch G model is investigated with the same loading agreement and boundary condition as clarified in section 5.2 to study the critical material property effects. As discussed in section 5.3.1, the masonry arch experimental report did not include the mortar material properties. For the numerical model, the mortar properties were chosen from previous research studies, where a similar mortar mix was investigated (Rots, 1997).

As noted in section 5.4, the experimental and numerical results comparison showed a good correlation regarding the failure mechanisms, the crack patterns of both results, and the load-displacement relationship. A range of material parameters were required by ABAQUS to develop an idealised and realistic behaviour of the numerical masonry arch.

This section contains a series of material property parametric studies to determine whether the validated model has an adequate range of applicability. The effect of varying material property values was assessed by comparing the load-displacement graphs with the experimental data.

A set of numerical models were created for this purpose. In subsequent sections, the values and results are discussed, focusing on the influence of different material properties: tension fracture energy G_I, the mortar tensile strength f_t, the mortar Young's modulus of elasticity E_b, and mortar plasticity using Drucker-Prager criteria.

In this section, the figures show the change of peak load variation ΔL and the initial elastic stiffness ΔK. These were used for the numerical and experimental values to be calculated as follows:

$$\Delta L = \frac{L_1 - L_2}{L_2}$$

Where:

ΔL: peak load variation.

L_1: numerical peak load.

L_2: experimental peak load.

$$\Delta K = \frac{K_1 - K_2}{K_2}$$

Where:

ΔK: initial elastic stiffness variation.

K_1: numerical initial elastic stiffness.

K_2: experimental initial elastic stiffness.

5.5.1 *Fracture energy G_f*

This section provides the numerical investigation of varying the value of fracture energy; Figure 5-35 compares the experimental result and the numerical model's result through a load-displacement graph of vertical displacement at the quarter span. The value of fracture energy, G_f, was input as 0.005, 0.012 and 0.12 N/mm in separate models. Figure 5-35 shows that variation in fracture energy had little influence on the load at the first crack during the initial linear response of the numerical models. In conclusion, all the curves during that stage of the first hinge formation had the same stiffness. The lowest value of fracture energy corresponded to the lowest peak load value. In contrast, the highest value of fracture energy corresponded to the highest peak load value, being 25% higher than the experimental value.

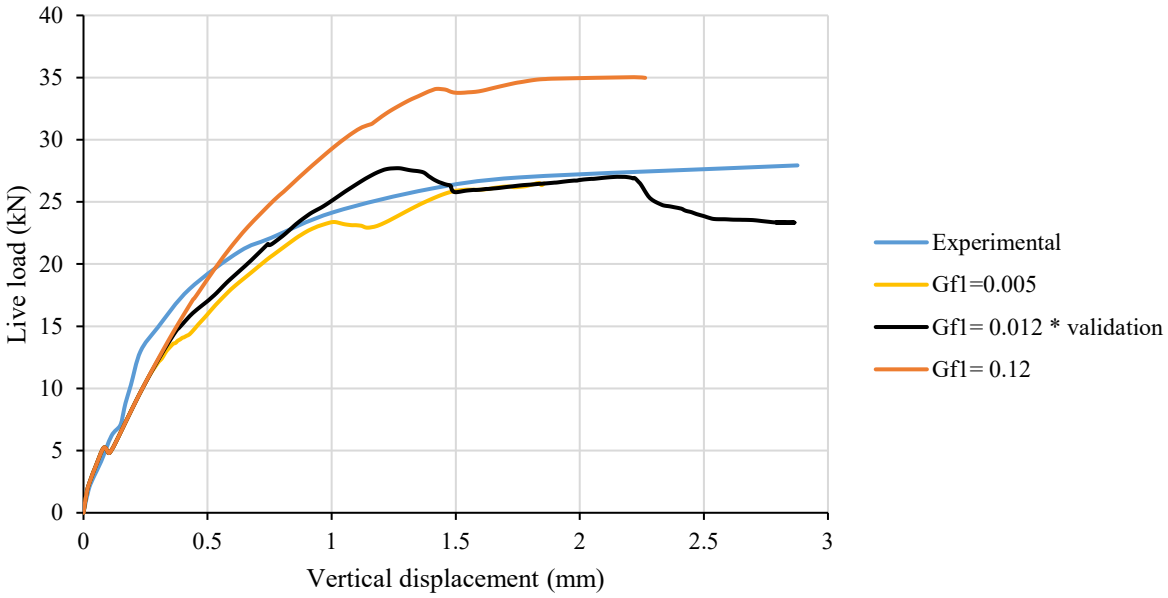

Figure 5-35: Load-displacement at quarter span to establish effect of fracture energy on behaviour.

Figure 5-36 and Figure 5-37 quantify the effect of varying the value of fracture energy on the peak load and initial stiffness of the numerical models, in comparison to the experimental test.

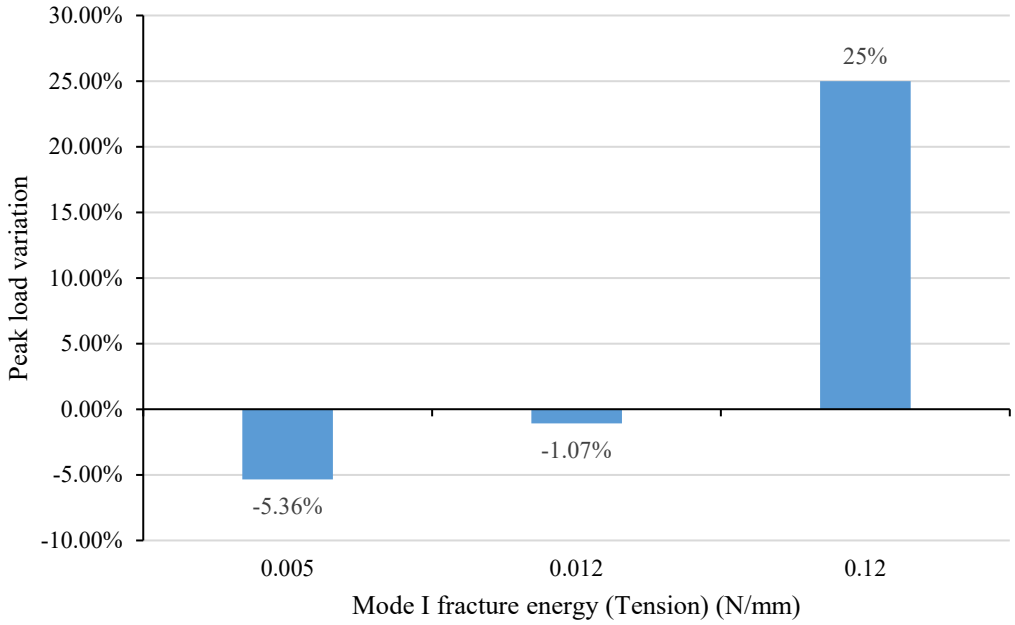

Figure 5-36: Mode I fracture energy effect on the masonry arch's peak load.

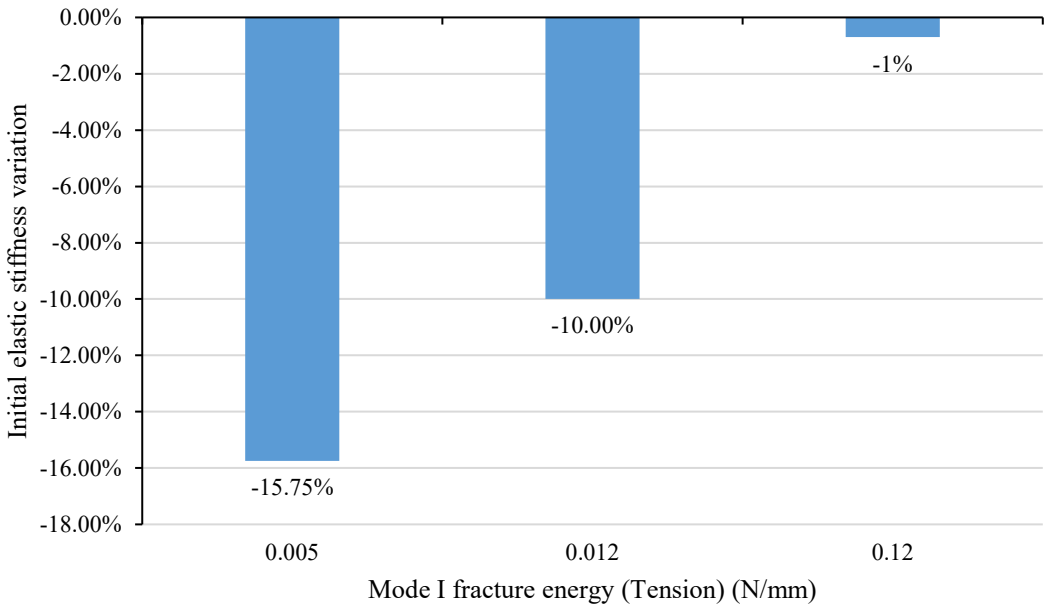

Figure 5-37: Mode I fracture energy effect on the masonry arch's elastic stiffness.

Similar numerical research on the same experimental masonry arch, conducted by Zhang et al. (2016), initially used a fracture energy value of 0.12 N/mm, which was incorrectly converted from J/m^2 based on values obtained from Rots (1997). However, this error was rectified in a subsequent publication by Grosman et al. (2021), where the correct values were used in the same numerical model as initially simulated by Zhang by the incorrect value.

Peak loads obtained by Zhang matched the experimental values but the model did not include full-thickness mortar (this is the only real difference in terms of arch barrel, between the models). Therefore, the effect of including fracture energy was minimal. The effect of overestimating the fracture energy by a factor of ten in this model produced a 25% overestimate of peak load.

5.5.2 *Tensile strength f_t*

To investigate the effect of varying the tensile strength of mortar three models were created with values of f_t input as 0.02, 0.26 and 0.5 N/mm^2 to represent varying from weak to strong mortar. Figure 5-38 compares the experimental and numerical model results using the load-displacement behaviour response of the arch at the quarter span.

As the mortar tensile strength controls the load at the first crack, Figure 5-38 shows small differences in the load at the first crack, after which the load-displacement curves diverge. The lowest value of f_t underestimates the peak load by about 20%, and the highest value of f_t overestimates the peak load by about 45%, as shown in Figure 5-39.

The initial elastic stiffness in Figure 5-40 shows that tensile strength has a direct effect on stiffness. In addition, the numerical result of the value of f_t 0.26MPa offers the best numerical representation but still high compared to the peak load variation in Figure 5-39.

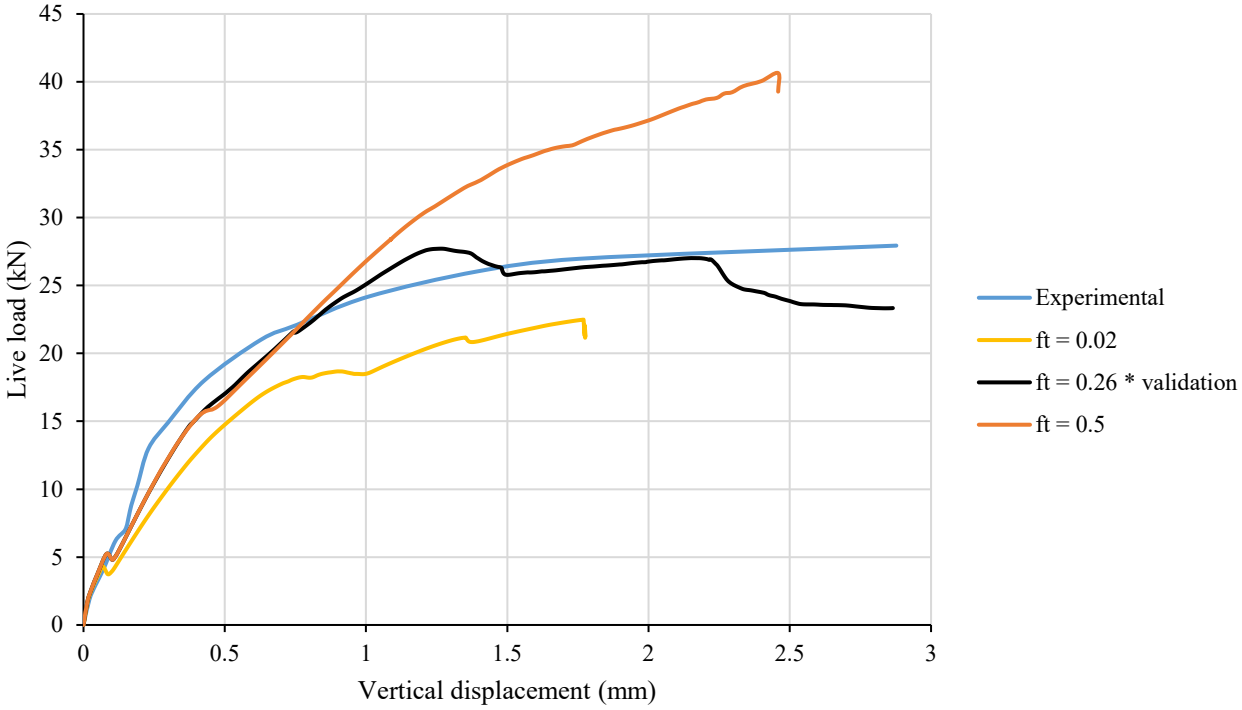

Figure 5-38: Load-displacement at quarter span to establish effect of tensile strength on behaviour.

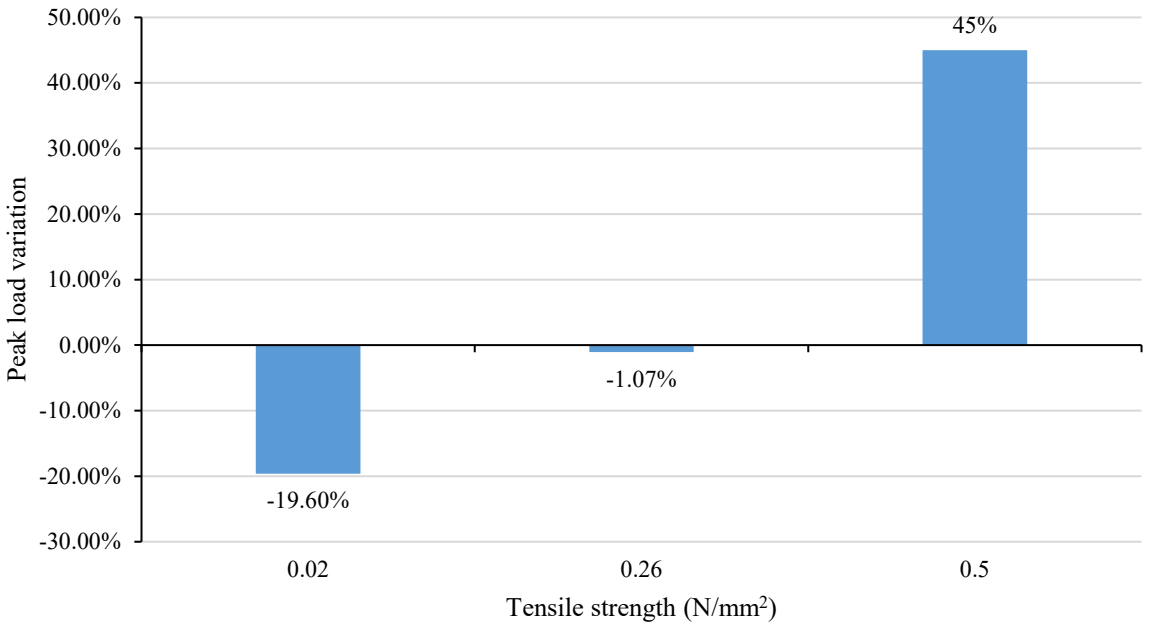

Figure 5-39: Tensile strength effect on the masonry arch's peak load.

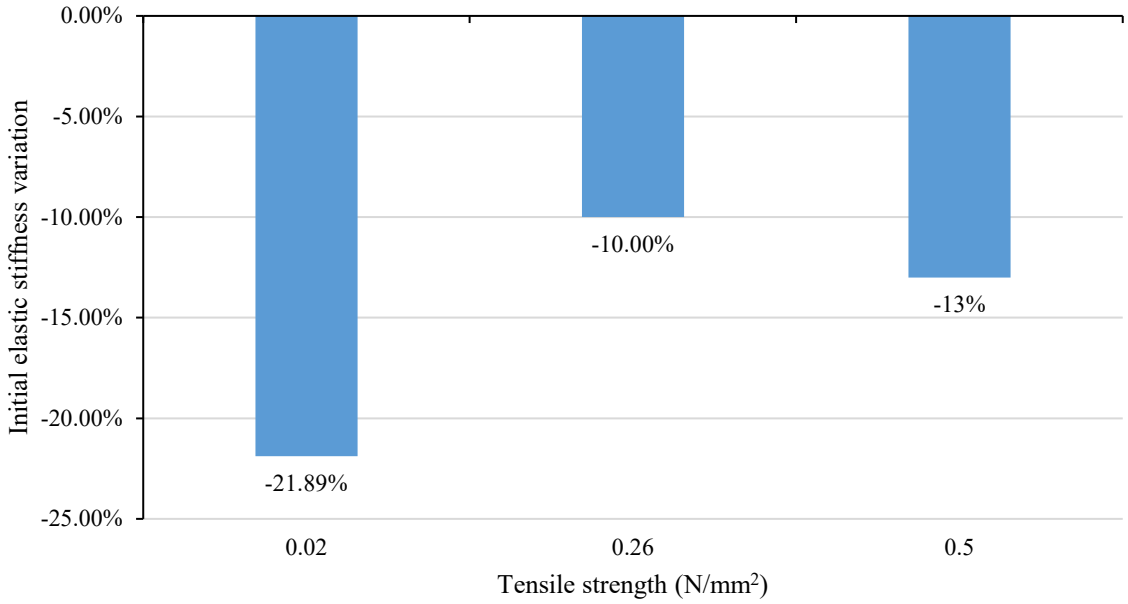

Figure 5-40: Tensile strength effect on the masonry arch's elastic stiffness.

5.5.3 *Mortar Young's modulus of elasticity E_m*

The influence of mortar Young's modulus change are presented in Figure 5-41 for values of E_m = 800, 1420 and 2000 N/mm^2. The initial stiffness of all models is very similar until first crack at 5kN, whereafter the model with E_m= 2000 N/mm^2 closely follows the experimental

data until 20kN live load. This model does not exhibit the ductile response of the experiment and fails abruptly.

The model with E_m= 800 N/mm^2 displays a stiffness almost 30% lower than the experiment but approaches its final peak load at collapse. The model with E_m= 1420 N/mm^2 offers a close approximation to the experimental data both in stiffness and peak load but shows a distinct failure at 2.2mm displacement.

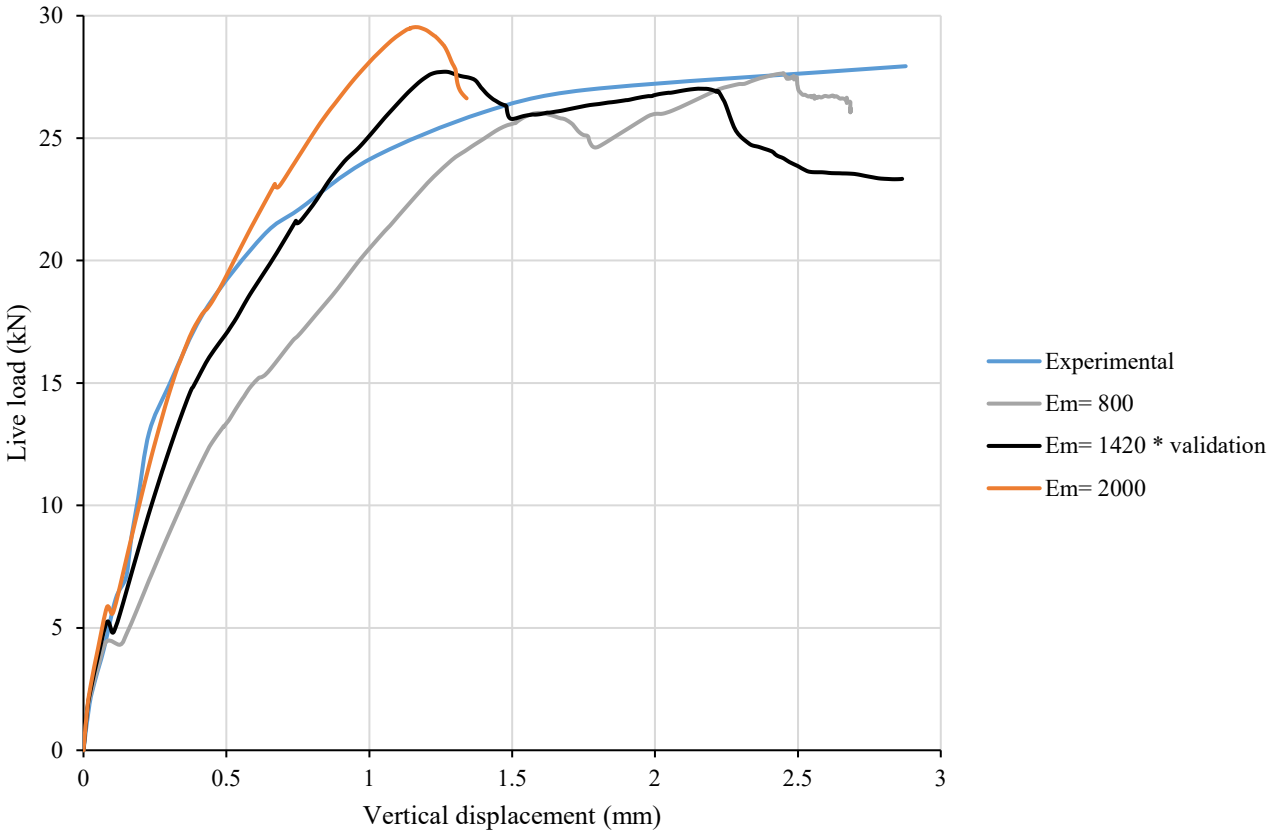

Figure 5-41: Load-displacement at quarter span to establish the effect of mortar Youngs modulus of elasticity of behaviour.

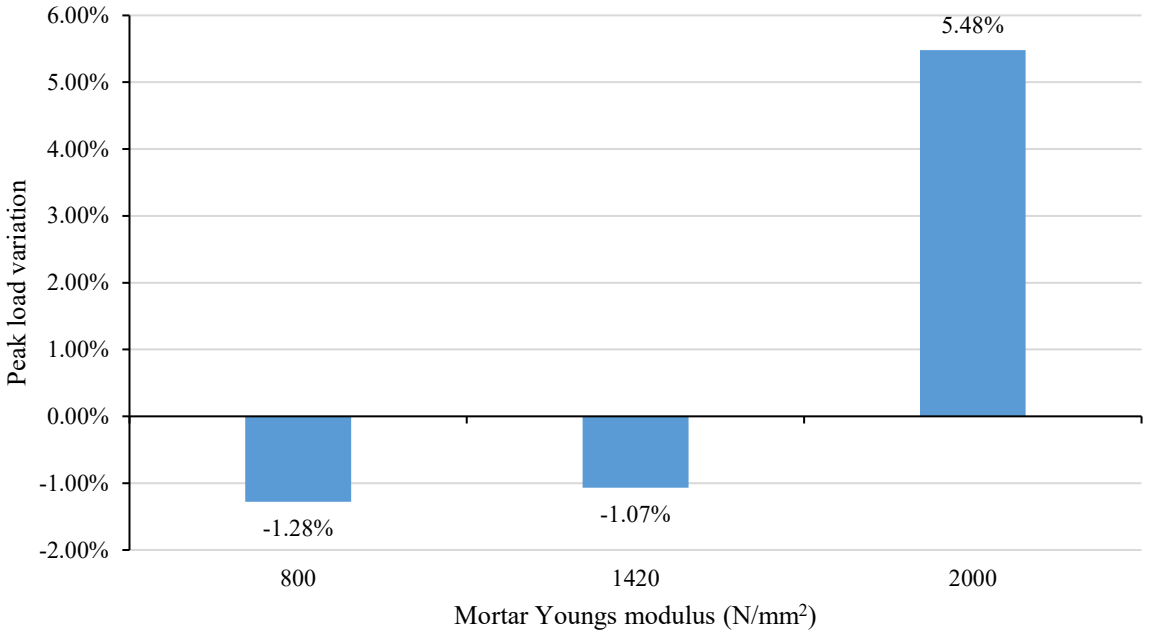

Figure 5-42: Mortar young modulus effect on the masonry arch's peak load.

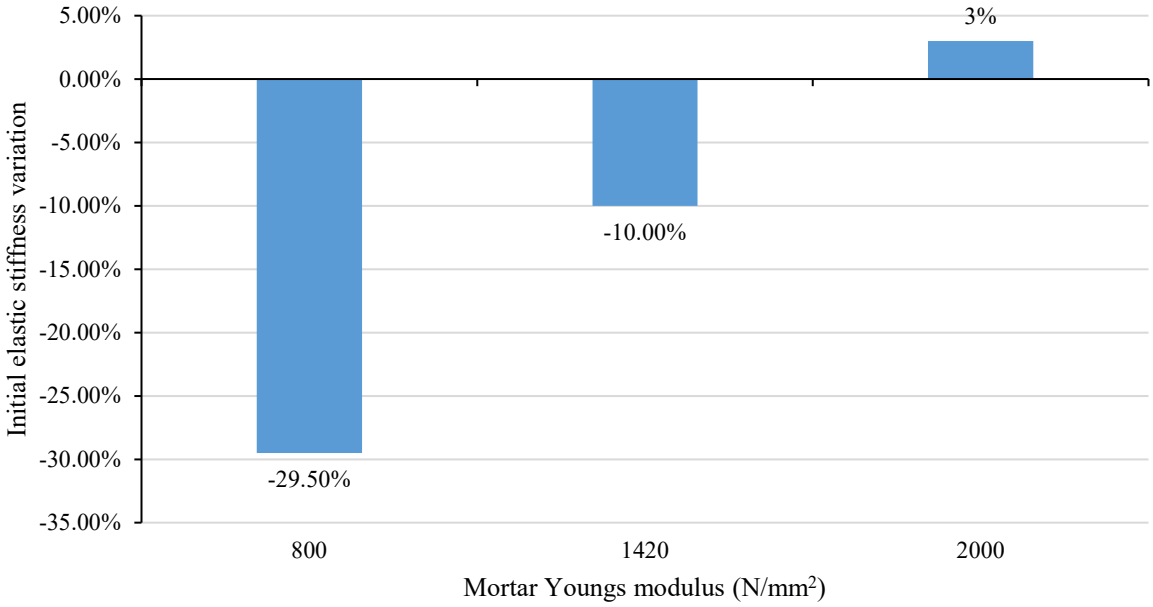

Figure 5-43: Mortar young modulus effect on the masonry arch's elastic stiffness.

5.5.4 *Mortar plasticity using Drucker-Prager criterion*

In this section, the effect of using Drucker-Prager failure criteria is investigated. In section 5.3.1, Mohr-Coulomb criteria was used to validate the numerical model as the requirements of this criteria were available in previous studies that used the same mortar mix used to construct

masonry arches at the University of Salford Heavy Structures Laboratory. However, the Drucker-Prager criterion requirements for hardening law values had to be taken from published research.

Table 5-9; Figure 5-44 were implemented in the Drucker-Prager model to present the stress-strain behaviour. The material property parameters have been selected from previous research based on representing the same mortar material used in the experimental tests.

The compressive curve of stress-strain is required for the Drucker-Prager model, as the experimental test report included the ultimate compressive values of mortar and brick only. Due to this, the compression curve behaviour was obtained from a study conducted by Kaushik et al. (2007). This study used the compressive strength value from experimental tests to obtain a stress vs strain curve for mortar, as shown in Figure 5-44. Abdulla et al. (2017) and Abdulla (2019), used this study to obtain the compression curves, and all the numerical masonry model failure modes were captured.

Table 5-9: Drucker-Prager model material properties for mortar joints (Rots, 1997).

Drucker-Prager model	Friction angle $\emptyset$	Dilation angle ψ	flow stress ratio*
	26.5	11	1.0

* Input as a default of 1.0 (ABAQUS, 2019).

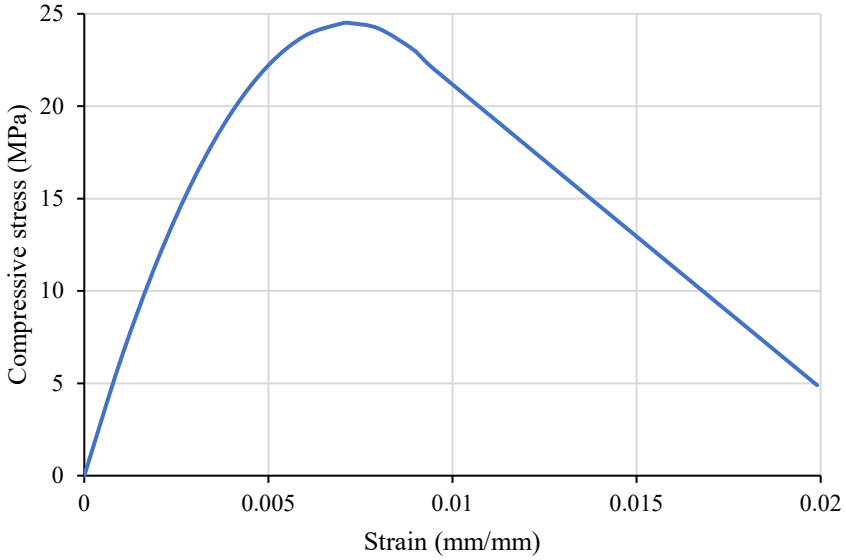

Figure 5-44: Drucker Prager compressive stress vs stain curve for mortar.

Compressive stress softening or hardening values are required to implement mortar crushing under compression using Drucker-Prager.

Figure 5-45 displays the vertical displacement at the quarter span for both experimental and numerical Mohr-Coulomb model results. It can be noticed that the curve behaviour is less smooth, and the maximum peak load is higher than the experimental and numerical curves. In addition, Figure 5-46 confirms that the change in the peak load of the model using Drucker-Prager parameters is significantly higher than the Mohr-Coulomb parameter model. Figure 5-47 demonstrates that the initial elastic stiffness of Drucker-Prager parameters is in closer agreement with the experimental initial elastic stiffness. In addition, the difference between the numerical results of plasticity criteria is negligible.

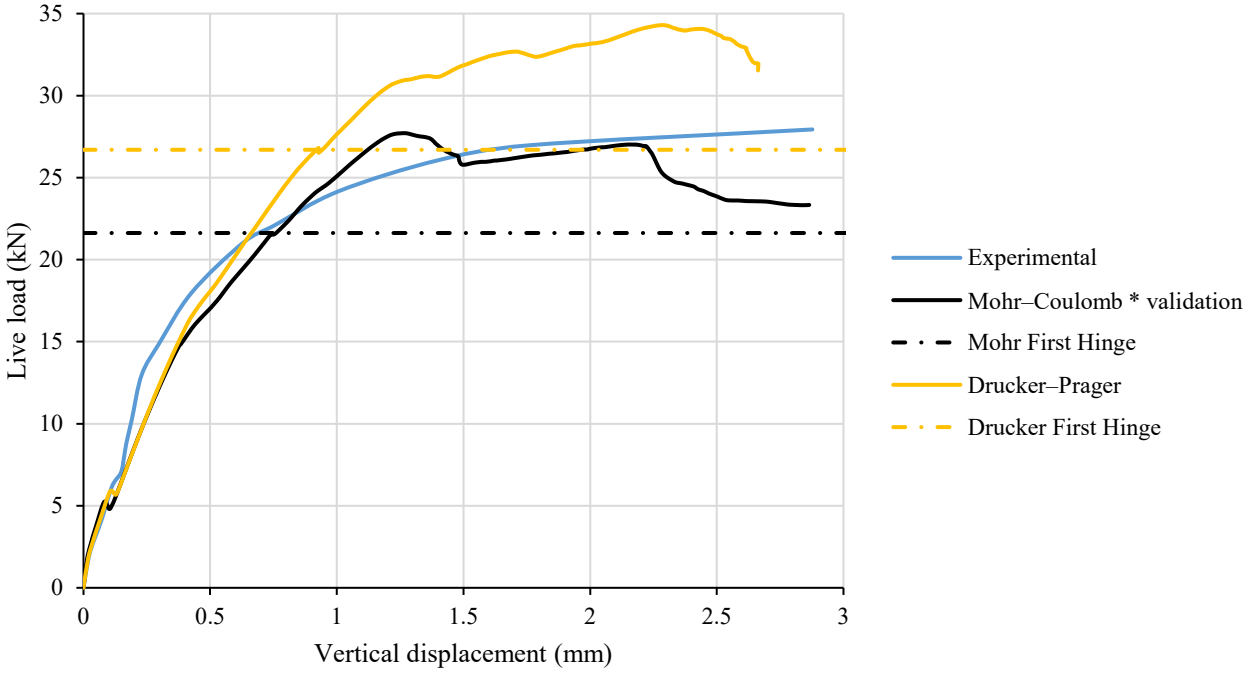

Figure 5-45: Load-displacement at the quarter span using various plasticity parameters.

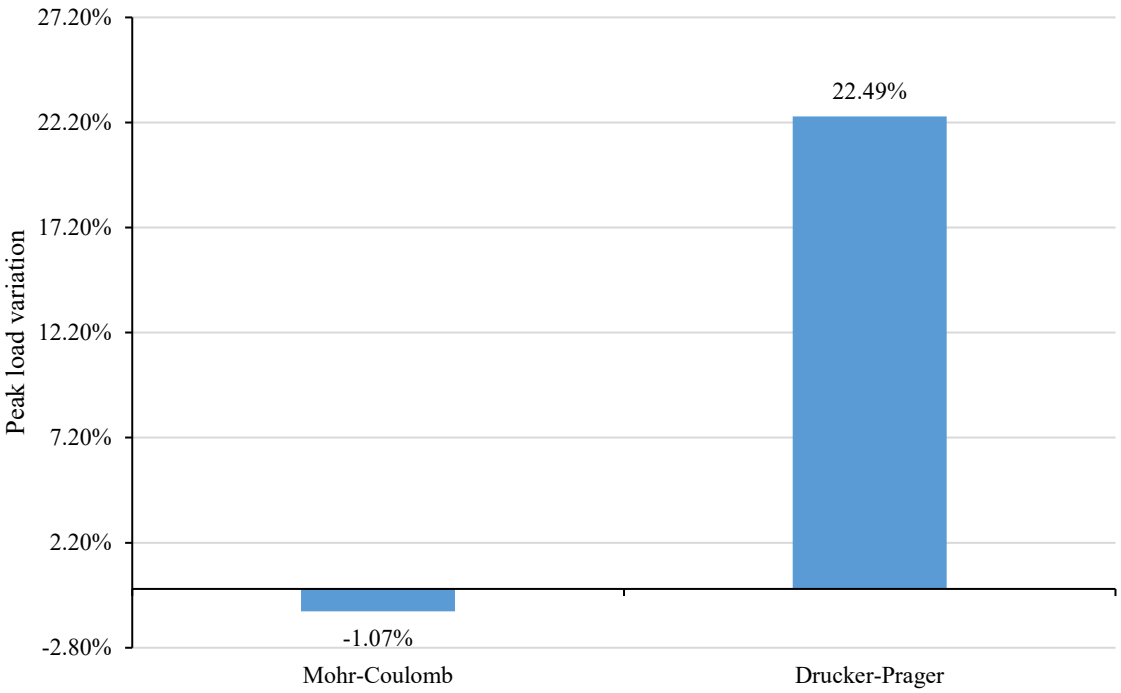

Figure 5-46: Various plasticity parameters influence the masonry arch's peak load.

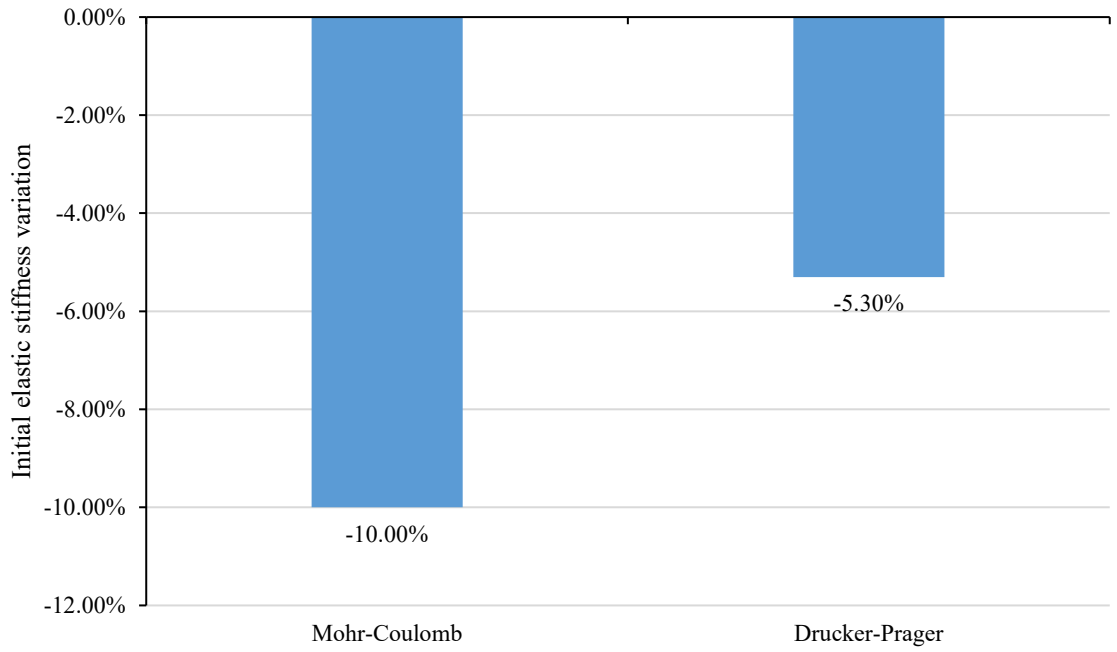

Figure 5-47: Various plasticity parameters influence the masonry arch's elastic stiffness.

Figure 5-48 shows the failure behaviour of the Drucker-Prager model and indicates that a four-hinge mechanism is fully formed. The hinges are located at the same position as the experimental test. Additionally, Figure 5-48 shows the same numerical model in the same state but cohesive interface failure is shown. This indicates ring separation has occurred at the quarter span location. This phenomenon was only observed at a significant level in the Drucker-Prager model.

Table 5-10 compares the load level and the crack locations of each hinge in the masonry arch of the experiment and the two numerical models. As mentioned in section 5.4.1, the Mohr-Coulomb criteria model provided a good correlation against the experimental test result in terms of the loading level at crack formation and crack locations. In contrast, the Drucker-Prager criteria model did not agree with the experimental test result in terms of ultimate load or the loading level of each hinge formation, which was higher than the experiment and Mohr-Coulomb numerical results. The crack locations of the first and second hinges are the same as in the experimental and Mohr-Coulomb, but the third and fourth hinges are formed in slightly different locations.

Table 5-10: Comparison of load level and crack locations for experimental test and two numerical models.

Hinge	Experimental			Numerical Mohr–Coulomb			Numerical Drucker–Prager		
	Live load (kN)	Crack location - brick numbers		Live load (kN)	Crack location - brick numbers		Live load (kN)	Crack location - brick numbers	
		Intrados	Extrados		Intrados	Extrados		Intrados	Extrados
Fist hinge	22	14/15	16/17	21.6	14/15	16/17	26.7	14/15 15/16	14/15 15/16
Second hinge	N/A	0/1	0/1	24	47	47	29.4	47	47
Third hinge	N/A	47	49	27.7	1/2	1/2	31	1/2; 2/3	-
Fourth hinge	28	27/28; 29/30	28/29; 30/31	27.7	27/28	27/28; 28/29	34.4	28/29	28/29

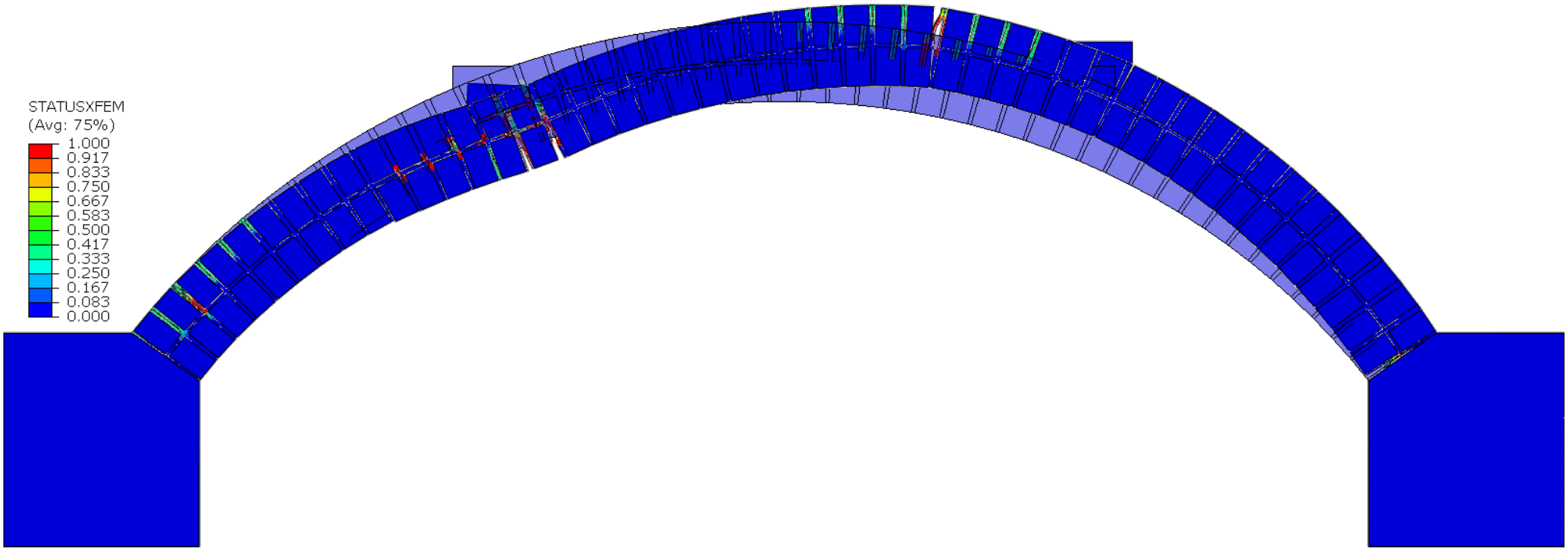

Figure 5-48: Drucker–Prager model of Arch G deformed shape showing entire four hinge mechanism.

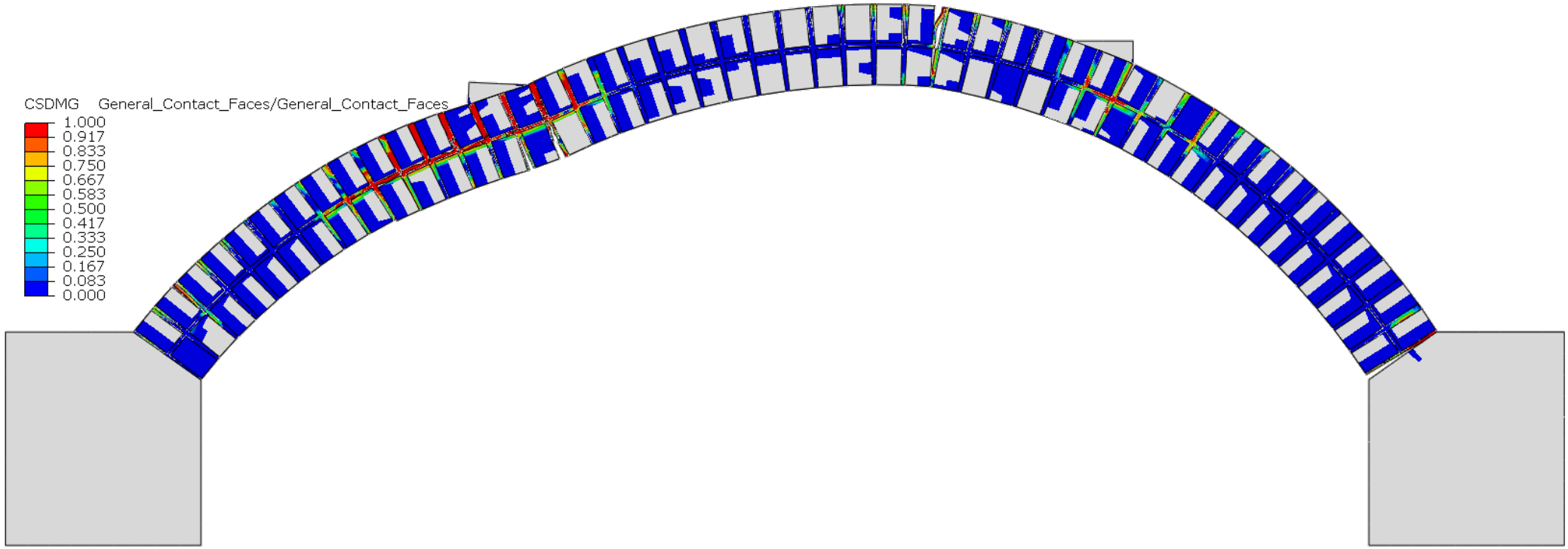

Figure 5-49: Drucker–Prager model of Arch G provided the interface's failure.

5.6 Summary

This chapter investigated and adopted the modelling and techniques of the finite element method identified in chapter 3 and used in chapter 4 to model masonry triplets. The principal characteristics illustrated in this chapter validate the experimental masonry arch test using a detailed micro-modelling approach with XFEM to crack full-thickness mortar joints. The conclusions of this chapter are as follows:

- The detailed micro-modelling approach was used to simulate the 3D masonry arch multi-rings with full-thickness mortar joints. Furthermore, cohesive interaction was used between unit-mortar interfaces to capture the non-linear failure at the interfaces. All this was through combining the constitutive model with the extended finite element method (XFEM) to crack the mortar element without any user-defined subroutines creating the crack (as per previous studies).
- Use of the XFEM method permitted each run to uniquely develop a crack pattern in accordance with defined constitutive laws, which has not been reported in the literature before.
- Masonry arch barrel failures, such as the four-hinge mechanism and interface failure, were captured using the computational models created using ABAQUS. It was shown in this section, that when compared to experimental data, the numerical models displayed very similar crack agreements and peak load until a four hinge failure mechanism formed.
- In order to determine the adequacy of the modelling, a mesh sensitivity study was undertaken using the ABAQUS defined mesh densities of coarse, normal, fine and very fine. It was shown that the normal mesh density produced an optimum representation of the load-displacement curve and was recommended for future modelling.
- Therefore, the critical failure mechanisms and the damage development behaviour of masonry arches can be predicted adequately. Modelling full-thickness mortar with the XFEM cracking method to identify the cracks through the mortar elements required the input of additional material properties and interaction properties. A detailed sensitivity study of the assumed values for the non-linear interface and the mortar plasticity criteria was undertaken.

- The detailed micro-modelling approach was an alternative technique to investigate the realistic behaviour of masonry arches under various loading conditions. Although it offers an opportunity to obtain significant detail and observe the development of failure mechanisms, the intrinsic disadvantages of the approach are the high cost of modelling software, considerable time demands, and the need for expertise in modeller resources.
- In order to evidence the adequacy of the FEA model input data, parametric studies were undertaken on four principal mortar material properties. Values were chosen that were higher and lower than the data used in the validated FEA model. In each case of fracture energy, tensile strength, Young's modulus of elasticity, the middle value (used in the validation model) was shown to offer the best overall fit. Finally, a study was undertaken to determine whether Drucker-Prager or Mohr-Coulomb offered the best constitutive law, and Drucker-Prager was shown to be inferior both in terms of peak load and load at first hinge formation.

  The recommended values are:

  - G_f= 0.012 N/mm
  - f_t = 0.26 N/mm^2
  - E_m = 1420 N/mm^2
- The Drucker-Prager constitutive law models were noted to exhibit ring separation to a much greater extent than the Mohr-Coulomb models. This is due to the Drucker-Prager using a post-yield softening stress-strain relationship for mortar.

Chapter Six

6 An Investigation of the Influence of Masonry Arch Abutment Movements

6.1 Introduction

The presented detailed micro-modelling technique for masonry arches, including the XFEM method to crack the mortar elements with cohesive interaction was validated via the arch G experimental test in chapter 5. In the current chapter, the validated numerical model of arch G is utilised in nonlinear numerical simulations to develop understanding of the response of multi-ring masonry arches under abutment movement in three different directions (vertical, horizontal and rotation).

The numerical model of the validated masonry arch retains the same arch geometry, material properties, loading arrangement and boundary conditions, reported in section 5.3.1. The foundation movement was at the right abutment of the arch, whereas the left abutment was fixed.

The abutment movement of masonry arch bridges is one of the most common failure modes. This may be due to soil instability, settlement under the arch foundation, soil compression in operational conditions or extreme events such as earthquakes and flooding. These factors may lead to the collapse of masonry arch bridges (Asteris & Plevris, 2015). As a result of abutment horizontal movement, the thrust line will eventually reach the arch extrados or intrados, indicating a through-thickness crack (or hinge) has formed.

The investigation is controlled by applying various displacement values at the right arch abutment under displacement control, every load case was applied in a unit time period (1 second). The analyses aim to describe the arch behaviour under foundation movement by increasing the displacement in each direction until the arch becomes unstable. It is reported in the literature (Melbourne et al., 2006) that arches can form collapse mechanisms, which are constituted by a combination of three hinges and abutment movement. Due to the abutment movement, a collapse mechanism will form when three hinges form in the arch barrel (rather than four); thus, masonry arch bridges suffering such movements must be monitored, assessed and repaired as necessary.

Masonry arch bridges, in reality, are regularly exposed to different combinations of foundation movements. This chapter presents the effects of the masonry arch bridge under combination movements at the abutments. The new movement combinations (horizontal and vertical directions) will increase the negative impacts on the arch barrel of the masonry arch bridge by causing radial and tangential cracks.

This chapter investigates different combination movements with a full 3D model to determine the most critical scenario. In addition, this study assists the understanding of the behaviour of masonry arch movement, as these types of bridges have complex geometry to analyse.

6.2 Masonry arch movement under two dead loads only

This section considers the numerical analysis of Arch G under foundation movements in various directions to investigate the masonry arch barrel's behavioural response under the influence of abutment movements.

The numerical simulation was undertaken in three static steps using quasi-static analysis. In the first step, gravity was applied to the whole masonry arch barrel to simulate the self-weight, as shown in Figure 6-1. Also, Figure 6-2 displays the second step, where the dead loads of 10kN were applied at quarter and three-quarter span. The reason for the dead loads is to replicate the original experimental test of arch G, which was validated in chapter 5. In the third step, the right abutment was moved under displacement control in various values, as indicated in Figure 6-3.

Section 6.2.1 and 6.2.2 explore the arch's behaviour by simulating horizontal and vertical movement of 10, 20, and 30 mm, respectively. These simulations were carried out in static load steps to understand how the arch behaves with each specific displacement value. This analysis was discovered to be time step dependant – the results were not consistent unless the time step was consistent across the different displacement values. For the 10 mm displacement, the simulation time was 1 second, resulting in a rate of 10 mm/s. To ensure the increments were uniform, the simulation times for the 20 mm and 30 mm displacements were set to 2 and 3 seconds respectively. The same behaviour was subsequently observed for all three displacement values using the same timestep rate, therefore only the 10mm displacement analyses were reported as this encapsulates the stage 4 failure at about 3mm displacement.

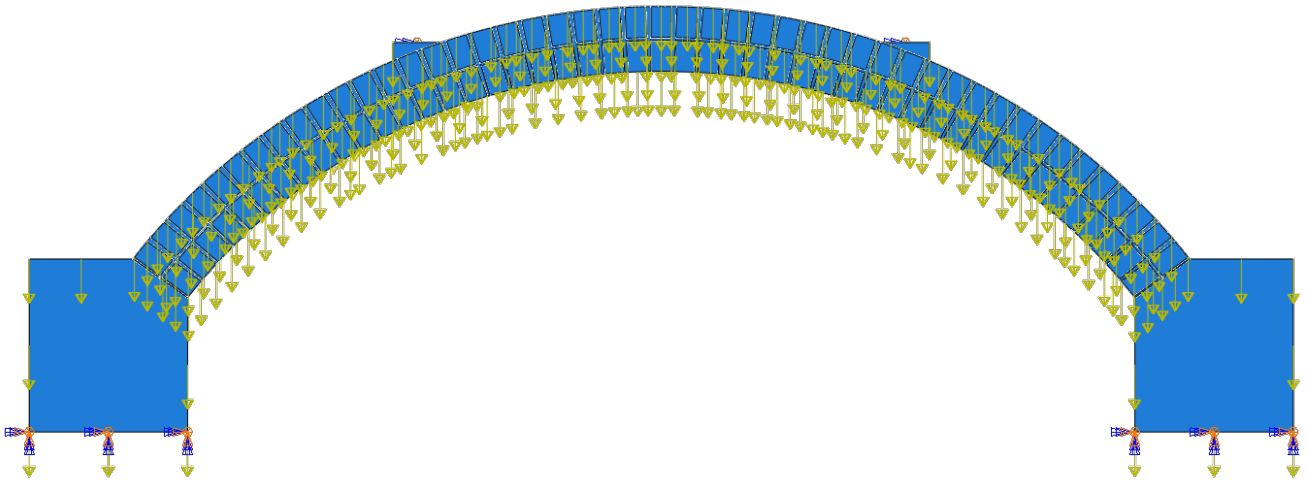

Figure 6-1: Gravity (self-weight) is applied to the multi-ring masonry arch.

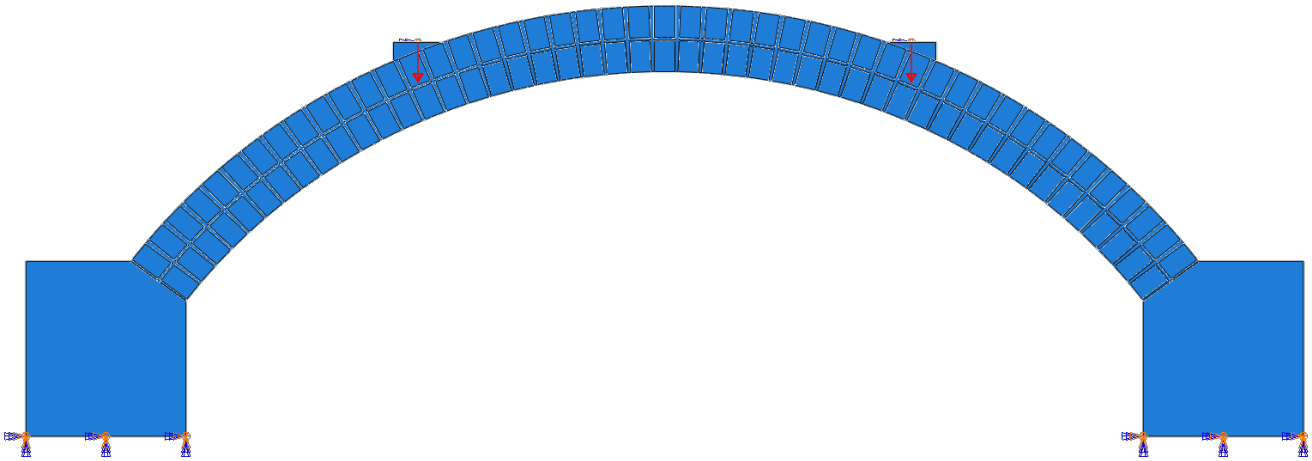

Figure 6-2: Dead loads of 10kN are applied at the arch quarter and three-quarter span each.

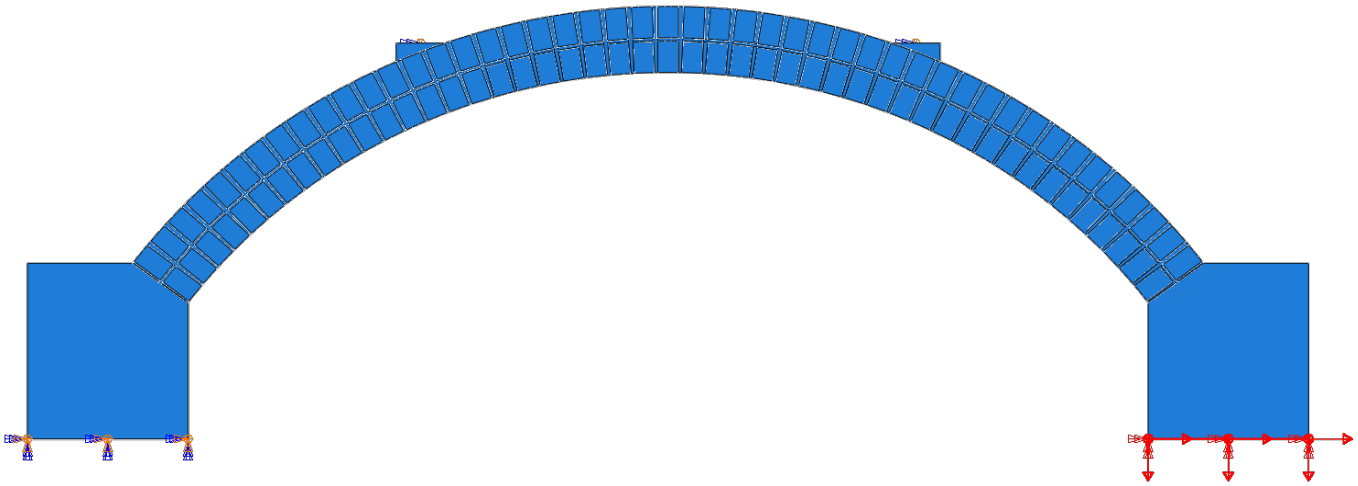

Figure 6-3: Various displacement applied at the right-hand abutment.

6.2.1 *Horizontal abutment movement analysis result*

Figure 6-4 displays horizontal reaction force and displacement at the right abutment for maximum outward horizontal movement of 10mm. Initially, Figure 6-4 shows that when the horizontal movement increases, the horizontal reaction also increases. After the maximum load of 6.45kN, the model abruptly loses stiffness and sharply strain softens until the reaction force approaches a minima of approximately 3.0kN.

Figure 6-5 and Figure 6-6 show cracking damage at the four steps in the 10mm horizontal movement model, which are indicated on Figure 6-4. The load levels at the four steps are 2.5kN, 6.0kN, 6.4kN, 3.4kN.

Figure 6-5 (a) shows that the mortar reached the initial yield point due to tension developing at the intrados of both quarter spans. Furthermore, these two opening cracks had not reached the inter-ring mortar joint at 6.4kN, as shown in Figure 6-5 (b). Also, at the same time, two more additional cracks started to open at the extrados of the right and the left abutment forming at the unit-mortar interface, as shown in Figure 6-5 (c).

Figure 6-6 (a) shows that the two cracks formed in the mortar at the quarter and three-quarter span have opened completely and reached the inter-ring mortar bedjoint, and it could also be seen that the two abutment cracks have wholly formed at the unit-mortar interfaces. These cracks form when the maximum tensile strength of the mortar is reached, showing that the masonry arch material model has a limited tensile capacity. The thrust line can now be accurately located at the four hinge points compression zones.

As the cracks continued to grow, the horizontal reaction force decreased, where Figure 6-6 (b) at 3.4kN shows that the interface failure passed the second ring at both left and right abutments and also at the quarter and three-quarter spans. The arch then entered a phase of plastic failure, indicated by continued displacement with no additional horizontal reaction force. The masonry arch had formed a complete four-hinge mechanism once the displacement at the right abutment reached 5mm, as displayed in Figure 6-7.

Figure 6-7 shows the horizontal movement of the arch model with 10mm applied displacement to investigate the behaviour of the arch barrel with the dead load applied at the quarter and three-quarter spans of the arch barrel. Furthermore, it shows that as the displacement of the right abutment increases, large rotations occur at the three-quarter span crack, which extends

across the entire arch width, and stability is only maintained by high compressive stress in the zone above the crack.

The analysis of the 10mm movement at the right abutment, resulted in two cracks at the quarter and three-quarter spans and a crack at each abutment. The cracks at the abutments were at the unit-mortar interface.

The location of the cracks was the same for the three displacement models, but the cracks within the mortar joints increased substantially with increasing displacement.

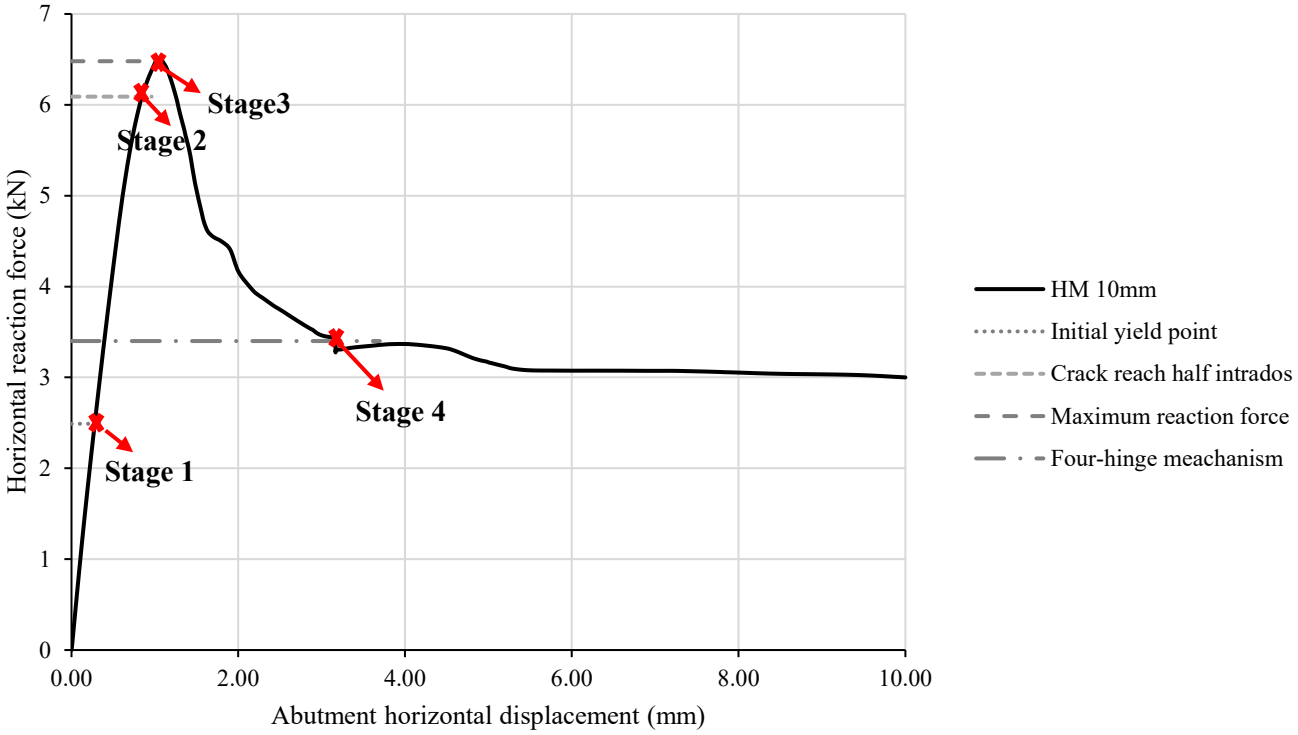

Figure 6-4: Horizontal reaction force against 10mm abutment horizontal displacement.

The general shape is very similar to the results of Zhang et al. (2017), who also investigated the post-yield behaviour of arches subject to abutment spreading. Displacements of up to 40mm were achieved with ADAPTIC models, as shown in Figure 3-10.

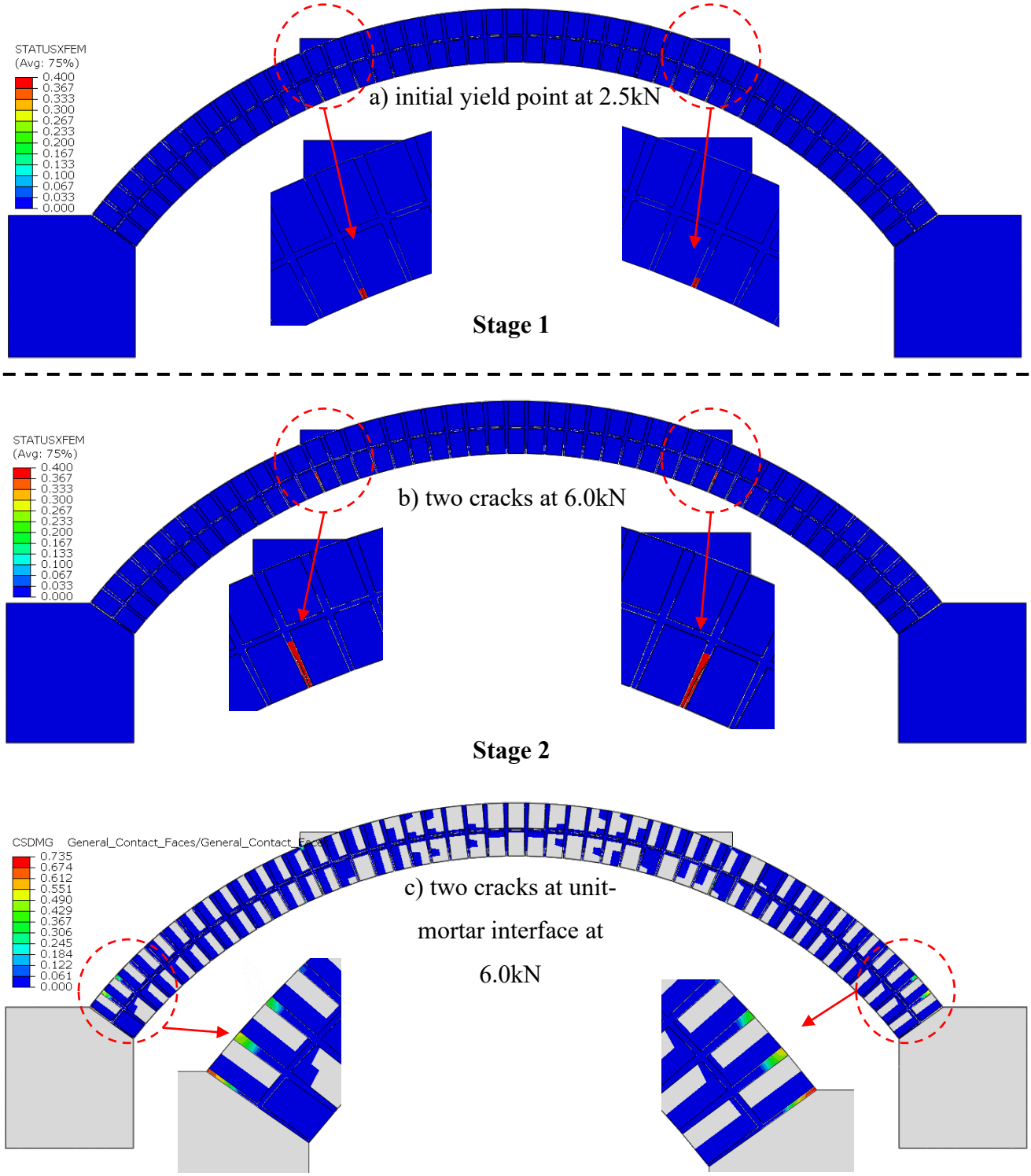

Figure 6-5: Crack simulation progress at stage 1 and 2 of 10mm horizontal abutment movement.

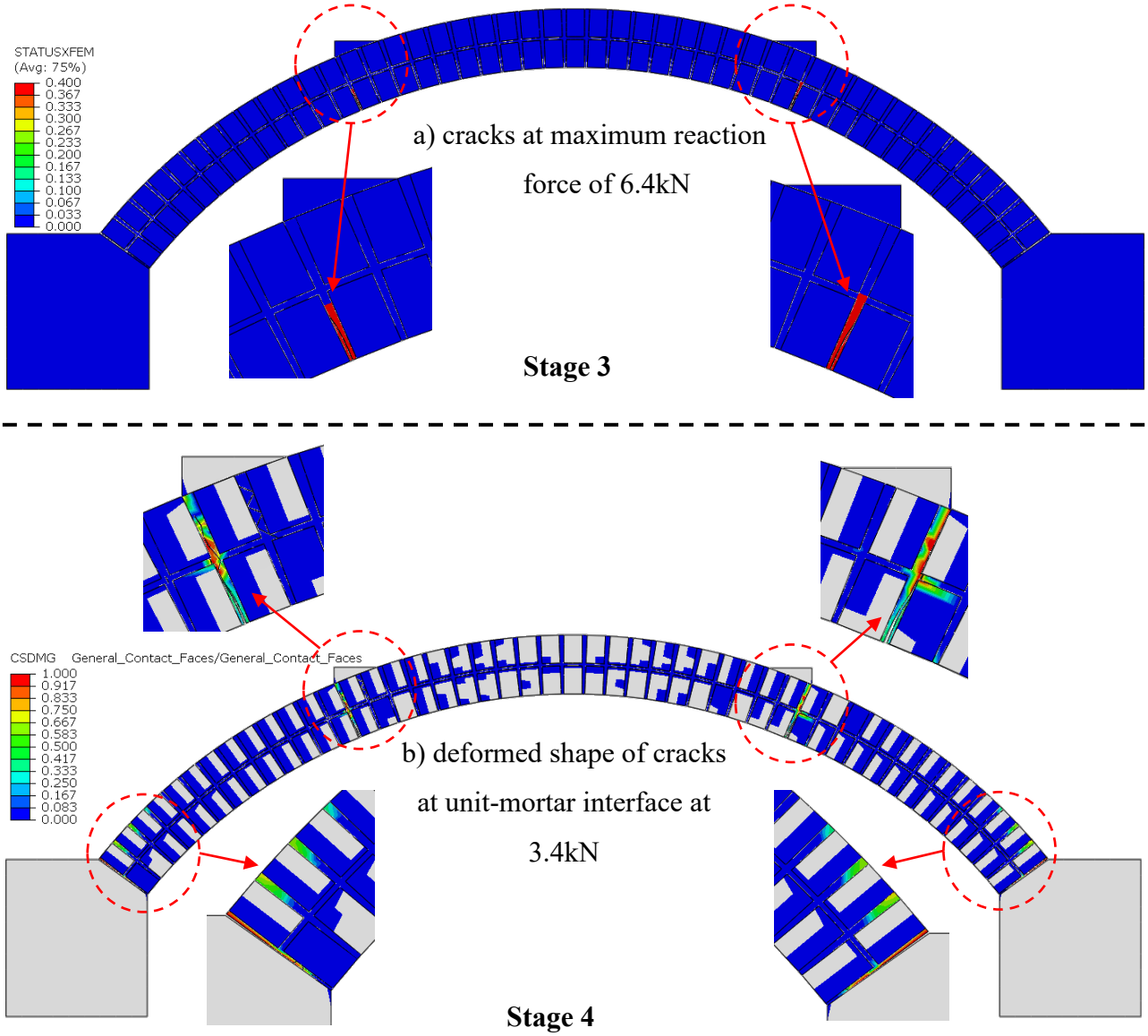

Figure 6-6: Crack simulation progress at stage 3 and 4 of 10mm horizontal abutment movement.

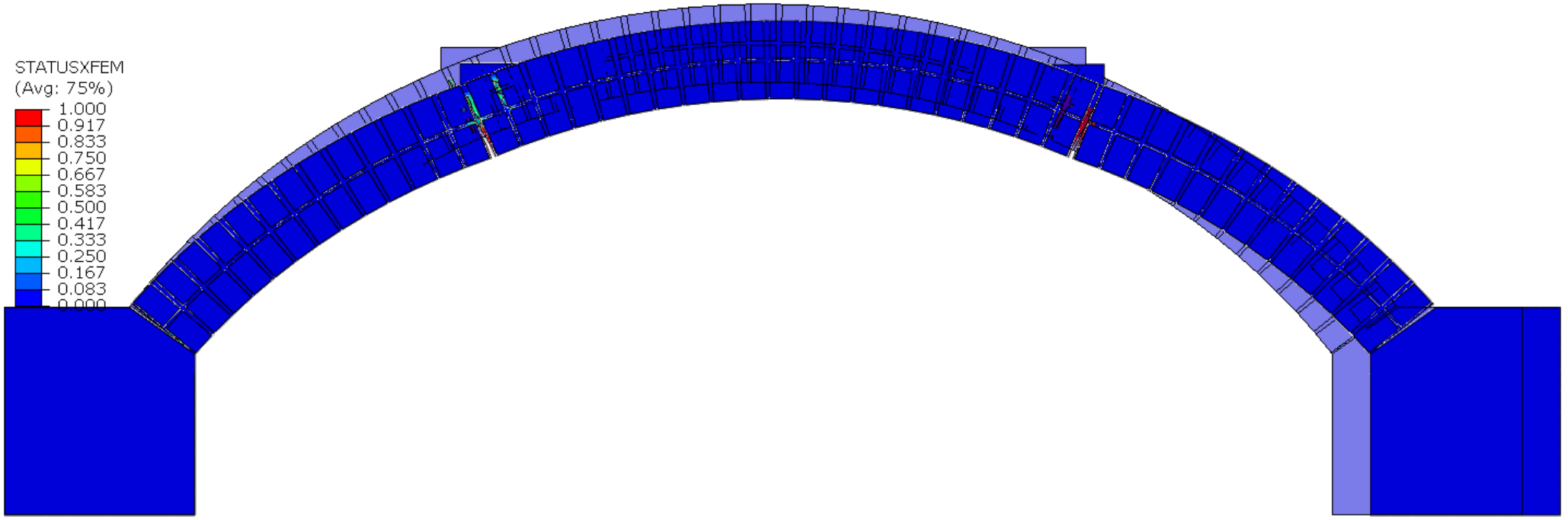

Figure 6-7: The last simulation step output of the arch deformation resulting from 10mm horizontal abutment movement (joint failure).

6.2.2 *Vertical abutment movement analysis result*

The second movement applied the displacement vertically downward at the right abutment. The maximum displacement value was 10mm. The gravity and dead loads were applied at the quarter spans, remaining consistent with the previous horizontal movement tests. Figure 6-8 shows the vertical reaction force for 10mm vertical displacement of the right abutment.

Figure 6-9 and Figure 6-10 show cracking damage at the four steps in the 10mm vertical movement model, which are indicated on Figure 6-8. The load levels at the four steps are 1.1kN, 2.5kN, 2.7kN and 2.22kN.

Figure 6-9 (a) shows the initial yield point crack existing at the three-quarter span of the arch and formed into the mortar joint at the same time as a vertical reaction force of 1.1kN, as shown in Figure 6-8. The crack at the three-quarter span occurred at the intrados and started to grow vertically, towards the extrados, as shown in Figure 6-9 (b). Figure 6-9 (c) indicates the start of unit-mortar interface failure at 2.5kN, located at both quarter spans growing vertically and horizontally.

Figure 6-10 (a) illustrates the unit-mortar interface failures at the maximum vertical reaction force of 2.7kN. At this stage three cracks have already formed at the quarter and three-quarter spans, and at the right-side abutment. The crack at the quarter span extends vertically towards the extrados and horizontally along the inter-ring bedjoint. The crack at the three-quarter span started as a crack into the radial mortar joint and then changed to a crack at the unit-mortar interface extending towards the extrados.

As the cracks continued to grow, the vertical reaction force abruptly decreased, eventually plateauing at stage 4 with a reaction force of 2.22kN. The arch then entered a phase of plastic failure, indicated by continued displacement with no additional vertical reaction force. The masonry arch had formed a complete four-hinge mechanism once the displacement at the right abutment reached 10mm, as shown in Figure 6-10 (b and c).

Figure 6-10 (c) shows further unit-mortar interface cracks opened at the quarter span of the arch barrel. Furthermore, this figure shows (the red colour zones) below the dead loads at the quarter and three-quarter span in the upper ring, where more cracks occurred due to shear slip, as evident in Figure 6-11.

The vertical displacement was increased to a maximum value of 10mm to investigate the behaviour under large displacement. However, cracks formed within the arch barrel (at four different locations), and ring separation occurred at the quarter span and the right-hand side of the arch, as shown in Figure 6-11 and Figure 6-12.

It is clear to deduce that a four hinge collapse mechanism has fully formed regardless of whether the crack forms fully within the mortar joint or along the interface between the unit and mortar joint.

Comparing Figure 6-7 and Figure 6-12, the rotation at cracks is significantly larger in horizontal movement than the vertical movement. The load at which four hinges are formed is higher for horizontal movement than vertical movement, (6.45 kN from Figure 6-4 and 2.7 kN from Figure 6-8 respectively at peak load).

Figure 6-11 and Figure 6-12 indicate minor (dispersed) cracks also formed around the left-hand abutment of the arch, adjacent to the major crack. Also, the four-hinge mechanism had fully formed, as shown in the figures. The model result suggests there will be a complete collapse if sufficient movement is applied.

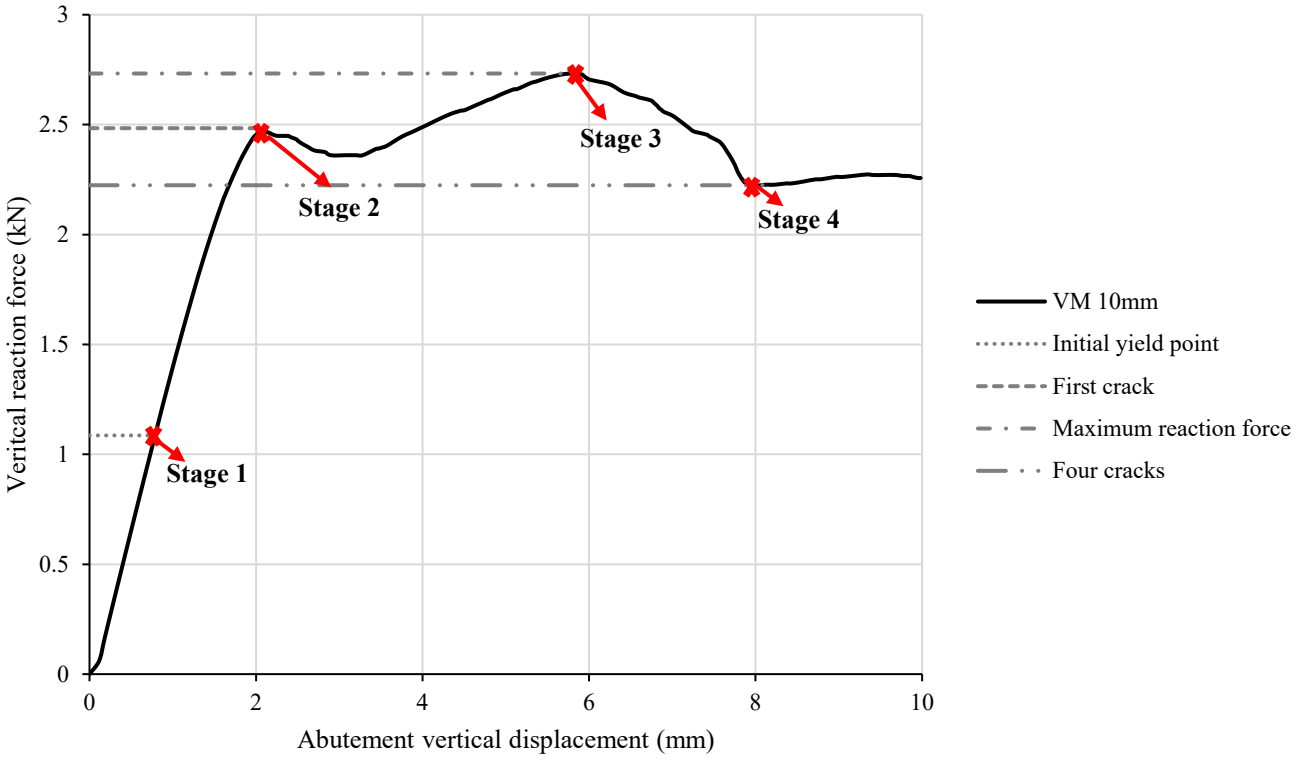

Figure 6-8: Vertical reaction force against 10mm abutment vertical displacement.

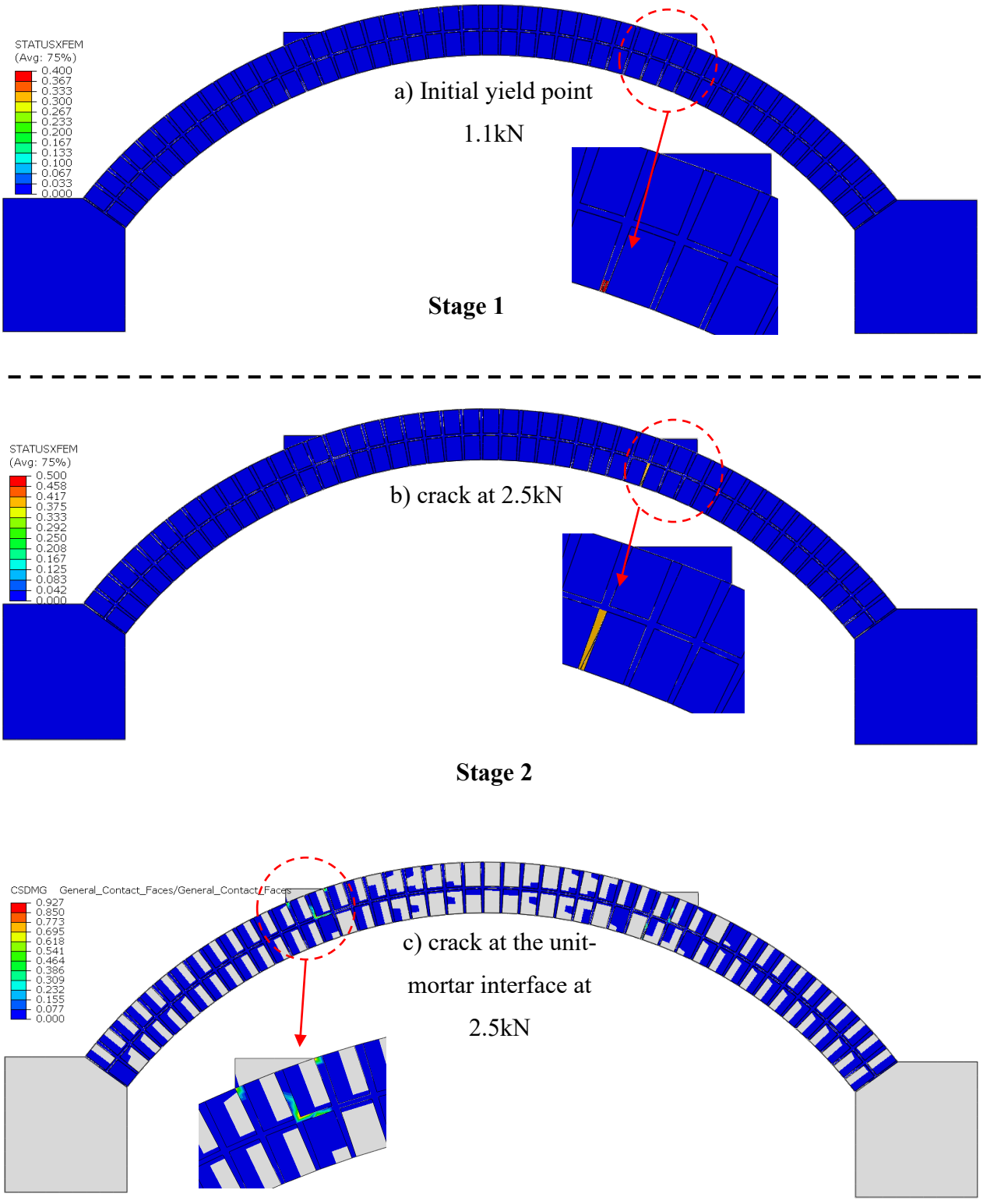

Figure 6-9: Crack simulation progress at stage 1 and 2 of 10mm vertical abutment movement.

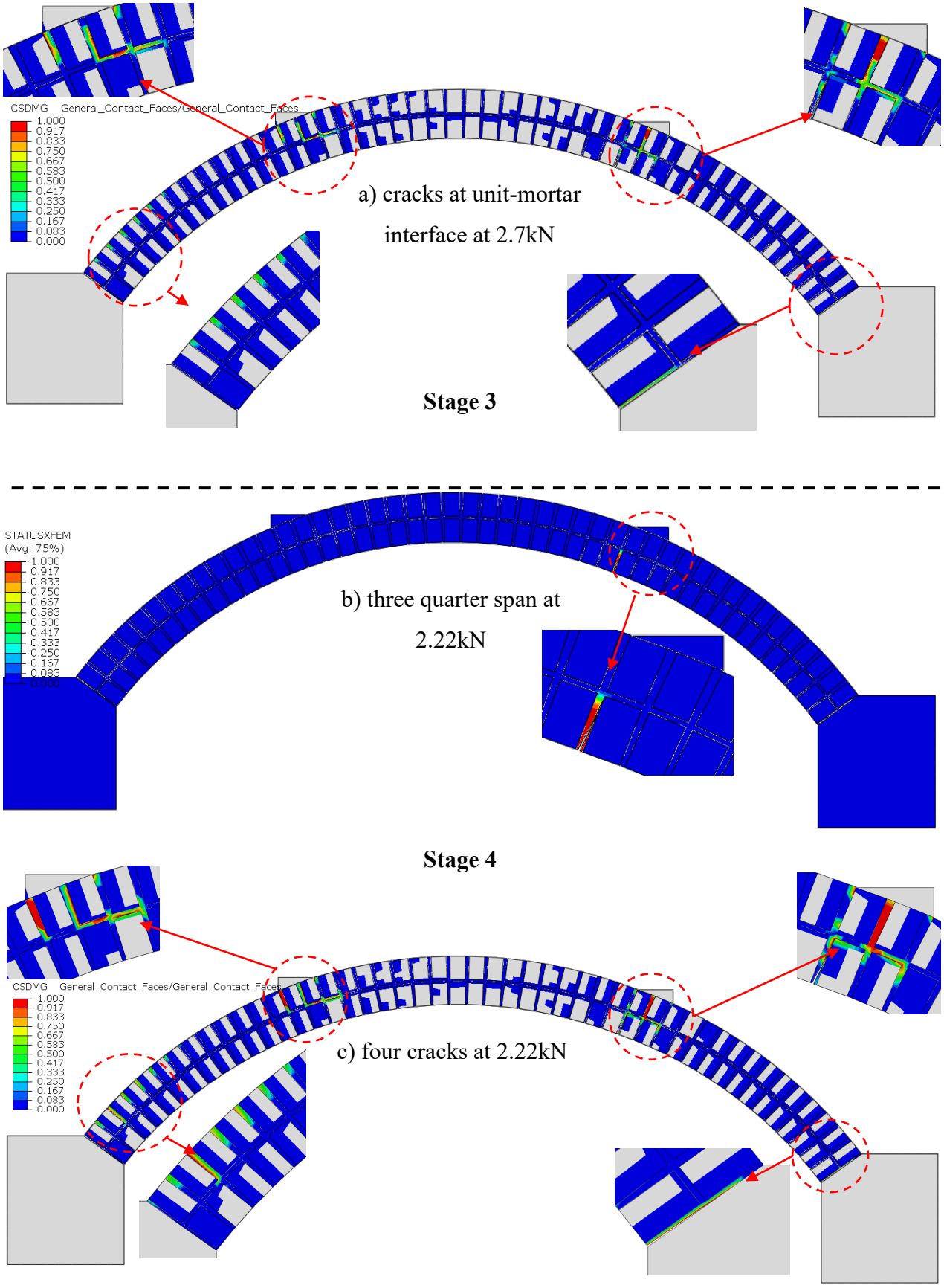

Figure 6-10: Crack simulation progress at stage 3 and 4 of 10mm vertical abutment movement.

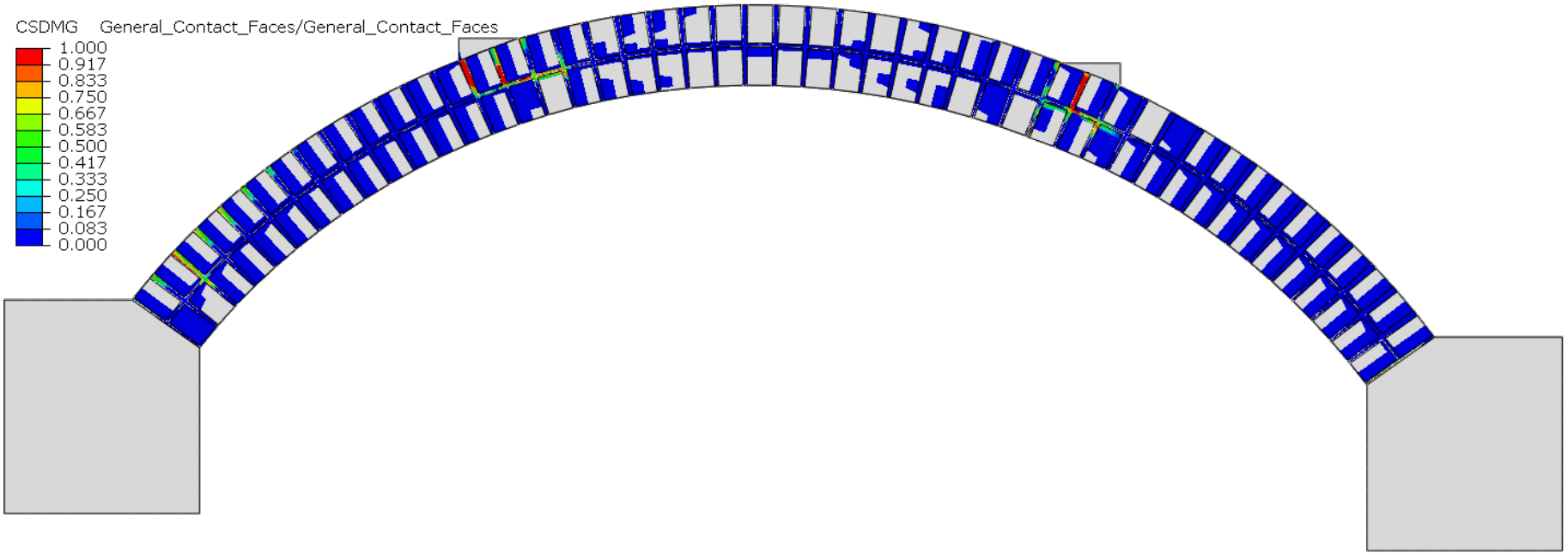

Figure 6-11: The last simulation step output of the arch deformation resulting from 10mm vertical abutment movement (interfaces failure).

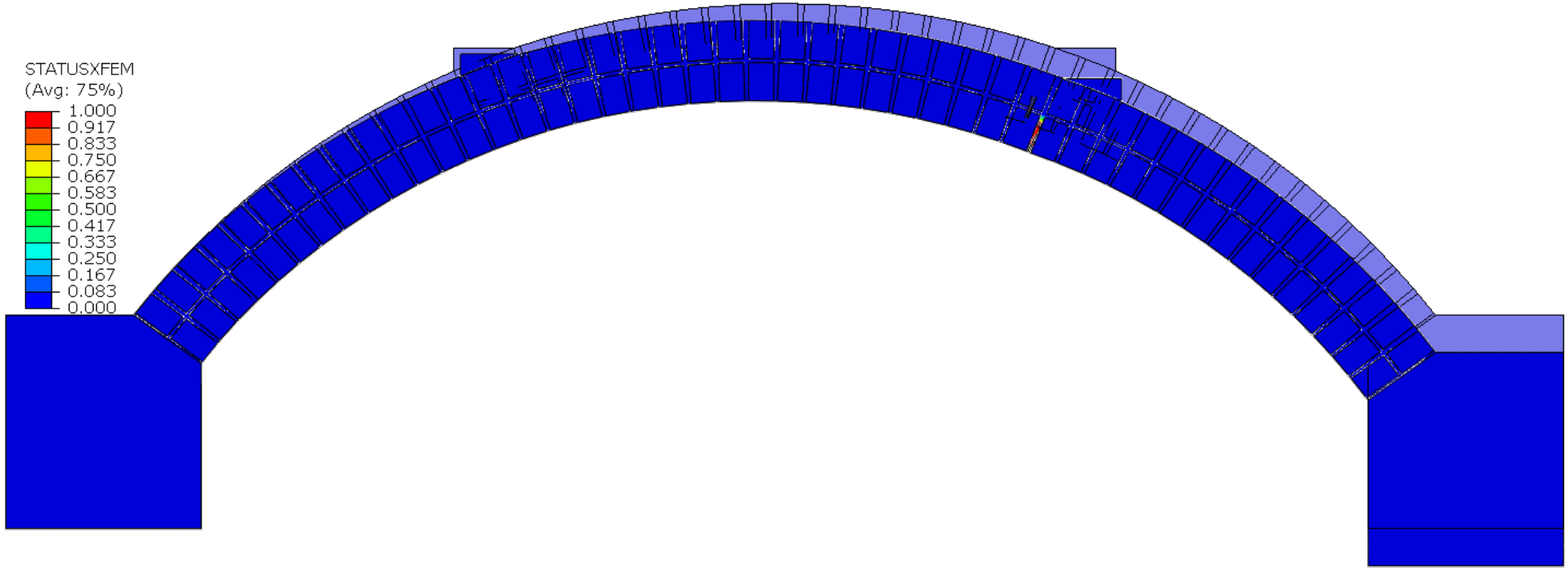

Figure 6-12: The last simulation step output of the arch deformation resulting from 10mm vertical abutment movement (joint failure)

6.2.3 *Rotational abutment movement analysis result*

The third movement was anti-clockwise rotation at the right abutment of 0.02 radians (or 5mm, as indicated on Figure 6-18), applied to the bottom of the right-hand abutment. ABAQUS software expressed the rotation degrees of freedom in radians, so the displacement values were converted into radians.

The rotational movement of 0.02 rad (5mm) severely affected the arch barrel. As a result of this displacement value, two hinges formed due to development of tension where the arch meets the abutments at the intrados, and one opening crack formed at the unit-mortar interface at the extrados of the middle of the arch barrel, as shown in Figure 6-17 and Figure 6-18. Figure 6-17 presents two further cracks, with notable ring separation at the quarter and three-quarter span.

Figure 6-14, Figure 6-15 and Figure 6-16 display each step of the 0.02 radians (5mm) rotational movement model, with Figure 6-13 a horizontal reaction force-displacement graph highlighting the crack sequence.

The initial yield point started to appear at 2.2kN, and an opening crack formed in the mortar joint at the intrados of the right-hand abutment, as shown in Figure 6-14 (a). Also, Figure 6-14 (b) shows the crack was growing towards the extrados of the arch at 7.8kN, where Figure 6-14 (c) displays the crack after it formed in the mortar joint; it changed direction and developed at the unit-mortar interfaces. The second crack started to appear in the unit-mortar interface at the intrados of the left-hand abutment, a green-coloured zone, meaning it had not been fully formed across all of the arch width.

Figure 6-13 shows a drop in the horizontal reaction force at 7.8kN, which started to increase again at 7.65kN. This means that the masonry arch model still resists the abutment movement until the four cracks formed in the arch barrel. The first two cracks began to grow towards the extrados of the arch, and two further opening cracks in the mortar joint appear at the quarter and three-quarter span of the arch extrados, as shown in Figure 6-15 (a). In addition, there is ring separation due to shear failure at the arch three-quarter span under the applied dead load location.

Figure 6-13 shows that the force-displacement curve starts the plastic region around 0.0035 radians, when the reaction force was at 9.65kN. The first crack at the right-hand abutment

reached the second ring with two crack failures in the mortar joint and at the unit-mortar interface with high compression stress in the uncracked mortar joint, as shown in Figure 6-15 (b & c). The second crack has two types of opening cracks, where at the intrados, the crack formed in the mortar and then the crack opened at the unit-mortar interface and passed through the inter-ring mortar bedjoint, as shown in Figure 6-15 (c).

As the horizontal reaction force decreased, the cracks grew into the arch barrel. Further, dispersed cracks had already opened at the unit-mortar interface in the middle of the arch barrel, as shown in Figure 6-16 (b). Figure 6-16 (a) displays that the cracks of the upper ring at the quarter and three-quarter span spread as ring separation and grew towards the arch's extrados. It can be noted in Figure 6-16 (a) that the crack at the quarter span grew only in the back view of the arch, which means the crack did not cross the masonry arch width.

The arch barrel does not have the capacity for further rotational displacement movement due to significant cracks formed at three locations, and ring separation had occurred at the quarter and three-quarter span of the arch barre, as shown in Figure 6-17.

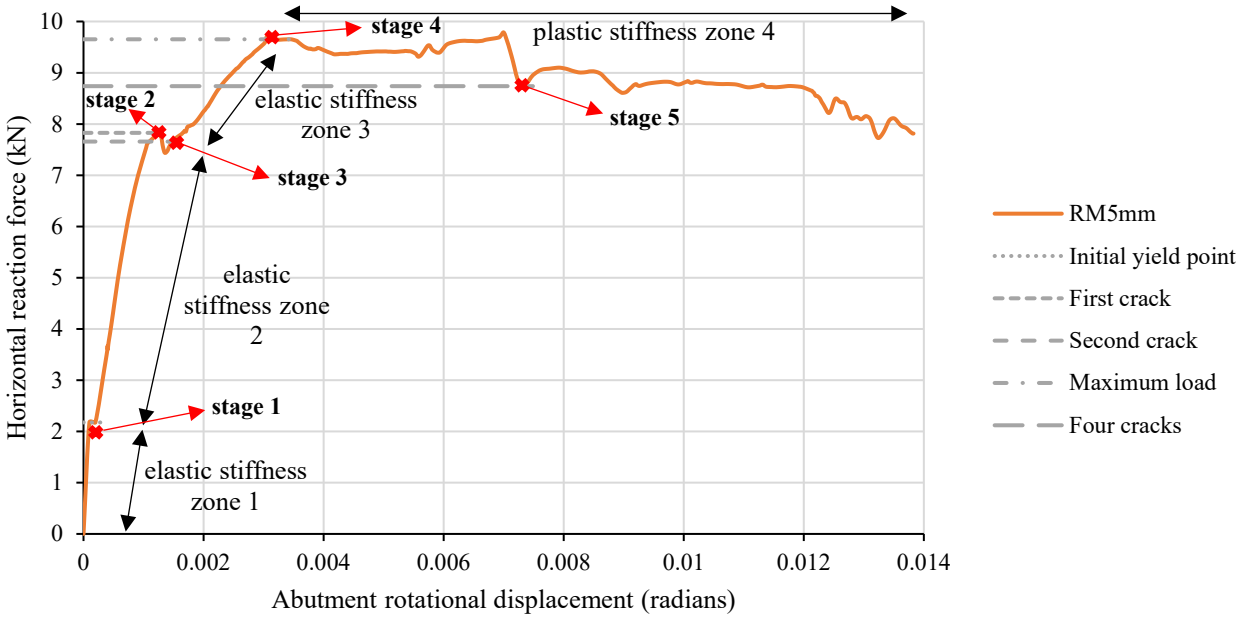

Figure 6-13: Horizontal reaction force against abutment rotation.

Figure 6-13 shows that abutment rotation leads to a ductile failure of the arch, as indicated by the long plastic displacement zone. There are also clear reductions in elastic stiffness as cracks develop in the barrel.

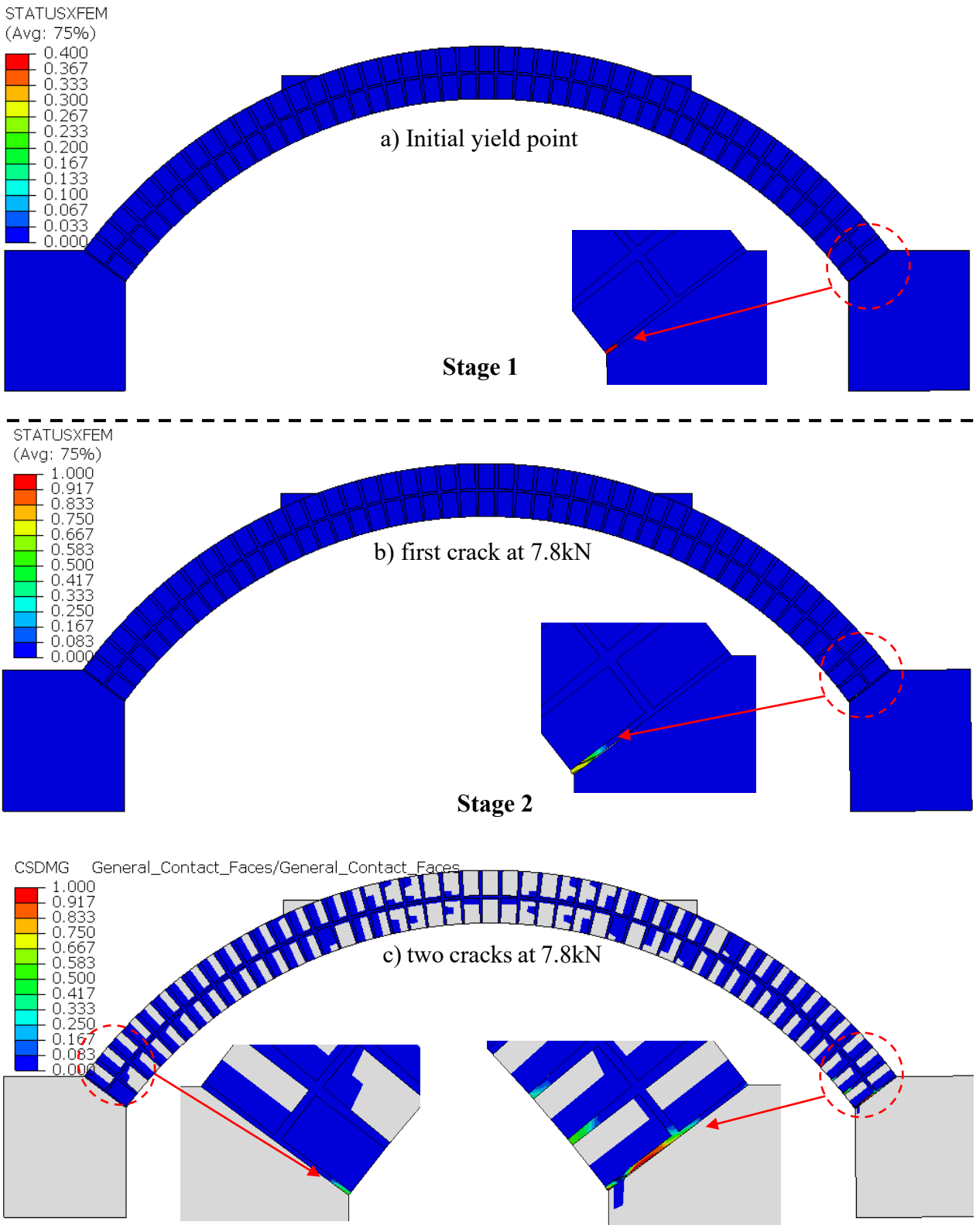

Figure 6-14: Crack simulation progress at stages 1 and 2 for right abutment rotation (0.02 rad).

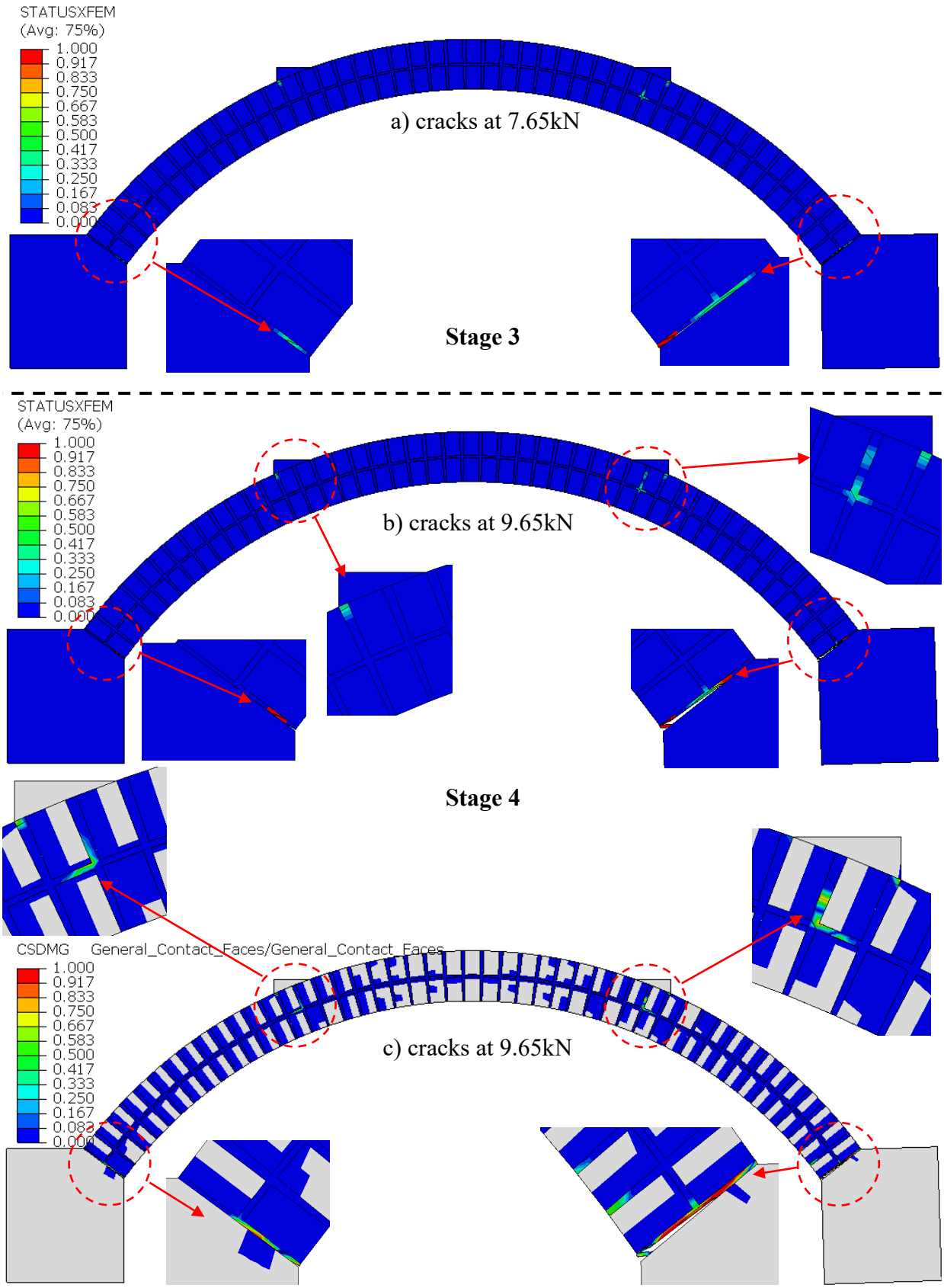

Figure 6-15: Crack simulation progress at stages 3 and 4 for right abutment rotation (0.02 rad).

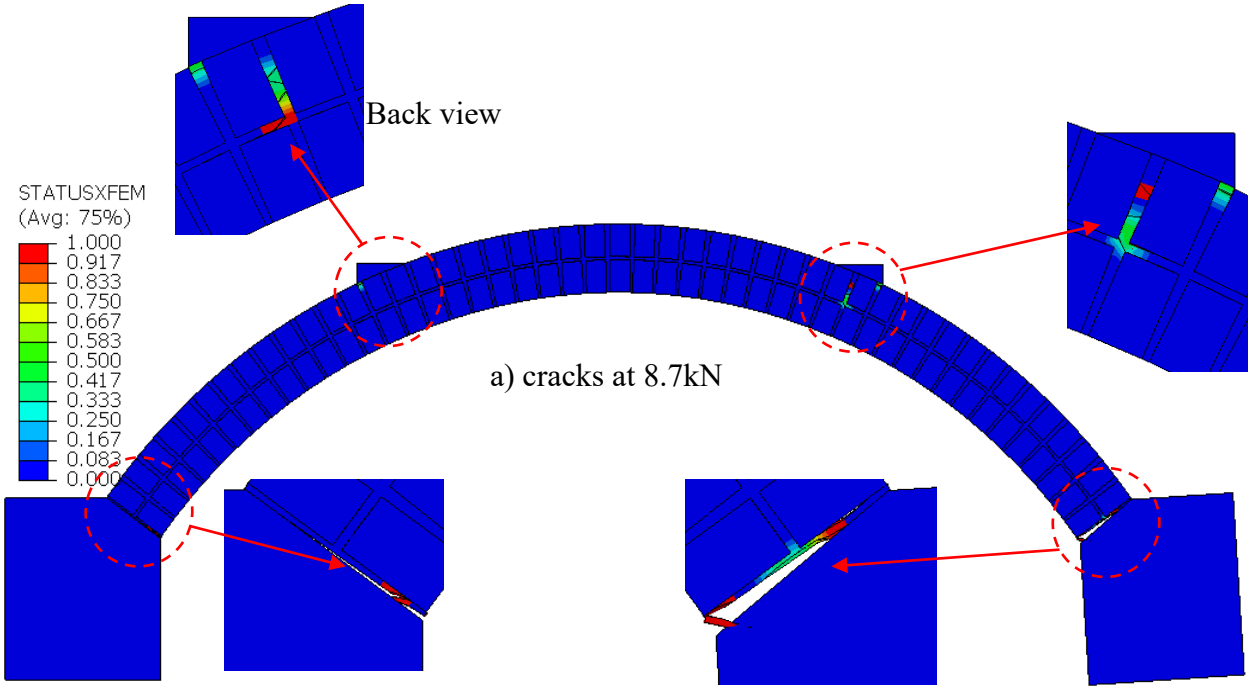

Stage 5

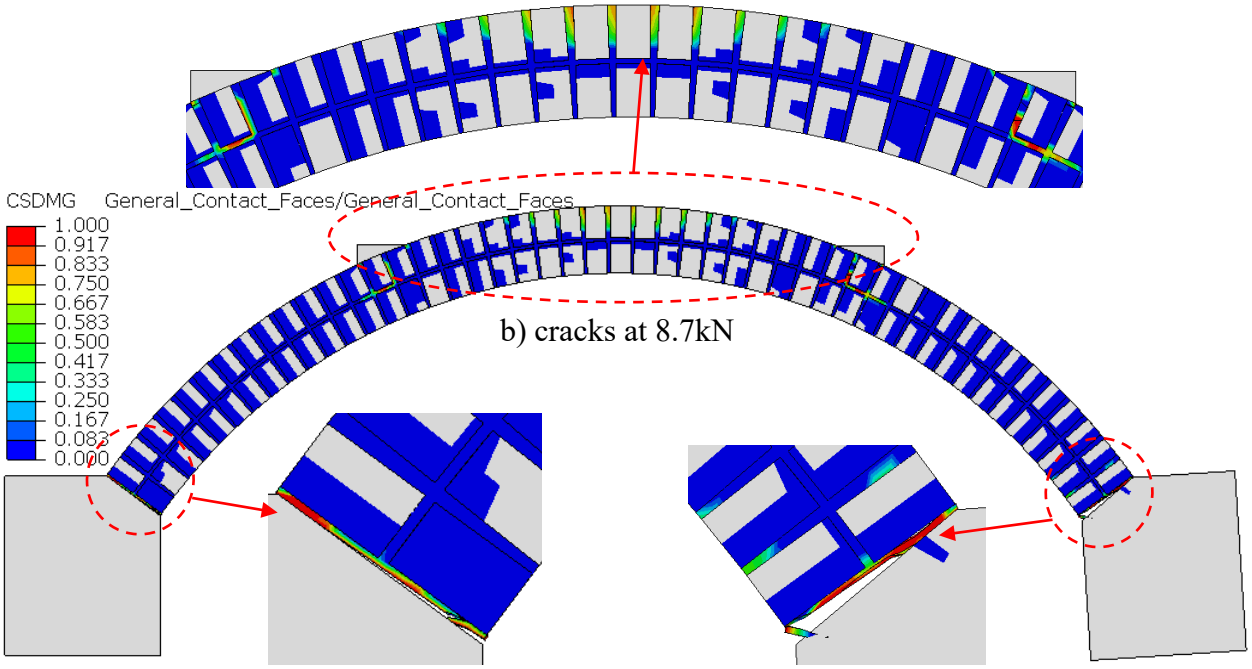

Figure 6-16: Crack simulation progress at stage 5 for right abutment rotation (0.02 rad).

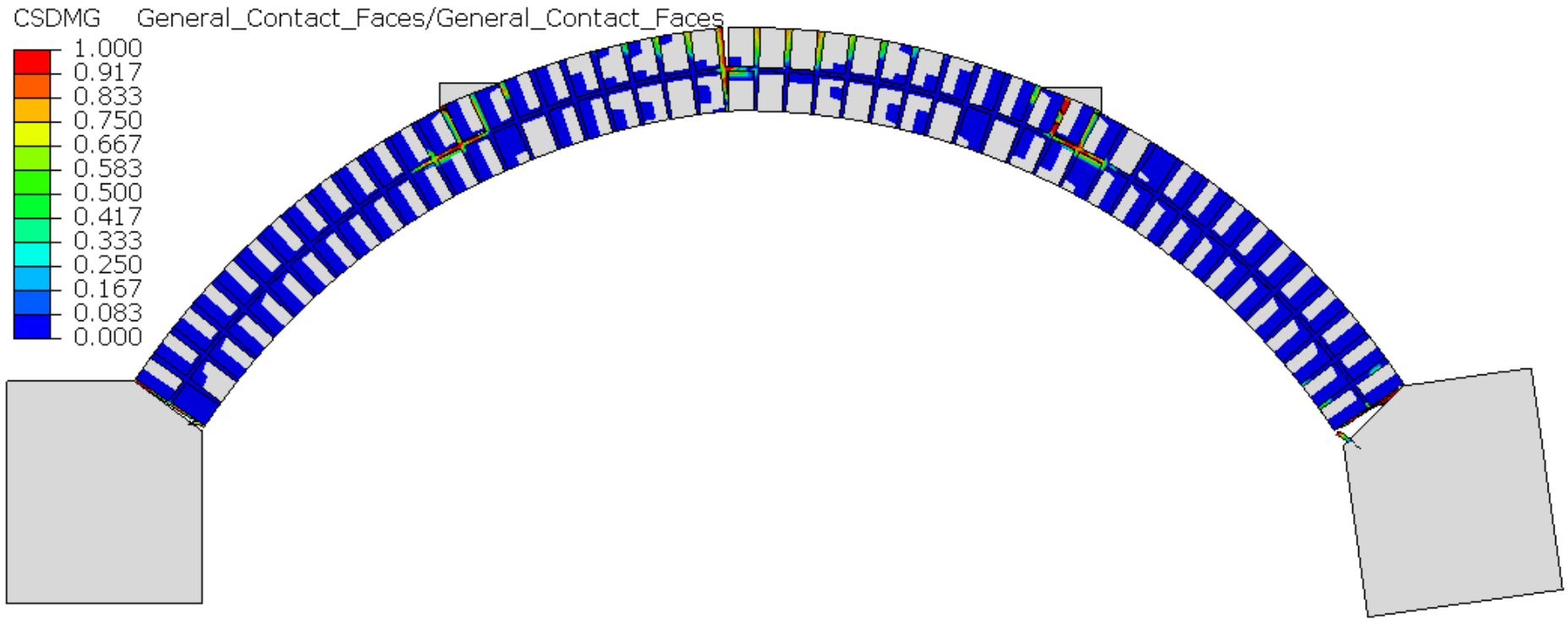

Figure 6-17: The last simulation step deformed shape for the right abutment 5mm (0.02 rad) rotational movement (interfaces failure).

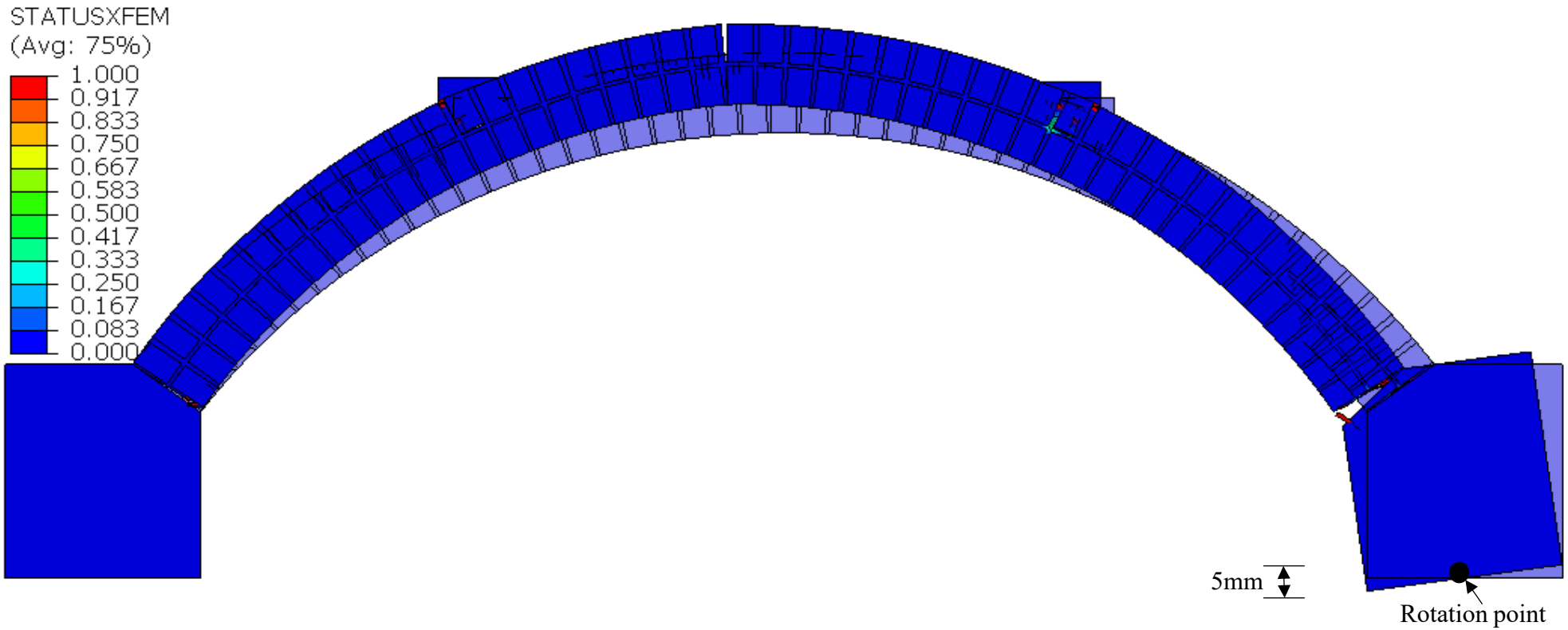

Figure 6-18: The last simulation step output of the arch deformation resulting from the right abutment 5mm (0.02 rad) rotational movement (cracking failure).

6.2.4 *Rotational inverse abutment movement analysis result*

This section reports the masonry arch model being subjected to clockwise rotation movement at the right abutment, and the displacement value is 0.04 radians (10mm).

The simulation progress of each step during movement of 10mm (0.04 rad) is highlighted in Figure 6-20 and Figure 6-21. Figure 6-19 displays the horizontal reaction force-displacement graph highlighting the crack progress.

The 0.04 radians (10mm) simulation outcomes are shown in Figure 6-22 and Figure 6-23, where this movement significantly impacted the arch barrel with four cracks at different locations. The rotation clockwise movement model became unstable at a displacement value of 0.04 radians (10mm) and caused significant hinges at the two springing's between the arch and the abutments. Furthermore, two cracks are formed under the dead load at the quarter and three-quarter span plus ring separation at the same locations, as shown in Figure 6-23. Therefore, the model does not have the capacity for further increased rotation displacement because crushing failure is imminently likely at the right abutment.

The initial yield point was at 2.7kN horizontal reaction force, and the opened initial crack formed in the mortar only at the extrados of the arch barrel, as shown in Figure 6-20 (a).This crack continued to grow towards the arch intrados and reached the mortar joint between the rings at 4.8kN, as shown in Figure 6-20 (b). However, Figure 6-20 (c) displays dispersed opened cracks formed at the unit-mortar interfaces at the right-hand abutment. Two more cracks also started developing at the intrados of the arch at the quarter span, and the second crack was at the left-hand springing at the extrados.

The second crack formed at the three-quarter span intrados of the arch barrel, including two crack types, which started as an opening crack formed at the unit-mortar interface, as shown in Figure 6-21 (b) and then grew into the mortar joint, as shown in Figure 6-21 (a). Furthermore, Figure 6-21 (a) shows an opened crack formed at the upper ring at the quarter span, where all these cracks occurred at 4.18kN horizontal reaction force of the right abutment. As a result, the masonry arch barrel did not have enough capacity to resist the movement and started to become unstable, as shown in Figure 6-22 and Figure 6-23.

The four-hinge mechanism failure had formed, the right-hand abutment had rotated entirely, and it could not take more movement to hold the arch model in place and carry any further load. In this scenario, the ring separation in the arch barrel started to appear at the three-quarter span at 4.18kN horizontal reaction force, as shown in Figure 6-21 (b), and then formed at the quarter span, as shown in Figure 6-22.

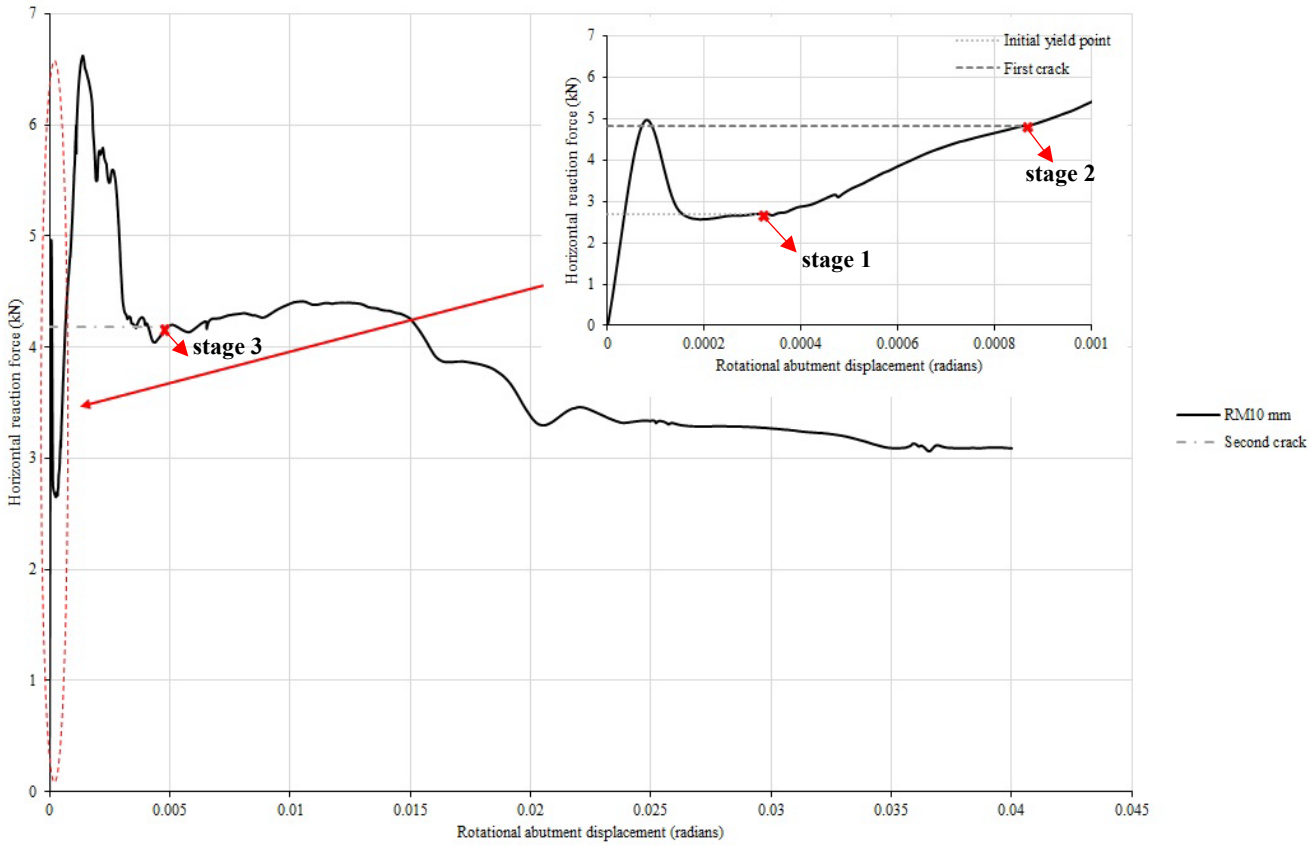

Figure 6-19: Horizontal reaction force against rotational abutment displacement.

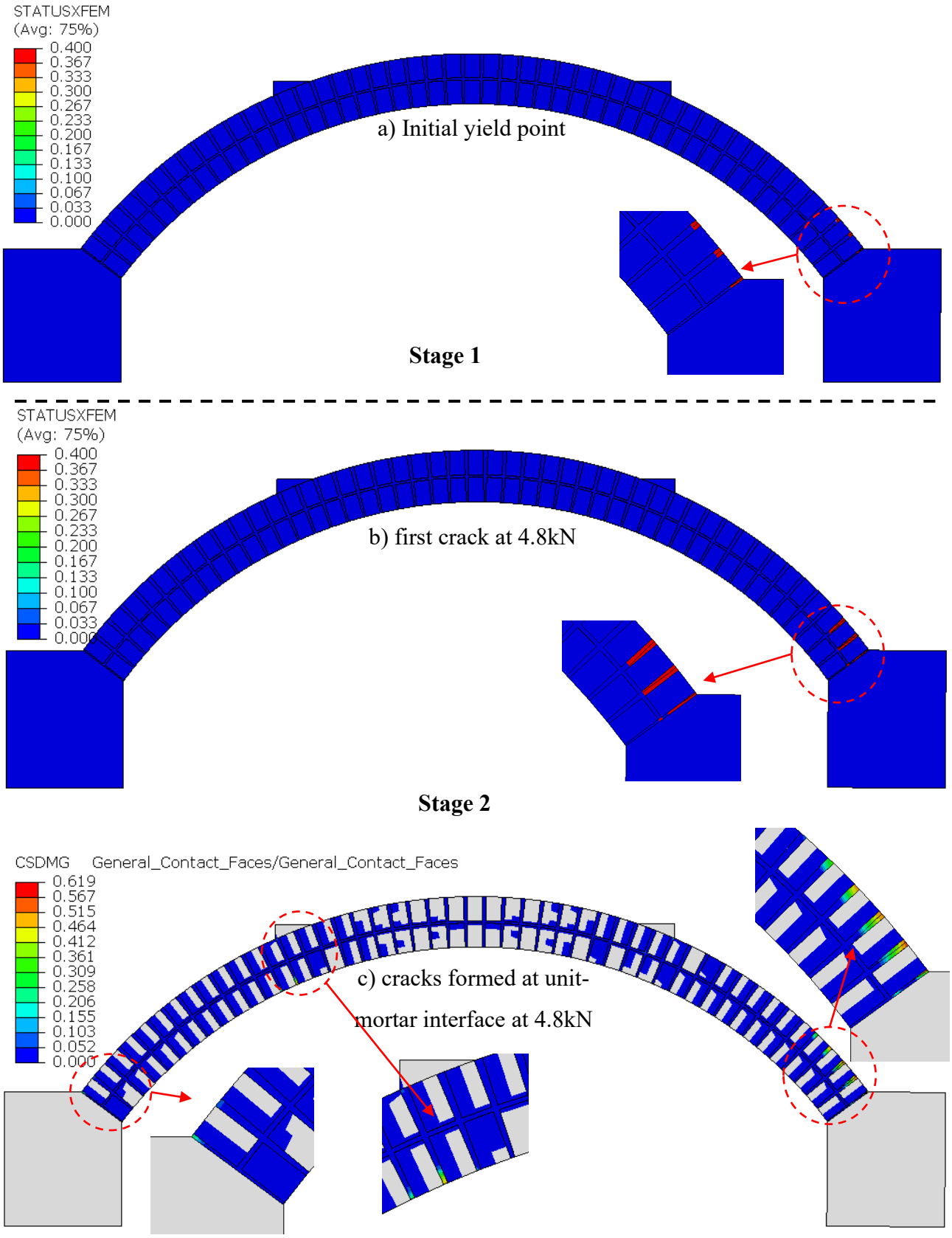

Figure 6-20: Crack simulation progress at stages 1 and 2 for right abutment rotation (0.04 rad).

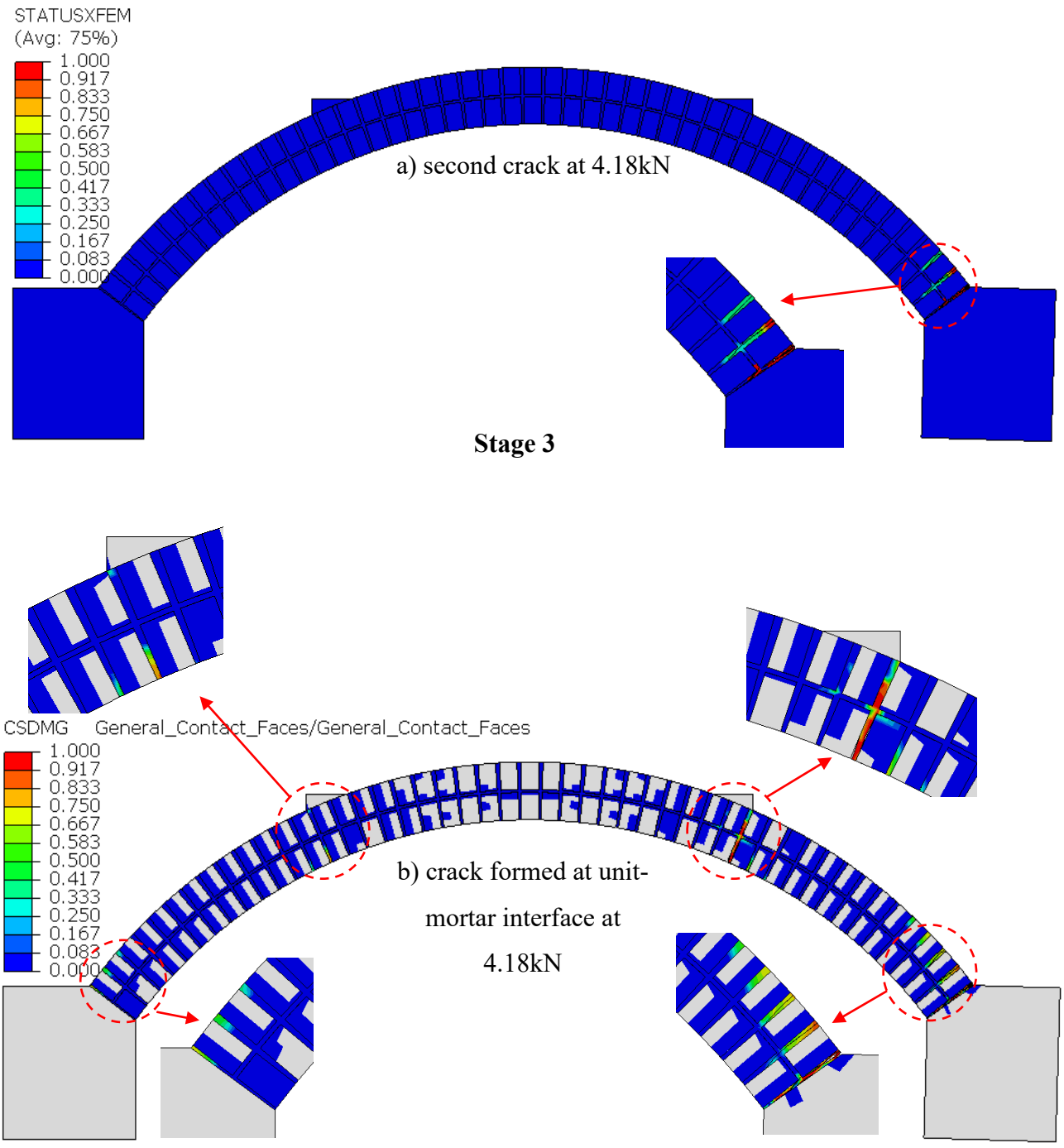

Figure 6-21: Crack simulation progress at stages 1 and 2 for right abutment rotation (0.04 rad).

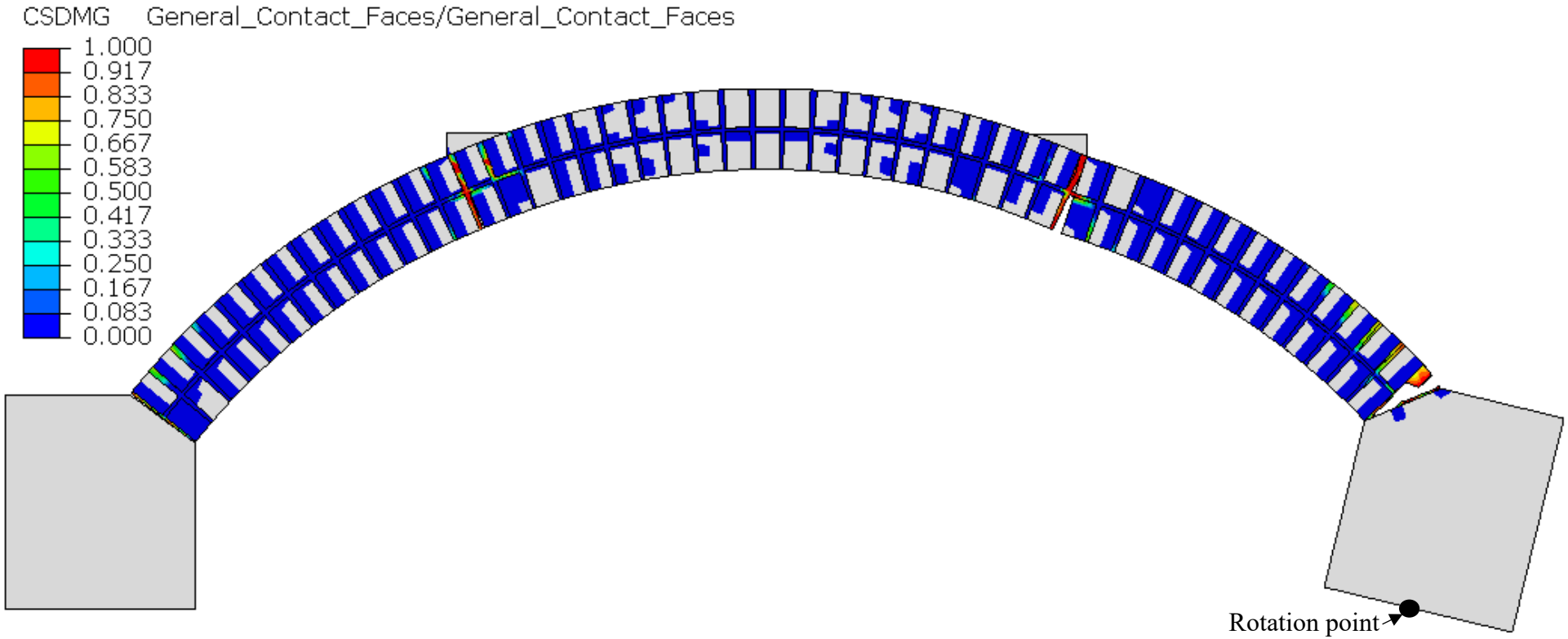

Figure 6-22: The last simulation step deformed shape for the right abutment 10mm (0.04 rad) rotational movement (interface failure).

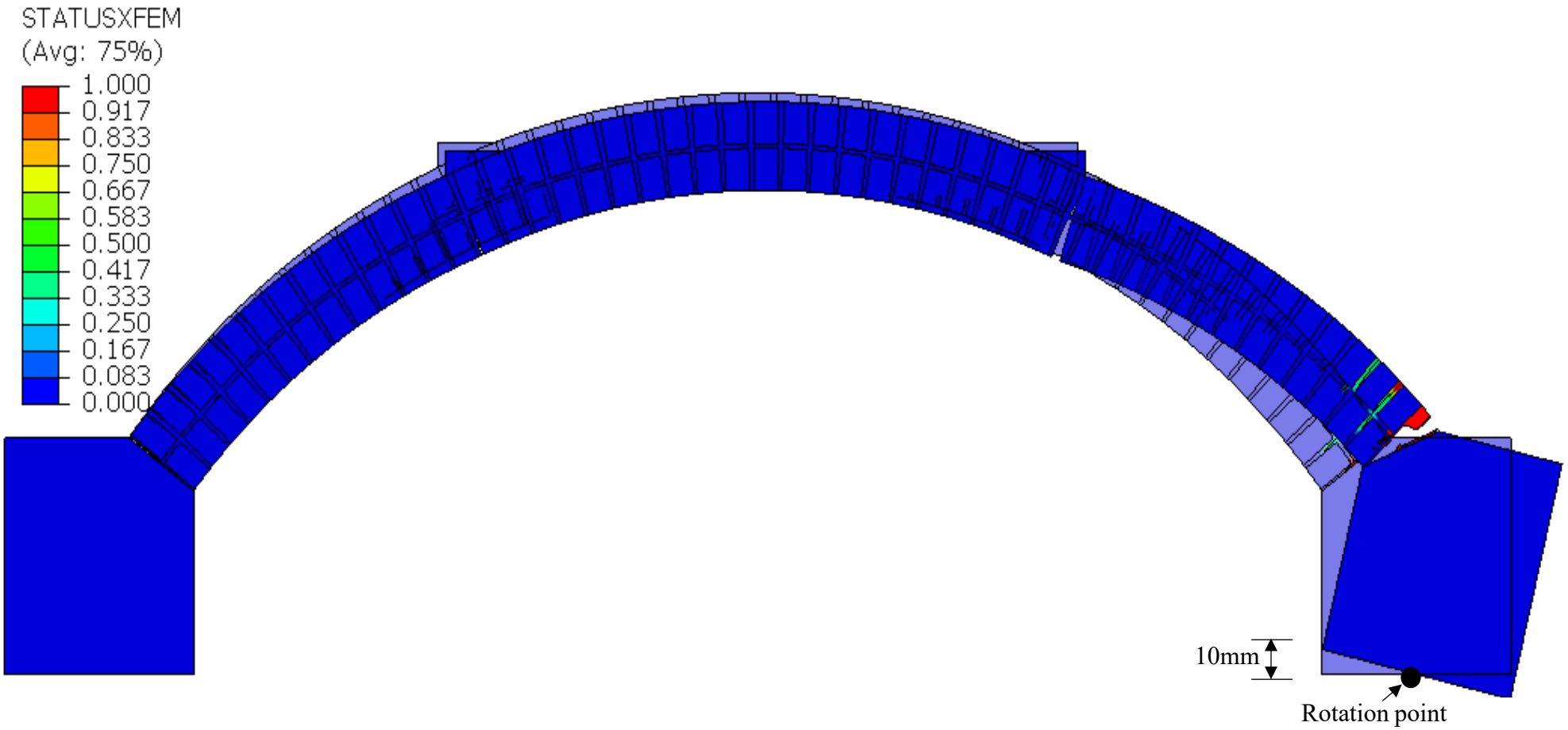

Figure 6-23: The last simulation step output of the arch deformation resulting from the right abutment 10mm (0.04 rad) rotational movement (cracking failure).

6.2.5 *Influence of horizontal & vertical combination abutment movements*

This section provides a combination movement analysis of horizontal and vertical movements of an abutment of 1mm.

This simulation of movement uses the same model and loading as the previous individual movement cases described in section 6.2. The model was loaded in three general static steps under displacement control. The combination movements in horizontal and vertical directions were applied simultaneously at the right abutment, as the simulation is a quasi-static analysis.

In general, the analysis of the displacement value of 1mm in both directions developed two major radial cracks, where the first crack formed in the mortar joint at the intrados of the quarter span under the dead load location, as shown in Figure 6-28. The second crack formed at the unit-mortar interface at the extrados of the left-hand side springing of the arch, as shown in Figure 6-27 (b). The third crack started to form at the unit-mortar interface at the intrados of the masonry arch, as shown in Figure 6-28.

The simulation progress of each step during the combination movement of 1mm was highlighted in Figure 6-26 and Figure 6-27. Figure 6-25 displays the vertical reaction force-displacement graph highlighting the crack process.

This analysis significantly impacted the arch barrel at the left-hand side, as two cracks formed in the arch barrel. Figure 6-24 shows the initial yield point that occurred at the horizontal reaction force of 2.12kN, as shown in Figure 6-26 (a); then, at the maximum reaction force, the crack had reached the inter-ring mortar joint, as shown in Figure 6-26 (b). Furthermore, at the maximum reaction force, the second crack formed at the unit-mortar interface, and further cracks started developing in the arch barrel, as shown in Figure 6-26 (c).

Figure 6-27 shows the arch behaviour at horizontal reaction force of 4.17kN. Both cracks have passed through the inter-ring mortar joint.

Mortar cracks started to occur under tension when the maximum tensile strength is reached. Moreover, the arch ring cracks represent the separation of the elements in tangential and radial directions. This shows that the masonry arch material model has a limited tensile capacity. Also,

the stress-strain material relationship provides that the masonry arch compressive strength is assumed to be limited to a material crushing strength value.

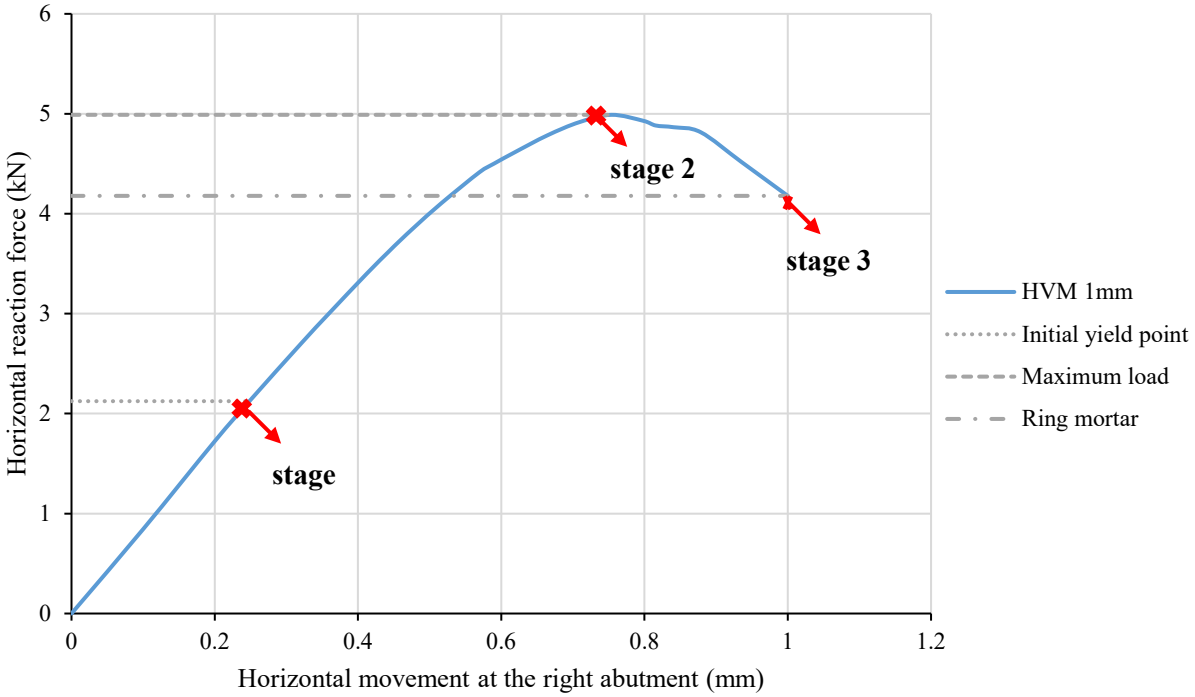

Figure 6-24: Horizontal reaction force - horizontal displacement of right abutment for horizontal and vertical movements of 1mm.

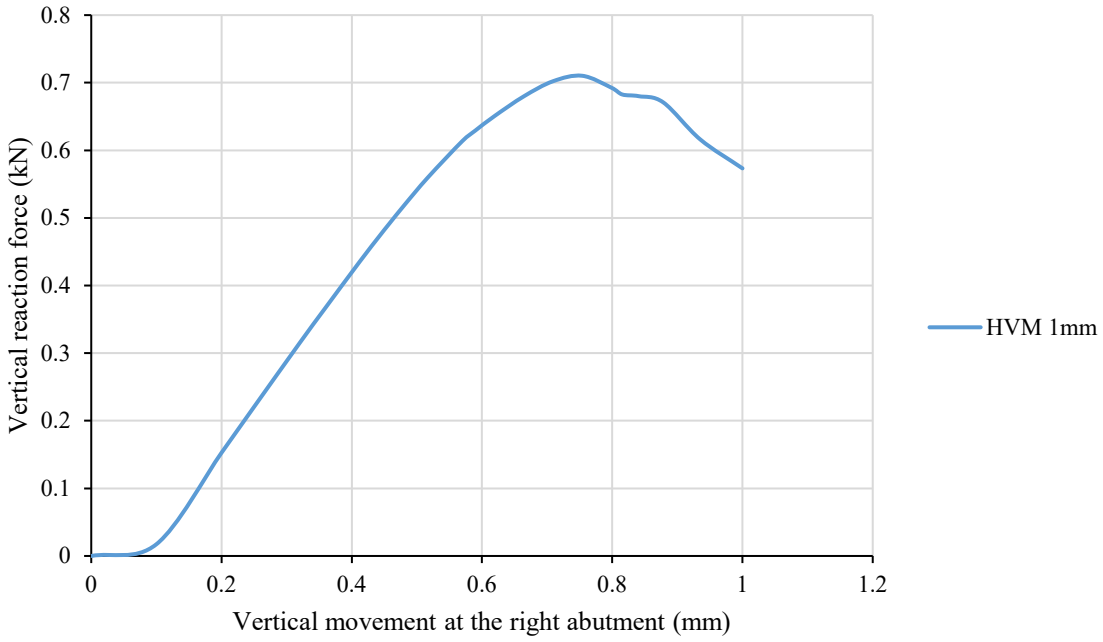

Figure 6-25: Vertical reaction force - vertical displacement of right abutment for horizontal and vertical movements of 1mm.

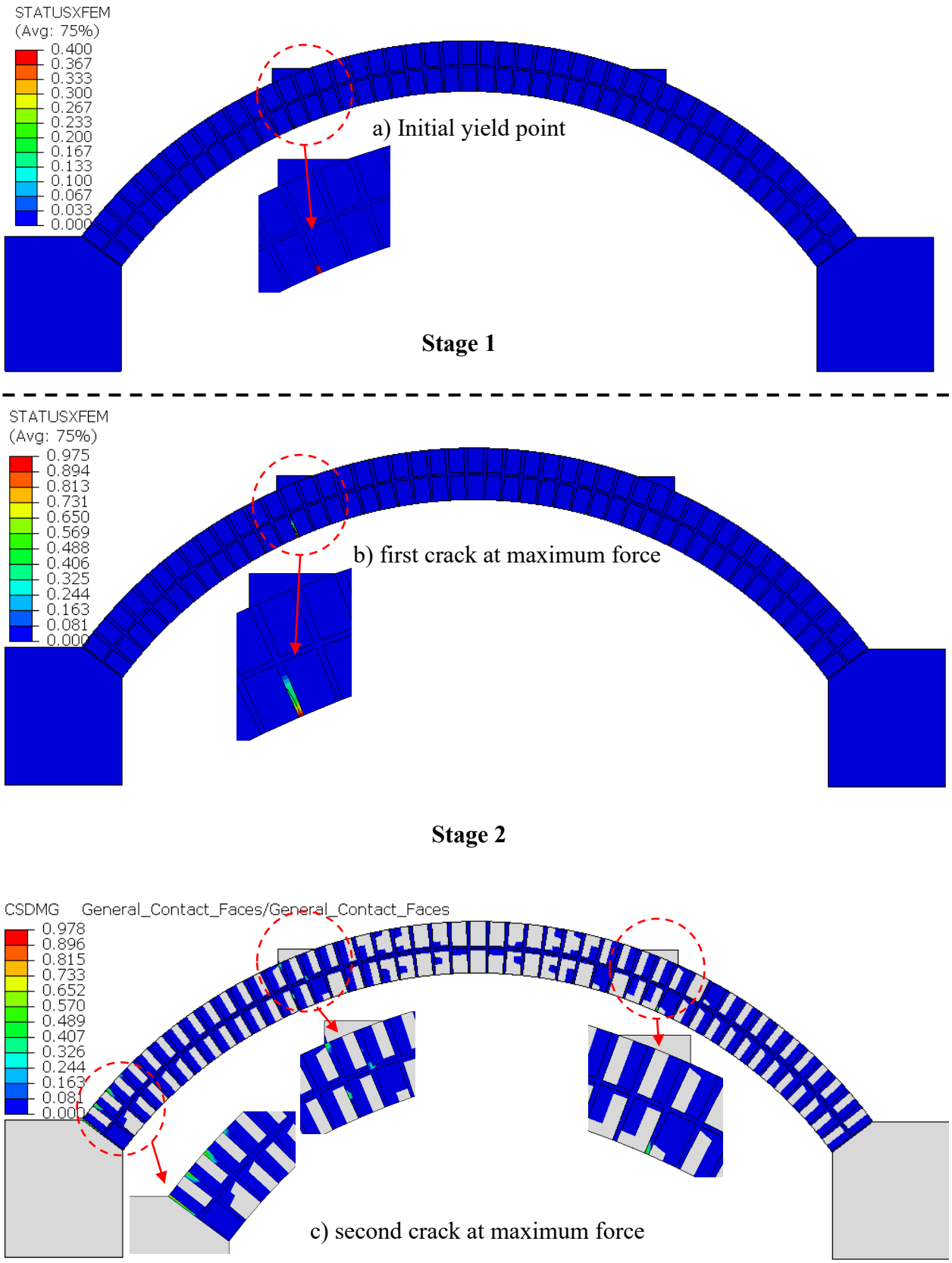

Figure 6-26: Crack simulation progress at stages 1 and 2 of right abutment 1mm combination movements.

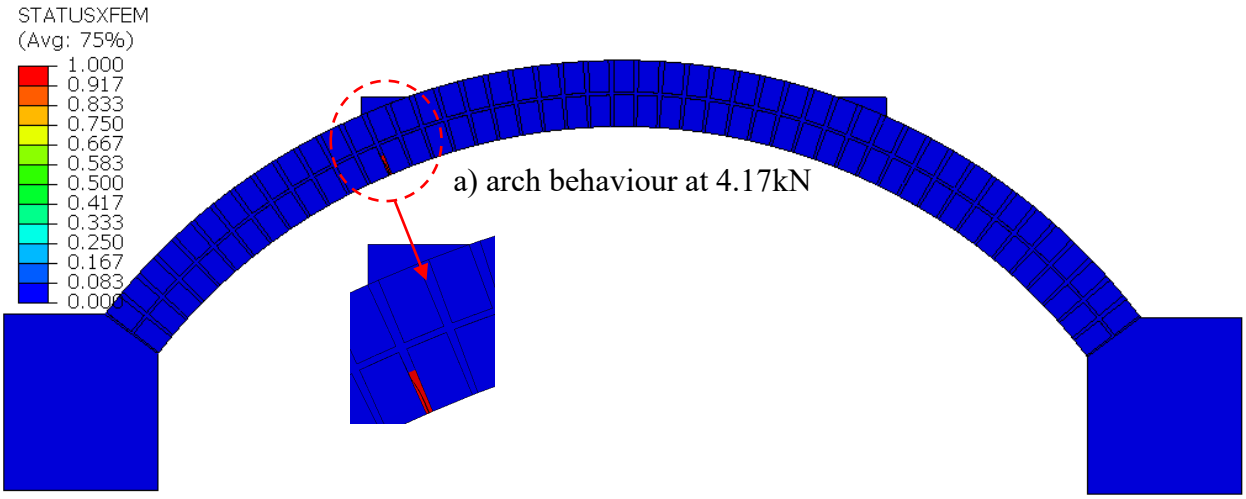

Stage 3

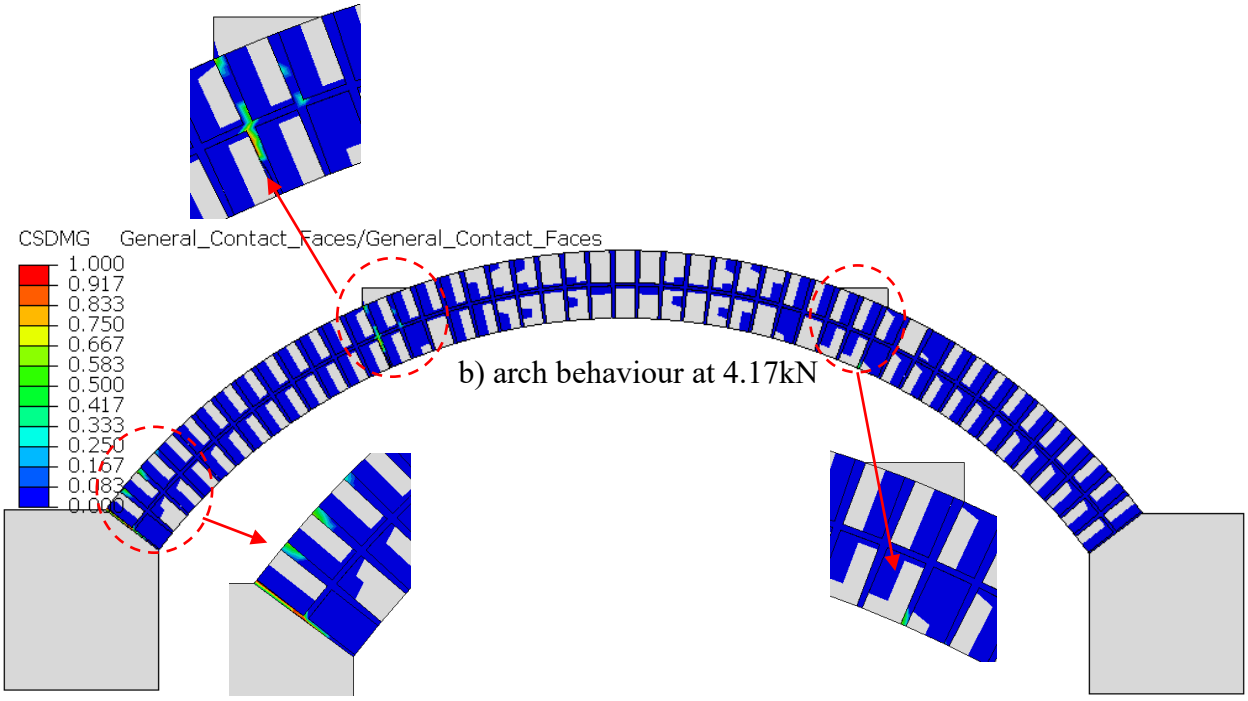

Figure 6-27: Crack simulation progress at stage 3 of right abutment 1mm combination movements.

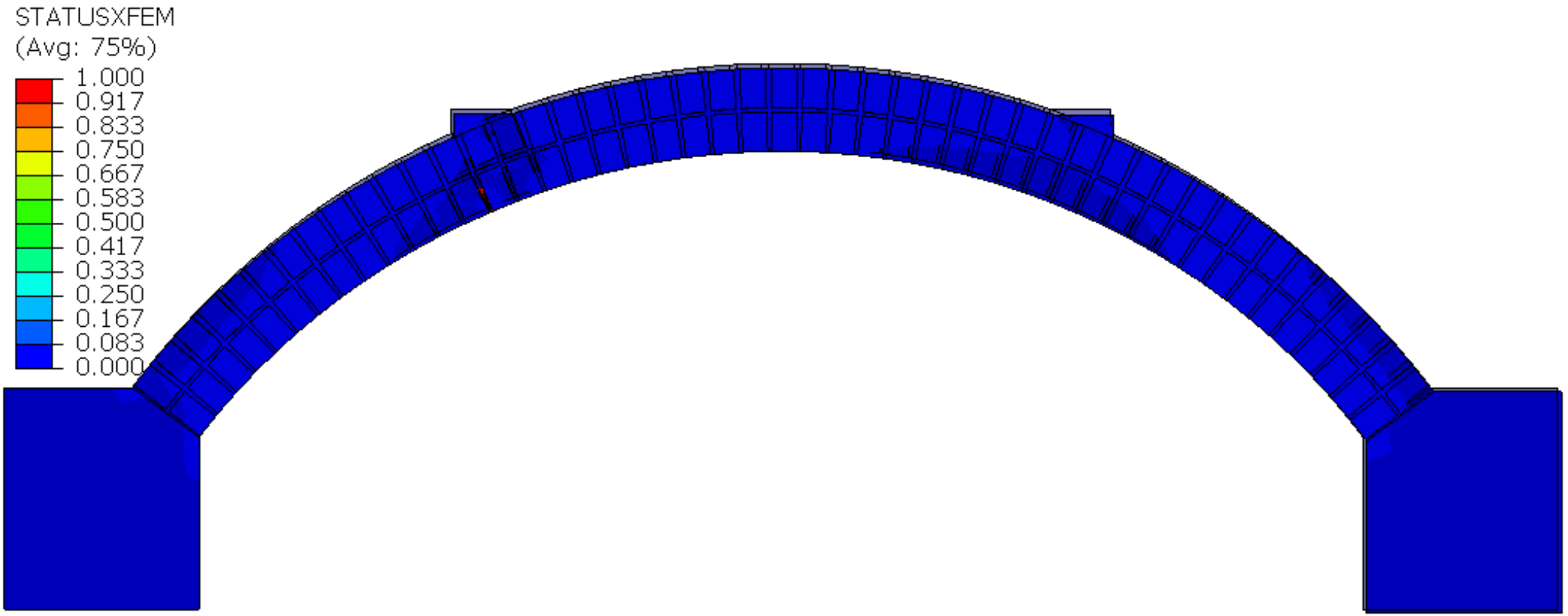

Figure 6-28: Deformed shape for 1mm combination movements (cracking failure).

6.3 Masonry arch movement under live load influences

This section provides a further numerical simulation model to investigate the Arch G responses to various direction displacements at the right abutment before the masonry arch was subjected to an imposed load at the quarter span location. The model analysed used static steps (quasi-static) analysis under displacement control. In addition, the validated masonry arch is used with the same arch geometry, material properties, interaction properties, and mesh density to the previous analysis models.

The model procedure was conducted using four steps,

1. In the first step, gravity was applied to generate the arch barrel self-weight, as shown in Figure 6-29.
2. In the second step, dead loads of 10kN were applied at the quarter and three-quarter spans each, as shown in Figure 6-30.
3. In the third step, the right abutment of the masonry arch model was displaced in different directions by various displacement values, as shown in Figure 6-31.
4. In the fourth step, the live load was applied at the quarter span of the arch under displacement control until the masonry arch model become unstable, as shown in Figure 6-32.

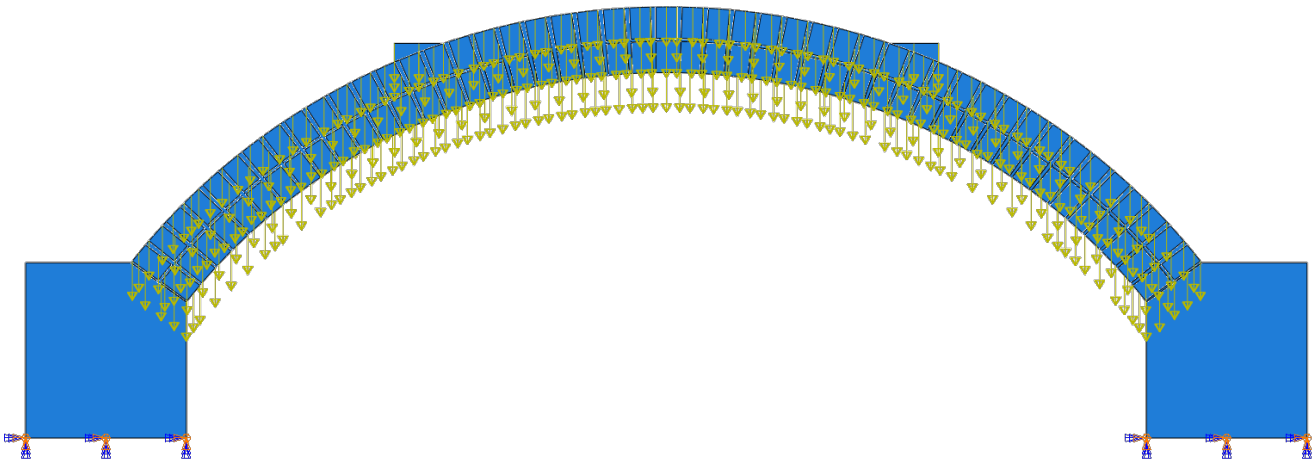

Figure 6-29: Gravity (self-weight) is applied on the masonry arch multi-ring.

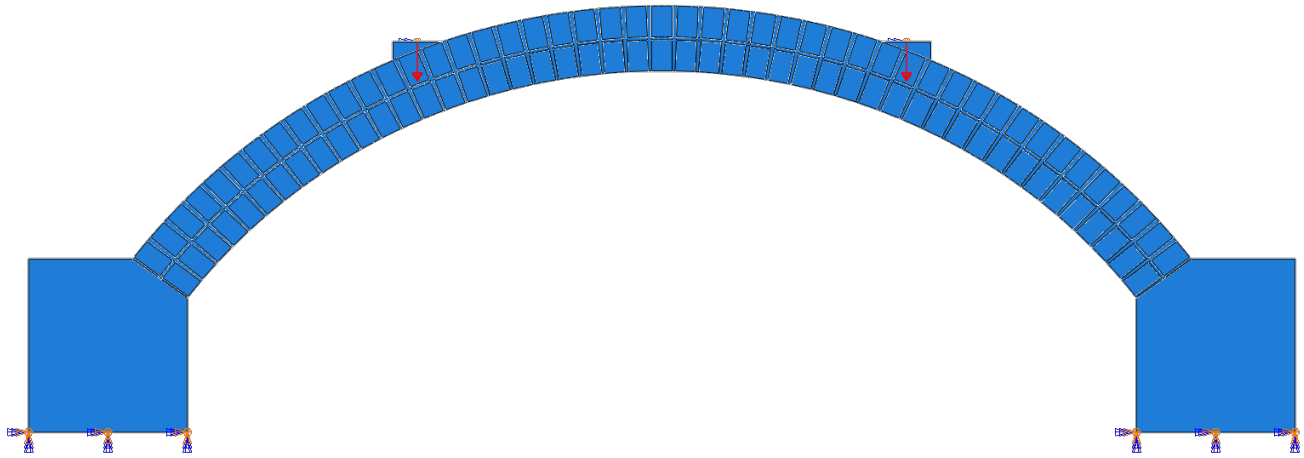

Figure 6-30: Dead loads of 10kN are applied at the quarter and three-quarter span each.

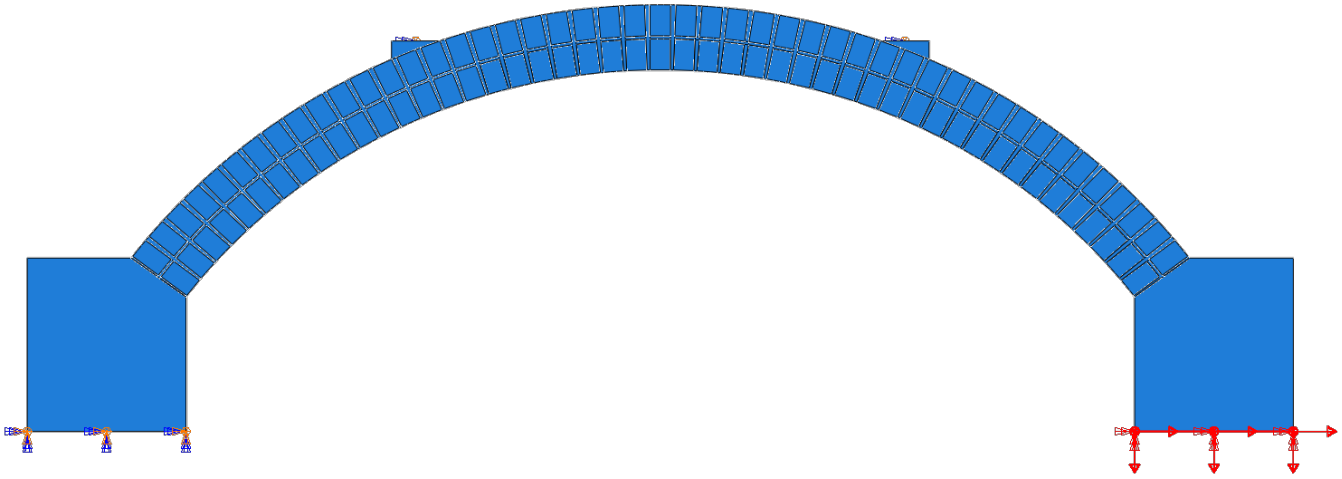

Figure 6-31: Various displacement is applied at the right-hand abutment.

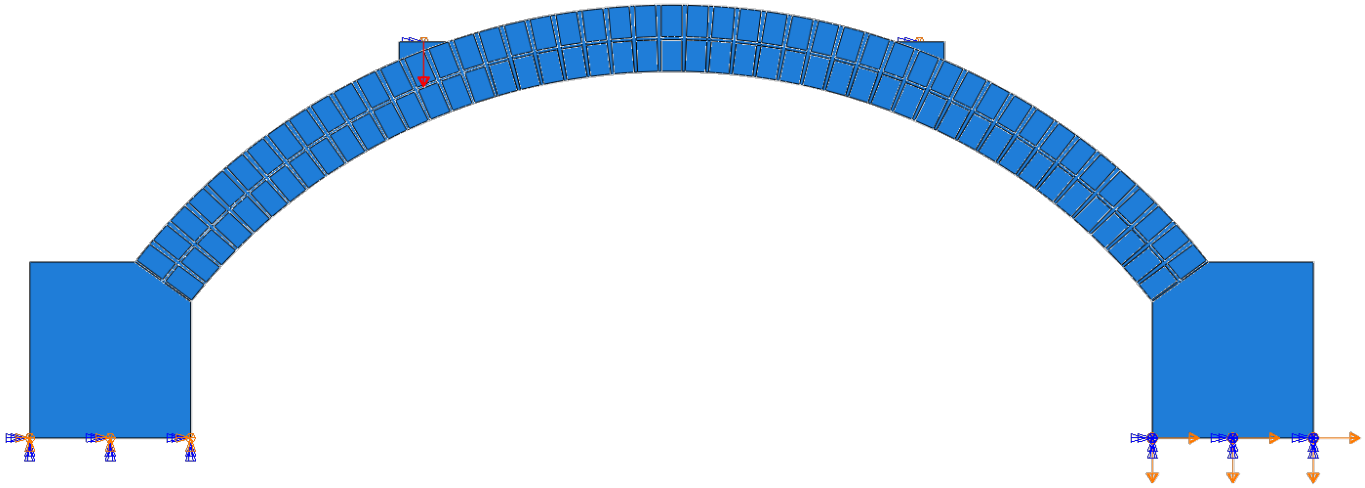

Figure 6-32: Live load is applied at the arch quarter span.

6.3.1 *Horizontal abutment movement analysis result*

This section provides the simulation analysis results of horizontal movement of 1mm, 5mm and 8mm before the live load was applied at the quarter span under displacement control. Figure 6-33 shows the graph of live load against the deflection at the quarter span, for four numerical models, which have fixed abutments, and abutments subject to 1, 5 and 8mm horizontal movements. Figure 6-36 and Figure 6-37 show cracking deformation only for the model which is subject to 8mm movement.

As a result of the horizontal movement of 8mm before the load was applied, there were already four significant cracks, where the first two cracks were located at the quarter and three-quarter span as opened cracks formed in the mortar joints at the arch intrados growing towards the arch extrados, as shown in Figure 6-36 (a). Also, Figure 6-36 (b) displays the other two opened cracks formed at the unit-mortar interface at the arch extrados. Figure 6-33 shows that the masonry arch barrel has a small capacity to resist the live load compared to the fixed masonry arch and the other horizontal movement values.

The live load was applied at the quarter span, and the four cracks grew further through the arch's thickness. The mortar joints continued separating until the last step of the numerical simulation, as shown in Figure 6-36 (c) and Figure 6-37. Also, because a full hinge had developed at the right abutment, the remaining mortar was under high compression.

As indicated in Figure 6-33, the horizontal movement and live load significantly changed the arch barrel behaviour. The effects of the 8mm horizontal movement were reduced load capacity of 5kN and an almost complete loss of stiffness. However, 1mm horizontal movement did not lead to a significant change in terms of peak load variation. Still, it led to a small difference in initial elastic stiffness compared to the masonry arch model fixed numerical simulation.

The 8mm horizontal movement numerical simulation greatly affected the masonry arch barrel. It reduced the peak load capacity and initial elastic stiffness of the arch compared to the fixed numerical simulation model results, as shown in Figure 6-33. It is confirmed by Figure 6-38, where it can be noted that the masonry arch model fully developed four hinge mechanism, due to the mortar joint at the three-quarter span of the arch completely cracking and separating the mortar joint between the two rings. Also, Figure 6-38 shows the crack at the quarter span cracking through the width of the arch.

Figure 6-33 shows a difference in the initial elastic stiffness between all results of the numerical models. There is a slight difference between the fixed masonry arch model and the 1mm horizontal movement model. However, there is substantial difference regarding the peak load variation and the elastic stiffness between the fixed numerical model and horizontal movement numerical models of 5mm and 8mm displacements.

It is noted that when horizontal movement is increased from 1mm to 5mm, there is a substantial drop in capacity of more than 80%, as shown in Figure 6-33.

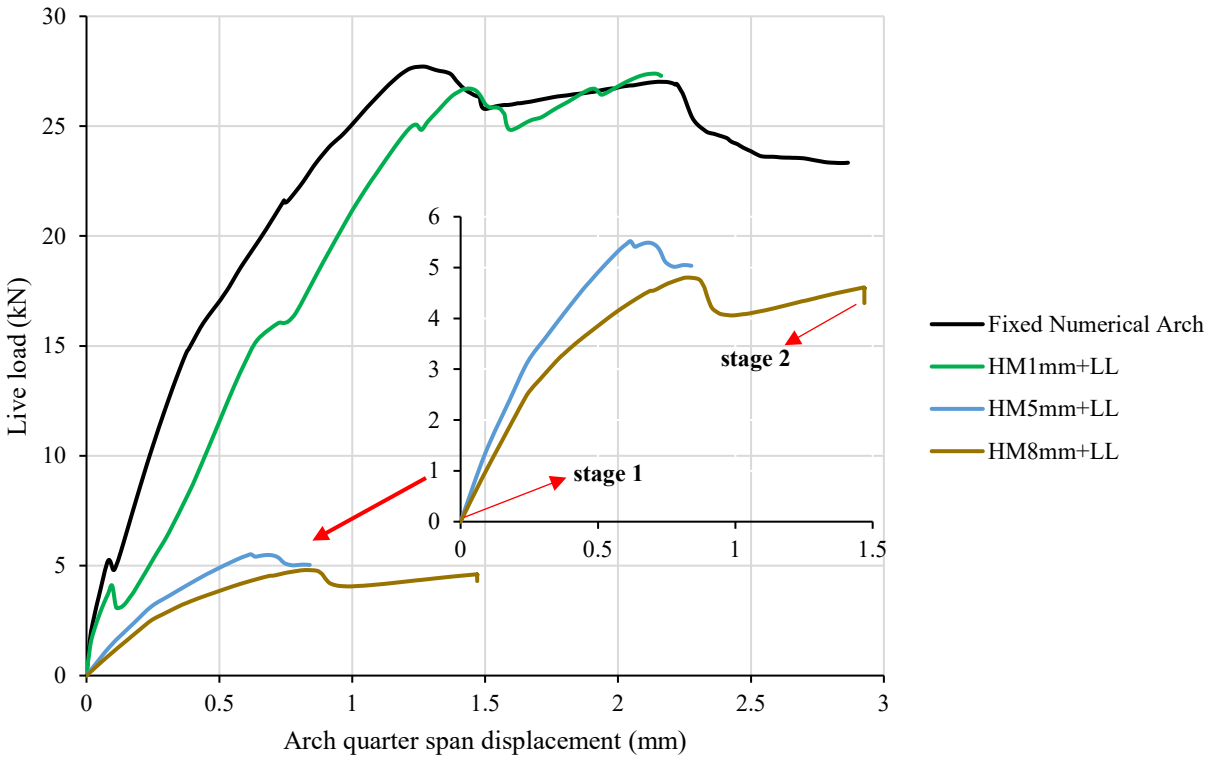

Figure 6-33: Live load against quarter span displacement for four numerical models subject to horizontal movement with live load.

The comparison between the rigid abutment model and the model with 1 mm horizontal movement reveals a negligible difference in peak load, approximately 1.4%. Conversely, the models with higher horizontal movements of 5 mm and 8 mm exhibit significant reductions in peak load, by around 83%. This indicates that a horizontal movement greater than 5 mm directly and substantially impacts the peak load, as illustrated in Figure 6-34.

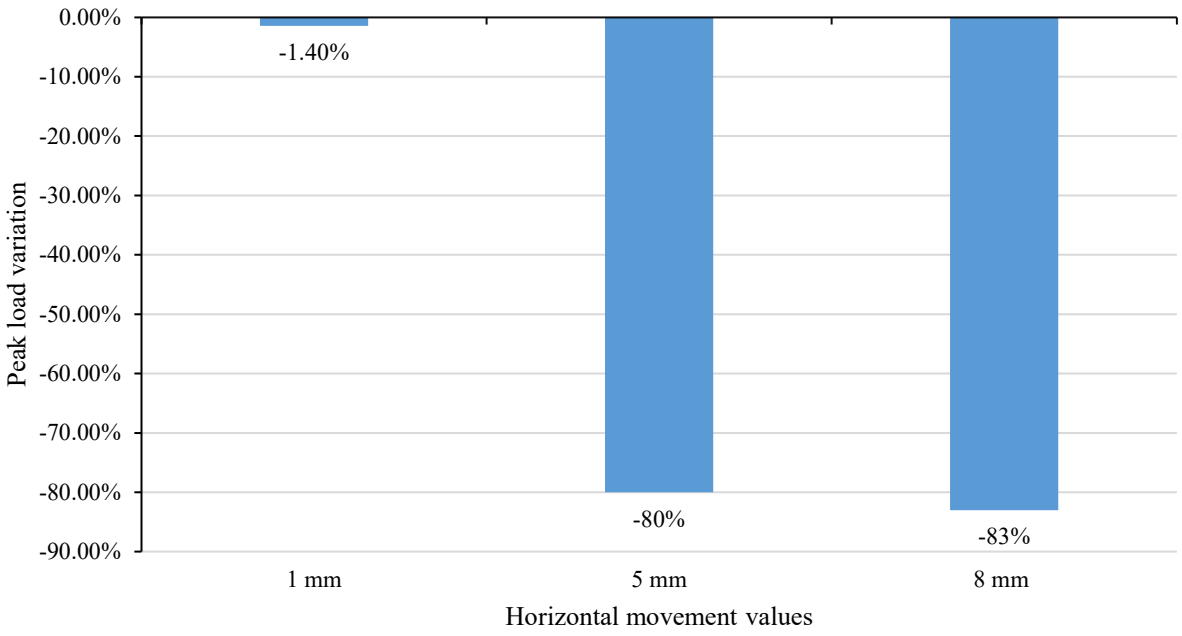

Figure 6-34: Effect of horizontal movement on the peak load of the masonry arch.

Figure 6-35 demonstrates that horizontal movement markedly influences the masonry arch and its initial elastic stiffness. For a horizontal movement of 1 mm, there is a 33% stiffness reduction compared to the fixed abutment, while the maximum reduction is observed for movements of 5 mm and 8 mm, with values varying between 70-80%.

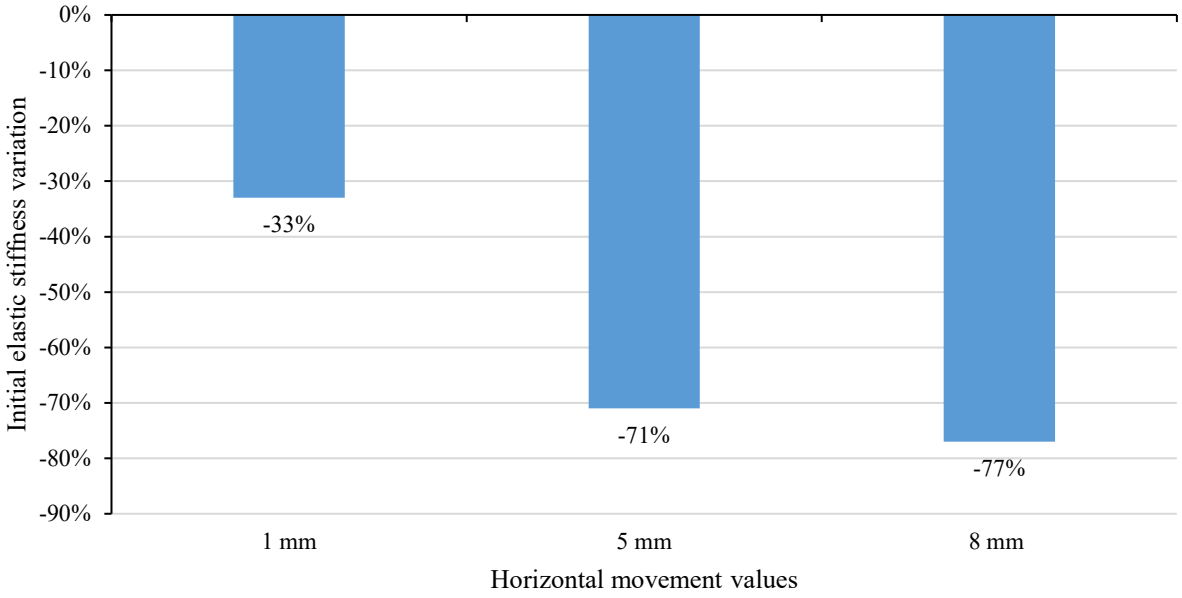

Figure 6-35: Effect of horizontal movement on the elastic stiffness of the masonry arch.

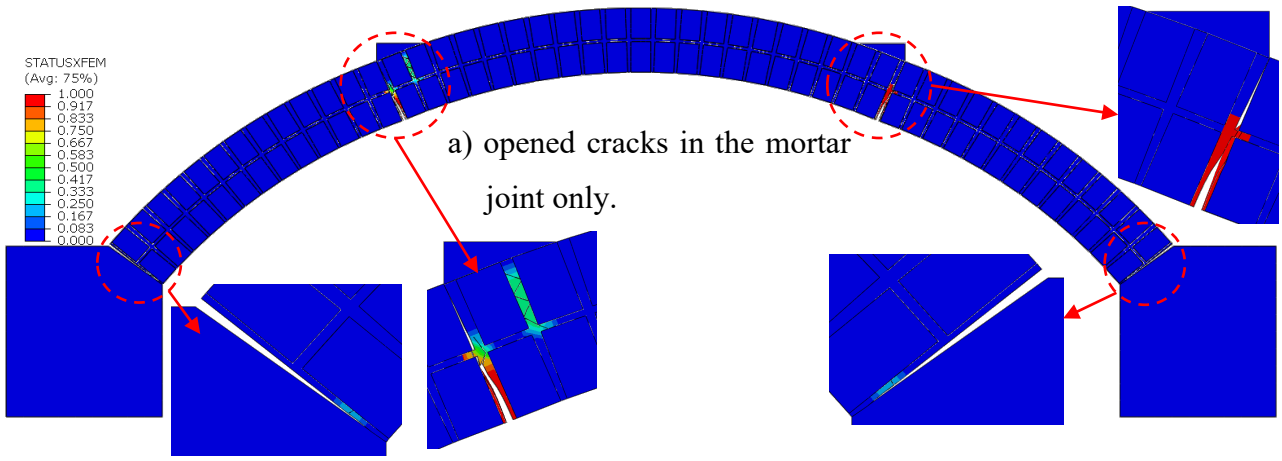

Stage 1

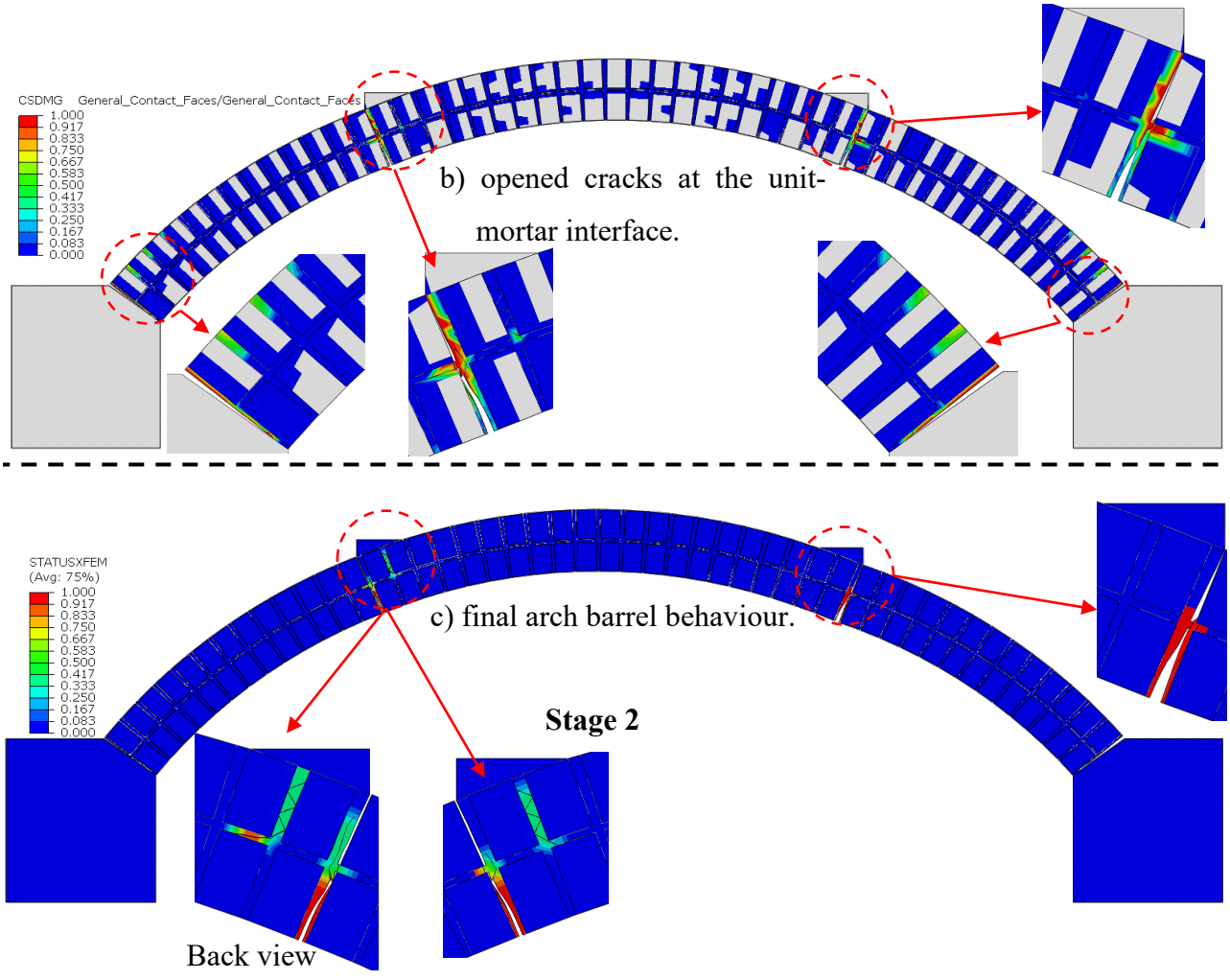

Figure 6-36: Crack simulation progress at stages 1 and 2 of the horizontal movement with live load.

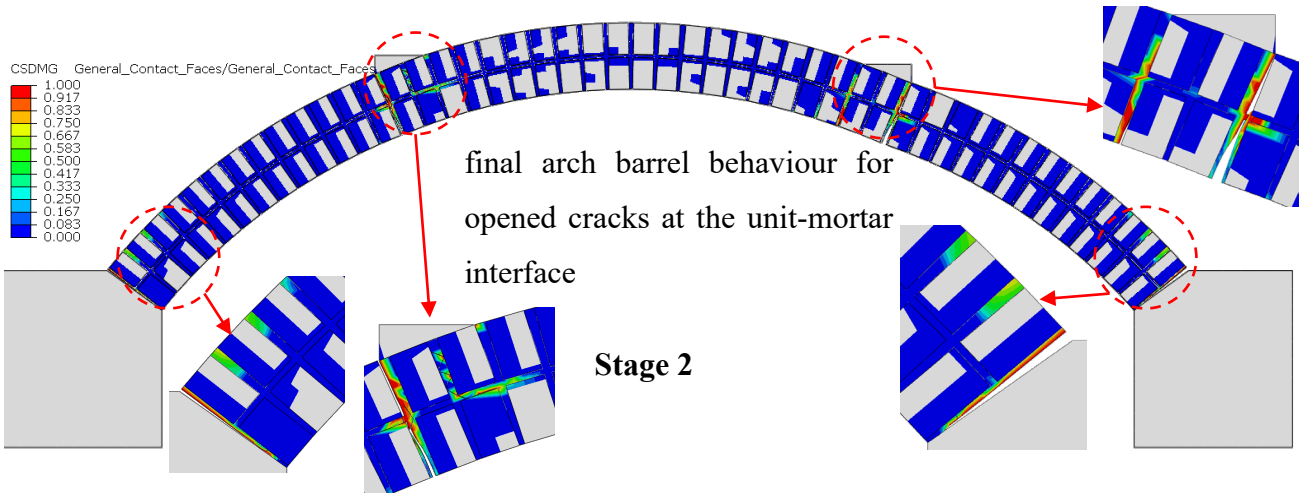

Figure 6-37: Crack simulation progress at stage 2 of the horizontal movement with live load.

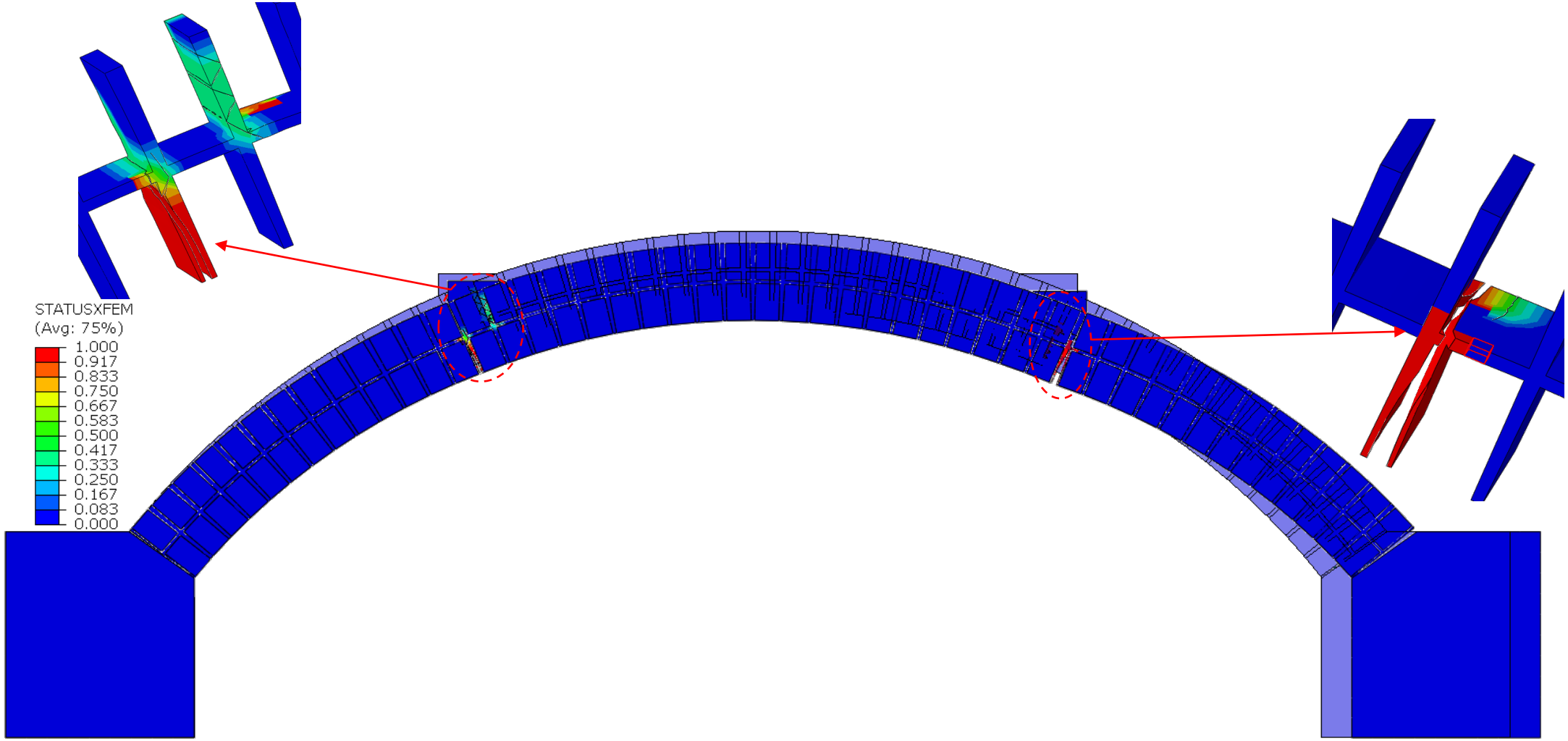

Figure 6-38: The final deformed shape for horizontal movement and live load (cracking failure).

6.3.2 *Vertical abutment movement analysis result*

This section provides the simulation analysis results of vertical movement of 1mm, 5mm and 10mm before the live load was applied at the quarter span under displacement control. Figure 6-39 shows the graph of live load against the deflection at the quarter span for fixed and vertical movements numerical models. Figure 6-42 and Figure 6-43 show only the worst-case scenario (10mm) has been explored.

Figure 6-39 generally shows that the initial elastic stiffness reduces as vertical movement increases. It can be noted that the elastic stiffness of the fixed and 1mm vertical movement numerical models remains the same until 16kN, where there is a considerable variation between the fixed and 10mm vertical movement numerical models in terms of initial elastic stiffness. The 10mm vertical movement model formed a mechanism at 26.5kN.

Before the load was applied to the arch barrel, one significant crack formed in the mortar joint due to the vertical movement of 10mm; Figure 6-42 (a) demonstrates that the crack at the intrados three-quarter span arch reached the inter-ring mortar joint. Four cracks also developed at the unit-mortar contact at the quarter and three-quarter span arch and the right hand side abutments, as shown in Figure 6-42 (b). The two cracks at the quarter and three-quarter span did not pass through the inter-ring mortar joint as part of the vertical mortar joints were still in contact with the brick interface before the live load was applied.

Figure 6-42 (c) shows the arch barrel behaviour after the live load was applied at 14.3kN; the four cracks also developed at the unit-mortar contact at the quarter and three-quarter span arch, and cracks at the right and left abutments changed direction. However, the crack at the quarter span started to form at the intrados. Also, the crack formed in the mortar joint at the three-quarter span started to close at the intrados and formed in the extrados at the unit-mortar joint due to the live load applied at the quarter span.

Figure 6-43 (a) confirmed at 23kN, where the crack at the intrados three-quarter span closed compared to before the live load was applied when it was entirely separated, as shown in Figure 6-42 (a). Also, Figure 6-43 (b) shows the delamination between the unit-mortar interface at the intrados quarter span, and the four cracks grew further through the arch's thickness. It can be noticed there is ring separation at the quarter and three-quarter span. However, it is not entirely

coloured red, the crack has not developed across the entire arch width, as shown in Figure 6-43 (b).

Figure 6-44 and Figure 6-45 illustrate the final simulation deformation shape of vertical movement before the live load was applied, where Figure 6-44 presented four cracks formed at the unit-mortar interface, which means the remainder of the uncracked joints are under high compression. Figure 6-45 shows one crack formed in the mortar joint at the three-quarter arch span. However, the crack in the radial joint did not cross the entire arch barrel, as shown in Figure 6-45.

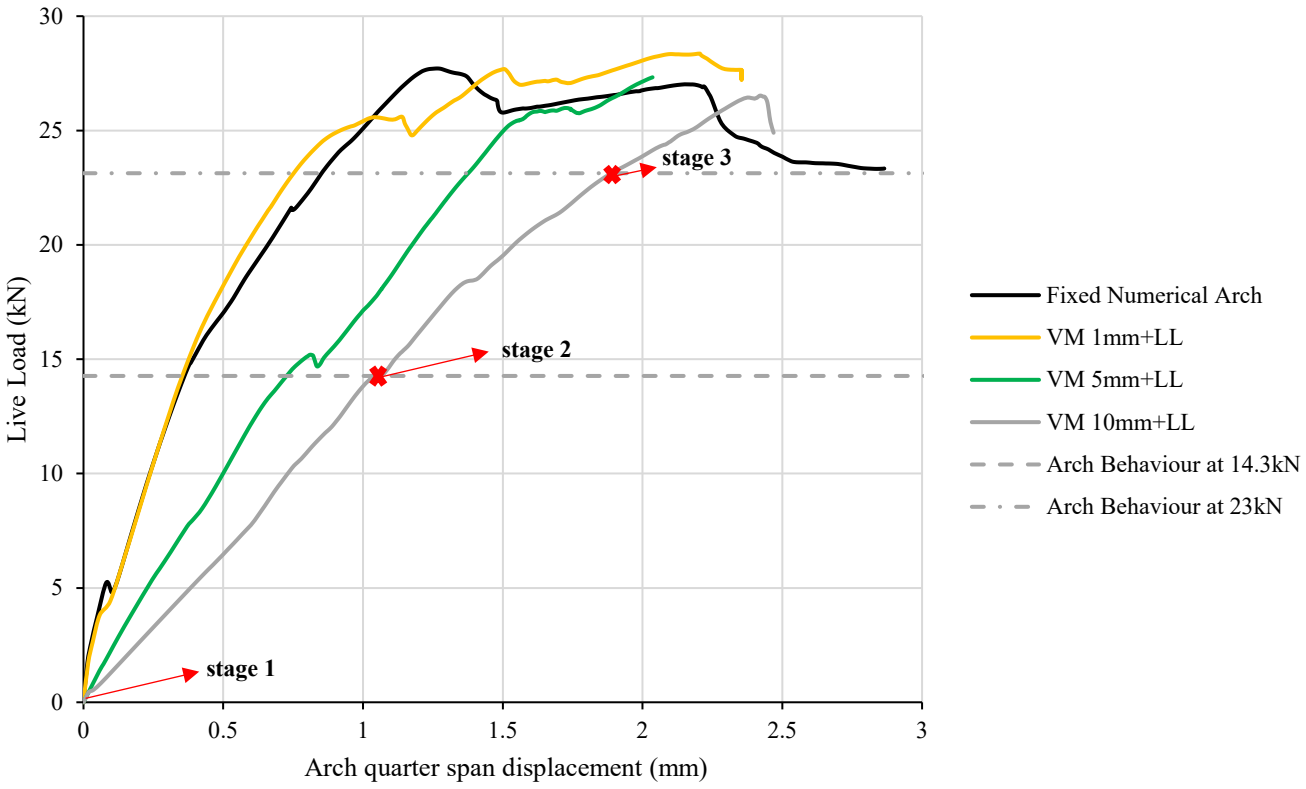

Figure 6-39: Live load against quarter span displacement for four models subject to vertical movement with live load.

Figure 6-40 compares peak loads for the vertical abutment movement models with that of the fixed abutment model. The effect of vertical movement on the peak load of the masonry arch numerical models for 1mm is less than 2%. There is less than 5% difference for the 5mm and 10mm movements.

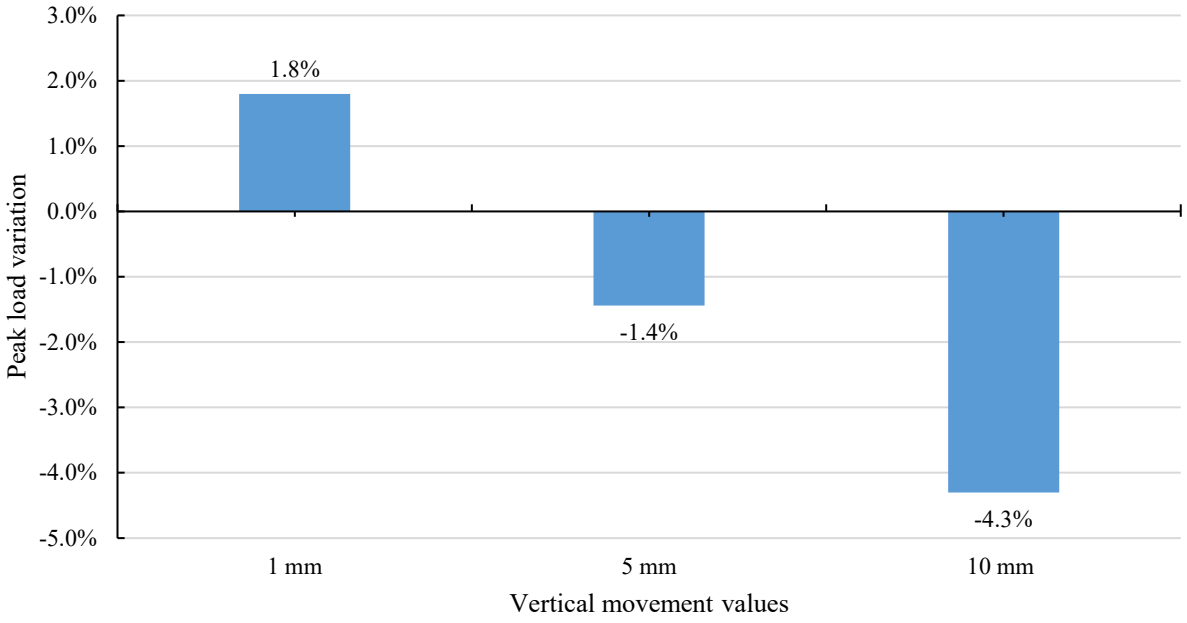

Figure 6-40: Effect of vertical movement on the peak load of the masonry arch.

Figure 6-41 displays the results of the effect of vertical movement on the initial elastic stiffness of the masonry arch. It is observed that the 1 mm vertical movement slightly improves the stiffness by approximately 3.7% (or rather the initial elastic stiffness occurs for longer). For the larger displacements, a 5 mm movement leads to a reduction of 40% and a 10 mm vertical movement results in a reduction of 62%.

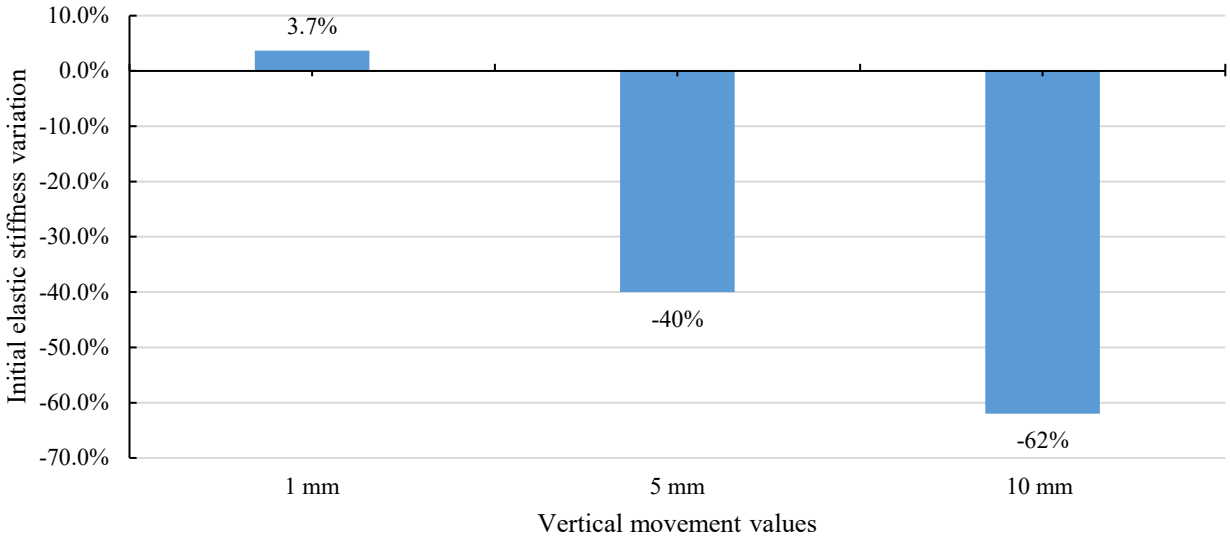

Figure 6-41: Effect of vertical movement on the elastic stiffness of the masonry arch.

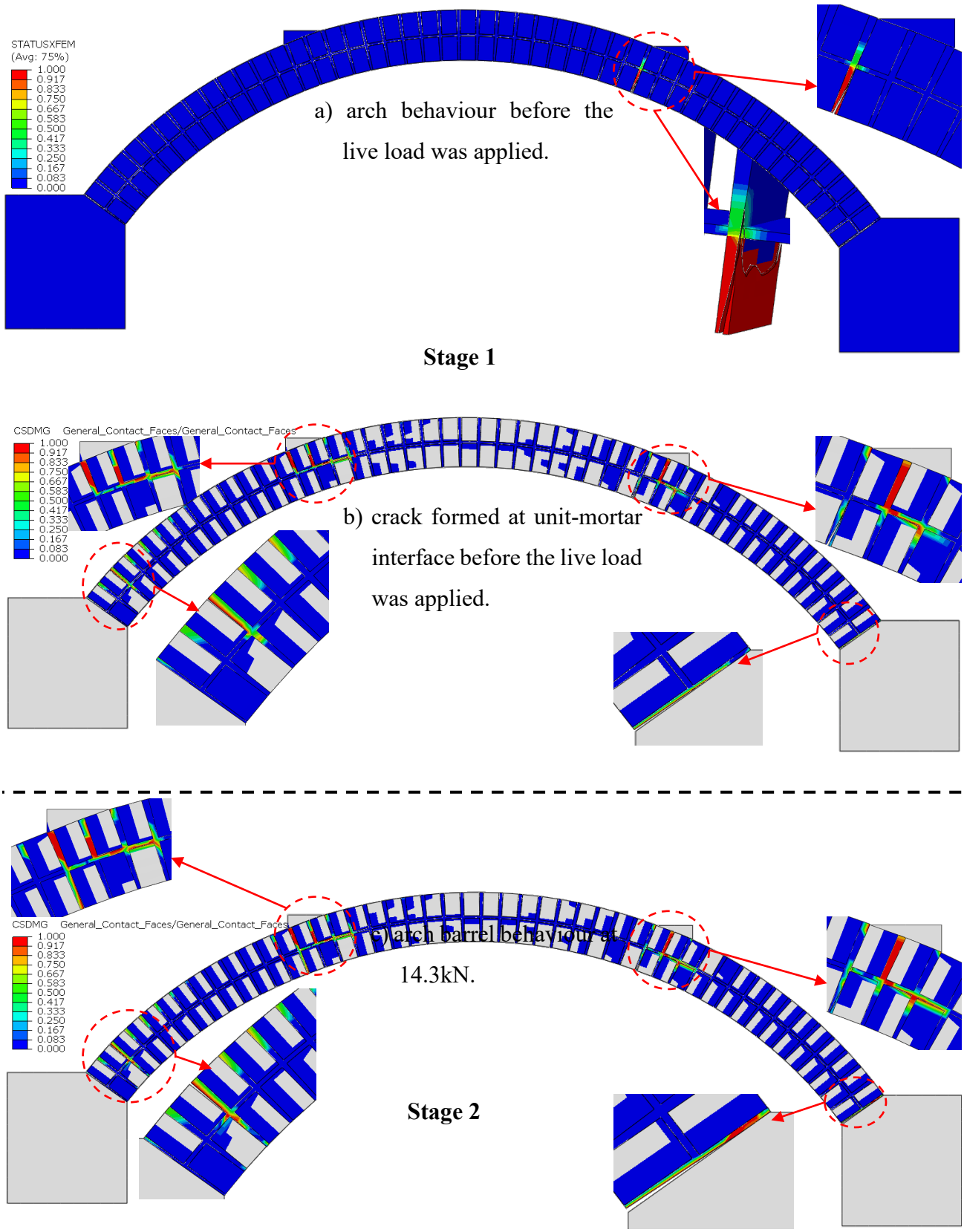

Figure 6-42: Crack simulation progress for stages 1 and 2 of vertical movement with live load.

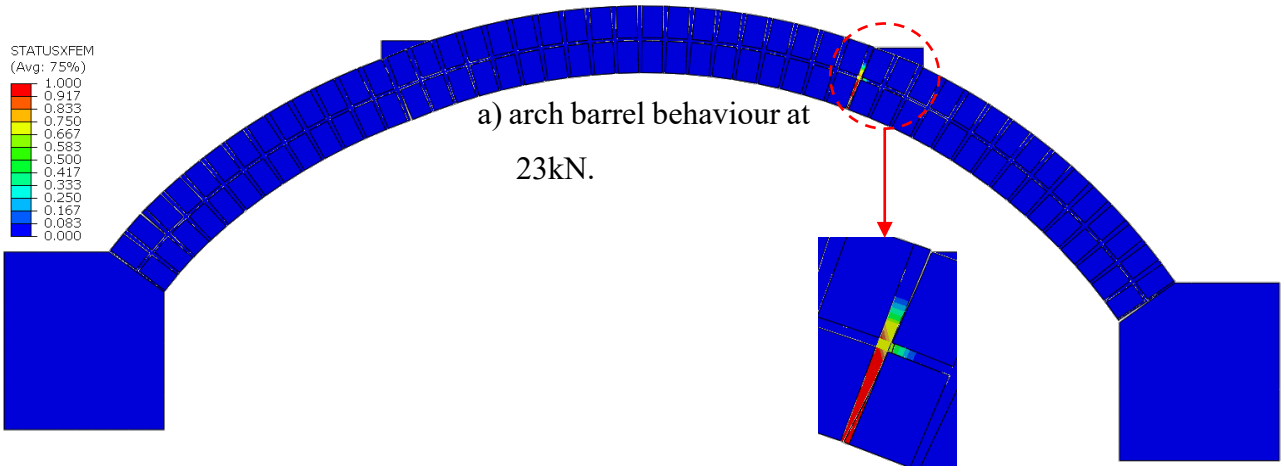

Stage 3

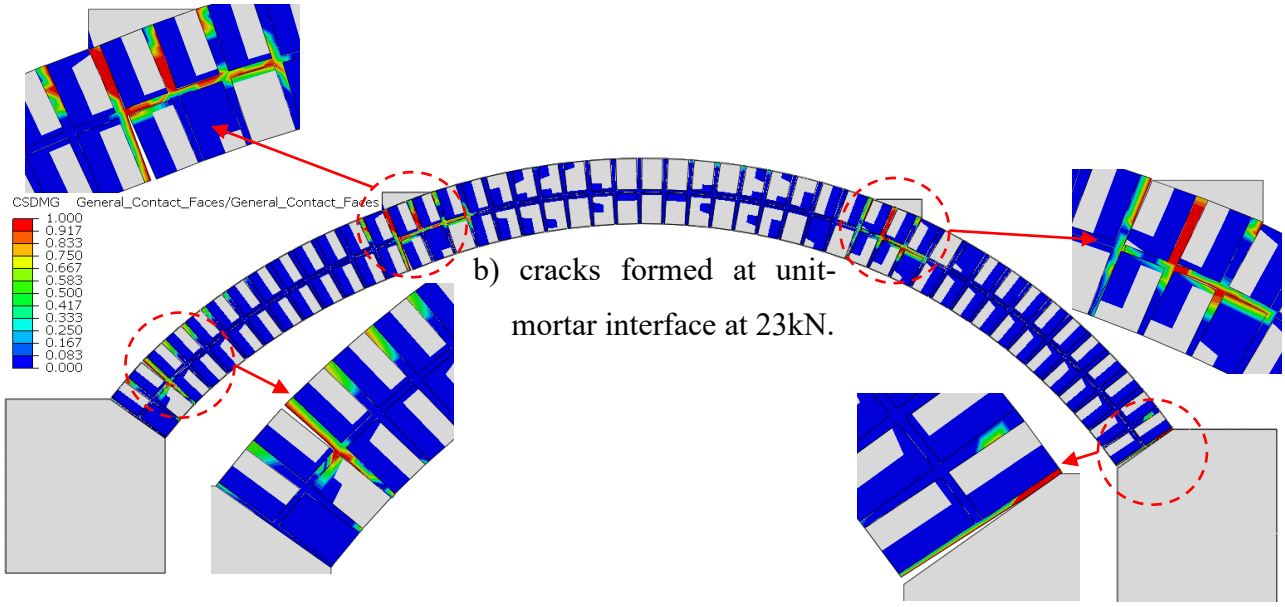

Figure 6-43: Crack simulation progress for stage 3 of vertical movement with live load.

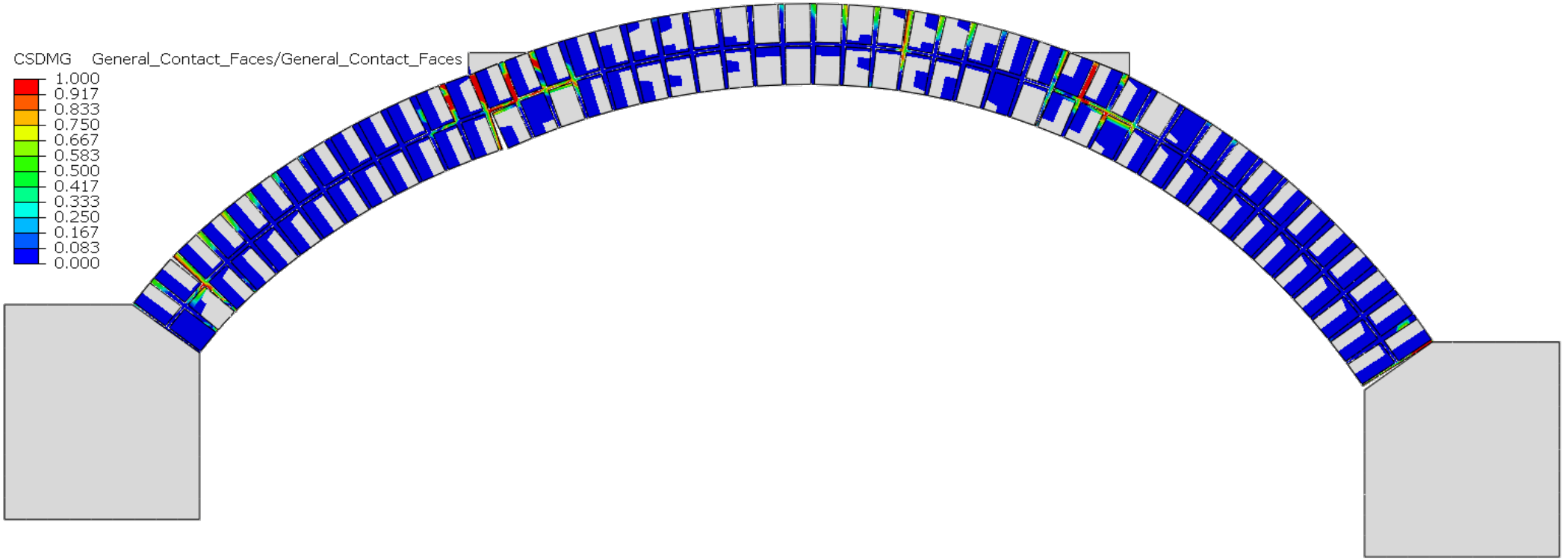

Figure 6-44: The final deformed shape crack at the interface for vertical movement and live load (interface failure).

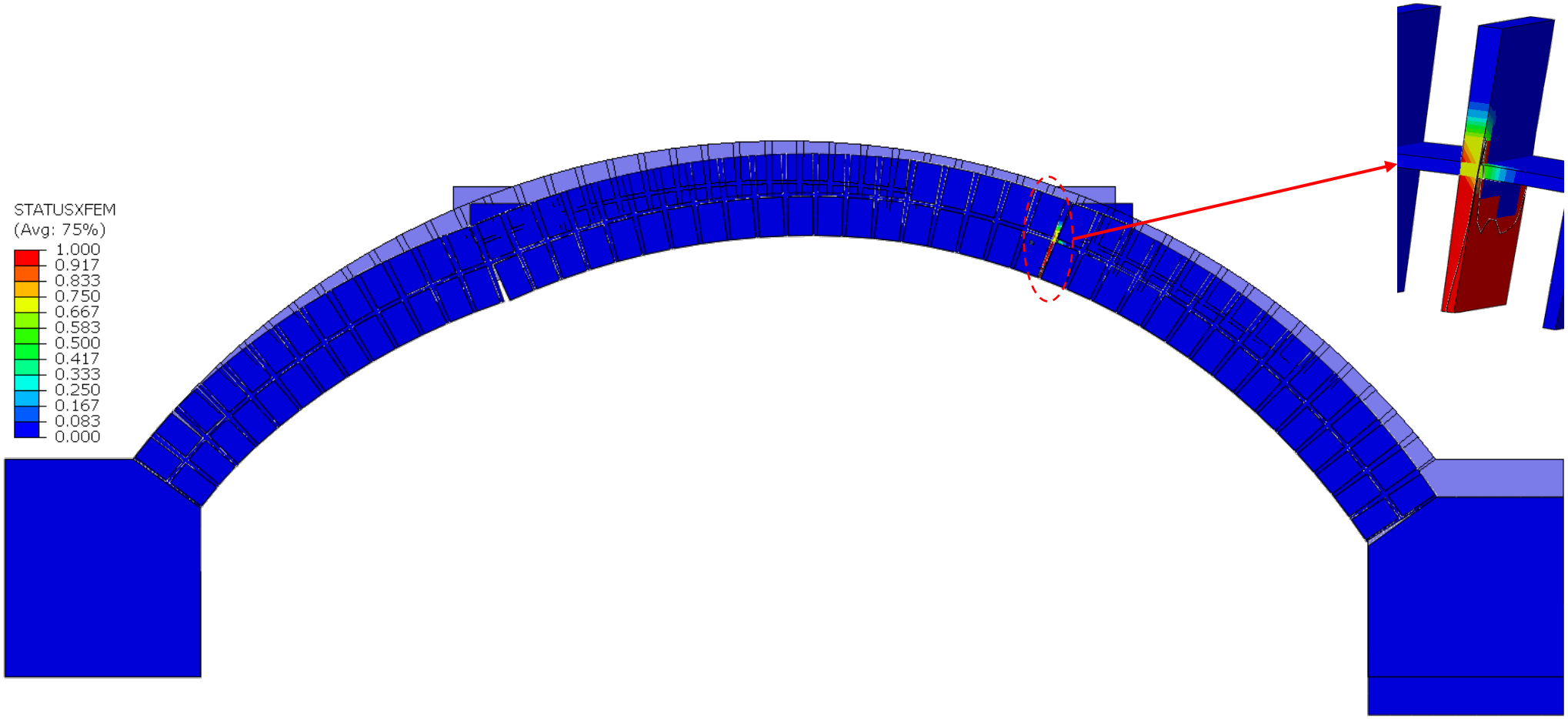

Figure 6-45: The final deformed shape for vertical movement and live load (cracking failure).

6.3.3 *Rotational inverse abutment movement analysis result*

In this section, numerical simulation was carried out to investigate the masonry arch model response subjected to 0.02 radians (5mm) displacement of specified rotational displacements before applying live load at the quarter span.

Figure 6-46 shows the comparison of live load against the deflection at the quarter span arch model of the fixed and rotational movement numerical model. It can be noted that the initial elastic stiffness of the rotational movement is considerably changed compared to the fixed numerical model. Also, the masonry arch barrel model reached its peak load at 6.2kN.

Figure 6-49 shows the behaviour of the masonry arch before the live load was applied. Figure 6-49 (a) shows two cracks formed in the mortar joints with dispersed cracks. The first crack formed at the extrados of the right abutment and the second cracked formed at the intrados of the quarter span and reached the inter-ring mortar joint. However, more cracks formed at the unit-mortar interface, as shown in Figure 6-49 (b).

Figure 6-49 (b) displays three cracks formed at the unit-mortar interface; two are significant as both red coloured at the quarter span upper ring and the three-quarter span intrados to the upper ring. There was a ring separation at the quarter and three-quarter span. Also, the third crack formed at the left abutment extrados, where it passed the inter-ring mortar joint.

Figure 6-50 shows the final simulation deformed shape of the rotational movement and live load analysis of the cracks formed at the unit-mortar interface. The cracks which had already formed before the live load was applied, which continued to grow and an additional crack formed at the quarter span intrados. The masonry arch barrel model at 6.2kN had formed the four-hinge mechanism.

Figure 6-51 shows the final simulation deformed shape of the rotational movement and live load analysis of the cracks formed in the mortar joint only, where the two cracks continued to grow in the mortar joint. The radial crack under live load at the quarter span reached the inter-ring mortar joint and the upper ring for the same joint was cracked in the unit-mortar joint, as shown in Figure 6-50.

The second crack formed at the right abutment due to the rotational movement but continued to grow during the live load applied at the quarter span, where a tiny part of the joint at the

intrados was uncracked and was under high compression, as shown in Figure 6-51. The influences of rotational movement on the masonry arch model are clear in terms of the elastic stiffness and peak load variation compared to the fixed masonry arch model.

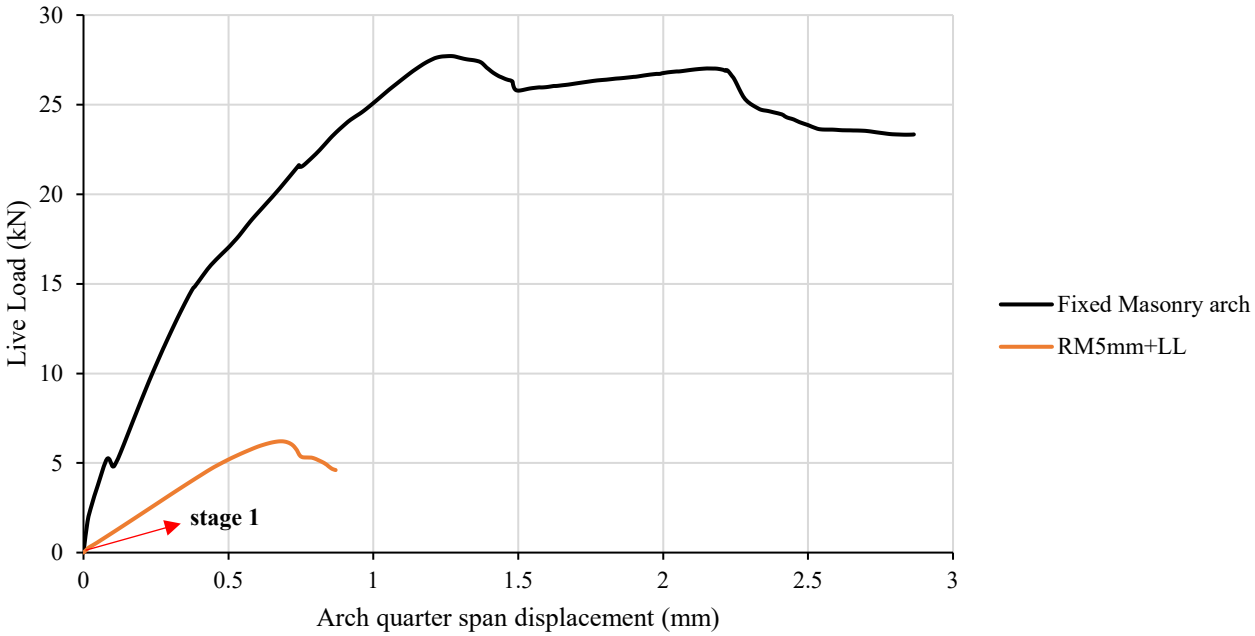

Figure 6-46: Comparison of numerical fixed and rotational movement and live load models of displacement at the quarter span results.

Figure 6-47 illustrates the impact of rotational movement on the peak load exerted against the fixed abutment within the numerical model. A significant reduction of 77% is evident, as shown in Figure 6-47.

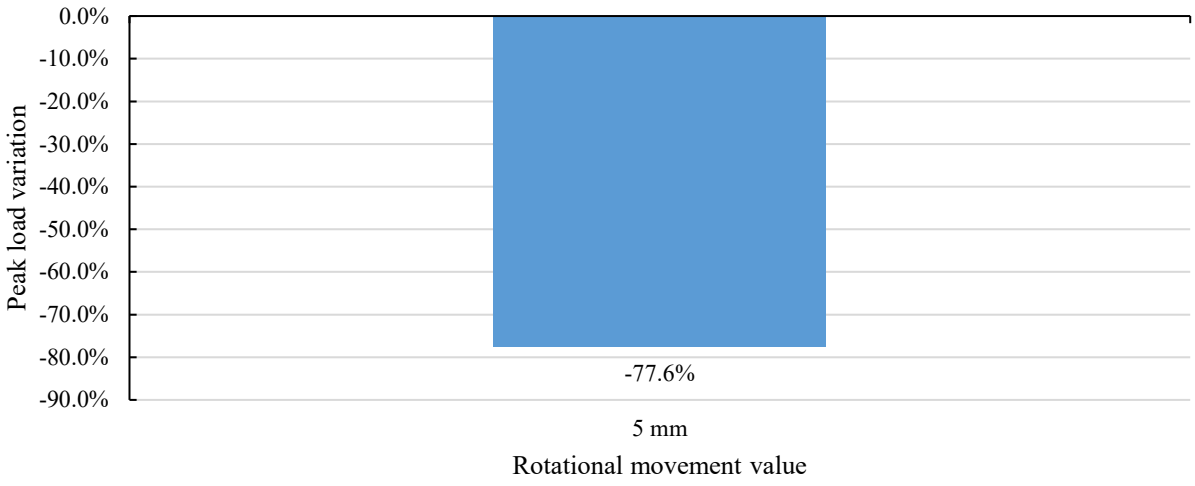

Figure 6-47: Effect of rotational movement on the peak load of the masonry arch.

Regarding the initial elastic stiffness of the masonry arch modelling of rotational and fixed abutments, Figure 6-48 shows a reduction of 67.7%.

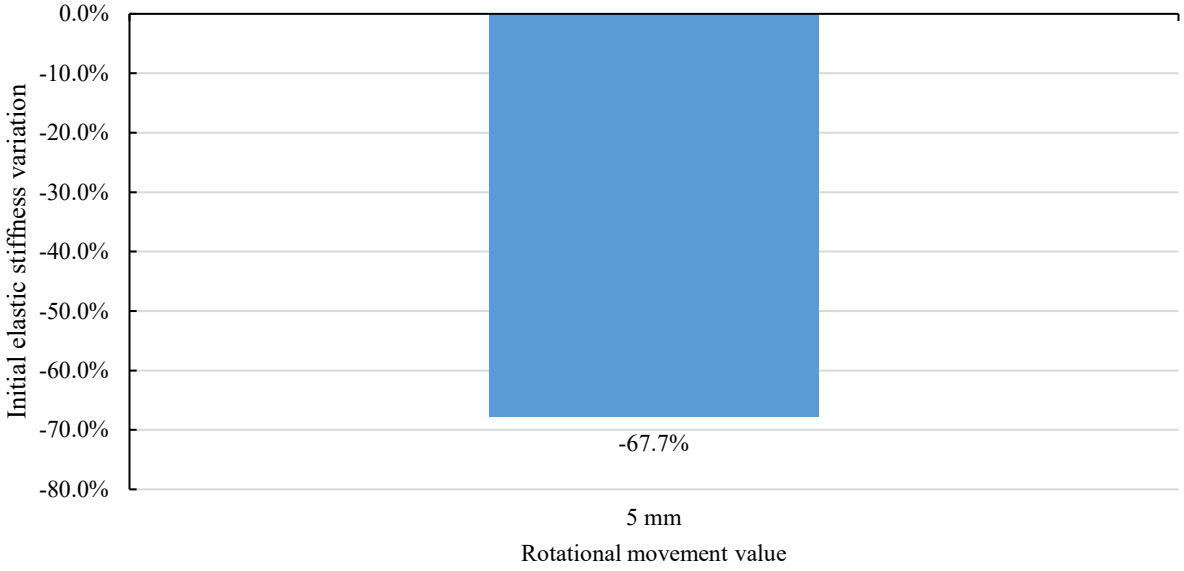

Figure 6-48: Effect of horizontal movement on the elastic stiffness of the masonry arch.

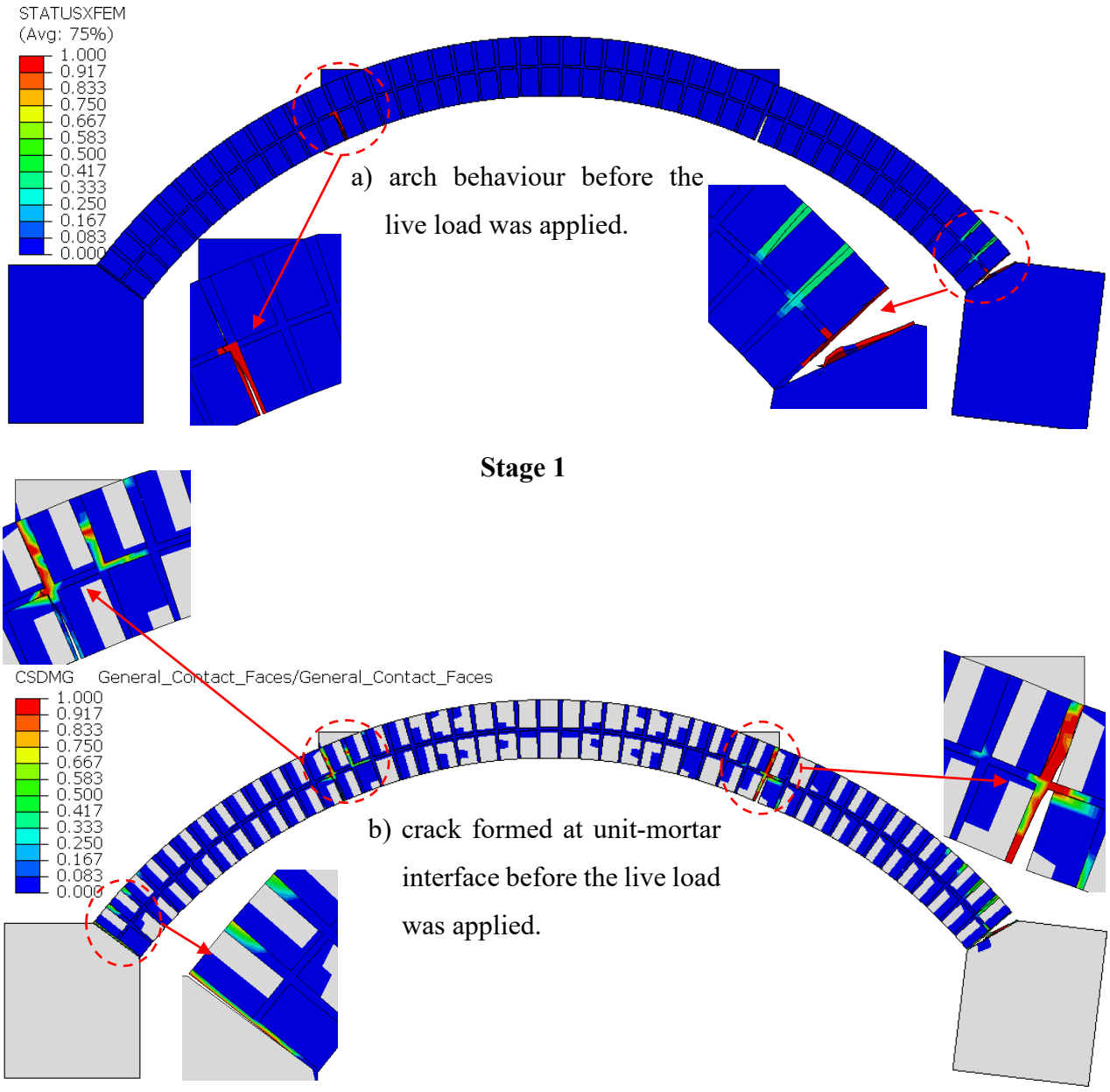

Figure 6-49: Crack simulation progress at stage 1 for rotational movement and live load.

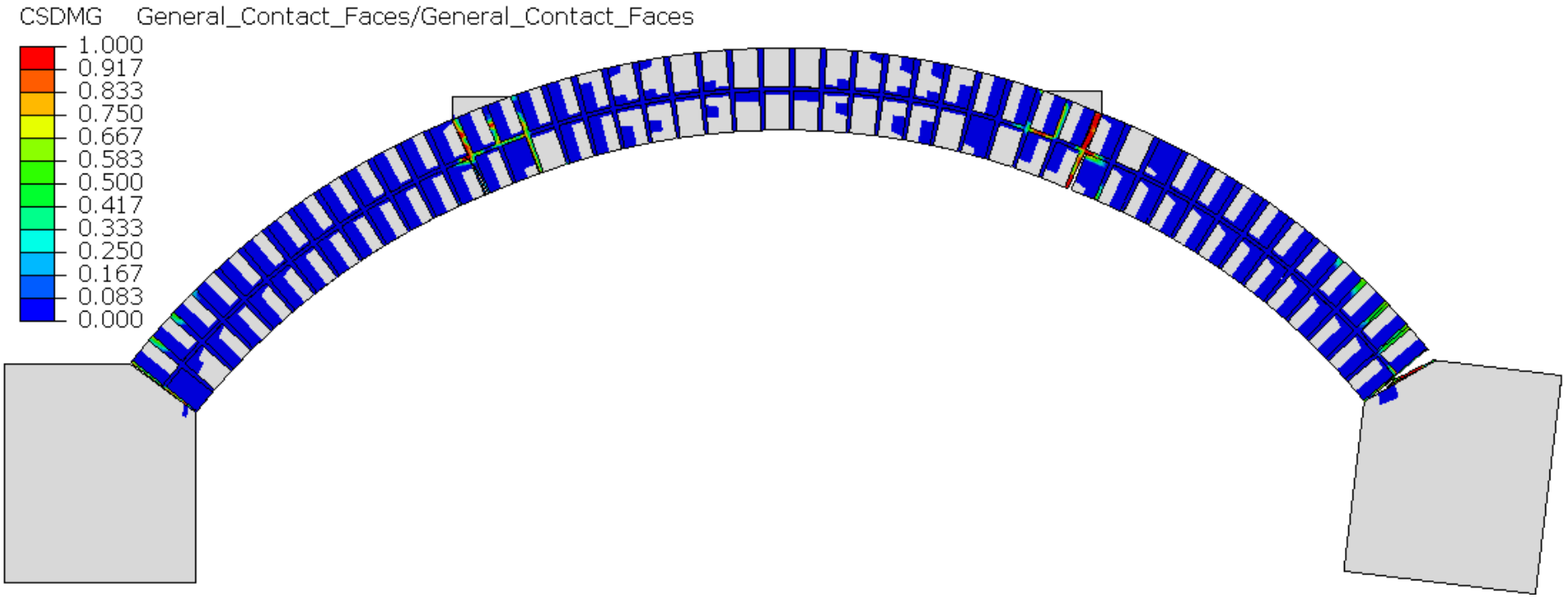

Figure 6-50: The final deformed shape crack at the interface for rotational movement and live load (interface failure).

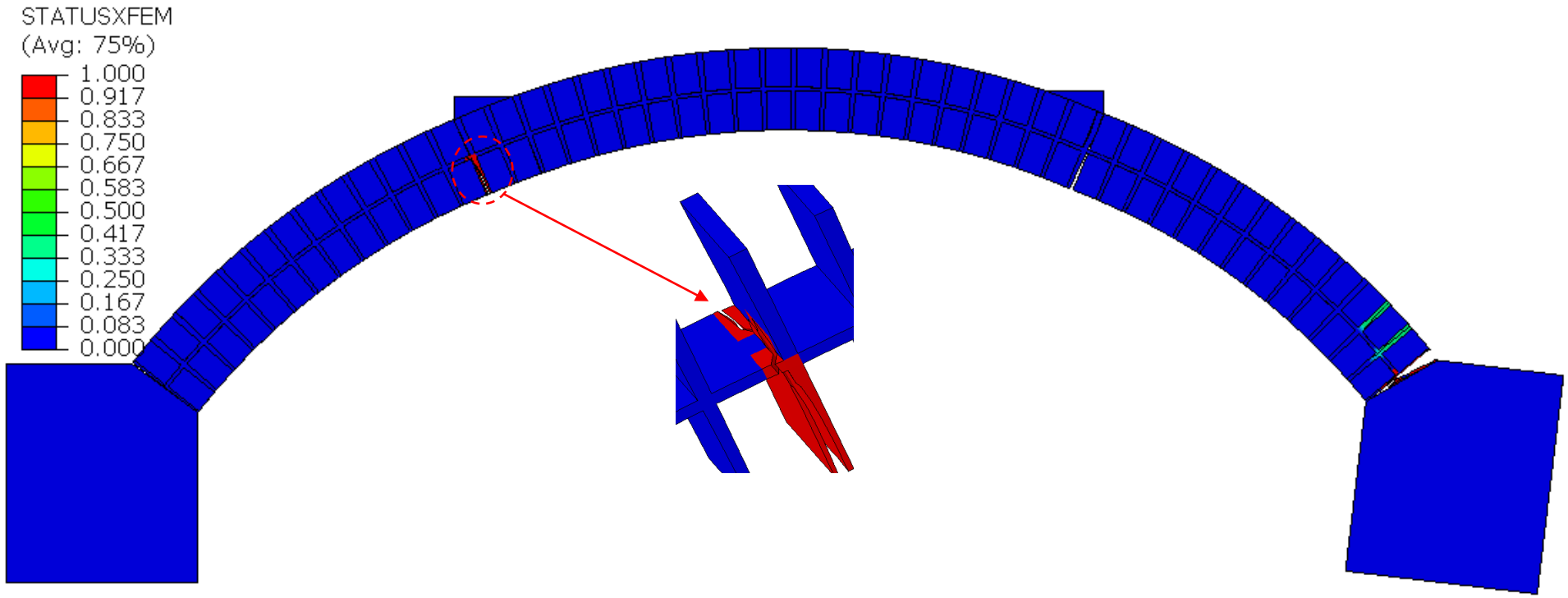

Figure 6-51: The final deformed shape for rotational movement and live load (cracking interface).

6.4 Double displacement influence in combination abutment movements

This section provides a full investigation where horizontal and vertical foundation movements are simultaneously applied in a ratio of 2:1. The investigation is carried out using the same full 3D model that was used in the individual movements analyses.

This section provides two numerical analysis models under a non-linear static time-history procedure. The same masonry arch model presented in section 6.2 was used, where the whole masonry arch was composed of 12,800 elements without any backfill on the arch.

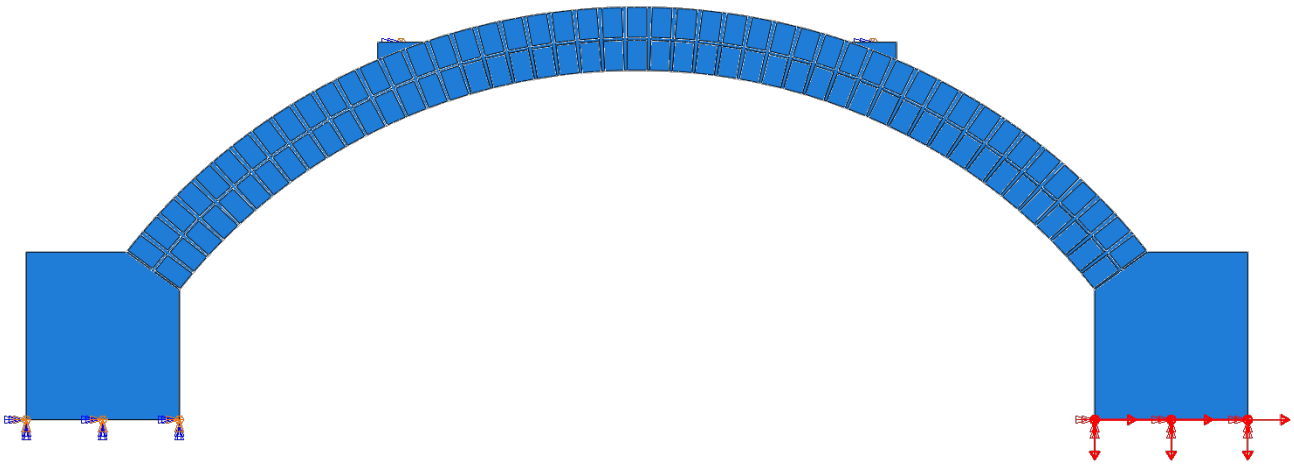

Figure 6-52: Finite element model of foundation movements of 10mm horizontally and 5mm vertically.

The analysis of the masonry arch model was carried out in three steps. In the first step, the acceleration due to gravity of 9.81 m/s^2 was applied to represent the self-weight of the masonry arch barrel. In the second step, the dead loads of 10kN were applied at the quarter and three-quarter span of the arch barrel to represent the typical backfill weight. In the third step, the combination movements were applied at the right abutment in two directions. The left abutment was fixed. The first analysis model displacement values were 10mm horizontally and 5mm vertically, applied to the bottom of the right abutment as shown in Figure 6-52.

Figure 6-53 (a), displays the opened cracks in the mortar joint for the 10mm horizontally and 5mm vertically movement at right abutment; two cracks occurred in the mortar joint at the intrados of the arch barrel, at the quarter and three-quarter spans under the dead loads. The crack at the quarter span passed the inter-ring mortar joint and reached the second ring, where the second crack at the three-quarter span reached the inter-ring mortar joint. Two cracks

occurred as opened cracks at the unit-mortar interface at the extrados of the arch barrel, as shown in Figure 6-53 (b). However, these two cracks reached the intrados of the arch barrel and the cracks occurred in the mortar joint under high bending stress, as shown in Figure 6-53 (a).

Figure 6-53 (b), exhibits that all four cracks have occurred through the whole arch barrel thickness, where the two cracks at the intrados quarter and three-quarter span have a combination of crack failure in mortar joint or at the unit-mortar interface. Also, a few small cracks (due to the crack's colour) occurred as opened cracks at the unit-mortar interface in each masonry arch barrel end.

The masonry arch model was subjected to combination movements of 10mm vertical and 5mm horizontal, and three cracks occurred in the arch barrel. Figure 6-54 (a), shows one opened crack that occurred in the mortar joint at the arch barrel intrados quarter span and a crack formed at the inter-mortar joint between the lower and upper rings next to the first crack. On the other hand, Figure 6-54 (b), displays two cracks that occurred as opened cracks at the unit-mortar interface at the arch intrados of the three-quarter span and reached the upper ring and another crack at the arch extrados of the left-hand abutment towards the intrados of the arch.

Regarding the first crack at the arch quarter span, Figure 6-54 (a), shows that the arch in the mortar joint reached the inter-ring mortar joint, but Figure 6-54 (b) shows that the crack continued towards the extrados as an opened crack at the unit-mortar interface.

In general, the outcome of these two simulations of double displacement in various vertical and horizontal directions proves that horizontal movement significantly influences the arch barrel more than the vertical direction. The second model has 10 mm vertical displacement, as the first model was 10mm horizontally, but the first has four major cracks, all of which have reached the arch's intrados or extrados. However, the second model has only three significant cracks, less than the horizontal model movement of 10mm displacement.

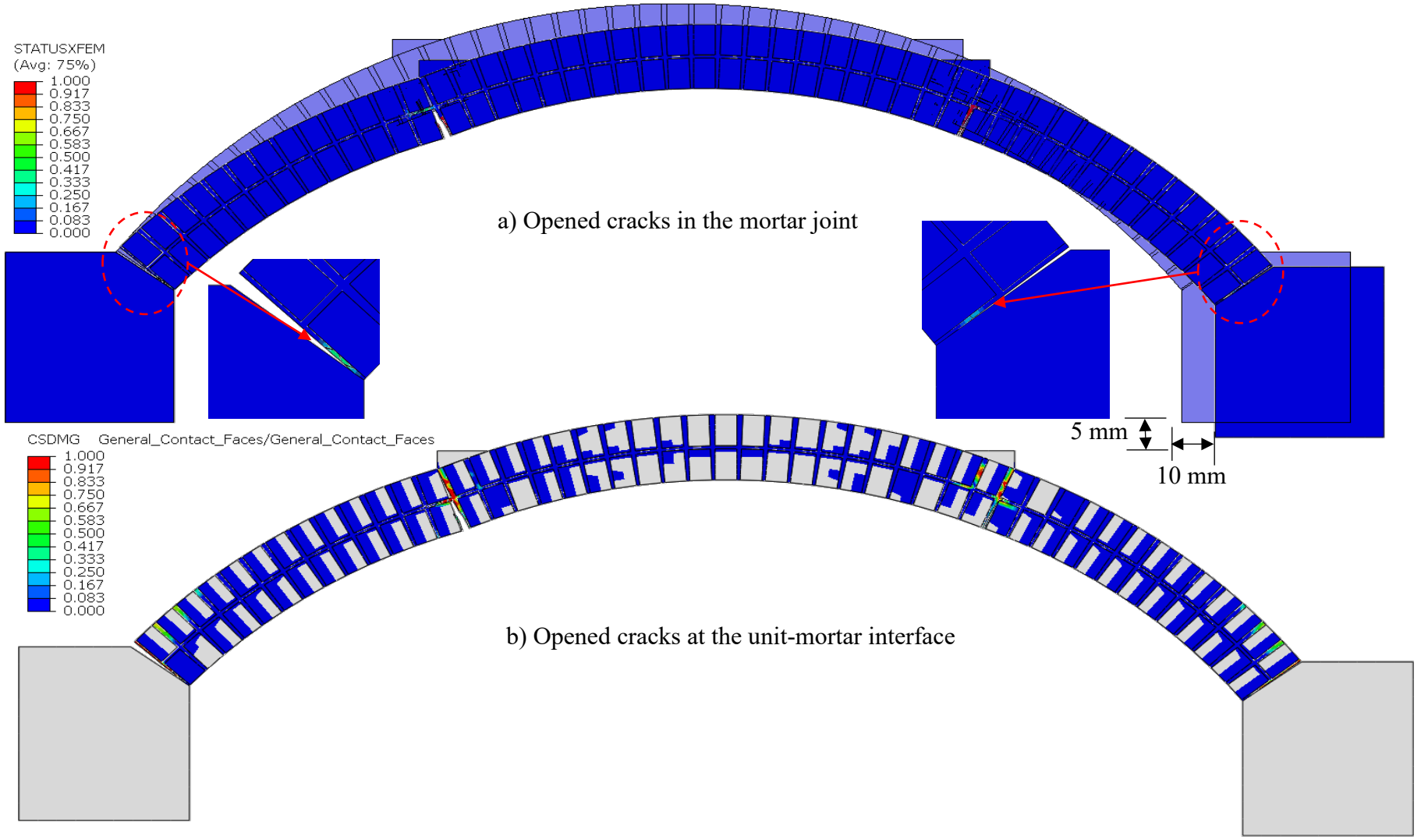

Figure 6-53: Deformed shape of 10mm horizontal and 5mm vertical combination movements.

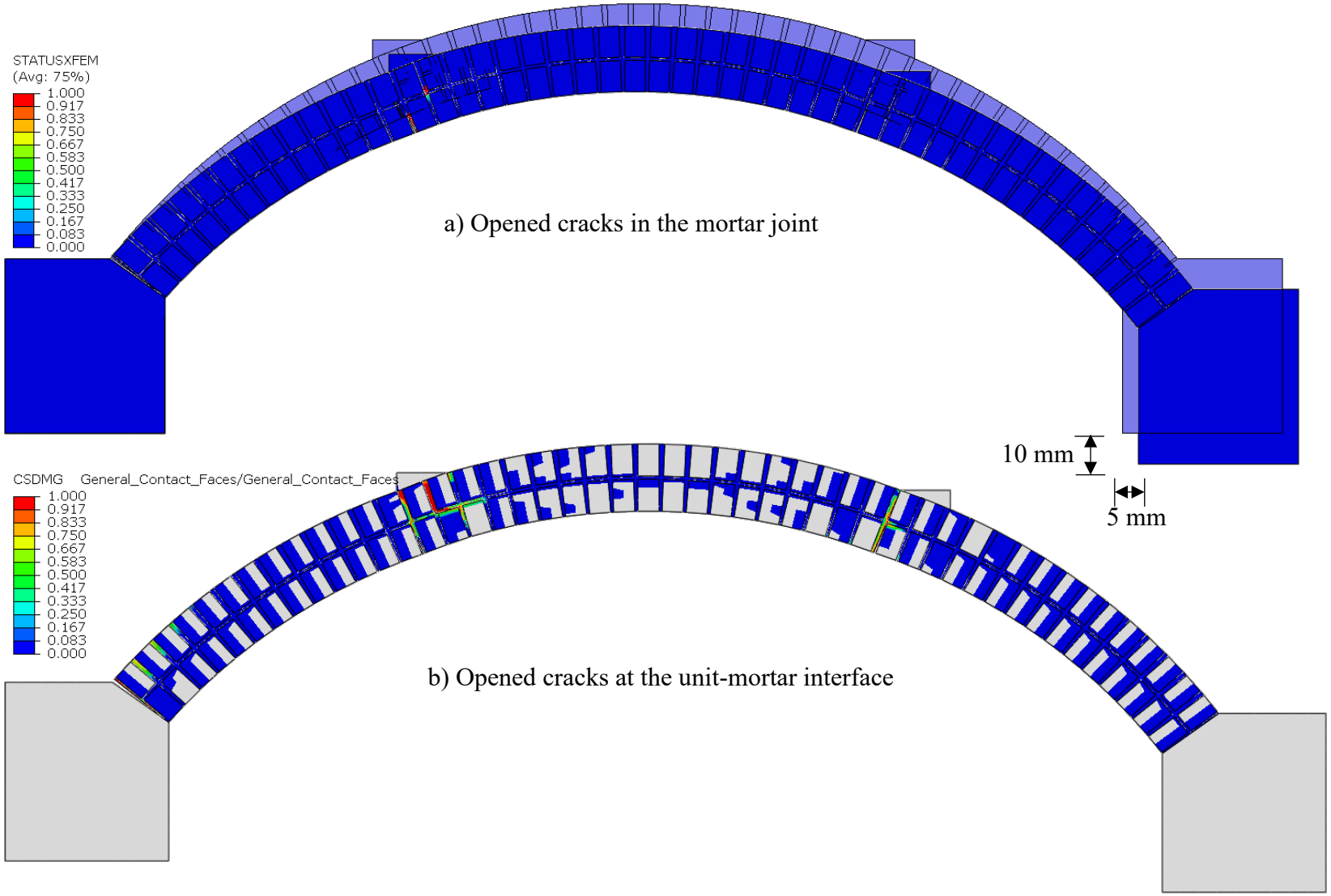

Figure 6-54: Deformed shape for 5mm horizontal and 10mm vertical combination movements.

6.5 Summary

This chapter investigated the influence of masonry arch abutment movements using numerical analysis for different movement directions and displacement amounts. This chapter included various simulations for masonry arch barrels under foundation movement, where section 6.2 presented the masonry arch experimental test using the same load arrangements. The two dead loads were applied before the movements were applied at the right abutment. This analysis aims to investigate the masonry arch barrel model behaviour and compare the reaction force of the arch barrel against the abutment movement displacement.

Section 6.3 presented the simulation of the arch G model under foundation movement in different directions. Before the abutment was moved, two dead loads were applied at the quarter spans of the arch barrel. After moving the abutment, the live load was applied at the quarter span to investigate the masonry arch behaviour.

The behaviour of a masonry arch subjected to foundation movement is highly dependent on the magnitude and direction of the movement and the strength and integrity of the arch's structure and materials. If the movement is minor, the arch may be able to accommodate it without significant damage. However, the movement can cause cracking, crushing, and even arch collapse if the movement is substantial.

The ability of an arch to endure vertical movement is determined by various criteria, including the strength and quality of the materials used, the geometry of the arch, the amount of movement, and any restraining features.

The root of failure mechanisms identified here is the development of cracking either in the mortar joint or unit-mortar interface. Arches are sized to keep the ring in compression but when large enough bending develops, the result is tensile stress (which manifests as cracking). Bending stress can develop as a result of loading on the arch ring or movement of foundations. In severe cases, this can result in the partial or complete collapse of the arch. Therefore, it is essential to ensure that the foundation of a masonry arch is appropriately designed and constructed to minimize the risk of movement and to monitor the arch regularly for signs of damage. The abutments are one of the most significant components of the masonry arch.

Referring to section 6.2, in comparison to the masonry arch with fixed abutments, the behaviour of the masonry arch subjected to foundation movement with two dead loads applied. Also, Table 6-1 provides the load arrangement and the crack locations of each movement:

- Fixed masonry arch model abutments had the first crack formed at the quarter span intrados at the mortar joint. However, once the crack reached the arch second ring extrados turned into an opened crack at the unit-mortar interface. In contrast, the second crack formed at the right abutment intrados (the crack started in the mortar joint and then began open crack at the unit-mortar interface). In contrast, the third and fourth cracks formed at the left abutment extrados and three-quarter span extrados. Also, these two cracks formed in the mortar joint.
- Horizontal movement model, the first two cracks were formed at the quarter and three-quarter spans of the arch intrados, and the cracks formed in the mortar joint. On the other hand, the third and fourth hinges formed at the right and left abutment extrados as opened cracks at the unit-mortar interface.
- Vertical movement model, the first crack formed at the three-quarter span intrados of the arch as an opened crack formed in the mortar joint. However, once the crack reached the second arch ring, it became an opened crack at the unit-mortar interface. Also, a small crack formed at the quarter span arch between the two arch rings formed as a crack in the mortar joint and then developed into an open crack at the unit-mortar interface at the extrados of the arch. The third crack formed at the right abutment intrados, and the fourth crack formed at the left abutment extrados; these two cracks formed opened cracks at the unit-mortar interface.
- The anti-clockwise rotation abutment movement model had the first crack formed at the arch right abutment intrados. This crack combined an opened crack in the mortar joint and at the unit-mortar interface. In addition, the second crack formed at the arch left abutment arch intrados as an opened crack at the unit-mortar interface. The third and fourth cracks formed at the quarter and three-quarter span of the arch between the arch rings towards the extrados. Also, the cracks combined opened cracks in the mortar joint and at the unit-mortar interface. It was noted that these two cracks developed along the arch thickness as ring separation. Furthermore, the fifth crack formed near the centre of the arch extrados.

- The masonry arch model subjected to clockwise rotation movement had the first crack formed at the arch right abutment extrados as an opened crack in the mortar joint towards the intrados of the arch. The second crack formed at the three-quarter span of the arch intrados as a combined opened crack in the mortar joint and at the unit-mortar interface. At the same time, the third crack formed at the intrados of the arch quarter span as an opened crack at the unit-mortar interface. However, a small crack appeared at the same joint in the second ring towards the arch extrados. The fourth crack formed at the arch left abutment extrados as an opened crack at the unit-mortar interface. As a result, it can be noted that the right-hand side of the arch had the two major cracks at the right abutment and at the three-quarter span.
- The masonry arch model subjected to horizontal and vertical combination abutment movement had the first crack at the quarter span intrados of the arch as an opened crack in the mortar joint towards the extrados. In contrast, the second crack formed at the arch left abutment extrados as an opened crack at the unit-mortar interface towards the intrados turned into a crack in the mortar joint. When the right-hand abutment is displaced, the majority of damage is located on the left-hand side of the arch.

Table 6-1: Comparison between the behaviour of fixed and moved masonry arch abutment models.

Model name	Load arrangement	Crack locations
Fixed Model	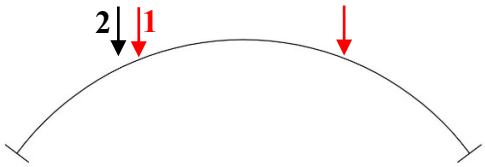	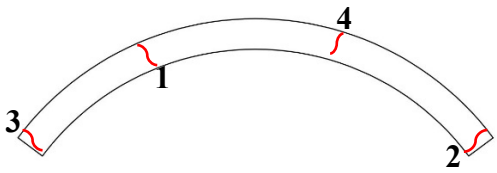
Horizontal Model	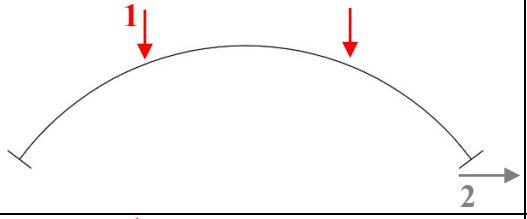	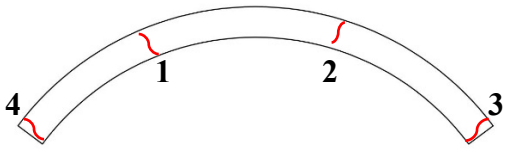
Vertical Model	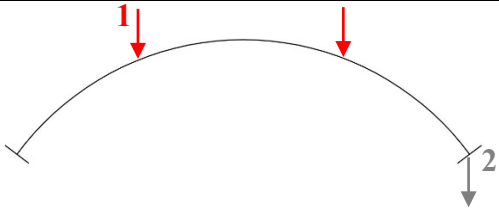	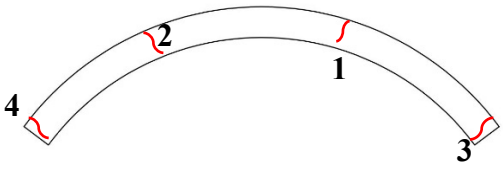
Anti-clockwise Model	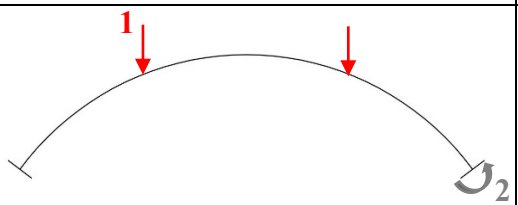	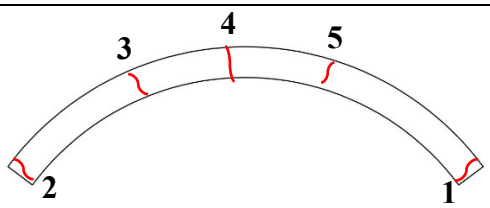
Clockwise Model	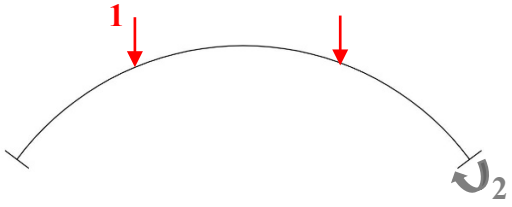	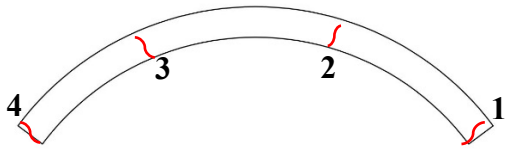
Horizontal and Vertical Combination Model	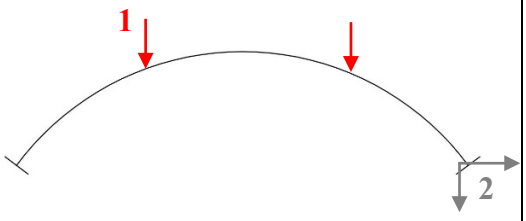	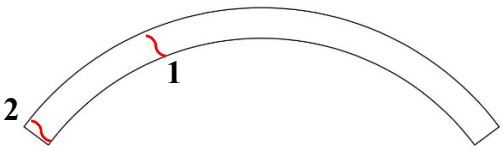

Referring to section 6.3, in comparison to the masonry arch with fixed abutments, the behaviour of the masonry arch subjected to foundation movement with two dead loads applied and live load applied at the quarter span after the foundation was moved. Also, Table 6-2 provides the load arrangement and the crack locations of each movement:

- The movement values for section 6.3 are less than those in section 6.2 due to the live load being applied after the movement of the foundation.
- In the horizontal movement with the live load model, the four cracks remain in the same locations as in the simulation of horizontal with two dead loads only. Furthermore, once the live load was applied, the cracks continued to grow. As a result, of the live load applied, the left-hand side of the arch barrel started to lift vertically. This changed the behaviour of the two cracks at the three-quarter span and right abutment, where the crack at the quarter span formed at the extrados of the arch as an opened crack at the unit-mortar interface. In addition, the two cracks at the quarter and three-quarter spans have cracked the inter-ring mortar joint, and it can be noted clearly in the final deformed figure that there was delamination between the units. With regard to capacity, it can be noted that the arch barrel can still resist static loads. Nevertheless, there was a considerable difference compared to the fixed abutment capacity, which has a minimal value.
- In the vertical movement with the live load model, the four crack locations remain at the same location as before the live load was applied. Once the load was applied at the arch quarter span, the crack at the quarter span formed at the arch intrados. Also, the fifth crack formed near the centre of the arch barrel at the arch extrados as an opened crack at the unit-mortar interface. This is due to the behaviour of the arch changing under the live load applied, where the right-hand side of the arch lifts vertically. Regarding the masonry arch capacity subjected to movement and live load, the arch model showed high resistance compared to the horizontal movement model. However, there is still a difference compared to the fixed masonry arch model, where the load-displacement graph showed a considerable difference in elastic stiffness.
- In the rotation movement with the live load model, the four cracks remain at the same locations. However, when the live load was applied, the cracks continued growing towards the intrados or extrados of the arch. Also, the crack at the arch quarter span (left-hand side of the location of the steel plate) had completely cracked the inter-ring

mortar, which means the rest of the mortar joint in the second ring is under high compression. In addition, a fifth crack formed at the arch intrados quarter span (right-hand side of the steel plate). The crack formed as an opened crack at the unit-mortar interface. Regarding the capacity compared to the other direction movements, following rotational movement the arch has less capacity to resist live load (the loss in capacity is more than 20kN), and the arch's stiffness significantly decreased, as demonstrated in Figure 6-46.

Table 6-2: Comparison between the behaviour of fixed and moved with live load masonry arch abutment models.

Model name	Load arrangement	Crack locations
Fixed Model	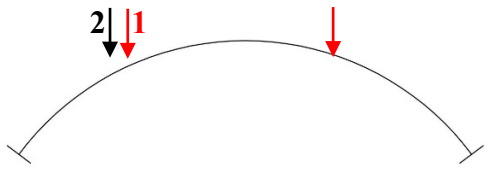	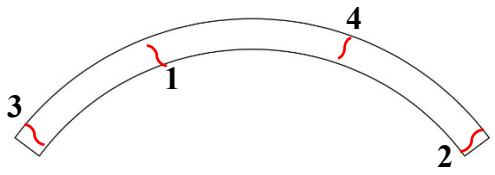
Horizontal Model	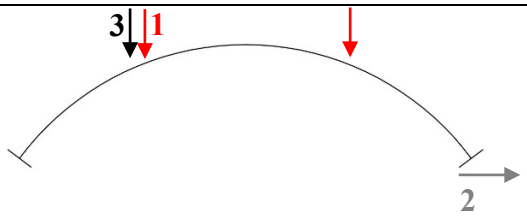	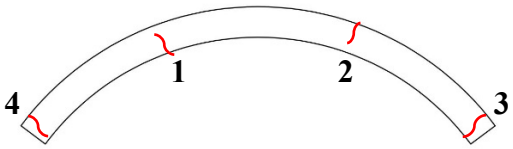
Vertical Model	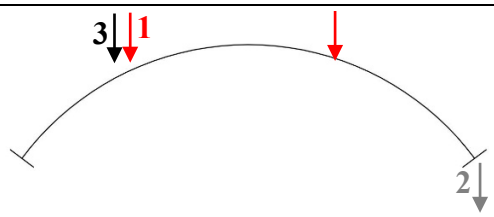	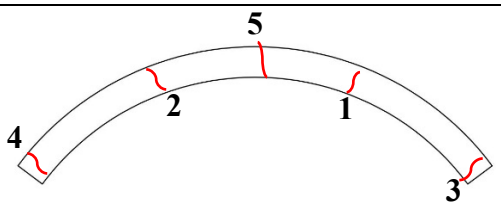
Clockwise Model	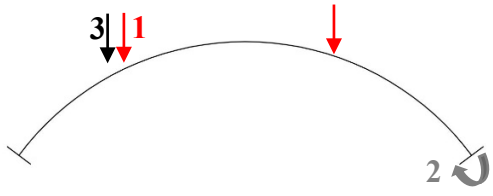	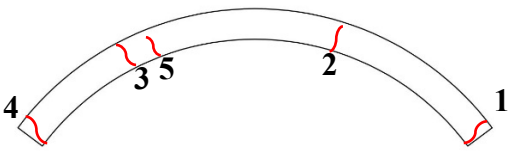

6.5.1 *General Comments*

The influence of abutment movements were numerically simulated after developing a hinge mechanism due to different abutment movement directions and values. As a result, masonry arches can still resist live loads (at the quarter span).

The behaviour and movement of the arch barrel under clockwise rotational movement has little resemblance to the arch under horizontal or vertical directions. The results of the rotational movement caused the arch barrel to rise, the span to decrease and a reduction in the arch thrust.

The rotational movement has significant influence on the masonry arch barrel in terms of movement with or without live load after the foundation was displaced compared to the vertical and horizontal movement.

According to the combination of movement in the horizontal and vertical direction, two significant cracks in the masonry arch barrel affected the arch barrel stiffness. Figure 6-24 presents the horizontal reaction force for the horizontal movement. This proves that two cracks are enough to influence the capacity of the arch.

When the level of abutment displacement in any direction increases, the masonry arch capacity will be reduced compared to the fixed masonry arch model. According to this, the worst movement scenarios were horizontal and rotational, as shown in Figure 6-33 and Figure 6-46. These figures showed a significant drop in the stiffness when the load was applied after the abutment had been moved horizontally or rotationally.

Appendix B provides numerical simulation deformation shapes of three movement types. Horizontal, vertical and rotational were applied to the right abutment with the self-weight of the arch barrel by applying gravity before the movement was applied to the right abutment. The purpose of these simulations with the arch's self-weight is to prove that the arch's crack locations will differ from the models with dead loads of 10kN for each arch quarter span subject to foundation movement (as validated against the experimental arch G test).

Double displacement influence in combination abutment movements without steel plate on the arch barrel are replicated in Appendix C. In comparing with and without steel plates simulation, there were no differences in the locations of the cracks. Still, there were differences in how many cracks formed, where the 10mm horizontally and 5mm vertically model with steel plates had four cracks, and the numerical model without steel plates had three cracks. The 5mm horizontal and 10mm vertical numerical model with steel plates had three cracks instead of two cracks in the numerical model without steel plates.

Zhang, 2015 also validated numerical model against the Arch G experimental tests, using different numerical modelling approaches. However, in some cases with small movement values, the location and load at each hinge formation agreed well with the numerical models presented here.

Chapter Seven

7 Conclusions and Future Works Recommendation

7.1 Review of aim and objectives

In the preceding chapters, a comprehensive numerical study examined the behaviour of a 3D masonry arch model under various movements. This section summarizes the thesis by revisiting the initial objectives, reviewing the literature, detailing the numerical modelling of the masonry arch and its limitations, discussing the study's outcomes, and concluding with recommendations for future work.

This thesis aimed to investigate the structural behaviour of the masonry arch subject to foundation movement. Prior research on masonry arches and bridges, particularly foundation movements, was limited to settlement and sliding. Often, these studies involved small abutment movement values that only partially represented comprehensive structural behaviour. Moreover, numerical simulation techniques employed in these studies did not adequately simulate mortar thickness. A detailed micro-modelling approach was adopted to address these gaps, employing cohesive interactions to model masonry triplets and arches. XFEM was introduced to capture crack propagation within the mortar joints without pre-defining crack locations. A multi-ring masonry arch model was developed and rigorously validated against experimental data on arch behaviour.

Four principal types of movement were investigated: horizontal, vertical, rotational, and reverse rotation. Additionally, combined horizontal and vertical movements were examined with varying values in each direction.

This study marks the inaugural application of full-thickness mortar joints with cohesive interactions at the unit-mortar interface in conjunction with XFEM for crack propagation in mortar joints. This approach was applied to analyse masonry arches on moving supports.

- Physical testing of masonry triplets in shear was conducted to establish an understanding of masonry behaviour and material properties. Twenty samples were tested in the laboratory to obtain nonlinear material and interface properties for the numerical simulation study.

- The numerical modelling of the masonry triplets was based on a detailed micro-modelling approach using the finite element method. The 3D numerical masonry triplet models were validated against experimental test results. Additionally, a parametric study was carried out to investigate the influence of nonlinear material and interface properties on the behaviour of the masonry triplet model.
- The analysis principles were developed to create and calibrate a 3D finite element method (FEM) model for authentic masonry arch structures on rigid abutments. This model was validated by comparison with experimental results from physical testing, including load-displacement graphs and arch barrel crack patterns.
- A mesh sensitivity study and material property parametric study were conducted on the validated masonry arch model to investigate the influence of the input data on the arch behaviour.
- The validated numerical masonry arch model with rigid abutments was used to investigate the behaviour of arches subjected to various foundation movements, including settlement, sliding, and rotation of one abutment, with a static load applied on the arch barrel. Additionally, inverse rotational movements and combinations of vertical and horizontal movements with different displacement values were examined.

7.2 Outcomes of this research

7.2.1 *Experimental and numerical investigations of the masonry triplet mechanical properties*

The experimental tests on brick and mortar were conducted to determine their compressive strength, shear strength, tensile strength, Young's modulus, friction coefficient, and friction angle. The unit-mortar interface's tensile and shear fracture energy was also calculated from direct tensile and shear stress tests. These material properties were then utilized in the numerical analysis of the masonry triplet. The study was validated and compared with the experimental results, showing good agreement regarding the behaviour and failure patterns in the mortar and at the interfaces. The key conclusions drawn from this study are as follows:

- XFEM can be used to simulate cracks in the mortar without predefining the initial crack position.

- Numerical models of couplets and triplets using XFEM displayed acceptable representation of structural behaviour, failure mechanisms and peak loads. This was determined by comparing shear stress-displacement graphs and implies that validated models of masonry arches can be created.
- Finite element analysis (FEA) model validation is required to ensure the numerical model provides an acceptable representation of reality. However, many FEA parameters are uncertain; hence, differences in the real structural behaviour and the FE model results are inevitable.
- By comparing numerical models of masonry triplets which use different constitutive models, it was determined that the Mohr-Coulomb criteria provided a superior replication of experimental post-yield behaviour, peak load and ductility.
- The dilation angle has minimal influence on the masonry triplet behaviour, for variation between zero and 20 degrees the peak shear stress changes by only 5.6%. The validated model with 1.0MPa pre-compression exhibited similar structural behaviour as the experimental test curve.
- The cohesion between the unit-mortar interface significantly influences the shear stress-displacement curve. The peak value of shear stress is directly proportional to the value of cohesion.
- The tensile and shear fracture energy values significantly affected the peak shear stress point and post-yield behaviour, from elasto-plastic to strain softening.

7.2.2 *Numerical investigation of the masonry arch*

The detailed micro-modelling approach was employed to simulate the 3D masonry arch with multiple rings, incorporating full-thickness mortar joints. Cohesive interaction between the unit-mortar interfaces was used to capture the nonlinear failure at these interfaces. This was achieved by integrating the constitutive model with the Extended Finite Element Method (XFEM), enabling the simulation of cracks in the mortar elements without the need for any user-defined subroutines, as in previous studies.

- The use of the XFEM method permitted each run to uniquely develop a crack pattern in accordance with defined constitutive laws.
- Masonry arch barrel failures, such as the four-hinge mechanism and interface failure, were captured using the computational models created using ABAQUS. It was shown

in this section, that when compared to experimental data, the numerical models displayed very similar crack arrangements and peak load until a four-hinge failure mechanism formed.

- In order to determine the adequacy of the modelling, a mesh sensitivity study was undertaken using the ABAQUS defined mesh densities of coarse, normal, fine and very fine. It was shown the normal mesh density produced an optimum representation of the load-displacement curve.
- Therefore, the critical failure mechanisms and the damage development behaviour of masonry arches can be predicted adequately. Modelling full-thickness mortar with the XFEM cracking method to identify the cracks through the mortar elements required the input of additional material properties and interaction properties. Therefore, a detailed sensitivity study of the assumed values for the non-linear interface and the mortar plasticity criteria was undertaken.
- The detailed micro-modelling approach was an alternative technique to investigate the realistic behaviour of masonry arches under various loading conditions. Although it offers an opportunity to obtain significant detail and observe the development of failure mechanisms, the intrinsic disadvantages of the approach are the high cost of modelling software, considerable time demands, and the need for expertise in modeller resources.
- In order to evidence the adequacy of the FEA model input data, parametric studies were undertaken on four principal mortar material properties. Values were chosen that were higher and lower than the data used in the validated FEA model. In each case of fracture energy, tensile strength, Young's modulus of elasticity, the middle value (used in the validation model) was shown to offer the best overall fit. Finally, a study was undertaken to determine whether Drucker-Prager or Mohr-Coulomb offered the best constitutive law, and Drucker-Prager was shown to be inferior both in terms of peak load and load at first hinge formation.

  The recommended values are:

  - G_f= 0.012 N/mm
  - f_t = 0.26 N/mm^2
  - E_m = 1420 N/mm^2
- The Drucker-Prager constitutive law models were noted to exhibit ring separation to a much greater extent than the Mohr-Coulomb models. This is due to the Drucker-Prager using a post-yield softening stress-strain relationship for mortar.

7.2.3 *Investigation of the masonry arch subjected to foundation movements*

- The influence of abutment movements was numerically simulated after developing a multi-hinge mechanism due to different abutment movement directions and values. As a result, masonry arches can still resist live loads (at the quarter span).
- The behaviour and movement of the arch barrel under clockwise rotational abutment movement has little resemblance to the arch under horizontal or vertical abutment movements. The results of the rotational abutment movement caused the arch barrel to rise, the span to decrease and a reduction in the arch thrust.
- In comparison to horizontal and vertical abutment movements cases, the rotational abutment movement has a more significant influence on the masonry arch barrel response.
- For the combination of abutment movement in the horizontal and vertical direction, two significant cracks in the masonry arch barrel are sufficient to affect the arch barrel stiffness.
- When the level of abutment displacement in any direction increases, the masonry arch capacity will be reduced compared to the fixed abutment masonry arch model. According to this, the worst abutment movement scenarios were horizontal and rotational, as shown in Figure 6-33 and Figure 6-46. These figures showed a significant drop in the stiffness when the load was applied after the abutment had been moved horizontally or rotationally. A graphical summary of the structural behaviour of masonry arch subjected to movements is contained in Appendix D, Table 6-1 and Table 6-2.
- Practical applications of this research relate to industrial needs in assessment of structural integrity of masonry arches which are exhibiting a degree of foundation movement, as yet there are limited resources for assessing engineers to make judgments about capacity reduction. It is hoped this research will provide some progression towards a solution to this problem.

7.3 Suggestions for further work

In the pursuit of the objectives of this thesis, the aim has been achieved, and a better understanding of the behaviour of masonry arch under foundation movement has been established. However, several topics have presented themselves which are worthy of further

investigation. Many relate to aborted avenues of finite element model development, which are particular to ABAQUS and may be summarised as follows:

1. As this study provided numerical simulations of masonry arches only, the next step is to take the validated model developed here and add the effects of backfill restraint. This is to establish if there is a significant backfill-structure interaction effect which is not reflected in the results of this thesis. This could address both cohesive and cohesionless soils.

2. This thesis set out to investigate the effects of foundation movement on the behaviour of masonry arches. Vertical settlement and horizontal sliding have been investigated in combination with cohesive interaction between mortar and brick units some artificial combinations of sliding and settlement have been investigated. However, the reality of foundation movement is not likely to precipitate as purely vertical or horizontal movement. In real arch bridges the foundation movement is induced by loading and subsequent soil compression, which will require the founding medium to also be modelled as an elastic medium (an elastic half-space).

3. The final finite element models are defined for a limited width of arch barrel equal to 455mm (the width of the experimental test arch). Perpend joint across the arch barrel were not modelled, this limitation could be removed. A student with a more powerful computer could examine a full-width arch (three-dimensional effect), to establish if there is a significant width effect which is not reflected in the results of this thesis.

References

ABAQUS. (2019). *Documentation (ABAQUS)*. ABAQUS user's guide.

Abdou, L., Saada, R. A., Meftah, F., & Mebarki, A. (2006). Experimental investigations of the joint-mortar behaviour. *Mechanics Research Communications*, *33*(3), 370-384.

Abdulla, K., Cunningham, L., & Gillie, M. (2018). Effectiveness of strengthening approaches for existing earthen construction. Structural Faults and Repair 2018-17th International Conference,

Abdulla, K. F., Cunningham, L. S., & Gillie, M. (2017). Simulating masonry wall behaviour using a simplified micro-model approach. *Engineering Structures*, *151*, 349-365.

Ahmad, S. H. S., Augusthus-Nelson, L., & Swift, G. M. (2015). Two-dimensional experimental and numerical modelling of a soil-filled masonry arch. *Geotechnical Engineering for Infrastructure and Development*. https://doi.org/10.1680/ecsmge.60678

Aita, D., Pedemonte, O., & Williams, K. (2015). *Masonry Structures: Between Mechanics and Architecture*. Springer.

Alejano, L. R., & Bobet, A. (2012). Drucker–Prager Criterion. *Rock Mechanics and Rock Engineering*, *45*(6), 995-999.

Ali, S. (1987). *Concentrated loads on solid masonry* [PhD Thesis, University of Newcastle].

Angelillo, M., Lourenço, P. B., & Milani, G. (2014). Masonry behaviour and modelling. In *Mechanics of masonry structures* (pp. 1-26). Springer.

Apreutesei, V., & Oliveira, D. V. (2005). *Strengthening of Stone Masonry Arch Bridges− Three Leaf Masonry Walls− State of the Art* [MSc Thesis, Universidade do Minho Escola de Engenharia]. Guimaraes, Portugal.

Asteris, P. G., & Plevris, V. (2015). *Handbook of Research on Seismic Assessment and Rehabilitation of Historic Structures*. IGI Global.

Asteris, P. G., Sarhosis, V., Mohebkhah, A., Plevris, V., Papaloizou, L., Komodromos, P., & Lemos, J. V. (2015). Numerical modeling of historic masonry structures. In *Handbook of research on seismic assessment and rehabilitation of historic structures* (pp. 213-256). IGI Global.

Augusthus-Nelson, L., Swift, G., Melbourne, C., Smith, C., & Gilbert, M. (2017). Large-scale physical modelling of soil-filled masonry arch bridges. *International Journal of Physical Modelling in Geotechnics*, *18*(2), 81-94. https://doi.org/10.1680/jphmg.16.00037

Barattucci, S., Sarhosis, V., Bruno, A. W., D'Altri, A. M., de Miranda, S., & Castellazzi, G. (2020). An experimental and numerical study on masonry triplets subjected to monotonic and cyclic shear loadings. *Construction and Building Materials*, *254*, 119313.

Bathe, K.-J. (1996). *Finite Element Procedures* Prentice-Hall.

Bayraktar, A., & Hökelekli, E. (2021). Seismic performances of different spandrel wall strengthening techniques in masonry arch bridges. *International Journal of Architectural Heritage*, *15*(11), 1722-1740.

BBC News. (2016a). *Elland Bridge flood damage: Government awards £5m towards rebuilding*. https://www.bbc.co.uk/news/uk-england-leeds-35337460

BBC News. (2016b). *Plans to replace Workington flood-hit bridge*. http://www.bbc.co.uk/news/uk-england-cumbria-12057819

BBC News. (2016c). *Pooley Bridge collapse: £300,000 temporary crossing approved*. http://www.bbc.co.uk/news/uk-england-cumbria-35295874

Beatie, G. (2003). *Joint fracture in reinforced and unreinforced masonry under quasi-static and dynamic loading* University of Liverpool].

Bennett, D. (1999). *The creation of bridges: from vision to reality-the ultimate challenge of architecture, design and distance*. White Lion Publishing.

Berto, L., Saetta, A., Scotta, R., & Vitaliani, R. (2004). Shear behaviour of masonry panel: parametric FE analyses. *International journal of solids and structures*, *41*(16), 4383-4405.

Block, P., DeJong, M., & Ochsendorf, J. (2006). As hangs the flexible line: Equilibrium of masonry arches. *Nexus Network Journal*, *8*(2), 13-24.

Blockley, D. (2012). *Bridges: the science and art of the world's most inspiring structures*. Oxford University Press.

Blockley, D. I. (2010). *Bridges: the science and art of the world's most inspiring structures*. Oxford University Press.

Bögöly, G. (2012). Diagnostic of stone masonry arch bridges. Conference of Junior Researchers in Civil Engineering,

Bolhassani, M. (2015). *Improvement of seismic performance of ordinary reinforced partially grouted concrete masonry shear walls*. Drexel University.

Brencich, A., & Morbiducci, R. (2007). Masonry arches: historical rules and modern mechanics. *International Journal of Architectural Heritage*, *1*(2), 165-189.

British Standards Institute. (2002). *Methods of Test for Masonry: Determination of Initial Shear Strength (BS EN 1052-3:2002)*.

British Standards Institute. (2011). *Methods of test for masonry units. Determination of compressive strength (BS EN 772-1:2011)*.

British Standards Institute. (2019). *Methods of test for mortar for masonry. Determination of flexural and compressive strength of hardened mortar (BS EN 1015-11:2019)*.

Brocks, W., Cornec, A., & Scheider, I. (2003). *Computational aspects of nonlinear fracture mechanics*. Institute of Materials Research, GKSS Research Centre.

Burroughs, P., Hughes, T. G., Hee, S., & Davies, M. C. R. (2002). Passive pressure development in masonry arch bridges. *Proceedings of the Institution of Civil Engineers-Structures and Buildings*, *152*(4), 331-339.

Callaway, P., Gilbert, M., & Smith, C. C. (2012). Influence of backfill on the capacity of masonry arch bridges. *Proceedings of the Institution of Civil Engineers - Bridge Engineering*, *165*(3), 147-157. https://doi.org/10.1680/bren.11.00038

Carol, I., López, C. M., & Roa, O. (2001). Micromechanical analysis of quasi-brittle materials using fracture-based interface elements. *International Journal for numerical methods in Engineering*, *52*(1-2), 193-215.

Catbas, F., Pakzad, S., Racic, V., Pavic, A., & Reynolds, P. (Eds.). (2013). *Topics in Dynamics of Civil Structures, Volume 4: Proceedings of the 31st IMAC, A Conference on Structural Dynamics, 2013*. Springer Science & Business Media.

Cavicchi, A., & Gambarotta, L. (2005). Collapse analysis of masonry bridges taking into account arch–fill interaction. *Engineering Structures*, *27*(4), 605-615.

Chatterjee, S. (1985). Assessment of old bridges. *Highways & Transportation*, *33*(2), 18-22.

Chen, W. F., & Saleeb, A. F. (1982). *Constitutive Equations for Engineering Materials. V. 1. Elasticity and Modeling*. Wiley.

Coccia, S., Di Carlo, F., & Rinaldi, Z. (2015). Collapse displacements for a mechanism of spreading-induced supports in a masonry arch. *International Journal of Advanced Structural Engineering (IJASE)*, *7*, 307-320.

Colla, C., McCann, D. M., & Forde, M. C. (2002). Using construction history as an aid to masonry bridge assessment. In *Proceedings of the International Conference Railway Engineering 2002, London*.

Corradi, M., & Filemio, V. (2004). A brief comparison between mechanical aspects and construction of arch bridges during the XVIIIth and XIXth centuries. In P. Roca & C. Molins (Eds.), *Arch Bridges IV–Advances in Assessment, Structural Design and Construction* (pp. 79-86). CIMNE.

Crisafulli, F. J. (1997). *Seismic behaviour of reinforced concrete structures with masonry infills* [PhD thesis, University of Canterbury].

Cundall, P. A., & Strack, O. D. (1979). A discrete numerical model for granular assemblies. *geotechnique*, *29*(1), 47-65.

Curtin, W. G., Shaw, G., Beck, J. K., Bray, W. A., & Easterbrook, D. (2008). *Structural masonry designers' manual*. John Wiley & Sons.

D'Altri, A. M., de Miranda, S., Castellazzi, G., & Sarhosis, V. (2018). A 3D detailed micro-model for the in-plane and out-of-plane numerical analysis of masonry panels. *Computers & structures*, *206*, 18-30.

D'Altri, A. M., Sarhosis, V., Milani, G., Rots, J., Cattari, S., Lagomarsino, S., Sacco, E., Tralli, A., Castellazzi, G., & de Miranda, S. (2020). Modeling strategies for the computational analysis of unreinforced masonry structures: review and classification. *Archives of computational methods in engineering*, *27*(4), 1153-1185.

Davey, N. (1953). *Tests on Road Bridges, National Building Studies Research Paper No. 16*. HMSO.

De Felice, G., De Santis, S., Lourenço, P. B., & Mendes, N. (2016). Methods and Challenges for the Seismic Assessment of Historic Masonry Structures. *International Journal of Architectural Heritage*, *11*(1), 143-160. https://doi.org/10.1080/15583058.2016.1238976

De Matías, J., Berenguer, F., Cortés, J. P., De Sanjosé, J. J., & Atkinson, A. (2013). Laser Scanning for the Geometric Study of the ALCÁNTARA Bridge and Coria Cathedral. *ISPRS-International Archives of the Photogrammetry, Remote Sensing and Spatial Information Sciences*, *1*(1), 51-56.

De Rubeis, A. (1998). On the definition of the geometrical safety factor of masonry arches. In *Arch Bridges* (pp. 119-122). CRC Press.

De Santis, S., & de Felice, G. (2014). A fibre beam-based approach for the evaluation of the seismic capacity of masonry arches. *Earthquake Engineering & Structural Dynamics*, *43*(11), 1661-1681.

Drosopoulos, G., Stavroulakis, G., & Massalas, C. (2008). Influence of the geometry and the abutments movement on the collapse of stone arch bridges. *Construction and Building Materials*, *22*(3), 200-210.

Elbeskeri, R. E. (2011). *A study of the bond performance of brickwork triplets made using modified mortar* [PhD thesis, University of Salford].

Fairfield, C. A., & Ponniah, D. A. (1994). Model tests to determine the effect of fill on buried arches. *Proceedings of the Institution of Civil Engineers-Structures and Buildings*, *104*(4), 471-482.

Fanning, P. J., Boothby, T. E., & Roberts, B. J. (2001). Longitudinal and transverse effects in masonry arch assessment. *Construction and Building Materials*, *15*(1), 51-60.

Ferrero, C., Calderini, C., Portioli, F., & Roca, P. (2021). Large displacement analysis of dry-joint masonry arches subject to inclined support movements. *Engineering Structures*, *238*, 112244.

Forgács, T., Sarhosis, V., & Ádány, S. (2021). Shakedown and dynamic behaviour of masonry arch railway bridges. *Engineering Structures*, *228*, 111474.

Forgács, T., Sarhosis, V., & Bagi, K. (2017). Minimum thickness of semi-circular skewed masonry arches. *Engineering Structures*, *140*, 317-336.

Foti, D., Vacca, V., & Facchini, I. (2018). DEM modeling and experimental analysis of the static behavior of a dry-joints masonry cross vaults. *Construction and Building Materials*, *170*, 111-120.

Franck, S. A., Bretschneider, N., & Slowik, V. (2020). Safety analysis of existing masonry arch bridges by nonlinear finite element simulations. *International Journal of Damage Mechanics*, *29*(1), 126-143.

Frangopol, D., & Tsompanakis, Y. (2014). *Maintenance and safety of aging infrastructure*. CRC Press.

Frézier, A. F. (1738). *La théorie de la pratique de la coupe des pierres et des bois, pour la construction des voûtes et autres parties de bâtiments civils et militaires ou traité de stéréotomie à l'usage de l'architecture* (Vol. 2). J.-D. Doulsseker le fils.

Galassi, S., Misseri, G., & Rovero, L. (2021). Capacity assessment of masonry arches on moving supports in large displacements: Numerical model and experimental validation. *Engineering Failure Analysis*, *129*, 105700.

Giamundo, V., Sarhosis, V., Lignola, G., Sheng, Y., & Manfredi, G. (2014). Evaluation of different computational modelling strategies for the analysis of low strength masonry structures. *Engineering Structures*, *73*, 160-169.

Gibbons, N., & Fanning, P. J. (2016). Progressive cracking of masonry arch bridges. *Proceedings of the Institution of Civil Engineers-Bridge Engineering*, *169*(2), 93-112.

Gilbert, M. (1993). *The behaviour of masonry arch bridges containing defects* [PhD Thesis, University of Manchester].

Gilbert, M., & Melbourne, C. (1994). Rigid-block analysis of masonry structures. *Structural Engineer*, *72*(21).

Gilbert, M., Nguyen, D. P., & Smith, C. C. (2007). Computational limit analysis of soil-arch interaction in masonry arch bridges. In P. B. Lourenco, D. V. Oliveira, & A. Portela (Eds.), *Proceedings of the 5th International Conference on Arch Bridges, 12-14 September 2007* (pp. 633-640). University of Minho, Department of Civil Engineering.

Gilbert, M., Smith, C., Wang, J., Callaway, P. A., & Melbourne, C. (2007). Small and large-scale experimental studies of soil-arch interaction in masonry bridges. In *5th International Conference on Arch Bridges ARCH* (Vol. 7, pp. 381-388).

Gilbert, M., Smith, C. C., Hawksbee, S. J., & Melbourne, C. (2013). Modelling soil-structure interaction in masonry arch bridges. In J. Radic, M. Kuster, & Z. Savor (Eds.), *Proceedings of the 7th International Conference on Arch Bridges* (pp. 613-620). SECON-CSSE.

Giordano, A., Mele, E., & De Luca, A. (2002). Modelling of historical masonry structures: comparison of different approaches through a case study. *Engineering Structures*, *24*(8), 1057-1069.

Goodman, R. E., Taylor, R. L., & Brekke, T. L. (1968). A model for the mechanics of jointed rocks. *Journal of the Soil Mechanics and Foundations Division*, *94*, 637-659.

Greco, F., Leonetti, L., Luciano, R., Pascuzzo, A., & Ronchei, C. (2020). A detailed micro-model for brick masonry structures based on a diffuse cohesive-frictional interface fracture approach. *Procedia Structural Integrity*, *25*, 334-347.

Grosman, S., Bilbao, A. B., Macorini, L., & Izzuddin, B. A. (2021). Numerical modelling of three-dimensional masonry arch bridge structures. *Proceedings of the Institution of Civil Engineers-Engineering and Computational Mechanics*, *174*(2), 96-113.

Harding, J. E., Parke, G. A. R., & Ryall, M. J. (1993). *Bridge Management: Inspection, Maintenance, Assessment, and Repair*. Elsevier Applied Science.

Haynes, J. (2020). *Bridge Engineering: A text for civil engineering students studying bridge design*. Kindle Direct. https://www.amazon.co.uk/

Haynes, J., Naggasa, A., Augusthus-Nelson, L., El-basir, F., & Alsaleh, A. (2019). *Modeling the behavior of radially pinned brick triplets* 9th International Conference on Arch Bridges, Porto, Portugal.

Hendry, A. (1998). *Structural masonry*. Bloomsbury Publishing.

Hendry, A., & Royles, R. (1985). Acoustic emission observations on a stone masonry bridge loaded to failure. In *Proceedings of Proceedings of the 2nd International Conference on Structural Faults and Repair Engineering* (pp. 285-291). Technics Press.

Hendry, A. W., Davies, S. R., Royles, R., Ponniah, D. A., Forde, M. C., & Komeyli–Birjandi, F. (1986). *Load test to collapse on a masonry arch bridge at Bargower, Strathclyde* https://trl.co.uk/reports/CR26

Hernoune, H., Benabed, B., Kanellopoulos, A., Al-Zuhairi, A. H., & Guettala, A. (2020). Experimental and numerical study of behaviour of reinforced masonry walls with NSM CFRP strips subjected to combined loads. *Buildings*, *10*(6), 103.

Heyman, J. (1969). The safety of masonry arches. *International Journal of Mechanical Sciences*, *11*(4), 363-385.

Heyman, J. (1982). *The masonry arch*. Ellis Horwood.

Heyman, J. (1996). *Arches, vaults and buttresses. Collected essays*. Variorum, Ashgate Publishing.

Heyman, J. (1998). *Structural analysis: a historical approach*. Cambridge University Press.

Hodgson, J. A. (1996). *The behaviour of skewed masonry arch bridges* [PhD Thesis, University fo Salford].

Hojdys, Ł., Kamiński, T., & Krajewski, P. (2013). Experimental and numerical simulations of collapse of masonry arches. In J. Radic, M. Kuster, & Z. Savor (Eds.), *Proceedings of the 7th International Conference on Arch Bridges* (pp. 739-746). SECON-CSSE.

Hubert, G. (1714). *Traité des Ponts*. Cailleau.

Huerta Fernández, S. (2006). Galileo was wrong: The geometrical design of masonry arches. *Nexus Network Journal*, *8*(2), 25-52.

Hughes, T. G. (1995). Analysis and assessment of twin-span mansonry arch bridges. *Proceedings of the Institution of Civil Engineers. Structures and buildings*, *110*(4), 373-382.

Hughes, T. G., & Blackler, M. J. (1997). A review of the UK masonry arch assessment methods. *Proceedings of the Institution of Civil Engineers. Structures and buildings*, *122*(3), 305-315.

Jagadeesh, T. R., & Jayaram, M. A. (2004). *Design Of Bridge Structures* (2nd ed.). PHI Learning Pvt. Ltd.

Kamiński, T. (2008). *Mesomodelling of masonry arches* 6th International Conference AMCM,

Kareem, K. M., Abdulla, K. F., Panto, B., & Cunningham, L. S. (2022). Numerical simulation of the in-plane lateral response of RC infill frames using a FEM-DMEM modelling approach. *Journal of Building Engineering*, *51*, 104305.

Kaushik, H. B., Rai, D. C., & Jain, S. K. (2007). Stress-strain characteristics of clay brick masonry under uniaxial compression. *Journal of Materials in Civil Engineering*, *19*(9), 728-739.

Kim, J. J., Fan, T., Reda Taha, M. M., & Shrive, N. G. (2014). Warning Signs of Impending Failure of Historical Masonry Structures. *9th International Masonry Conference*, *28*(3), 65-70.

Koksal, H. O., Doran, B., Kuruscu, A. O., & Altönsoy, F. (2010). *Modelling the in-plane behavior of unreinforced masonry walls* MONUBASIN-8th International Symposium on the Conservation of Monuments in the Mediterranean Basin,

Koksal, H. O., Doran, B., Kuruscu, A. O., & Kocak, A. (2016). Elastoplastic Finite Element analysis of masonry shear walls. *KSCE Journal of Civil Engineering*, *20*(2), 784-791.

Labuz, J. F., & Zang, A. (2012). Mohr–Coulomb failure criterion. *Rock Mechanics and Rock Engineering*, *45*(6), 975-979.

Li, Y., & Wierzbicki, T. (2009). *Mesh-size effect study of ductile fracture by non-local approach.* SEM Annual Conference, Albuquerque, New Mexico, June 1–4.

LimitState. (2019). *LimitState:RING Manual*. https://www.limitstate.com/ring

Liu, B., Drougkas, A., & Sarhosis, V. (2023). A material characterisation framework for assessing brickwork masonry arch bridges: From material level to component level testing. *Construction and Building Materials*, *397*, 132347.

Liu, W. B., Gheni, M., & Yu, L. (2011). Effect of mesh size of finite element analysis in modal analysis for periodic symmetric struts support.

Liu, Y., & Glass, G. A. (2013). Choose the Best Element Size to Yield Accurate FEA Results While Reduce FE Models's Complixity. *British Journal of Engineering and Technology*, *1*, 13-28.

Livesley, R. K. (1978). Limit analysis of structures formed from rigid blocks. *International Journal for Numerical Methods in Engineering*, *12*(12), 1853-1871. https://doi.org/10.1002/nme.1620121207

Logan, D. L. (2016). *A first course in the finite element method*. Cengage Learning.

Loo, Y.-C., & Yang, Y. (1991). Cracking and failure analysis of masonry arch bridges. *Journal of Structural Engineering*, *117*(6), 1641-1659.

Lotfi, H. R., & Shing, P. B. (1994). Interface model applied to fracture of masonry structures. *Journal of Structural Engineering*, *120*(1), 63-80.

Lourenço, P. (1996). *Computational strategy for masonry structures* [PhD thesis, Delft University of Technology and DIANA Research].

Lourenço, P. B. (1998). Experimental and numerical issues in the modelling of the mechanical behaviour of masonry. In P. Roca, J. L. González, E. Oñate, & P. B. Lourenço (Eds.), *Structural Analysis of Historical Constructions II* (pp. 57-91). CIMNE.

Lourenço, P. B. (2002). Computations on historic masonry structures. *Progress in Structural Engineering and Materials*, *4*(3), 301-319.

Lourenço, P. B., & Rots, J. G. (1997). Multisurface interface model for analysis of masonry structures. *Journal of engineering mechanics*, *123*(7), 660-668.

Lourenço, P. B., Rots, J. G., & Blaauwendraad, J. (1998). Continuum model for masonry: parameter estimation and validation. *Journal of Structural Engineering*, *124*(6), 642-652.

Lucio, N., & Bartolomeo, V. (2015). Assessment of Masonry Arch Bridges using FEM and Elasto-Plastic Model. In I. J. Rudas (Ed.), *Recent Researches in Mechanical and Transportation Systems* (pp. 193-198). http://www.wseas.us/e-library/conferences/2015/Salerno/ICTA/ICTA-27.pdf

Macorini, L., & Izzuddin, B. A. (2011). A non-linear interface element for 3D mesoscale analysis of brick-masonry structures. *International Journal for numerical methods in Engineering*, *85*(12), 1584-1608.

Mang, H. A., Lackner, R., Meschke, G., & Mosler, J. (2003). *Computational Modeling of Concrete Structures*. Elsevier.

Martín-Caro Álamo, J. A. (2013). *Puentes de fábrica: los puentes ferroviarios dentro del patrimonio industrial* [Factory bridges: The railway bridges within the industrial heritage]. ADIF - Administrador de Infraestructuras Ferroviarias.

McKenzie, W. M. (2001). *Design of structural masonry*. Palgrave New York.

Melbourne, C., & Gilbert, M. (1995). The behaviour of multiring brickwork arch bridges. *Structural Engineer*, *73*(3).

Melbourne, C., Gilbert, M., & Wagstaff, M. (1995). The behaviour of multi-span masonry arch bridges. In C. Melbourne (Ed.), *Arch Bridges. Proceedings of the First International Conference on Arch Bridges held at Bolton, UK 3-6 September 1995* (pp. 489-497). Thomas Telford.

Melbourne, C., & Hodgson, J. (1995). The behaviour of skewed brickwork arch bridges. Arch Bridges: Proceedings of the First International Conference of Arch Bridges,

Melbourne, C., McKibbins, L. D., Sawar, N., & Sicilia Gaillard, C. (2006). *Masonry arch bridges: condition appraisal and remedial treatment*. CIRIA.

Melbourne, C., & Tomor, A. K. (2004a). *Fatigue Behaviour of Un-reinforced Masonry Arches (Arch tests A, G, C, E, M, O)*. University of Salford, School of Computing, Science and Engineering. http://www.smart.salford.ac.uk/research.php-research=fatigue.html

Melbourne, C., & Tomor, A. K. (2004b). Fatigue performance of composite and radial-pin reinforcement on multi-ring masonry arches. In *Fourth International Conference on Arch Bridges, Barcelona*.

Melbourne, C., & Tomor, A. K. (2005). *Effect of weak/deteriorated masonry on the performance of arch bridges (Arch tests RS)*.

Melbourne, C., Wang, J., Tomor, A., Holm, G., Smith, M., Bengtsson, P., Bien, J., Kaminski, T., Rawa, P., & Casas, J. (2007). Masonry arch bridges background document D4. 7. In *Sustainable Development Global Change & Ecosystems Integrated Project*. Sixth Framework Programme.

Melbourne, C., Wang, J., & Tomor, A. K. (2007). A new masonry arch bridge assessment strategy (SMART). *Proceedings of the Institution of Civil Engineers - Bridge Engineering*, *160*(2), 81-87. https://doi.org/10.1680/bren.2007.160.2.81

Milani, G., & Lourenço, P. B. (2012). 3D non-linear behavior of masonry arch bridges. *Computers & structures*, *110*, 133-150.

Miller, D., Noland, J., & Feng, C. (1979). Factors influencing the compressive strength of hollow clay unit prisms. Proceedings 5th International Brick Masonry Conference.,

Mohebkhah, A., Tasnimi, A. A., & Moghadam, H. A. (2008). Nonlinear analysis of masonry-infilled steel frames with openings using discrete element method. *Journal of Constructional Steel Research*, *64*(12), 1463-1472.

Mojsilović, N., Simundic, G., & Page, A. W. (2010). Load tests on masonry wallettes subjected to cyclic shear. In *Proceedings of the 8th International Masonry Conference* (pp. 487-496).

More, S. T., & Bindu, R. (2015). Effect of mesh size on finite element analysis of plate structure. *International Journal of Engineering Science and Innovative Technology*, *4*(3), 181-185.

Naggasa, A. (2022). *Behaviour of the masonry arch bridge under foundation movement* Proceedings of the 24th Young Researchers Conference, London, UK. https://pure.coventry.ac.uk/ws/portalfiles/portal/56033242/Proceedings_YRC_2022.pdf

Naggasa, A., Augusthus Nelson, L., & Haynes, B. (2018). *Use of finite element analysis to investigate the structural behaviour of masonry arch bridges subject to foundation settlement* 10th International Masonry Conference, Milan, Italy.

Ng, K.-H. (1999). *Analysis of masonry arch bridges*

Nobile, L., & Bartolomeo, V. (2014). Methods for the assessment of historical masonry arches. In *Proceedings 5th European Conference of Civil Engineering (ECCIE'14)* (pp. 160-167).

Ochsendorf, J. (2006). Masonry arch on spreading supports. *Structural Engineer*, *84*(2), 29-34.

Ochsendorf, J. A., Hernando, J. I., & Huerta, S. (2004). Collapse of masonry buttresses. *Journal of Architectural Engineering*, *10*(3), 88-97.

Oliveira, D. V., Lourenço, P. B., & Lemos, C. (2010). Geometric issues and ultimate load capacity of masonry arch bridges from the northwest Iberian Peninsula. *Engineering Structures*, *32*(12), 3955-3965.

Olofsson, I., Elfgren, L., Bell, B., Paulsson, B., Niederleithinger, E., Sandager Jensen, J., Feltrin, G., Täljsten, B., Cremona, C., & Kiviluoma, R. (2005). Assessment of European railway bridges for future traffic demands and longer lives–EC project "Sustainable Bridges". *Structure and Infrastructure Engineering*, *1*(2), 93-100.

Page, J. (1993). *Masonry arch bridges. TRL-State of the art review, Department of Transport*. HMSO.

Pelà, L., Cervera Ruiz, M., & Roca Fabregat, P. (2010, 4th to 7th July 2010). FEM analysis of orthotropic masonry walls via localized damage models. The eight International masonry conference

Pippard, A. J. S. (1947). *The experimental study of structures*. Arnold.

Pippard, A. J. S. (1948). The Approximate Estimation of Safe Loads on Masonry Bridges. In Institution of Civil Engineers (Ed.), *The civil engineer in war: A symposium of papers on war-time engineering problems* (pp. 365-372). ICE.

Pippard, A. J. S., & Ashby, R. J. (1939). An experimental study of the voussoir arch (includes photographs, plates and appendix). *Journal of the Institution of Civil Engineers*, *10*(3), 383-404.

Pippard, A. J. S., Tranter, E., & Chitty, L. (1936). The mechanics of the voussoir arch (includes appendix). *Journal of the Institution of Civil Engineers*, *4*(2), 281-306.

Plumbridge, W., Matela, R., & Westwater, A. (2003). Non-linear Finite Element Analysis. *Structural Integrity and Reliability in Electronics: Enhancing Performance in a Lead-Free Environment*, 305-318.

Ponnuswamy, S. (2008). *Bridge engineering*. Tata McGraw-Hill Education.

Raut, P. (2012). Impact of mesh quality parameters on elements such as beam, shell and 3D solid in structural analysis. *International Journal of Engineering Research Applications*, *2*, 99-103.

Rots, J. G. (1991). Numerical simulation of cracking in structural masonry. *HERON*, *36*(2), 49-63.

Rots, J. G. (1997). *Structural masonry: an experimental/numerical basis for practical design rules*. AA Balkema.

Royles, R., & Hendry, A. W. (1991). Model tests on masonry arches. *Proceedings of the Institution of Civil Engineers*, *91*(2), 299-321. https://doi.org/10.1680/iicep.1991.14997

Ryall, M. J., Parke, G. A. R., & Harding, J. E. (2000). *The manual of bridge engineering*. Thomas Telford.

Salter, G. (2013). *Spanning the Centuries - The Masonry Arch*. https://www.engineersireland.ie/EngineersIreland/media/SiteMedia/groups/societies/heritage/Gary-Salter-11-11-2013.pdf?ext=.pdf

Sarhat, S. R., & Sherwood, E. G. (2014). The prediction of compressive strength of ungrouted hollow concrete block masonry. *Construction and Building Materials*, *58*, 111-121.

Sarhosis, V. (2011). *Computational modelling of low bond strength masonry* [PhD Thesis, University of Leeds].

Sarhosis, V., De Santis, S., & de Felice, G. (2016). A review of experimental investigations and assessment methods for masonry arch bridges. *Structure and Infrastructure Engineering*, *12*(11), 1439-1464. https://doi.org/10.1080/15732479.2015.1136655

Sarhosis, V., Forgács, T., & Lemos, J. V. (2019a). A discrete approach for modelling backfill material in masonry arch bridges. *Computers & structures*, *224*, 106108.

Sarhosis, V., Forgács, T., & Lemos, J. V. (2019b). Modelling backfill in masonry arch bridges: a DEM approach. Proceedings of ARCH 2019: 9th International Conference on Arch Bridges,

Sarhosis, V., & Lemos, J. (2018). A detailed micro-modelling approach for the structural analysis of masonry assemblages. *Computers & structures*, *206*, 66-81.

Sarhosis, V., Oliveira, D. V., & Lourenco, P. B. (2016). On the Mechanical Behavior of Masonry. In V. Sarhosis, K. Bagi, J. V. Lemos, & G. Milani (Eds.), *Computational Modeling of Masonry Structures Using the Discrete Element Method* (pp. 1-27). IGI Global. https://doi.org/10.4018/978-1-5225-0231-9.ch001

Sarhosis, V., & Sheng, Y. (2014). Identification of material parameters for low bond strength masonry. *Engineering Structures*, *60*, 100-110.

Schlegel, R., & Rautenstrauch, K. (2004). Failure analysis of masonry shear walls. *Numer Model Discrete Mater*, 15-18.

Segurado, J., & Llorca, J. (2004). A new three-dimensional interface finite element to simulate fracture in composites. *International journal of solids and structures*, *41*(11), 2977-2993.

Seward, D. (2014). *Understanding structures: analysis, materials, design*. Palgrave Macmillan.

Shing, P. B., Lofti, H. R., Barzegarmehrabi, A., & Bunner, J. (1992). Finite element analysis of shear resistance of masonry wall panels with and without confining frames. In *Proceeding, 10th World Conference On Earthquake Engineering* (pp. 2581-2586). AA Balkema.

Silva, R., Costa, C., & Arêde, A. (2019). Nonlinear analysis of a multispan stone masonry bridge under railway traffic loading. International Conference on Arch Bridges,

Silva, R., Costa, C., & Arêde, A. (2022). Numerical methodologies for the analysis of stone arch bridges with damage under railway loading. *Structures*, *39*, 573-592.

Singhal, V., & Rai, D. C. (2014). Suitability of half-scale burnt clay bricks for shake table tests on masonry walls. *Journal of Materials in Civil Engineering*, *26*(4), 644-657.

Smith, H. S. (1965). *The world's great bridges*. Harper & Row.

Susila, G. A., Mandal, P., & Swailes, T. (2016). Strengthening and retrofitting strategy for masonry (new build construction in Indonesia). Applied Mechanics and Materials,

Susila, I. G. A., Mandal, P., & Swailes, T. (2015). ANALISA DRIFT-BASE FRAGILITY: EVALUASI HASIL EKSPERIMENTAL DAN NUMERIKAL DINDING BATU BATA DAN RANGKA KAYU.

Sutcliffe, D., Yu, H., & Page, A. (2001). Lower bound limit analysis of unreinforced masonry shear walls. *Computers & structures*, *79*(14), 1295-1312.

Tao, Y. (2013). *Fibre reinforced polymer (FRP) strengthened masonry arch structures* [PhD Thesis, University of Edinburgh].

Taylor, N., & Mallinder, P. (1993). The brittle hinge in masonry arch mechanisms. *Structural Engineer*, *71*(20), 359-366.

Thavalingam, A., Bicanic, N., Robinson, J. I., & Ponniah, D. A. (2001). Computational framework for discontinuous modelling of masonry arch bridges. *Computers & structures*, *79*(19), 1821-1830.

Tralli, A., Chiozzi, A., Grillanda, N., & Milani, G. (2020). Masonry structures in the presence of foundation settlements and unilateral contact problems. *International journal of solids and structures*, *191*, 187-201.

Tsutsui, M., Mizuta, Y., & Sakata, T. (2010, 2010). Line of thrust and theoretical load of masonry arch bridge.

Tubaldi, E., Macorini, L., & Izzuddin, B. A. (2018). Three-dimensional mesoscale modelling of multi-span masonry arch bridges subjected to scour. *Engineering Structures*, *165*, 486-500.

UIC Code 778-3R. (1994). Recommendations for the assessment of the load carrying capacity of existing masonry and mass-concrete arch bridges. *Paris: International Union of Railways*.

Van Zijl, G. (2004). Masonry Shear Response Characterisation. *Masonry International*, *17*(1), 26-32.

Wang, J. (2004). *The three dimensional behaviour of masonry arches* [PhD thesis, University of Salford]. http://usir.salford.ac.uk/id/eprint/26960/

Wang, J., Haynes, B., & Melbourne, C. (2013). A comparison between the MEXE and Pippard's methods of assessing the load carrying capacity of masonry arch bridges. *ARCH '13. Proceedings of the 7th International Conference on Arch Bridges. Trogir-Split, Croatia. October 4-6, 2013.*, *1*(1), 589-596. http://usir.salford.ac.uk/id/eprint/29550/

Wang, J., & Melbourne, C. (2010). Mechanics of MEXE method for masonry arch bridge assessment. *Proceedings of the Institution of Civil Engineers-Engineering and Computational Mechanics*, *163*(3), 187-202.

Weekes, L. (1998). *Internal experimental report in support of journal paper "The behaviour of masonry jack arches"* [Unpublished report]. Univeristy of Salford

Yang, Y. (1991). *Progressive failure analysis of masonry arch bridges* [PhD Thesis, University of Wollongong].

Yazdani, M., & Habibi, H. (2021). Residual Capacity Evaluation of Masonry Arch Bridges by Extended Finite Element Method. *Structural Engineering International*, 1-12.

Ye, C., Acikgoz, S., Pendrigh, S., Riley, E., & DeJong, M. (2018). Mapping deformations and inferring movements of masonry arch bridges using point cloud data. *Engineering Structures*, *173*, 530-545.

Zampieri, P., Amoroso, M., & Pellegrino, C. (2019). The masonry buttressed arch on spreading support. *Structures*, *20*, 226-236.

Zampieri, P., Faleschini, F., Zanini, M. A., & Simoncello, N. (2018). Collapse mechanisms of masonry arches with settled springing. *Engineering Structures*, *156*, 363-374.

Zampieri, P., Zanini, M. A., Faleschini, F., Hofer, L., & Pellegrino, C. (2017). Failure analysis of masonry arch bridges subject to local pier scour. *Engineering Failure Analysis*, *79*, 371-384.

Zhang, S., Richart, N., & Beyer, K. (2018). Numerical evaluation of test setups for determining the shear strength of masonry. *Materials and Structures*, *51*(4), 1-12.

Zhang, Y. (2015). *Advanced nonlinear analysis of masonry arch bridges* [PhD Thesis, Imperial College London].

Zhang, Y., Macorini, L., & Izzuddin, B. A. (2016). Mesoscale partitioned analysis of brick-masonry arches. *Engineering Structures*, *124*, 142-166.

Zhang, Y., Macorini, L., & Izzuddin, B. A. (2017). Numerical investigation of arches in brick-masonry bridges. *Structure and Infrastructure Engineering*, *14*(1), 14-32.

Zhang, Y., Tubaldi, E., Macorini, L., & Izzuddin, B. A. (2018). Mesoscale partitioned modelling of masonry bridges allowing for arch-backfill interaction. *Construction and Building Materials*, *173*, 820-842.

Zienkiewicz, O. C., Taylor, R. L., & Zhu, J. Z. (2005). *The finite element method: its basis and fundamentals*. Elsevier.

Zucchini, A., & Lourenço, P. B. (2002). A micro-mechanical model for the homogenisation of masonry. *International journal of solids and structures*, *39*(12), 3233-3255.

Zucchini, A., & Lourenço, P. B. (2004). A coupled homogenisation–damage model for masonry cracking. *Computers & structures*, *82*(11-12), 917-929.

Appendix A

This section shows numerical simulation deformation shapes of three movement kinds, horizontal, vertical, and rotational, which were applied to the right abutment using gravity before the movement was applied to the right abutment.

As mentioned in chapters 5 and 6, the experimental test of arch G had two dead loads applied on the arch barrel. Hence, the validated model had the same two dead loads. The purpose of these simulations with the arch's self-weight is to demonstrate that the crack locations in the masonry arch will differ from the models with dead loads of 10kN per arch quarter span.

These simulations show that crack locations are different for models subject to self-weight only, and subject to self-weight and dead loads.

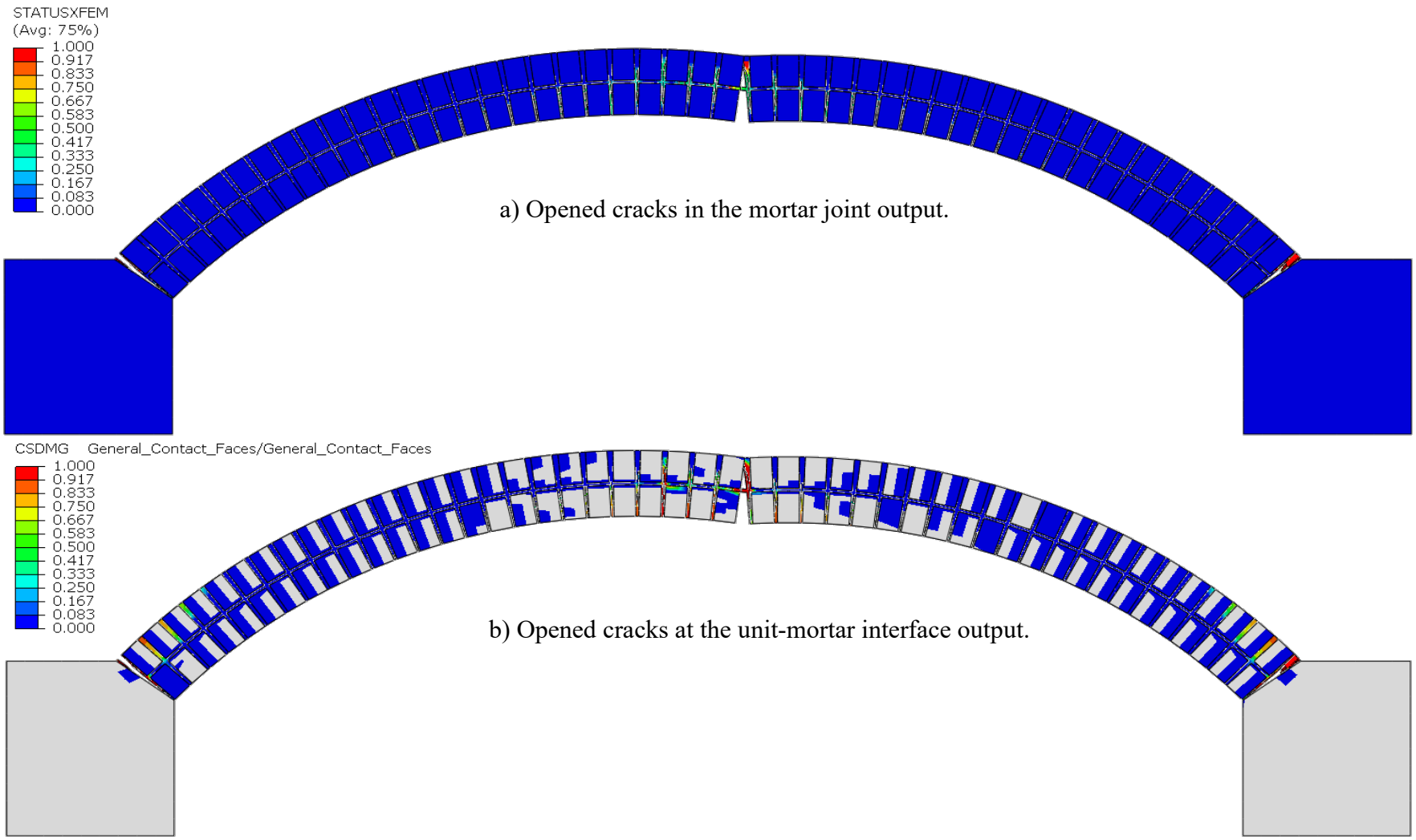

Figure 7-1: Self-weight arch deformed shape subjected to the horizontal movement of 80mm.

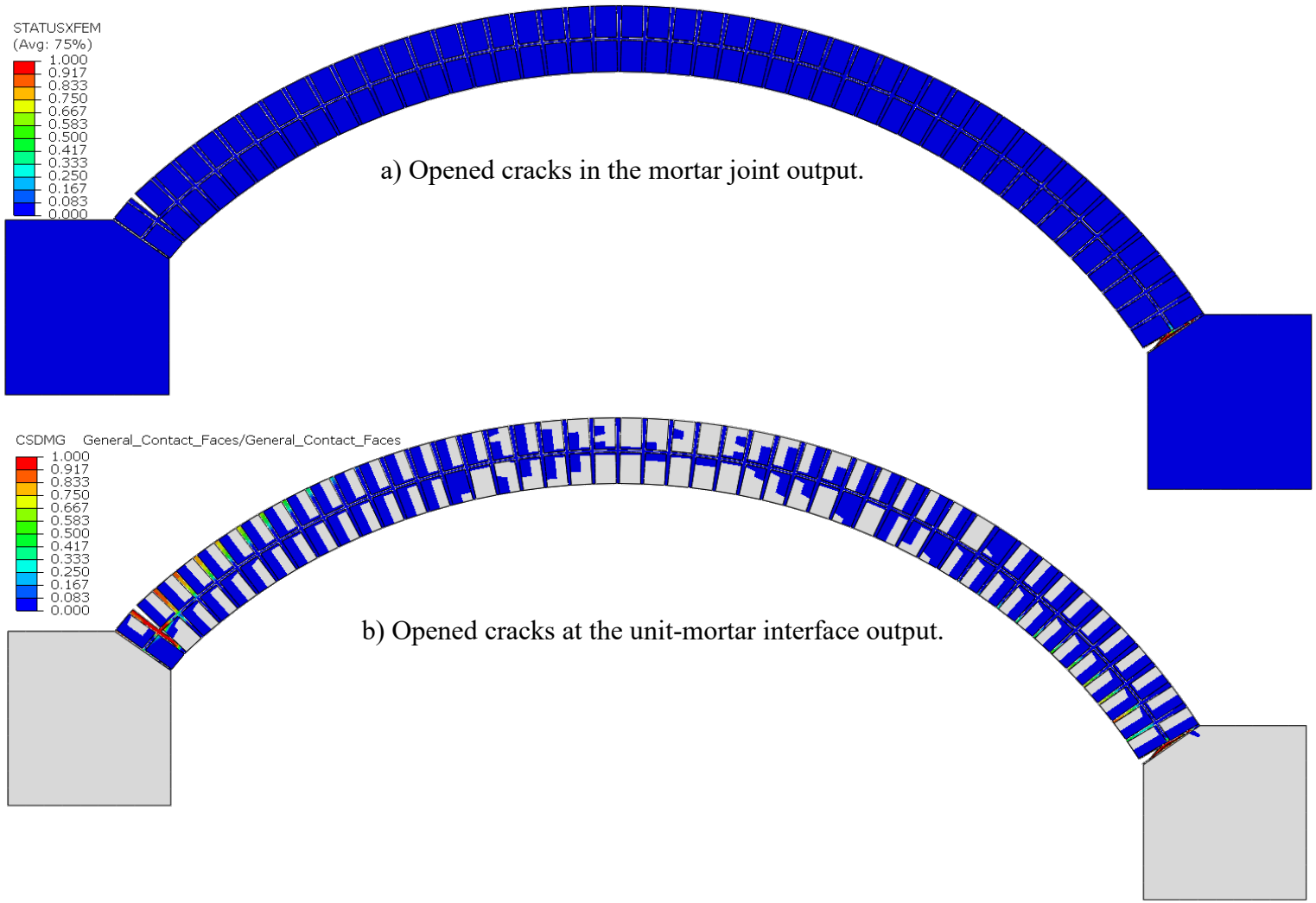

Figure 7-2: Self-weight arch deformed shape subjected to the vertical movement of 65mm.

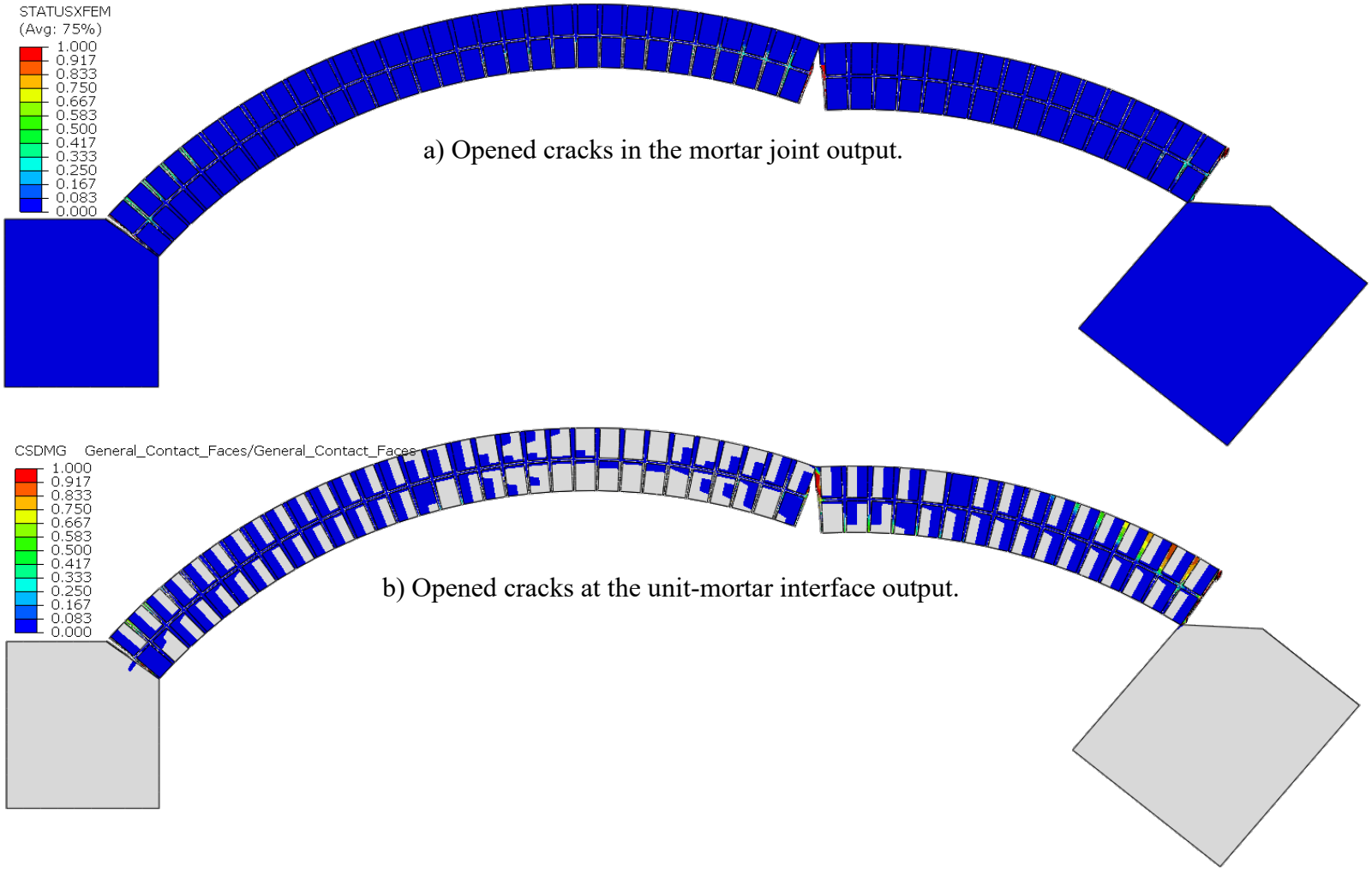

Figure 7-3: Self-weight arch deformed shape subjected to the rotational movement of 20 radians.

Appendix B

Double displacement influence in combination abutment movements without steel plate on the arch barrel:

This section includes the same masonry arch barrel model movement type as in section 6.4, but without steel plates at the quarter and three-quarter span of the arch to investigate the load being applied with an angle instead of a flat surface as in previous sections.

The simulation analysis process in this section is similar to the previous section regards load arrangement, which was simulated in three static steps, where gravity was applied in the first step. The two dead loads were applied at the quarter and three-quarter span without steel plates, and then the displacement was applied at the right abutment, as shown in Figure 7-8.

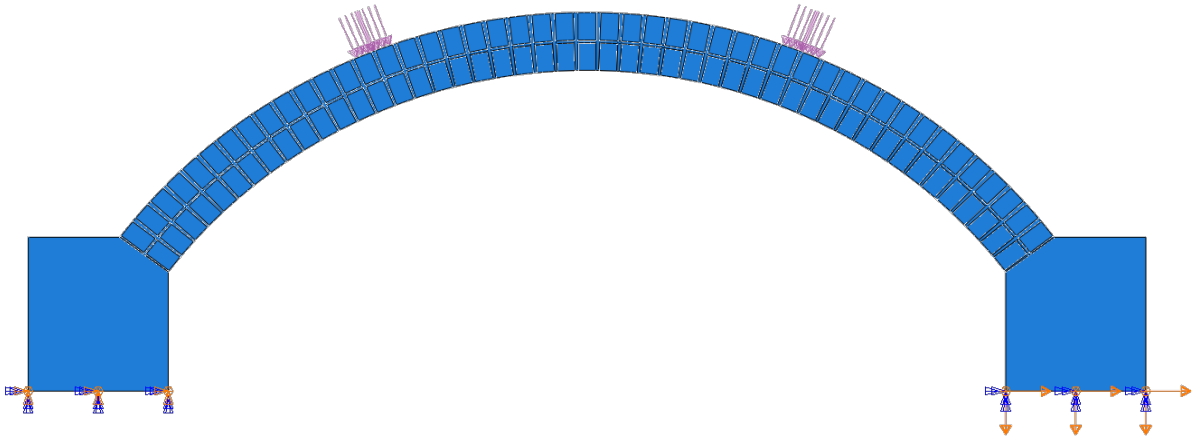

Figure 7-4: Masonry arch model without steel plates of foundation movements of 10mm horizontally and 5mm vertically.

The masonry arch barrel could not be tested without steel plates and applying the load with an angle instead of flat surfaces. Still, these simulations investigate this issue's behaviour in modelling simulation.

Small cracks started to appear in the left side of the arch above the springing extrados after the movement started in the right abutment. As a result of the increased displacement value at the right abutment, these small cracks started to progress in the direction of the arch intrados.

Due to the increased displacement value, the second crack was located at the arch quarter span above the dead load point as shown in Figure 7-9.

The third crack occurred at the three-quarter span under the dead load point at the intrados towards the extrados of the arch barrel. Although the crack had occurred here, it can be noted that the crack reached the upper ring. Figure 7-9bshows the numerical simulation final stage of the masonry arch failure deformed shape. Also, this joint had a shear failure, where the intact mortar interface split from the brick interface.

The arch barrel displaced 9mm vertically at the quarter span under the dead load position and 7mm vertically at the three-quarter span under the dead load position. These measurements were taken after the final analysis of this model.

This combination movements analysis of 10mm horizontal and 5mm vertical highlighted four significant cracks in the arch barrel. This type of analysis, where two movements are simultaneously occurring, allows a better understating of the arch barrel subjected to double combination movements.

Since displacement is greatest at the quarter span, tensile and compressive stresses will be greatest at this point. Since the depth of tension cracking is larger, there is little mortar remaining in contact to transmit the arch compression forces and crushing was indicated in the displaced shape.

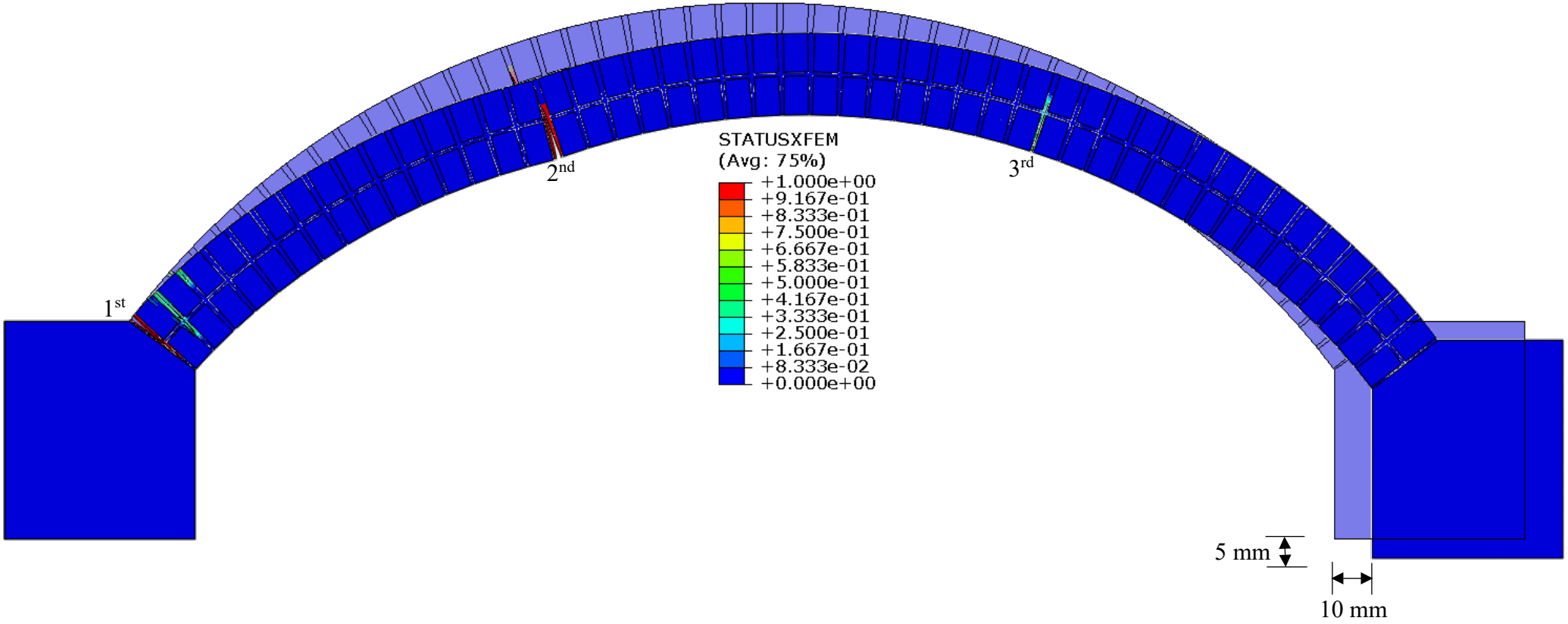

Figure 7-5: Deformed shape of 10mm horizontal and 5mm vertical combination movements.

The combination movements for the second analysis, displacement values at the right abutment were 5mm horizontally and 10mm vertically. The analysis steps, material properties and the model geometry are identical to the previous analysis.

The masonry arch model behaved linearly during the start of the abutment movement. However, the first cracks started to appear at the left springing and one crack at the three-quarter span under the dead load point. The cracks continued to develop within the joints since the abutment kept moving in two directions simultaneously. As a result, this caused the formation of two hinges and other major cracks around the two hinges in the arch barrel.

The first hinge started to occur above the left springing at the extrados, where the joint experienced high compression at the intrados. Also, the joint entirely cracked across the width of the arch at the final stage. The second hinge occurred at the intrados under high compression at the extrados as shown in Figure 7-10.

The arch barrel displaced 4.5mm vertically at the quarter span under the dead load position and 10.6mm vertically at the three-quarter span under the dead load position, where these measurements were taken after the final analysis of this model. Therefore, this led to a significant effect on the load capacity and the stiffness of the arch barrel.

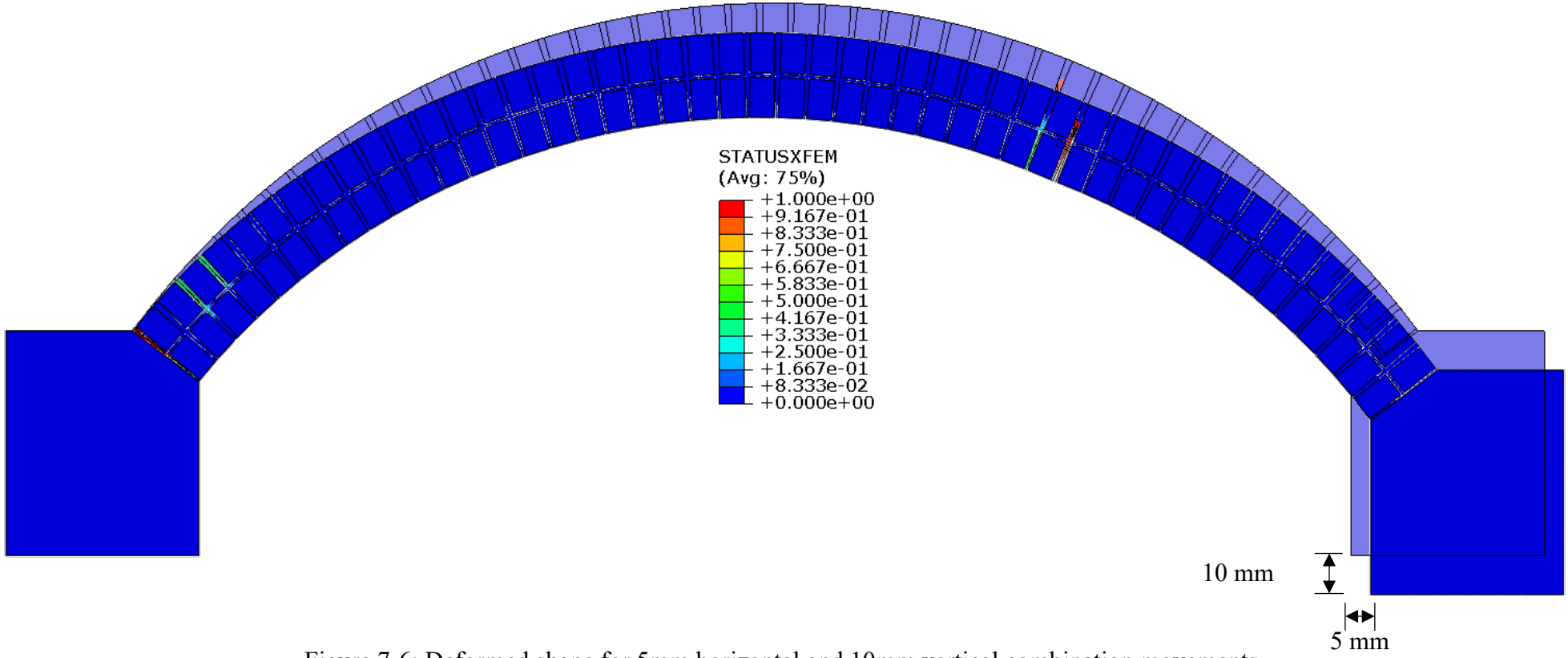

Figure 7-6: Deformed shape for 5mm horizontal and 10mm vertical combination movements.

Appendix C

This section presents a graphical summary of the observed structural behaviour for the movement combinations.

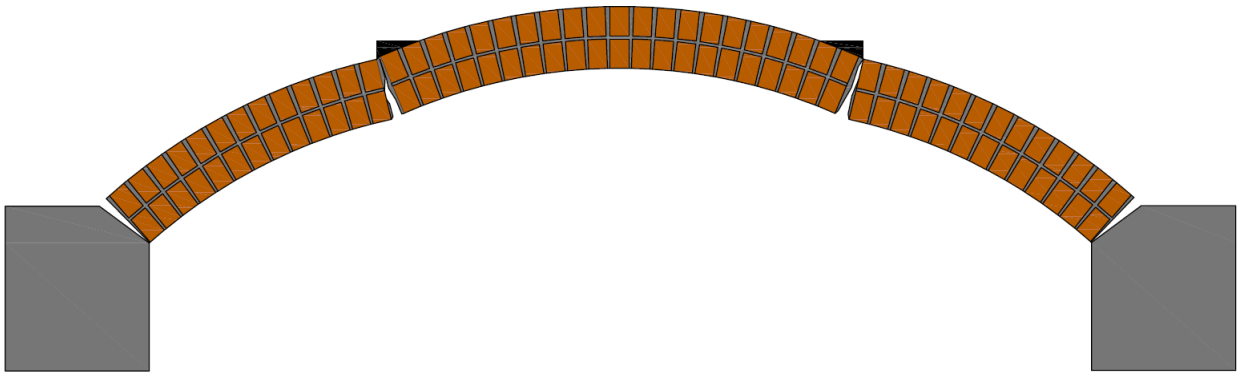

Figure 7-7: Masonry arch behaviour subjected to horizontal 30mm displacement.

Foundation horizontal movement increments lead to four hinge mechanism forms, as shown in Figure 7-7.

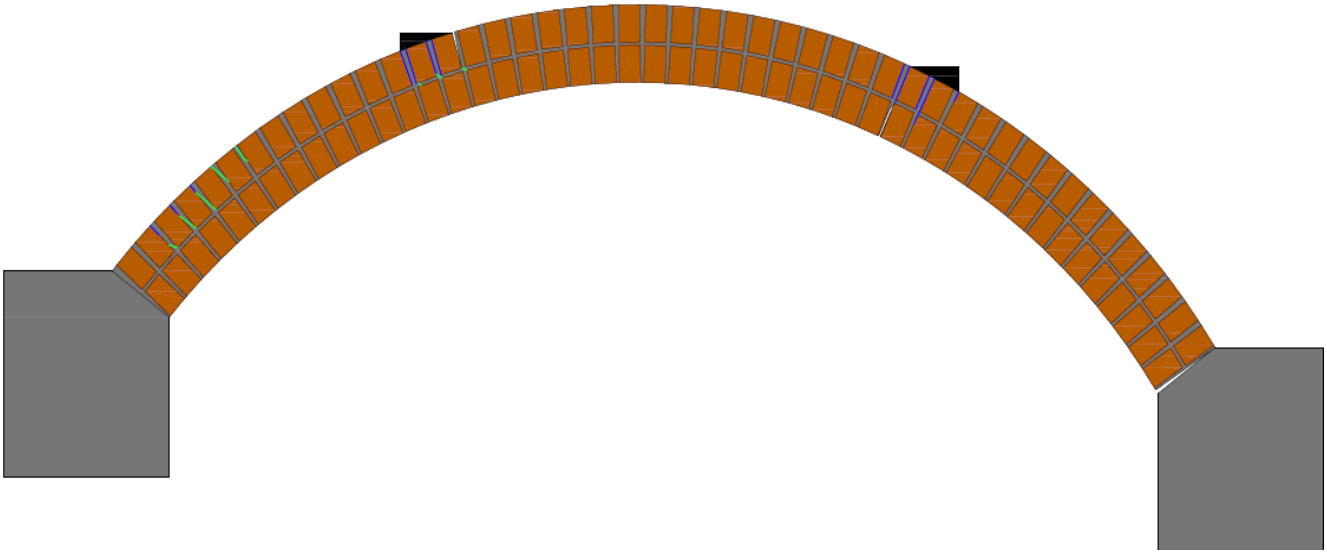

Figure 7-8: Masonry arch behaviour subjected to vertical 30mm displacement.

Foundation vertical movement increments lead to increased cracks opened at the unit-mortar interface and cracks in the mortar joint but to a significantly smaller extent than horizontal movement. The majority of the arch barrel appears to remain intact, as shown in Figure 7-8.

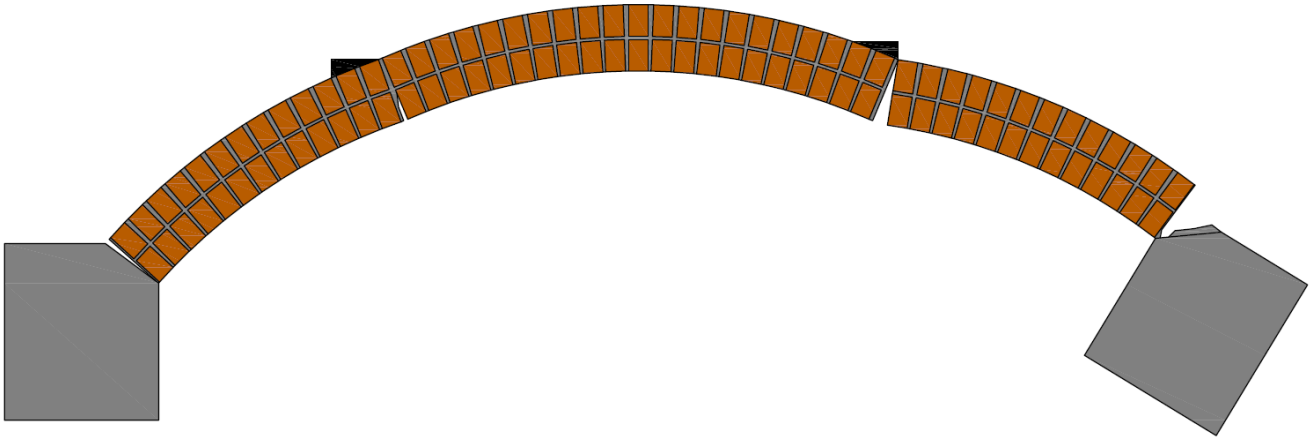

Figure 7-9: The masonry arch behaviour subjcted to 15mm (0.06 rad) rotational movement.

The rotational foundation movement shows complex structural behaviour. The 15mm (0.06 rad) movements show four major cracks, especially at the right and left side abutments and the three-quarter span, as shown in Figure 7-9.

Figure 7-10 shows the behaviour of a masonry arch subjected to 5mm (0.02 rad) rotational movement, providing three significant cracks. Two cracks occurred at the intrados of the right and left side abutments and the third crack at the extrados centre of the arch barrel.

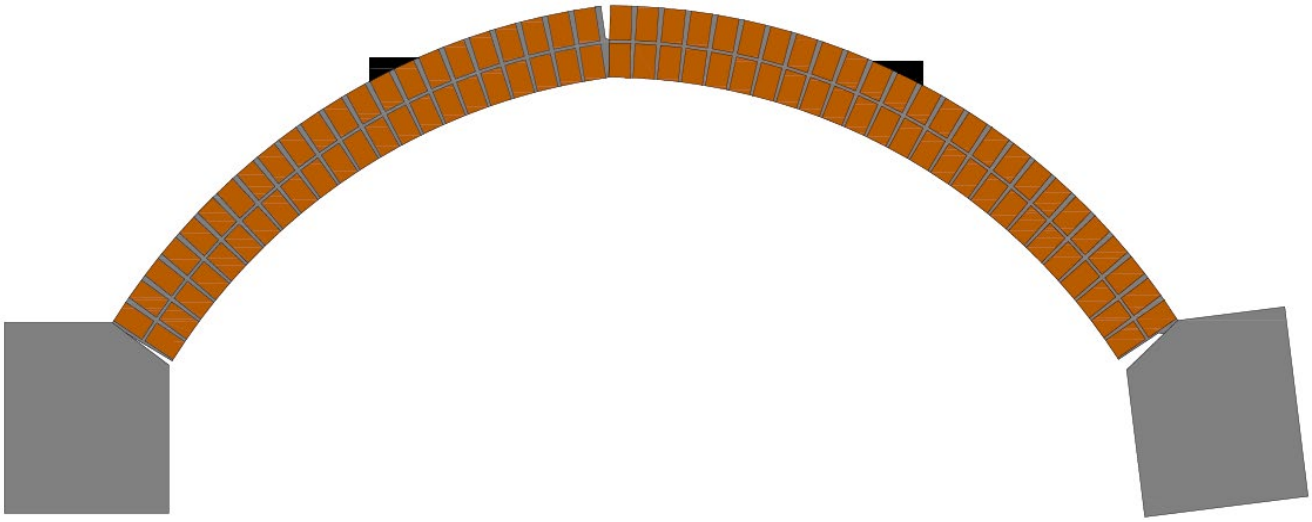

Figure 7-10: The masonry arch subjected to 5mm (0.02 rad) rotational movement.

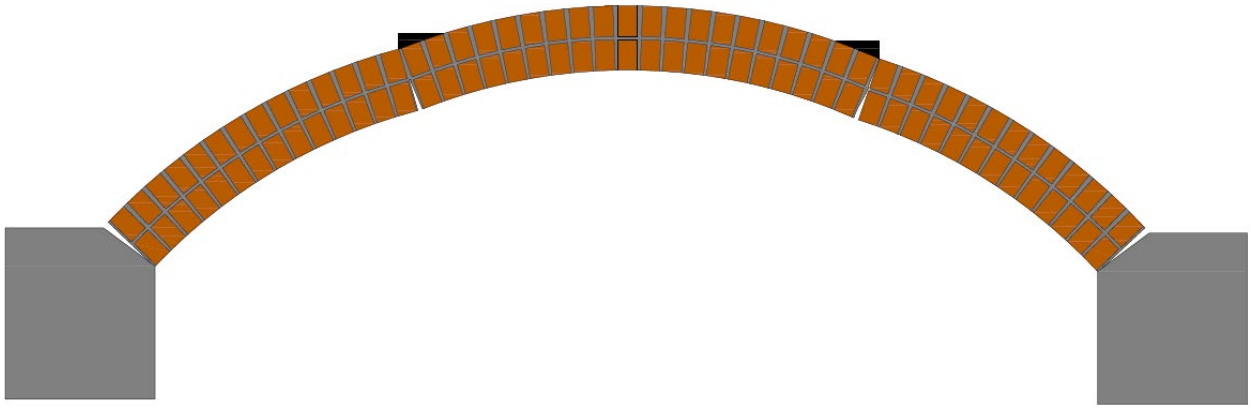

Figure 7-11: The masonry arch behaviour subjected to horizontal movement 8mm then live load.

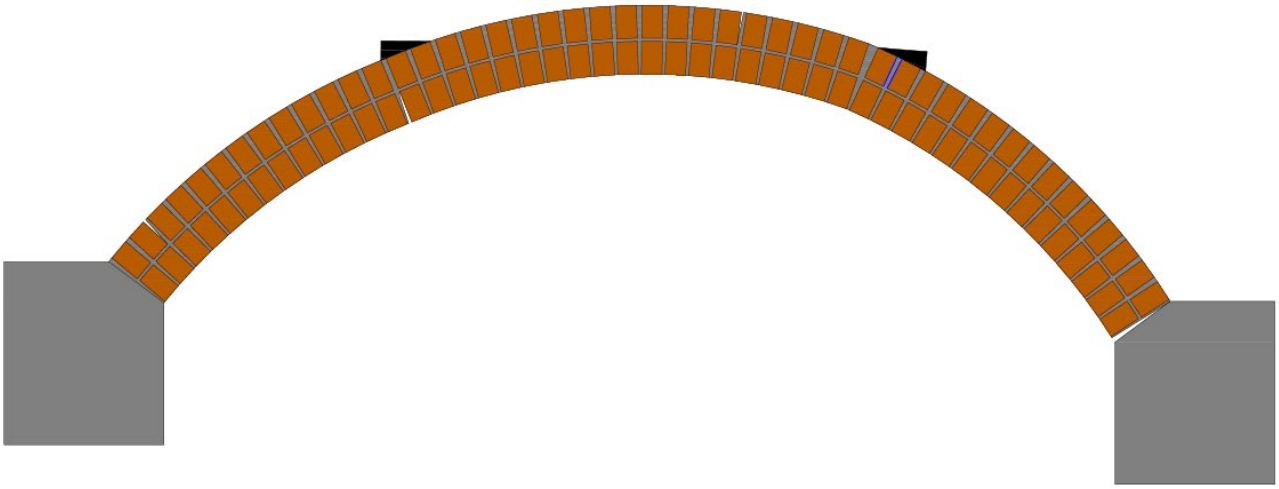

Figure 7-12: The masonry arch behaviour subjected to vertical movement 10mm then live load.

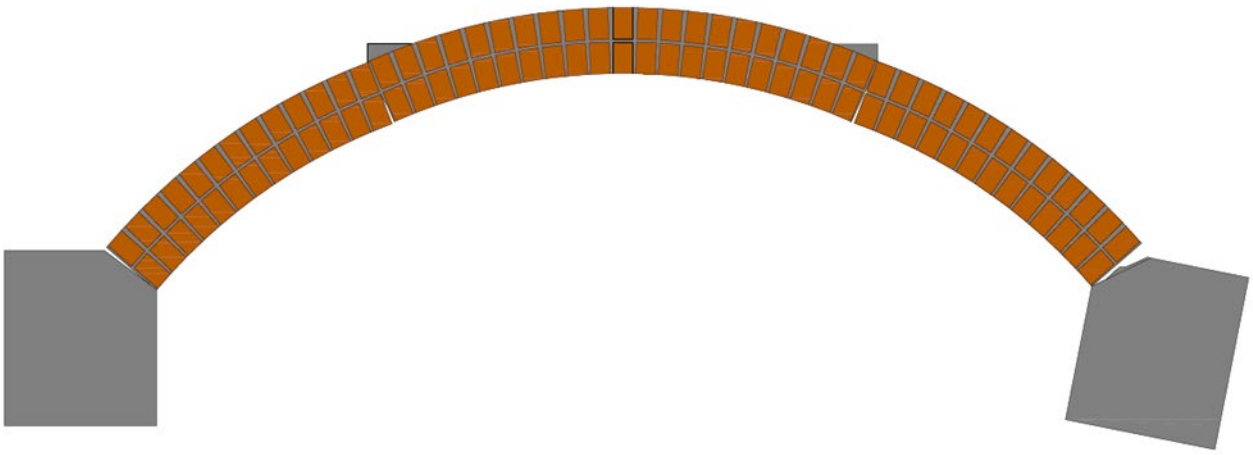

Figure 7-13: The masonry arch behaviour subject to rotational movement and then live load.